Title
Metabolic and Mechanical Maturation of hiPSC-Derived Heart-on-a-Chip platform for COVID-19 Therapeutics Cardiac Liability Screens

Author
Charrez, Berenice Lucie Mechthild

Publication Date
2020

Peer reviewed|Thesis/dissertation

Metabolic and Mechanical Maturation of hiPSC-Derived Heart-on-a-Chip platform for COVID-19 Therapeutics Cardiac Liability Screens

By

Bérénice Lucie Mechthild Charrez

A dissertation submitted in partial satisfaction of the
Requirements for the degree of
Joint Doctor of Philosophy
With University of California, San Francisco
In
Bioengineering
In the
Graduate Division
Of the
University of California, Berkeley

Committee in Charge:

Professor Kevin E. Healy, Chair
Professor Bruce R. Conklin
Professor Aaron M. Streets
Professor Evan W. Miller

Fall 2020

Metabolic and Mechanical Maturation of hiPSC-Derived Heart-on-a-Chip platform for COVID-19 Therapeutics Cardiac Liability Screens

by
Bérénice Lucie Mechthild Charrez

University of California, Berkeley

Abstract

Metabolic and Mechanical Maturation of hiPSC-Derived Heart-on-a-Chip platform for COVID-19 Therapeutics Cardiac Liability Screens

By

Bérénice Lucie Mechthild Charrez

Joint Doctor of Philosophy

With University of California, San Francisco, in Bioengineering

University of California, Berkeley

Professor Kevin E. Healy, Chair

With highly regulated safety requirements, the average cost of drug development is $2.5B, which has increased by more than 9-fold since 1979. Preclinical studies include both *in vitro* and *in vivo* studies in non-human models to determine the efficacy and toxicity of the compound before any administration to people. However, no commonly used platforms accurately predict drug effects on patients, since they do not mimic human physiology. The fourth reason for drug withdrawal from the market in the last 70 years were unexpected side effects on the cardiovascular system, such as toxicity or dysfunction of the heart, associated with life-threatening conditions. Accordingly, the FDA has mandated that all drugs must be screened for the potential to alter ventricular repolarization prior to human studies. There is an urgent need to develop tools to diminish time and costs of the drug development pipeline while getting safer and more efficient cardiotoxicity screening. A big advance for 2D in vitro assays for cardiotoxicity screens was the discovery of human induced pluripotent stem cells (hiPSC) from which cardiomyocytes with patients genetics could be derived. However, one challenge remains : hiPSC-derived cardiomyocytes (CM) show immature metabolic and mechanical properties, questioning their prognostic capabilities. In this thesis, we demonstrated that the combination of 3D culture of hiPSC-CM in microphysiological systems (heart-on-a-chip) with fatty-acid based media, synergized to promote maturation of hiPSC-CM metabolism and electrophysiology. To further improve the maturation of the tissues we screened through different confinement chamber designs and selected for parameters that enhance mechanical, morphological and

contractility outcomes of tissues. As the COVID-19 pandemic hit, we saw the opportunity for our matured cardiac system to rapidly predict cardiotoxicity associated with potential therapeutics (hydroxychloroquine combination with azithromycin) in a mock clinical trial experimental design as well as in an acute dose escalation study. The high content system can help clinicians rapidly evaluate safety properties of potential therapeutics in crisis times to hopefully accelerate access of patients to treatment.

Für Joachim,
Um zu beenden was du angefangen hast.
Pour Lucie,
Que tu en sois fière là où tu es.

Table of Contents

Acknowledgements

First and foremost, I would like to thank Kevin Healy, for the unique opportunity to perform my master thesis in his laboratory, to offer me a scientist position after that which finally turned into a full PhD degree as part of UC Berkeley and UCSF joint Bioengineering program. I would like to thank him for providing me the financial support to perform outstanding research in a cutting-edge field, for giving me the freedom to work and write a full grant to improve the understanding of nanoplastics on human health, and for allowing me to present my work at international conferences. I am thankful for his mentorship, time and patience to help me strive in the program and receive the *Lloyd Award For Excellent Research And Great Leadership*. With the start of the COVID-19 pandemic within my last year of PhD, he allowed me to use our platform for the common good as a toxicity screen for COVID-19 therapeutics, and use all data acquired as final chapters of this thesis. During the writing of the thesis, he showed great virtual support, allowing me to successfully graduate by December 2020. I am thankful for everything I learned and the countless opportunities this PhD will give me to impact the medical sector.

I would like to thank my thesis committee, Aaron Streets, Evan Miller and Bruce Conklin, for their precious time and advice throughout the second half of my program. They helped me better define my priorities and timelines. They also showed a lot of support and advice about research but also post-graduation job search. I would also like to thank Lydia Sohn and Todd McDevitt, who were part of my qualifying exam committee and helped me better define research priorities.

I am extremely grateful to Nathaniel Huebsch, who mentored me during my master thesis and early in my PhD program. We worked very closely on developing the maturation media, which led to a publication in Nature BME. He is a very knowledgeable and inspiring scientist with whom I continuously learned. As he left the Healy Lab, we worked virtually together to address the reviewers' comments. He was extremely patient and responsive, and further helped me with career advising.

I am thankful to Verena Charwat, who joined the lab half way through my thesis. We shared a lot of the experimental work, and had a really good dynamic. In stressful times like deadlines or pandemic, together with Brian Siemons, we complemented each other and could run experiments rapidly for quality results. I was also honored to be a close friend for both of them outside lab. Thanks for the memories, whether in lab, on a boat or at barbecues.

I would like to thank Andrew Edwards, who started as collaborator as part of the computational physiology team of Simula. He is an extremely knowledgeable person, very patient and willing to help. I will be eternally thankful for his support throughout my thesis. His responsiveness and objectiveness helped me focus, take the right decisions, and get the most learning out of any situation.

I have had the pleasure to work closely with Åshild Telle from the Simula team. Our virtual communication was quite efficient. She brought me back into maths and coding, with a lot of patience. It allowed me to automate most of the data analysis and accelerate my graduation.
David Cleres was a master student in the Healy Lab, who helped me automate the contraction force measurement. A very talented engineer whom I really enjoyed working with, and learn image processing from.

As part of Simula, I would like to thank Henrik Finsberg for writing scripts that helped us get high quality data, faster. He was also very patient and responsive anytime I had a question regarding his scripts, as I was modifying them to better fit our needs. Sam Wall was extremely helpful in the mechanical analysis of the tissue and gave Åshild and I precious advices. Aslak Tveito and Karoline Jaegger had an important role in the computational modeling of the tissue's maturation, I thank them both for their time on that project through which I learned a lot. And, of course I need to thank Aslak for having me at the Simula summer school, a very interesting and fun program I had the honor to be part of.

Finally, I want to thank all past and present lab members of the Healy Lab, who helped with experimental support, advising, as well as mental support in challenging times. They have all brought joy to my work, and outside work during lunches, at beer gardens, parties or adventures. I specially want to thank Ishan Goswami, Gabriel Neiman, Nikhil Deveshwar, Silvio Weber, Felipe Lee-Montiel, Shane Browne and David Wartmann with whom we have had countless debates and laughs.

I will be eternally grateful to my family, Eleonore, Joseph and Olivier for their support and the constant inspiration they give me to strive for the best at any given situation. They have always empowered me to follow my passions and my dreams, to make the best decisions for my career, whether it would entail leaving to the other side of the world, seeing them only twice a year, or taking part in very risky adventures. Eleonore has given me the love for networking, for team work and for communities. She has inspired me to work hard and empower women around me to reach for their dreams. She has been extremely supportive and I owe her every unique experience that made me who I am. Thank you for being so strong and inspiring. I grew up trying to show Joseph what I was capable of, to make him proud of my achievements. I have, since, strengthened that mindset which brought me to always seek for the limits towards a bigger impact. I have always been admirative of his passion and talent for his work and will honor that by directing my life decisions into enjoying everything I do, and do it well. I will always remember the fun moments spent with Olivier and am looking forward to having the opportunity to share a lot more adventures with him. I am very proud of him and am constantly trying to improve myself and my achievements to inspire him. I love you all.

I would not have been where I am now without Ana and Diamantino, both of them having educated me since my youngest age. I have learned from them how to believe in my abilities despite what others could say. Ana taught me how to work around fear and hesitation to stand for my beliefs and my dreams. She has also inspired me to respect, be inclusive and respected by anyone regardless of their background, age or nationality. Thanks for always being here.

Thank you Nicolas for following me wherever I am since the beginning, for believing in me and my abilities to reach for the moon. Thank you for being my best friend, my confident, my encyclopedia, my life coach and my adventure partner. I am looking forward to spending precious moments with you in the near future.

For the past years, I have had the chance to live at the “Birdhouse”, an apartment in Berkeley with a nice view on the Golden Gate Bridge. What made it so special was all the people who shared it with me over the years. You have all enlightened my life, supported me in hard times, were great workout partners ; I will never forget our fondues and adventures. This goes to Ronan, Eloise, Melanie, Olivier, Daniele, Daniel, Arnaud, Adrien, Lucia, and others.

I have had a tremendous support from so many dear friends in the Bay Area during my thesis, from adventures, to parties, to dinners, career advices or mental support. My life at Berkeley would not have been the same without you all. Thank you Rosemary, Dan, Amer, Sabin, Samer, Fabien, Josh, Valentine, Thomas, Sevan, Ahmed, Simon, Lucas, Quentin, Gino, Felix, Fabian, Ben, Steele, Yu.

Sailing being such an important part of my life, I will be eternally thankful for all the team members of Paradox, Smart Recruiters, Velvet Hammer, Envolee, Viva Mexico, Orion, Centomiglia and any other boat I had the pleasure to sail on during my time here. A very special thanks to Peter, Jeff, Arthur, Jerome, Zach, Natalie, Hannah, Tom, Mark and Pearl.

I had the honor to be part of Cal Triathlon team for the last two years of my thesis. Starting from scratch, the coaches and the team helped me learn about the sports, about my body and my mental and physical abilities. Limits are much further than anyone can think, and this powerful thought helped me push through my PhD. Very special thanks to Thomas who got me into the sport and shared with me the outstanding adventure of participating to a full distance Ironman. I am also extremely grateful to Jonathan, an amazing training partner, and inspirational friend.

Far from the eyes but close to the heart are all my friends overseas, especially in Switzerland, who always send the right messages to make me laugh, and whom I would always look forward to see at our yearly reunion on December 31st. I especially think of Nicolas, Maxence, Daniel, Jane, Laureanne, Emilie, Jonathan, Samuel, Vil. With Francois, Sylvain, Martin, Adrien, Lauri and “Gerard” I have also shared unforgettable memories in the US.
I also want to thank Jonathan, Marc, Azat, Arabella, Noemie, Ezequiel, Malo, Sidney, Jade, Alec, Sandro, Pawel, Sylvain, Georges, Maxence, for being friends I can always count on.

I am grateful I had the opportunity to be part of the MaiTai community, through which I met inspiring leaders, successful investors and entrepreneurs who shared with me unique life stories and inspired me to follow their path into the entrepreneurial world. Sacha and Bill have always advised me and given me opportunities to understand and learn from their career. Thank you for believing in my leadership and entrepreneurial skills.

A small thought to the kitesurfing community who was an important part of my life in the early years of my thesis. Especially Nick, Amil, Joey, Nicolas, Stephans and Felix.

And thanks to everyone else who crossed my path in the past 4 years. It has been an amazing journey.

Chapter 1 Introduction

With highly regulated safety requirements, the average cost of drug development is $2.5B, which has increased by more than 9-fold since 1979. Moreover, the current drug development process lasts between 10 and 15 years, starting with the discovery of a new compound through research to its commercialization [1]. Only 10% of drugs that successfully enter clinical trials will finally be approved by the FDA[2, 3]. Drug development includes preclinical and clinical studies. In 2010, pre-clinical costs per drug accounted for 63% of the total costs (USD 1.1 billion) and 4-7 years to proceed with human clinical trials[4]. Preclinical studies include both *in vitro* and *in vivo* studies in non-human models to determine the efficacy and toxicity of the compound before any administration to people[5]. These studies are costly and poorly represent of the effect of the drug on humans. *In vitro* studies usually consist of experiments on two-dimensional (2D) monolayer cell culture. Because of their 2D properties, they are easy to handle and infrastructure exists for routine analysis; however, they lack the physiological and physical environment that influences *in vivo* tissues. Indeed, supporting cells and vascularization *in vivo* provides a controlled gradient of nutrients, paracrine factors and cytokines that highly influence the cells' maturation, proliferation and behavior[6, 7]. In addition, physical signaling such as pressure, electrical stimuli, or dynamic mechanical force, absent in an *in vitro* environment, have a critical role in development, maturation, morphology and repair[8]. *In vivo* platforms are also poorly representative of human response to certain drug compounds [9]. Nine out of ten experimental drugs fail in clinical studies[10] because neither 2-dimensional cell cultures (*in vitro*) or animal studies (*in vivo*) accurately predict the drug effect on the human body (**Figure 1A**), since they do not mimic the human physiology, notably regarding to ion channels, biological pathways and pharmacokinetic properties[11]. This issue is directly correlated to drug side effects, accounting for more than 110'000 deaths and 700'000 life-threatening disabilities per year[12].

Interestingly, the fourth reason for drug withdrawal from the market in the last 70 years were unexpected side effects on the cardiovascular system, such as toxicity or dysfunction of the heart, associated with life-threatening conditions[13]. Accordingly, the FDA has mandated that all drugs must be screened for the potential to alter ventricular repolarization prior to human studies. There is an urgent need to develop tools to diminish time and

costs of the drug development pipeline while getting safer and more efficient cardiotoxicity screening.

A big advance for 2D in vitro assays for cardiotoxicity screens of compounds was the discovery of induced pluripotent stem cells (iPSC), where differentiated mouse fibroblast were successfully reprogrammed into pluripotent stem cells[14], using four necessary factors, Oct3/4, Sox2, c-Myc, and Klf4 at specific timepoints. This discovery further enabled the reprogramming of human dermal fibroblasts and the differentiation of human iPSC (hiPSC) into cell types of the three germ layers[15]. hiPSCs are an ideal tool for disease modelling and personalized medicine as they can be generated from diseased patients' own cells. Due to their pluripotency and self-renewal capacity, any type of tissue from the three germ layers can be obtained in an unlimited amount through differentiation of hiPSCs. Research has thus been focused on developing protocols for differentiating them into specific cell types for drug screening, disease modelling [16] or potential cell-based therapy for neurodegenerative [17] or liver disorders[18] for example. iPSCs are also importantly used in the context of cardiovascular toxicity whereby 2D culture of hiPSC-derived cardiomyocytes (CM, [19, 20]) demonstrated successful pre-clinical outcomes as part of the CiPA initiative, which was initiated to assess the proarrhythmic risk of novel cardio therapeutics[21, 22].

However, one challenge remains : hiPSC-derived cardiomyocytes (CM) show immature metabolic and mechanical properties[23-26]. In particular, hiPSC-CM exhibit automaticity (spontaneous beating without electrical stimulation) and longer action potentials (445±73msec for ventricular-like hiPSC-CM, versus 270-300msec directly measured by patch-clamp of primary human adult left-ventricular cardiomyocytes)[27-32]. Furthermore, iPSC-CM lack t-tubules and show disorganized sarcomeres, leading to different excitation–contraction coupling properties. Additionally, hiPSC-CM showed an overexpression of Na+/Ca+ exchange and reduced repolarization leading to a higher sensitivity for drugs blocking L-type Ca2+ currents and K+ flow[33]. It is known that cellular behavior, function, regeneration and fate are affected by a 3D structure of the tissue[34] as well as the spatial and temporal control of physical and chemical micro-environmental cues[35]. Therefore, the development of a 3D *in vitro* model may help to overcome the limitations of 2D iPSC models by replicating *in vivo* conditions.

In the recent years, cardiac organoids became popular *in vitro* human models for cardiac drug screening. Cardiac organoids (**Figure 1B**) can be defined as an *in vitro* 3D cellular cluster capable of self-renewal and self-organization, and exhibiting similar organ functionality as the tissue of origin. These organoids rely on artificial extracellular matrices (ECM) to facilitate their self-organization[36]. They are more physiologically representative of human tissues than a cell monolayer and require less instrumentation and

manipulations than animal models. However, they also have several limitations. Organoid cultures lack native microenvironment, they have a necrotic core [37], they are unable to mimic in vivo factors and cytokine gradient as well as biomechanical forces and they depend on an artificial ECM[38].

Another example of engineered cardiac muscle is the so-called cardiopatch, developed by Shadrin et al.[39] (**Figure 1C**) where human pluripotent stem cell-derived cardiomyocytes were encapsulated in hydrogels and polymerized in molds before being cultured in media-containing well plates. Cardiopatches are free-floating dynamic culture of miniature, cylindrically shaped heart tissue that exhibited promising functionality. The main disadvantage is the complexity of the loading protocol and the dependency on hydrogel as structural support. Additionally, to measure biomechanical properties of the tissues, patches had to be manually cut and connected to external force transducers, further complexing the system.

There are several other engineered heart tissue systems, all of them mimicking *in vivo*-like micro-environment through 3D confinement[40] (**Figure 1D**), chronic electrical pacing[41, 42] (**Figure 1E**) or resting pre-load and strain[43-47] (**Figure 1F**). They have been shown to mature hiPSC-CM to some extent by enhancing physiologic hypertrophy, and lead to pharmacology more closely correlated to the one of the adult human heart. However, just like cardiopatches or organoids, EHM typically have big tissue constructs (>2mm long), making them expensive to fabricate. Additionally, since tissues are cultured in well-plates, the tissue to media volume ratio is not physiological, preventing relevant levels of biomarkers required for regulating cardiac homeostasis, while allowing for the potential accumulation of biological wastes.

To summarize :

- Drug development process is extremely cost and time intensive
- Despite high regulations, adverse drug reactions with cardiovascular liabilities are a significant problem
- The problem is due to state-of-the-art drug screening platforms (*in vitro* and *in vivo*) not mimicking the human cardiac physiology
- Typical *in vitro* platforms are 2D cardiomyocyte culture that lack physiological and physical environment of adult human tissues
- hiPSC-derived cardiomyocytes open new doors for disease modeling and patient specific drug screening, although their immature electrophysiology and mechanics questions their use
- hiPSC-derived 3D engineered heart tissues improve the prognostic capability by promoting physiologic hypertrophy. However, full electrophysiological or metabolic maturity of hiPSC-CM is not achieved. The systems are expensive due to

significant amounts of cells required, specific user knowledge is needed to handle the complex systems, they require invasive techniques for contraction measurements and do not have physiological tissue to media volume ratio

To solve the problems stated above, we decided to use microfluidics technology (**Figure 2A**). This technology is cheap and provides accurate flow control at a micron scale. Adapted from the semi-conductor field, microfluidics was initially used as an analysis system to replace traditional macro-scale assays and perform proof-of-concept experiments. These so-called lab-on-a-chip technologies reduce the sample volume needed, the cost of reagents, get faster response time, increase the scalability substantially for screening applications and provide more control and predictability of the microenvironment[48]. The platform also enables to get *in situ* monitoring of real-time electrical, mechanical, chemical, visual responses of biological processes through engineered biosensors such as cantilever, microelectrodes, fluorescence microscopes, or pH sensors. It is important to mention that materials used to fabricate microfluidics for biological applications require several properties: they have to allow free diffusion for small molecules and air, be optically clear for visual data analysis, biocompatible as well as cheap and easy to obtain. Polydimethylsiloxane (PDMS) is the most commonly used polymer for microfluidic device fabrication [49]. Microfluidic devices quickly evolved towards organ-on-a-chip technology, opening doors to novel drug toxicity screening and disease modelling applications for lung[50], kidney [51, 52], liver [53, 54] or heart[55, 56].

In my thesis, I used 3D confinement, controlled flow conditions and integrated mechanical and electrical sensors provided by microfluidics, with hiPSC-derived cells for cheap, controlled and reliable, drug screening platform, named the cardiac MPS [11]. The tissues in the cardiac MPS were composed of a combination of 80% CM and 20% stromal cells differentiated from the same hiPSC line (**Figure 2B**), to closely mimic cellular composition of adult heart tissue[57]. The cell combination was loaded into the cell chamber of the MPS, and in 2-3 days after loading, the cells self-arrange into a 3D micro-tissues (μ-tissues), combined with microfluidic “vasculature”, to create microscale systems that capture the geometrical structure of the native organs (e.g., ventricular myocardium). Integrated electrodes allow for point stimulation and electrical signal recording while PDMS anchors and pillars allow for tissue support and contraction force measurement respectively (**Figure 2C**). 3D confinement of the tissue promotes alignment of the cells in the longitudinal direction and their uniaxial and synchronized contraction (**Figure 2D, left**) where 65% of the vectors were oriented within +/- 25 degrees of the x-axis (**Figure 2D, right**), comparable to rat cardiac sections[58]. Sarcomeric immunostaining of tissues extracted from the MPS, confirm the uniaxial alignment of the tissue, at a cellular level (**Figure 2E**). Tissues stained for connexin 43, show some instances of transversal connexin expression (**Figure 2F**), a hallmark of adult ventricular myocardium [59].

An example of the predictive value of the cardiac MPS is best demonstrated with the drug Verapamil, that generates a false positive with hiPSC-CMs in 2D due to an unacceptable safety margin. Our MPS predicts a much higher safety margin of 18, in better concordance with large-scale tissue models from pigs and engineered heart tissue[60]. These observations are highly significant, since our cardiac MPS correctly predicted the safety of the drug, which 2D hiPSC-CM cultures did not. The cardiac MPS can generate low cost and high-content results comparable to the industry gold standard of human myocardial tissue slices, or isolated rat primary cardiomyocytes.

However, one problem remains : hiPSC derived cardiomyocytes do not show a fully mature electrophysiology, they exhibit immature CM properties, supported by the presence of connexin expression over the entire surface of the tissue, limiting their utility in regenerative medicine and disease modeling. Because we want our system to be as representative as possible to human physiology for drug screening, the second chapter of this thesis focuses on the development of a novel maturation media to improve the metabolic maturation of the MPS cardiac tissue. However, the combination of aligned, 3D culture in microphysiological systems with maturation media does not lead to consistent maturation of tissue mechanics or morphology. Therefore, chapter 3 focuses on further improving the maturation of the tissues by screening through different confinement chamber designs and selecting for parameters that enhance mechanical, morphological and contractility outcomes of tissues. As the COVID-19 pandemic hit, and clinicians were pressed to treat patients in critical stages without FDA approved protocols, clinical trials were started with repurposed anti-viral drugs. Hydroxychloroquine (HCQ) and azithromycin (AZM) combination therapy rapidly became the prominent treatment for hospitalized COVID-19 treatments. Unfortunately, each drug has known cardiac complications and little was known about the safety outcomes of their combination. We saw the opportunity for our matured cardiac system to rapidly predict cardiotoxicity associated with each drug and the polytherapy in a mock clinical trial experimental design, described in chapter 4. In the last months of my work, the FDA had revoked the emergency use authorization for HCQ and AZM as COVID-19 treatment that it granted 4 months prior. This triggered political and scientific debates illustrating important problems such as the authorization of potentially ineffective or unsafe therapeutics, while diverting resources from screening of effective drugs. I therefore wanted to better understand the effects of each drug and their combination by exposing MPS tissues to acute dose escalation of both compounds. The high content system could help clinicians rapidly evaluate safety properties of potential therapeutics in crisis times to hopefully accelerate access of patients to treatment and better allocate clinical resources.

1.1 Metabolically-Driven Maturation of hiPSC-Cell Derived Cardiac Chip

Metabolic cues like glucose levels are a key facet of the heart's soluble environment that may be particularly important to cardiomyocyte maturation. Postnatally, the heart switches from glycolysis to fatty-acid oxidation as its primary source of adenosine triphosphate[61, 62]. In chapter 2 of this document, we hypothesized that recapitulating postnatal switching could enhance electrophysiological and metabolic maturation of hiPSC-CM. Using Robust Experimental design, we identified a maturation media (MM) that improved calcium handling in MPS derived from two genetically distinct hiPSC sources and allowed the cardiac MPS to correctly assess false positive and negative drug response. In both genotypes, MM produced metabolic maturation, and a trend toward a more robust calcium transient and enhanced contractility at low extracellular calcium. Finally, we employed mathematical modeling and gene expression data to explain the observed changes in electrophysiology and pharmacology of MPS exposed to maturation media. In contrast, the same media had no effects on 2D hiPSC-CM monolayers. These results suggest that systematic combination of 3D confinement and metabolic cues can enhance the electrophysiological maturation of hiPSC-derived cardiomyocytes. These results also suggest that maturation media can both improve overall tissue physiology and minimize artificial differences in pharmacology of hiPSC-CM due to non-genetic sources of variability (e.g. clonal variation). Potentially, this can subsequently reveal true pharmacogenomic relationships.

1.2 Heart-on-a-chip design changes for improved loading efficiency, tissue contractility, and pharmacology response

In chapter 2, we demonstrate that the combination of aligned, 3D culture in microphysiological systems (MPS; heart-on-a-chip) with fatty-acid based media synergized to promote maturation of hiPSC-CM electrophysiology and metabolism for pharmacology results in more reminiscent adult human cardiomyocytes[63]. However, this approach did not lead to consistent maturation of tissue mechanics or morphology. In chapter 3, we further improve the maturation of the tissues by screening through different confinement chamber designs and selecting for parameters that enhance mechanical, morphological and contractility outcomes of tissues while enabling for robust cell loading and tissue formation in the systems.

Some of the parameters included fixed rigid anchors to act as structural support for the tissue. Additionally to the anchors, we iterated through designs that improved tissue quality and remodeling while allowing for contraction force measurements, a critical metric to be assessed for cardiotoxicity drug screening platform[64]. Inspired by epithelial cells traction force measurements[65-68], we integrated polydimethylsiloxane (PDMS) micro-

pillars in the cell chamber to measure contraction force through simple microscopy imaging and mathematical calculations. Compared to techniques involving external force transducers[69], this system is less invasive and not-terminal [68, 70]. The optimal pillar array design was further modified by varying chamber dimensions (such as width or length), hypothesizing that it would have an impact on mechanical outcomes. Indeed, 3D confinement promotes uniaxial and synchronized beating, which correlates to an increase in contraction force and physiologic hypertrophy[40, 43, 46]. To improve the robustness of the system, efficient and reproducible loading of cardiomyocytes in cell chambers is necessary. We therefore also varied the design of inlet valves[71] and used a design of experiment approach to efficiently identify the impact of each factor (length, width, valve) on tissue mechanics, or loading. The optimal factor dimensions were determined and used for the final design iteration, whereby mechanics, electrophysiology and pharmacology response were assessed. Importantly, tissues in the final preferred design successfully showed physiological responses to drugs targeting specific mechanical pathways, making our platform relevant to accelerate drug safety and efficacy screening. Together these results show the importance of mechanics and tissue morphology for improved prognostic capabilities of heart-on-a-chip systems.

1.3 In Vitro Safety "Clinical Trial" of the Cardiac Liability of Hydroxychloroquine and Azithromycin as COVID19 Polytherapy

Chapter 2 and 3 show that the improved metabolic and mechanical maturation of our system resulted in physiologically relevant electrophysiology, metabolism, mechanics and contractility. We also showed the ability of our platform to successfully exhibit physiological responses to drugs targeting specific mechanical or electrophysiological pathways, making our platform relevant to accelerate drug safety and efficacy screening. Chapter 4 will focus on extending the use of our matured platform as an analogous to a Phase I safety clinical trial, for better understanding and predicting cardiac liability associated with HCQ and AZM polytherapy and hopefully accelerate the access of patients to safe treatments.

When the World Health Organization declared a global pandemic on March 11th 2020, little was known about the pathogenesis of the severe acute respiratory syndrome coronavirus 2 (SARS-CoV-2). With the absence of FDA-approved medicines for the treatment or prevention of COVID-19, clinicians have been pressed to treat patients in critical stages without FDA approved protocols. They have therefore relied on several small-scale clinical studies to repurpose compounds approved by regulatory bodies as monotherapies in the hope of improving patient outcomes. Early clinical trials identified chloroquine (CQ), hydroxychloroquine (HCQ) and azithromycin (AZM) as promising drugs to help treat or reduce the effects of SARS-CoV-2 [72-76]. However, all those compounds have known cardiac complications, and their effects on the heart in polytherapy are unknown. HCQ inhibits hERG (IKr) potassium channels, it is known to increase in QT interval of

cardiomyocytes, and can induce arrhythmias that are responsible for sudden death [77]. AZM is also associated with an increased risk of cardiovascular death, due to Torsade de Pointes (TdP) and polymorphic ventricular tachycardia [78]. With respect to polytherapy, clinical trials have demonstrated a synergistic effect of HCQ and AZM to prolong QT interval [79, 80]; however, alterations in arrhythmic event frequency were controversial when compared to HCQ or AZM alone.

We therefore used our cardiac MPS to assess the electrophysiology and calcium handling of the tissues during "clinical trial-like" drug exposures. We showed that HCQ and AZM significantly increase 80% repolarization time (APD_{80}) and rhythm instabilities, starting at clinically relevant exposure days, and were accompanied with arrhythmia and TdP instances. HCQ+AZM combination also showed a significant increase in APD_{80}, however, few instabilities or arrhythmic events were observed. The outcomes of this chapter suggest that chronic drug exposure in this MPS format elicits arrhythmic outcomes similar to those observed in published clinical trials for both HCQ or AZM monotherapies [79-84], as well as their polytherapy[81]. This study demonstrates that a complex in vitro tissue model (i.e., cardiac MPS) can predict arrhythmias and rhythm instabilities under experimental conditions similar to a safety clinical trial. Our MPS can help clinicians in clinical trial design, and help to identify relevant biomarkers to monitor during clinical trials for potential COVID-19 therapeutics.

1.4 Heart Microphysiological System For Cardiac Liability Prediction Of Hydroxychloroquine And Azithromycin As COVID19 Therapeutics

Despite global efforts, it took seven months between the official announcement of global pandemic and the first FDA-approved medicines for the treatment of COVID-19 infection. During this timeframe, clinicians focused their efforts on repurposing drugs, such as hydroxychloroquine (HCQ) or azithromycin (AZM) to treat hospitalized COVID-19 patients. Early non-randomized trials showed promising effect of the drug combination on viral load reduction, which encouraged the FDA to grant an emergency use of authorization for both compounds. However, evidences for the safety and efficacy of the treatment were scarce and more recent clinical trials refuted the efficacy of the treatment against COVID-19 and shared concerns about cardiac liability associated with both drugs. This issue clearly illustrates the need for screening tools to increase the speed at which potential therapeutics are evaluated, especially in crisis periods like the current pandemic.

We wanted to further understand the cardiac liability associated with HCQ and AZM by exposing MPS tissues to acute dose escalation of each drug and their combination. An experiment that can give outcomes in a few hours compared to the mock clinical trial described in the previous chapter. In this chapter, we successfully report a QT increase in HCQ treated tissue, and its correlation to arrhythmic events, consistent with the clinical

literature[79, 85]. Our MPS shows no change in QT interval upon acute exposure to AZM, while still observing a significant increase in arrhythmic events. These results suggest that our MPS system can not only predict arrhythmias, but it can also pick up phenomenon by which these arrhythmia arise even though QT prolongation is absent[86]. Polytherapy showed a synergetic increase of QT interval when compared to monotherapy treatments supporting literature data that observed a worsening of QT interval increase with the combination of both therapies [79, 84, 87]. We also observed the presence of arrhythmic instances, although the amount was unchanged compared to monotherapies, suggesting no worsening of arrhythmic behavior, as supported by clinical data[83]. Finally, proteomics analysis of effluent enabled to discover biomarkers that were directly correlated with cardiotoxicity and showed cellular damage.

All together, these data suggest that our high content in vitro heart muscle model can aid clinicians to rapidly evaluate safety properties of potential therapeutics in crisis times to hopefully accelerate access of patients to treatment and better allocate clinical resources.

1.5 References

1. C.P. Adams, V.V.B., *Estimating the cost of new drug development: is it really $802 million?* health affairs, 2006. **2**: p. 420-428.
2. Joseph A DiMasi, H.G.G., Ronald W Hansen, *Innovation in the pharmaceutical industry: New estimates of R&D costs* J Health Econ, 2016.
3. Olivier J. Wouters, M.M., Jeroen Luyten, *Estimated Research and Development Investment Needed to Bring a New Medicine to Market, 2009-2018.* JAMA, 2020: p. 844–853.
4. Paul, S., *How to improve R&D productivity: the pharmaceutical industry's grand challenge.* Nat. Rev. Drug Discov, 2010.
5. J. A. Dimasi, R.W.H., and H. G. Grabowski, *The price of innovation : new estimates of drug development costs.* J Health Econ, 2003. **22**: p. 151-185.
6. Kadota, S., Pabon, L., Reinecke, H., Murry, C. E., *In Vivo Maturation of Human Induced Pluripotent Stem Cell-Derived Cardiomyocytes in Neonatal and Adult Rat Hearts.* Stem Cell Reports, 2017: p. 278-289.
7. Fong, A.H., et al. , *Three-Dimensional Adult Cardiac Extracellular Matrix Promotes Maturation of Human Induced Pluripotent Stem Cell-Derived Cardiomyocytes.* Tissue Engineering, 2016: p. 1016-1025.
8. Hiroshi Kurazumi , M.K., Mako Ohshima, Yumi Yamamoto, Yoshihiro Takemoto, Ryo Suzuki, Shigeru Ikenaga, Akihito Mikamo, Koichi Udo, Kimikazu Hamano, Tao-Sheng Li, *The effects of mechanical stress on the growth, differen- tiation, and paracrine factor production of cardiac stem cells.* PloS One, 2011.
9. Bayzigitov, D.R., et al., *Human Induced Pluripotent Stem Cell-Derived Cardiomyocytes Afford New Opportunities in Inherited Cardiovascular Disease Modeling.* Cardiol Res Pract, 2016. **2016**: p. 3582380.
10. Administration, F.a.D. *FDA Issues Advice to Make Earliest Stages Of Clinical Drug Development More Efficient*. 2006; Available from: http://www.fda.gov/NewsEvents/Newsroom/PressAnnouncements/2006/ucm108576.htm.
11. Mathur, A., et al., *Human iPSC-based cardiac microphysiological system for drug screening applications.* Sci Rep, 2015. **5**: p. 8883.
12. Lee M., F.A.J., Lerman L. O., Lerman A. , *Personalized medicine in cardiovascular diseases.* Korean Circulation Journal, 2012: p. 583-591.
13. Kumsal Kocadal, S.S., Fehmi Burak Alkas, Semra Sardas, *Drug-associated cardiovascular risks: A retrospective evaluation of withdrawn drugs.* North Clin Istamb, 2019.
14. K. Takahashi, S.Y., *Induction of Pluripotent Stem Cells from Mouse Embryonic and Adult Fibroblast Cultures by Defined Factors.* Cell, 2006. **2**: p. 663-676.
15. K. Takahashi, K.T., M. Ohnuki, M. Narita, T. Ichisaka, and K. Tomoda, *Induction of Pluripotent Stem Cells from Adult Human Fibroblasts by Defined Factors.* Cell, 2007: p. 861-872.
16. López-otín, C.S.-v.a.C., *iPSCs : On the Road to Reprogramming Aging.* Trends Mol. Med., 2016: p. 1-12.

17. R. Li, Y.B., T. Liu, X. Wang, and Q. Wu, *Induced pluripotency and direct reprogramming : a new window for treatment of neurodegenerative diseases.* Protein&Cell, 2013: p. 415-424.
18. S. T. Rashid, S.C., N. Hannan, S. J. Marciniak, E. Miranda, G. Alexander, I. Huang-Doran, J. Griffin, L. Ahrlund-Richter, J. Skepper, R. Semple, A. Weber, D. A. Lomas, and L. Vallier, *Modeling inherited metabolic disorders of the liver using human induced pluripotent stem cells.* J. Clin. Invest., 2010: p. 3127–3136.
19. Lian, X., et al., *Efficient differentiation of human pluripotent stem cells to endothelial progenitors via small-molecule activation of WNT signaling.* Stem Cell Reports, 2014. **3**(5): p. 804-16.
20. Lian, X., et al., *Robust cardiomyocyte differentiation from human pluripotent stem cells via temporal modulation of canonical Wnt signaling.* Proc Natl Acad Sci U S A, 2012. **109**(27): p. E1848-57.
21. Blinova, K., et al., *International Multisite Study of Human-Induced Pluripotent Stem Cell-Derived Cardiomyocytes for Drug Proarrhythmic Potential Assessment.* Cell Reports, 2018. **24**(13): p. 3582-3592.
22. Blinova, K., et al., *Comprehensive Translational Assessment of Human-Induced Pluripotent Stem Cell Derived Cardiomyocytes for Evaluating Drug-Induced Arrhythmias.* Toxicol Sci, 2017. **155**(1): p. 234-247.
23. Laflamme, M.A. and C.E. Murry, *Heart regeneration.* Nature, 2011. **473**(7347): p. 326-35.
24. Ogle, B.M., et al., *Distilling complexity to advance cardiac tissue engineering.* Science Translational Medicine, 2016. **8**(342).
25. Vunjak Novakovic, G., T. Eschenhagen, and C. Mummery, *Myocardial tissue engineering: in vitro models.* Cold Spring Harb Perspect Med, 2014. **4**(3).
26. Robertson, C., D.D. Tran, and S.C. George, *Concise review: maturation phases of human pluripotent stem cell-derived cardiomyocytes.* Stem Cells, 2013. **31**(5): p. 829-37.
27. Iseoka, H., et al., *Pivotal Role of Non-cardiomyocytes in Electromechanical and Therapeutic Potential of Induced Pluripotent Stem Cell-Derived Engineered Cardiac Tissue.* Tissue Eng Part A, 2018. **24**(3-4): p. 287-300.
28. Paci, M., et al., *Human induced pluripotent stem cell-derived versus adult cardiomyocytes: An in silico electrophysiological study on effects of ionic current block.* British Journal of Pharmacology, 2015. **172**(21): p. 5147-5160.
29. Lemoine, M.D., et al., *Human iPSC-derived cardiomyocytes cultured in 3D engineered heart tissue show physiological upstroke velocity and sodium current density.* Scientific Reports, 2017. **7**(1): p. 1-11.
30. Ma, J., et al., *High purity human-induced pluripotent stem cell-derived cardiomyocytes: electrophysiological properties of action potentials and ionic currents.* AJP: Heart and Circulatory Physiology, 2011. **301**(5): p. H2006-H2017.
31. Spencer, C.I., et al., *Calcium transients closely reflect prolonged action potentials in iPSC models of inherited cardiac arrhythmia.* Stem Cell Reports, 2014. **3**(2): p. 269-281.
32. Liang, P., et al., *Drug screening using a library of human induced pluripotent stem cell-derived cardiomyocytes reveals disease-specific patterns of cardiotoxicity.* Circulation, 2013. **127**(16): p. 1677-1691.

33. M. Paci, J.H., B. Rodriguez, and S. Severi, *Human induced pluripotent stem cell-derived versus adult cardiomyocytes: an in silico electrophysiological study on effects of ionic current block.* Br. J. Pharmacol., 2015: p. 5147-5160.
34. Roel G.M Breuls, T.U.J., Theo H Smit, *Scaffold Stiffness Influences Cell Behavior: Opportunities for Skeletal Tissue Engineering.* Open Orthop. J., 2008: p. 103-109.
35. M. P. Lutolf, P.M.G., and H. M. Blau, *Designing materials to direct stem-cell fate.* Nature, 2009: p. 433–441.
36. A. Fatehullah, S.H.T., and N. Barker, *Organoids as an in vitro model of human development and disease.* Nat. Cell Biol., 2016: p. 246–254.
37. Sergei Grebenyuk, A.R., *Engineering Organoid Vascularization.* Front Bioeng Biotechnol, 2019.
38. Jihoon Kim, B.-K.K., Juergen A. Knoblich *Human organoids: model systems for human biology and medicine.* Nature Reviews Molecular Cell Biology, 2020: p. 571-584.
39. Shadrin, I.Y., et al., *Cardiopatch platform enables maturation and scale-up of human pluripotent stem cell-derived engineered heart tissues.* Nat Commun, 2017. **8**(1): p. 1825.
40. Huebsch, N., et al., *Miniaturized iPS-Cell-Derived Cardiac Muscles for Physiologically Relevant Drug Response Analyses.* Scientific Reports, 2016. **6**(November 2015): p. 1-12.
41. Godier-Furnémont, A.F.G., et al., *Physiologic force-frequency response in engineered heart muscle by electromechanical stimulation.* Biomaterials, 2015. **60**: p. 82-91.
42. Nunes, S.S., et al., *Biowire: a platform for maturation of human pluripotent stem cell-derived cardiomyocytes.* Nat Methods, 2013. **10**(8): p. 781-7.
43. Mannhardt, I., et al., *Human Engineered Heart Tissue: Analysis of Contractile Force.* Stem Cell Reports, 2016. **7**(1): p. 29-42.
44. Ma, Z., et al., *Three-dimensional filamentous human diseased cardiac tissue model.* Biomaterials, 2014. **35**(5): p. 1367-77.
45. Tulloch, N.L., et al., *Growth of engineered human myocardium with mechanical loading and vascular coculture.* Circulation Research, 2011. **109**(1): p. 47-59.
46. Tiburcy, M., et al., *Defined Engineered Human Myocardium With Advanced Maturation for Applications in Heart Failure Modeling and Repair.* Circulation, 2017. **135**(19): p. 1832-1847.
47. Zimmermann, W.H., et al., *Tissue Engineering of a Differentiated Cardiac Muscle Construct.* Circulation Research, 2002. **90**(2): p. 223-230.
48. E. K. Sackmann, A.L.F., and D. J. Beebe, *The present and future role of microfluidics in biomedical research.* Nature, 2014: p. 181–189.
49. X. Zhang, L.L., and C. Luo, *Gel integration for microfluidic applications.* Lab Chip, 2016.
50. D. Huh, B.D.M., A. Mammoto, M. Montoya-Zavala, H. Y. Hsin, and D. E. Ingber, *Reconstituting Organ-Level Lung Functions on a Chip.* Science, 20110: p. 1662–1668.
51. Takayama, S.K.a.S., *Organ-on-a-chip and the kidney.* Kidney Res. Clin. Pract., 2015: p. 165–169.

52. K.-J. Jang, A.P.M., G. A. Hamilton, L. A. McPartlin, S. Chung, K.-Y. Suh, and D. E. Ingber, *Human kidney proximal tubule-on-a-chip for drug transport and nephrotoxicity assessment.* Integr. Biol. (Camb). 2013: p. 1119–29.
53. D. Bavli, S.P., E. Ezra, G. Levy, M. Cohen, M. Vinken, J. Vanfleteren, M. Jaeger, and Y. Nahmias, *Real-time monitoring of metabolic function in liver-on-chip microdevices tracks the dynamics of mitochondrial dysfunction.* Proc. Natl. Acad. Sci., 2016.
54. Felipe T. Lee-Montiel, A.L., Laure Dumont, Caleb S. Lee, Nathaniel Huebsch, Verena Charwat, Hideaki Okochi, Matthew J. Hancock, Brian Siemons,Steven C. Boggess, Ishan Goswami, Evan W. Miller, Holger Willenbring, Kevin Healy, *Integrated hiPSC-based liver and heart microphysiological systems predict unsafe drug-drug interaction.* Biorxiv, 2020.
55. F. An, Y.Q., X. Liu, R. Zhong, and Y. Luo, *Organ-on-a-chip: New platform for biological analysis.* Chem. Insights, 2015: p. 39–45.
56. A. Marsano, C.C., M. Lemme, P. Occhetta, E. Gaudiello, E. Votta, G. Cerino, A. Redaelli, and M. Rasponi, *Beating heart on a chip: a novel microfluidic platform to generate functional 3D cardiac microtissues.* Lab Chip, 2015: p. 599–610.
57. Alexander R. Pinto, A.I., Malina J. Ivey, Jill T. Kuwabara, Michelle L. D'Antoni, Ryan Debuque, Anjana Chandran, Lina Wang, Komal Arora, Nadia Rosenthal, Michelle D. Tallquist, *Revisiting Cardiac Cellular Composition.* Circ Res, 2016.
58. Gregory B. Sands, B.H.S., Ian J. LeGrice, *Virtual Sectioning of Cardiac Tissue Relative to Fiber Orientation*, in *30th Annual International IEEE EMBS Conference*. 2008: Vancouver, British Columbia, Canada.
59. Nicholas S. Peters, N.J.S., Stephen M. Rothery, Christopher Lincoln, Magdi H. Yacoub, Colin R. Green, *Spatiotemporal Relation Between Gap Junctions and Fascia Adherens Junctions During Postnatal Development of Human Ventricular Myocardium.* American Heart Association, 1994. **90**.
60. Huebsch, N., et al., *Automated Video-Based Analysis of Contractility and Calcium Flux in Human-Induced Pluripotent Stem Cell-Derived Cardiomyocytes Cultured over Different Spatial Scales.* Tissue Engineering Part C: Methods, 2015. **21**(5): p. 467-479.
61. Lopaschuk, G.D. and J.S. Jaswal, *Energy Metabolic Phenotype of the Cardiomyocyte During Development, Differentiation, and Postnatal Maturation.* Journal of Cardiovascular Pharmacology, 2010. **56**(2): p. 130-140.
62. Makinde, A.-O., P.F. Kantor, and G.D. Lopaschuk, *Maturation of fatty acid and carbohydrate metabolism in the newborn heart*, in *Molecular and Cellular Effects of Nutrition on Disease Processes*, G.N. Pierce, et al., Editors. 1998, Springer US: Boston, MA. p. 49-56.
63. Huebsch, N., et al., *Metabolically-Driven Maturation of hiPSC-Cell Derived Heart-on-a-Chip*. 2020, Cold Spring Harbor Laboratory.
64. Kenichi Arai, D.M., Shoko Takao, Anna Nakamura, Manabu Itoh, Takahiro Kitsuka, Koichi Nakayama *Drug response analysis for scaffold-free cardiac constructs fabricated using bio-3D printer.* Scientific Reports, 2020.
65. J. Lee, M.L., T. Oliver, A. Ishihara, and K. Jacobson, *Traction Forces Generated by Locomoting Keratocytes.* J. Cell Biol., 1994: p. 1957–1964.

66. O. du Roure, A.S., A. Buguin, R. H. Austin, P. Chavrier, P. Silberzan, and B. Ladoux, *Force mapping in epithelial cell migration.* Proc. Natl. Acad. Sci. , 2005: p. 2390–2395.
67. Saez, E.A., M. Ghibaudo, O. du Roure, J.-M. Di Meglio, P. Hersen, P. Silberzan, a Buguin, and B. Ladoux, *Traction forces exerted by epithelial cell sheets.* J. Phys. Condens. Matter, 2010.
68. N. J. Sniadecki, C.S.C., *Microfabricated Silicone Elastomeric Post Arrays for Measuring Traction Forces of Adherent Cells.* Methods Cell Biol., 2007. **83**: p. 313-328.
69. N. Huebsch, P.L., N. Deveshwar, C. I. Spencer, L. M. Judge, M. A. Mandegar, C. B. Fox, T. M. A. Mohamed, Z. Ma, A. Mathur, A. M. Sheehan, A. Truong, M. Saxton, J. Yoo, D. Srivastava, T. A. Desai, P.-L. So, K. E. Healy, and B. R. Conklin, *Miniaturized iPS-Cell-Derived Cardiac Muscles for Physiologically Relevant Drug Response Analyses.* Sci. Rep., 2016.
70. M. L. Rodriguez, B.T.G., L. M. Pabon, S. J. Han, C. E. Murry, and N. J. Sniadecki, *Measuring the contractile forces of human induced pluripotent stem cell-derived cardiomyocytes with arrays of microposts.* J. Biomech. Eng., 2014. **136**.
71. Klammer, I.B., A.; Dura, G.; Mokwa, W.; Schnakenberg, *A novel valve for microfluidic PDMS-based systems.* 2008 IEEE 21st International Conference on Micro Electro Mechanical Systems, 2008.
72. Gautret, P., et al., *Hydroxychloroquine and azithromycin as a treatment of COVID-19: results of an open-label non-randomized clinical trial.* Int J Antimicrob Agents, 2020: p. 105949.
73. Yao, X., et al., *In Vitro Antiviral Activity and Projection of Optimized Dosing Design of Hydroxychloroquine for the Treatment of Severe Acute Respiratory Syndrome Coronavirus 2 (SARS-CoV-2).* Clin Infect Dis, 2020.
74. Wang, M., et al., *Remdesivir and chloroquine effectively inhibit the recently emerged novel coronavirus (2019-nCoV) in vitro.* Cell Res, 2020. **30**(3): p. 269-271.
75. Huang, M., et al., *Treating COVID-19 with Chloroquine.* J Mol Cell Biol, 2020.
76. Xueting Yao, et al., *In Vitro Antiviral Activity and Projection of Optimized Dosing Design of Hydroxychloroquine for the Treatment of Severe Acute Respiratory Syndrome Coronavirus 2 (SARS-CoV-2).* Clinical Infectious Diseases, 2020. **71**(15): p. 732-739.
77. Jankelson, L., et al., *QT prolongation, torsades de pointes, and sudden death with short courses of chloroquine or hydroxychloroquine as used in COVID-19: A systematic review.* Heart Rhythm, 2020.
78. Ray, W.M., K. ; Hall, K.; Arbogast, P.; Stein, M., *Azithromycin and the Risk of Cardiovascular Death.* The New England Journal of Medicin, 2012.
79. Bessière, F., et al., *Assessment of QT Intervals in a Case Series of Patients With Coronavirus Disease 2019 (COVID-19) Infection Treated With Hydroxychloroquine Alone or in Combination With Azithromycin in an Intensive Care Unit.* JAMA Cardiology, 2020.

80. Chorin, E., et al., *QT Interval Prolongation and Torsade De Pointes in Patients with COVID-19 treated with Hydroxychloroquine/Azithromycin.* Heart Rhythm, 2020.
81. Cipriani, A., et al., *Arrhythmic profile and 24-hour QT interval variability in COVID-19 patients treated with hydroxychloroquine and azithromycin.* International Journal of Cardiology, 2020.
82. Vouri, S.M., T.N. Thai, and A.G. Winterstein, *An evaluation of co-use of chloroquine or hydroxychloroquine plus azithromycin on cardiac outcomes: A pharmacoepidemiological study to inform use during the COVID19 pandemic.* Research in Social and Administrative Pharmacy, 2020.
83. Rosenberg, E.S., et al., *Association of Treatment With Hydroxychloroquine or Azithromycin With In-Hospital Mortality in Patients With COVID-19 in New York State.* JAMA, 2020.
84. Chorin, E., et al., *The QT Interval in Patients with SARS-CoV-2 Infection Treated with Hydroxychloroquine/Azithromycin.* 2020.
85. Asensio, E., et al., *Recommendations for the measurement of the QT interval during the use of drugs for COVID-19 infection treatment. Updatable in accordance with the availability of new evidence.* Journal of Interventional Cardiac Electrophysiology, 2020.
86. Yang, Z., et al., *Azithromycin Causes a Novel Proarrhythmic Syndrome.* Circulation: Arrhythmia and Electrophysiology, 2017. **10**(4): p. e003560.
87. Mercuro, N.J., et al., *Risk of QT Interval Prolongation Associated With Use of Hydroxychloroquine With or Without Concomitant Azithromycin Among Hospitalized Patients Testing Positive for Coronavirus Disease 2019 (COVID-19).* JAMA Cardiology, 2020.

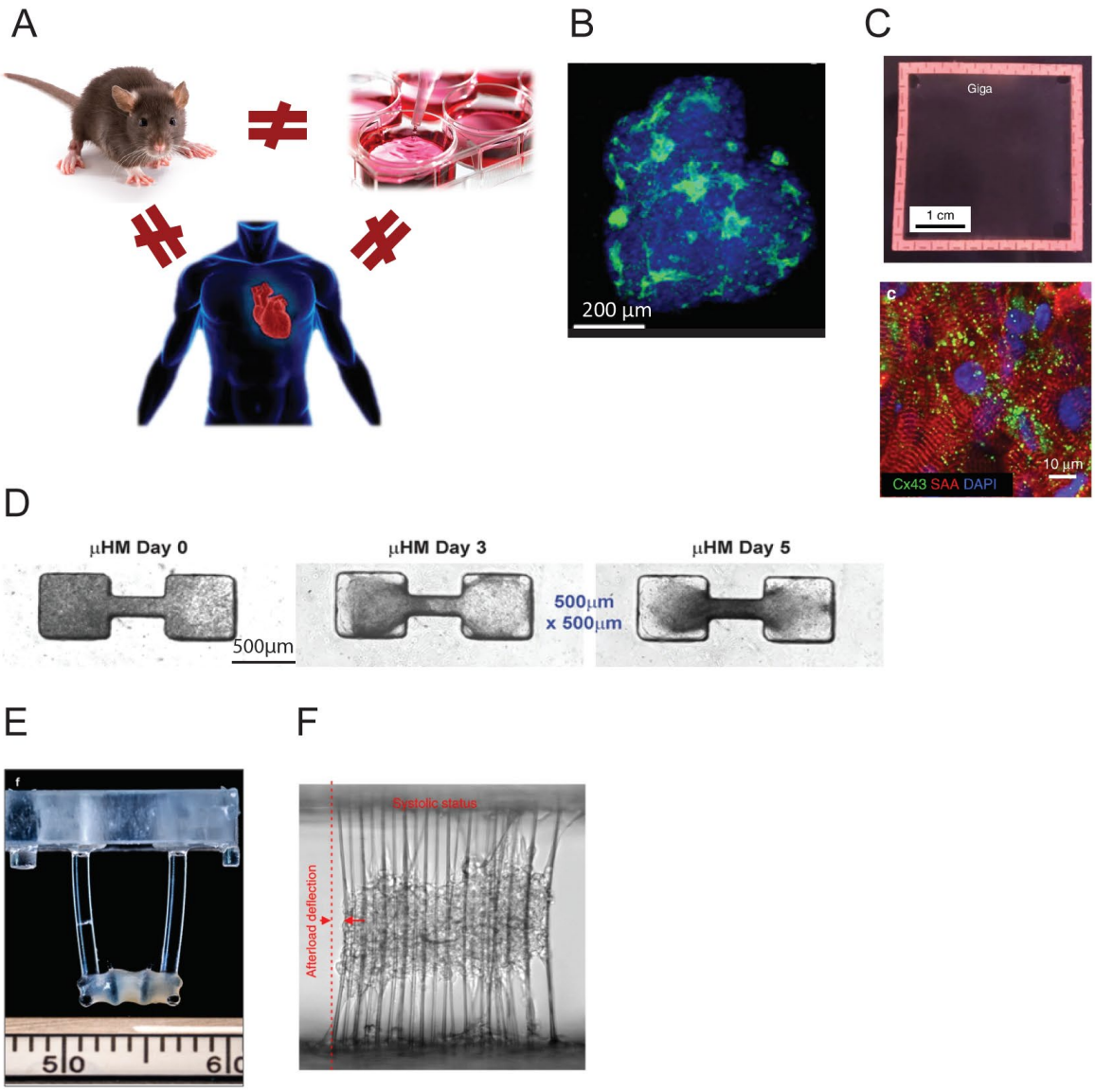
A
B
C
Giga
1 cm
200 µm
c
10 µm
Cx43 SAA DAPI
D
µHM Day 0
µHM Day 3
µHM Day 5
500µm
500µm
x 500µm
E
F
Systolic status
Afterload deflection

Figure 1

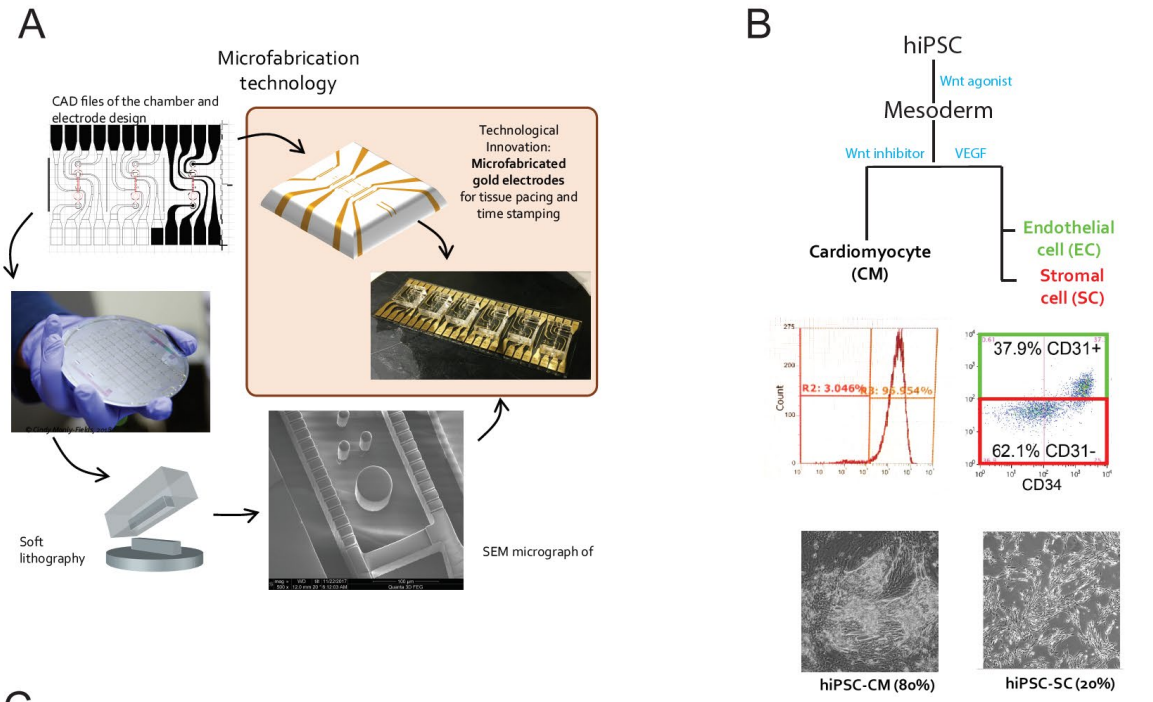

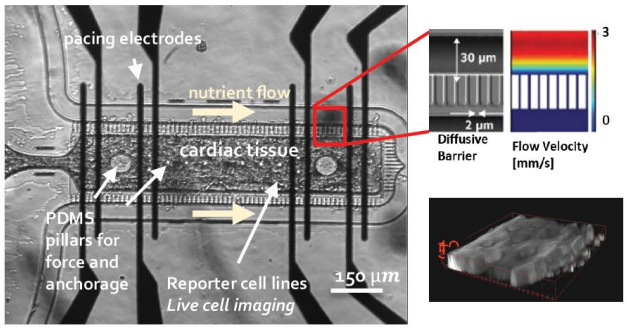

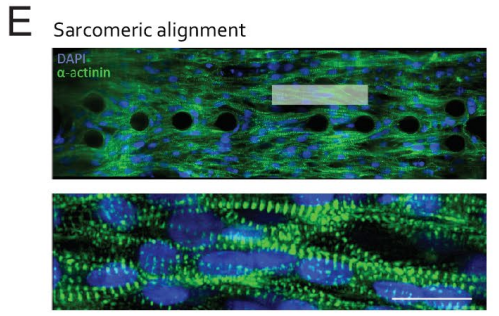

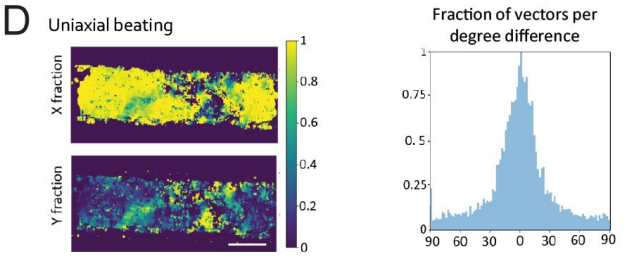

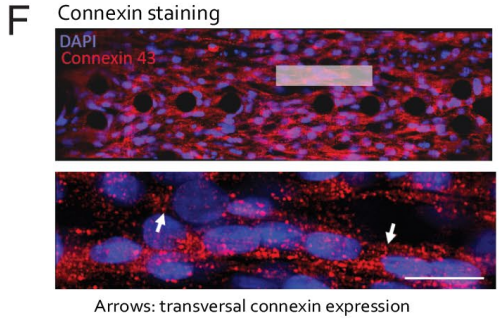

Arrows: transversal connexin expression

Figure 2

Chapter 2 Metabolically-Driven Maturation of hiPSC-Cell Derived Heart-on-a-Chip

2.1 Abstract

Human induced pluripotent stem cell derived cardiomyocytes (hiPSC-CM) are a promising *in vitro* tool for drug development and disease modeling, but their immature electrophysiology limits diagnostic utility. Tissue engineering approaches involving aligned 3D cultures enhance hiPSC-CM structural maturation but are insufficient to induce mature electrophysiology. We hypothesized that mimicking post-natal switching of the heart's primary ATP source from glycolysis to fatty acid oxidation could enhance electrophysiological maturation of hiPSC-CM. We combined hiPSC-CM with microfabricated culture chambers to form 3D cardiac microphysiological systems (MPS) that enhanced immediate microtissue alignment and tissue specific extracellular matrix (ECM) production. Using Robust Experimental design, we identified a maturation media that improved calcium handling in MPS derived from two genetically distinct hiPSC sources. Although calcium handling and metabolic maturation were improved in both genotypes, there was a divergent effect on action potential duration (APD): MPS that started with abnormally prolonged APD exhibited shorter APD in response to maturation media, whereas the same media prolonged the APD in MPS that started with aberrantly short APD. Importantly, the APD of both genotypes was brought near the range of 270-300ms observed in human left ventricular cardiomyocytes. Mathematical modeling explained these divergent phenotypes, and further predicted the response of matured MPS to drugs with known pro-arrhythmic effects. These results suggest that systematic combination of biophysical stimuli and metabolic cues can enhance the electrophysiological maturation of hiPSC-derived cardiomyocytes. However, they also reveal that maturation-inducing cues can have differential effects on electrophysiology depending on the baseline phenotype of hiPSC-CM. *In silico* models provide a valuable tool for predicting how changes in cellular maturation will manifest in drug responsiveness.

2.2 Introduction

Human induced pluripotent stem cell (hiPSC) technology provides an exciting opportunity for disease modeling and drug discovery. An immediate goal for cardiac tissue models formed from hiPSC-derived cardiomyocytes (hiPSC-CM) is to reduce and refine the use of animal testing in the drug development pipeline[1]. Inherent differences between species have historically diminished the ability of animal models to prognosticate drug safety and efficacy. Microphysiological systems (MPS), or organ-chips, combine 3D-architecture of tissue micro-environments with the ability to interrogate key physiological

functions (for example, cardiomyocyte action potential) and well-defined delivery profiles for nutrients.

A challenge with using hiPSC-CM to predict drug safety and efficacy is the immaturity of hiPSC-CM[2-5]. In particular, hiPSC-CM exhibit automaticity (spontaneous beating without electrical stimulation) and longer action potentials (445±73msec for ventricular-like hiPSC-CM, versus 270-300msec directly measured by patch-clamp of primary human adult left-ventricular cardiomyocytes)[6-11]. Culturing hiPSC-CM or human embryonic stem cell (hESC) derived cardiomyocytes (hESC-CM) within the *in vivo*-like micro-environment of Engineered Heart Muscle (EHM[12-21]), or MPS[22] has been shown to mature hiPSC-CM to some extent by enhancing physiologic hypertrophy, and lead to pharmacology more closely correlated to the one of the adult human heart. However, these approaches have not led to consistent electrophysiological maturation of hiPSC-CM.

In addition to 3D culture approaches, bioreactor-based strategies such as chronic electrical pacing or cyclic strain (typically applied over 2-4 weeks in culture) enhance maturity of hESC-CM and hiPSC-CM[15, 18, 23, 24]. Collectively these methods are promising, but no single approach applied thus far has been sufficient to induce full maturation of pluripotent stem cell derived cardiomyocytes. Furthermore, many of the existing approaches require prolonged culture periods (in some cases approaching one month), large scale formats, and/or complex setups to execute. These issues would lead to cost and logistical limitations for their translation to higher-throughput analyses that would be essential to use these technologies for drug development.

As bioreactor approaches have limited scalability, and tissue engineered micro-environments alone are not sufficient to induce hiPSC-CM maturation consistent with the adult heart, there has been a focus on combining tissue engineering approaches with soluble cues. Consistent with the notion that micro-environmental cues can enhance hiPSC-CM maturity, transplanting hiPSC-CM into neonatal rodent hearts enhances maturation[25]. One possible explanation for this result is that the milieu of the heart contains soluble cues that enhance cardiomyocyte maturity. Reductionist approaches have used specific soluble cues from the fetal and post-natal heart, including cytokines[26, 27], micro-RNAs[28], heart specific extracellular matrix[29] and hormones[30] to enhance the maturity of hESC-CM and hiPSC-CM.

Metabolic cues like glucose levels provide another key facet of the heart's soluble environment that may be particularly important to cardiomyocyte maturation. Postnatally, the heart switches from glycolysis to fatty-acid oxidation as its primary source of ATP[31, 32] . Previously, 2D hiPSC-CM monolayers and engineered tissues exposed to glucose-depleted, fatty-acid enriched media exhibited more mature metabolic profiles and physiology compared to hiPSC-CM cultured in standard media[33-36]. However, fatty-acid based media has not been studied in the context of MPS, and potential population variance in cellular response to fatty-acid media has not been explored. We hypothesized that the combination of aligned, 3D culture and fatty-acid could enhance electrophysiological

maturation of hiPSC-CM within cardiac MPS. We investigated hiPSC-CM derived from two distinct donor lines labeled WTC[37] and SCVI20[38]. Both lines were derived from healthy individuals who did not harbor known cardiomyopathy-associated mutations. Using a Design of Experiments approach[39-41], in MPS derived from WTC hiPSC, we identified fatty-acid based Maturation Media (MM) that led to a more mature metabolic phenotype and improved calcium handling in MPS. These changes were associated with shortened, adult-like Action Potential Duration (APD) in WTC-MPS. MM-treated MPS also exhibited changes in expression of ion-channel and calcium handling genes, including Sarcolipin (SLN).

In contrast, MM had different effects on MPS derived from SCVI20 hiPSC. At baseline, monolayers and SCVI20 hiPSC-CM - derived MPS had extremely short action potentials. Whereas MM markedly shortened APD in WTC MPS, the same media prolonged APD in SCVI20 MPS. In both cases, MM treatment led to APD within the range of 270-300msec expected for adult human left-ventricular cardiomyocytes. In both genotypes, MM produced metabolic maturation, and a trend toward a more robust calcium transient ($\Delta F/F_0$) and enhanced contractility at low extracellular calcium. To understand these differential responses to common media, we used mathematical modeling to predict the contribution of specific current fluxes and calcium handling machinery to action potentials and calcium transients. These models predicted that individual currents were very different between immature MPS of different genotypes, despite both basal hiPSC having been derived from healthy male volunteers who did not harbor genetic diseases. MM treatment led to a convergent set of ion currents and calcium handling parameters, and the MM-induced changes in simulated currents were consistent with shifts in the pharmacology of MM versus Standard Media (SM). These results suggest that maturation media can both improve overall tissue physiology and minimize artificial differences in pharmacology of hiPSC-CM due to non-genetic sources of variability (e.g. clonal variation). Potentially, this can subsequently reveal true pharmacogenomic relationships.

2.3 Results and Discussion

2.3.1 Robust Design Experiments Indicate Optimal Carbon Sourcing for Mature Beating Physiology in WTC-Derived hiPSC-Cardiac MPS

We optimized fabrication of hiPSC-CM derived cardiac MPS[22] to enhance the consistency of multilayer tissue self-assembly (**Fig. 1A-C**) and subsequent achievement of aligned sarcomeres and uniaxial beating **(Fig. 1D,E)**. To minimize batch-to-batch variability in cellular composition that might hinder drug screening studies, we formed cardiac MPS that mimicked the mass composition of the human heart by combining a defined cocktail[42] of 80% WTC hiPSC-CM and 20% isogenic hiPSC-SC (**Supplemental Methods, Fig. S1,S2**). We employed Robust Experimental Design to screen for the effects of glucose, oleic acid, palmitic acid, and albumin (bovine serum albumin, BSA) levels

on WTC MPS maturity (**Table 1**). MPS were incubated with different fatty-acid media for ten days before their beating physiology and calcium flux were assessed. Optimal media would reduce automaticity (e.g. reduce spontaneous beating rate), while reducing the interval between peak contraction and peak relaxation (a surrogate for APD) in field-paced tissues (**Fig. 2A-C**), and maintaining a high level of beating prevalence during pacing (defined as the percent of the tissue with substantial contractile motion; **Fig. 2D**). Beating interval correlated with rate-corrected Full-Width Half Maximum calcium flux time, FWHM (**Fig. 2B,E,G**), and beating prevalence correlated with calcium flux amplitude (**Fig. 2D,F,G**). The strong correlations between calcium flux and contractile motion with respect to timing and amplitude suggest that none of the medias used in this screen disrupt calcium-contraction coupling.

Screening experiments did not suggest a significant role for either oleic or palmitic acid alone in inducing shortened beating intervals and calcium transient duration (**Fig. 2B**). However, these fatty acids did have effects on beating physiology in the context of concurrent glucose deprivation: completely omitting glucose while adding in galactose in MPS treated with media having only oleic acid or palmitic acid eliminated beating under 1Hz pacing. In contrast, treatment with glucose-free (galactose containing) media that was supplemented with both fatty acids (Media 9; **Fig. 2H**) partially rescued this deficiency. This is consistent with the ability of hiPSC-CM to use both these fatty acids as ATP sources[35]. Thus, we concluded that the optimal media should include both palmitic and oleic acids. Furthermore, although absolute glucose deprivation would likely force fatty acid oxidation, and previous work has established galactose combined with fatty acids as a viable ATP source for healthy hiPSC-CM in monolayer cultures[35, 43], we observed that in MPS, complete glucose deprivation dramatically reduced beating prevalence and calcium transient amplitude, even in the presence of 10mM galactose. This prompted us to adjust the glucose level media to a low but non-zero level of 0.5g/L (2.75mM; ~10% of the level in standard RPMI Media).

As the inclusion of higher levels of BSA appeared to diminish beating interval without severely affecting prevalence or calcium flux, we concluded that an ideal maturation media would contain this higher level (2.5%, vs. 0.25% contained in standard, B-27 supplemented media; **Fig. 2B,E**). This led to a new Maturation Media (herein referred to as “MM”): glucose free RPMI basal media supplemented with 2% B-27, 0.5g/L glucose (2.8mM), 10mM galactose, 2.25% BSA (to a final concentration of 2.5% BSA, including the BSA contained in B-27), 125μM oleic acid and 100μM palmitic acid. MM exhibited a substantial portion of the beneficial effects of glucose free, fatty acid enriched media on reducing beating interval, without a concurrent loss of beating prevalence with 1 Hz pacing (**Fig. 2H, I**).

2.3.2 Maturation-Media Induced Changes in Action Potential and Calcium Transients for WTC MPS

In WTC MPS, MM reduced APD from the prolonged levels we observed for Standard Media (RPMI containing B-27 supplement; SM) treated MPS (**Fig. 3A,B,E**). Interestingly, however, switching from SM to MM had no measurable effects on APD or automaticity when hiPSC-CM were cultured in confluent 2D monolayers (**Fig. 3E, S3E,F**). GCaMP6f based analysis of Ca^{2+} handling revealed that baseline-normalized calcium amplitude ($\Delta F/F_0$) was significantly increased by fatty-acid based MM in WTC MPS **(Fig. 3G).** However, we did not observe a significant change in the in the maximum calcium upstroke velocity in paced tissues (**Fig. 3H**)**.** Likewise, action potential upstroke timing was not significantly affected by MM pre-treatment, although there was a trend toward shorter action potential upstroke times in MM pre-treated WTC MPS and hiPSC-CM monolayers (**Fig. S3A**).

Due to concerns about potential cytotoxicity of high levels of BSA and palmitic acid[44, 45]), we also repeated APD studies on WTC MPS treated with MM in which we independently varied levels of these two components. The complete absence of palmitic acid and reduction of BSA levels to those provided by B-27 alone from MM led to APD that was not significantly different from APD observed for SM treated MPS (M1; **Fig. S3G**). In the absence of palmitic acid, the addition of a high dose of BSA appeared to be somewhat toxic to cardiac tissues, as the prevalence of beating in these samples (M2) was nearly zero, making it difficult to interpret the apparent APD (**Fig. S3H**). Interestingly, palmitic-acid enriched media still had significant effects on APD reduction, while negative effects of high albumin dosing were slightly reduced, when the total amount of albumin present was reduced below 2.5%. However, since the APD observed with 1% BSA (M4; Fig. S3G) was significantly lower than the APD for adult human left ventricular cardiomyocytes, we assumed these tissues might fall outside the ideal physiologic range for drug testing. Thus, MM with 125μM oleic acid, 100μM palmitic acid, 0.5g/l glucose, 10mM galactose and 2.5% BSA was used for all subsequent studies.

Although several types of fatty acids have been shown to enhance maturation of hiPSC-CM monolayers and engineered heart tissues, here we found that it was necessary to include palmitic acid specifically (**Fig. S3G**). This suggests that although generalized metabolic effects such as oxidation-induced DNA damage response[34] are likely important to electrophysiological maturation of hiPSC-CM *in vitro*, events affected directly by palmitic acid, such as palmitoylation of calcium channel subunits[46] or receptors[47] may also be involved. Furthermore, although it was possible to reduce APD with maturation media that included oleic acid and palmitic acid without increased albumin (M4: **Fig. S3G**), this treatment yielded APD that fell below the target range of adult cardiomyocytes. It is possible that albumin, which is a fatty-acid carrier *in vivo*, provided a more temporally stable dose of fatty acids to cells cultured within the MPS. The concentration of albumin in MM is not markedly dissimilar from the 3.5-5% albumin level found in human blood[48].

Finally, the finding that fatty-acid based maturation media had significant effects on action potential and pharmacology within WTC MPS, but not 2D hiPSC-CM monolayers, suggests the need to incorporate advanced 3D co-culture models during development of protocols to mature hiPSC-CM, and likely other hiPSC-derived tissue cells.

2.3.3 Divergent Effects of Maturation Media on APD in Genetically Distinct hiPSC-Cardiomyocytes

We next tested fatty-acid based MM in a genetically distinct set of hiPSC-CM, SCVI20. In contrast to WTC, SCVI20 exhibited much shorter APD at baseline, ranging from 250 to 350ms in monolayers and 150 to 400ms in MPS (**Fig. 3C**). Treatment of SCVI20 MPS for 10 days with MM prolonged APD, so that APD_{80} fell within a very similar range to what we observed for MM-treated WTC MPS **(Fig. 3D,F)**, and within the range of 300 to 400msec observed for human adult ventricular cardiomyocytes (Brandenburger *et al.* 2012; ref. [49]). Interestingly, analysis of Ca^{2+} handling using OGB-1-AM revealed that MM treatment produced a similar trend toward increased background normalized calcium amplitude ($\Delta F/F_0$) in SCVI20 MPS as it did in WTC (**Fig. 3I**). However, this trend was not statistically significant in SCVI20. Importantly, because GCaMP6f and OGB-1-AM have different affinity for Ca^{2+} and different mechanisms for Ca^{2+} induced fluorescence (K_D of 375nM for GCaMP[50] and K_D of 170nM for OGB-1[51]), one cannot directly compare the $\Delta F/F_0$ response between MPS derived from these different lines. Despite not enhancing $\Delta F/F_0$ in SCVI20, MM did significantly increase the Ca2+ upstroke velocity for MPS of this genotype (**Fig. 3J**). There was no trend between media type and upstroke timing in SCVI20 MPS (**Fig. S3B**).

The differences in $cAPD_{80}$ of SCVI20 and WTC MPS in response to MM prompted us to test the effects of this media on a third cell line, SCVI273. This additional line responded similarly to WTC in terms of APD shortening effects of MM (**Fig. S3C**). However, there was no trend toward increased $\Delta F/F_0$ (**Fig S3D**). As with SCVI20, this lack of change in $\Delta F/F_0$ is likely to reflect the difference in calcium affinity of OGB-1 versus GCaMP6f[50],[51].

2.3.4 Pre-Treatment of hiPSC-Derived-Cardiomyocyte Based MPS with Maturation Media Supports a Shift Toward a more Mature Metabolic Phenotype

Maturation-media induced changes in the state of mitochondria within iPSC-cardiomyocytes in MPS were next assessed. Mitochondrial inner transmembrane potential, as measured with MitoTracker Red, was markedly upregulated by MM in both WTC and SCIV20 (**Fig. 4**). This suggests an increase in oxidative phosphorylation[52] in MM treated MPS. Antibody-staining revealed that overall mitochondrial density did not change, but mitochondrial organization shifted with MM treatment in both genotypes (**Fig. 4A-D**). SM

produced short filaments and rounded structures, whereas MM treatment yielded a mitochondrial structure of extended filaments and networks. Similar filamentous networks of mitochondria, running perpendicular to Z-lines, have been observed previously during postnatal development of rodent cardiomyocytes[53]. Interestingly, although iPSC-cardiomyocyte monolayers treated with MM showed upregulation of maximum Oxygen Consumption Rate (OCR) in Seahorse assays, they did not show marked increased in mitochondrial membrane potential (**Fig. 4E,F, Fig. S4**). These data indicate that fatty acid-based MM directly alters the metabolic state of iPSC-cardiomyocytes, as has been shown in previous studies[34, 35]. The finding that MM caused more substantial shifts in mitochondrial state in MPS as opposed to monolayer culture is consistent with our finding that MM caused much less significant changes in physiology of monolayers as compared to MPS (**Fig. 3**). This may reflect a lower ATP consumption rate in monolayers, which are not doing active mechanical work, as contrasted to cardiomyocytes in MPS that contract against PDMS posts.

2.3.5 Pre-Treatment of hiPSC-Derived-Cardiomyocyte Based MPS with Maturation Media Supports Inotropic Responsiveness

MM treatment did not result in changes in gross sarcomere structure within WTC or SCVI20 MPS, as assessed by staining for sarcomeric α-Actinin (ACTN2; **Fig. 5A-B**). Quantitative analysis of sarcomere morphology with Fourier-Transform based methods[43, 54] was consistent with these qualitative observations, and suggested no substantial changes in sarcomere organization as a result of MM treatment (**Fig. S5A-B**). Expression and localization of β-Myosin Heavy Chain and MLC-2v, two sarcomere-associated proteins which typically mark mature, ventricular-like iPSC-cardiomyocytes, were very similar in MM and SM pre-treated MPS (**Fig. S5C-G**). There was a trend toward upregulation of MLC-2v protein in SCVI20 MPS, consistent with previous observations by Mills *et al.* that palmitic-acid enriched, glucose depleted media increased MLC-2v levels[34].

When we measured force developed in MPS via the deflection of PDMS pillars in the chamber (**Supplemental Methods; Fig. S6)**, we found that both SM and MM-pre-treated WTC MPS exhibited a robust dose response to increased extracellular calcium, with a maximal range of stress similar to adult human heart tissue slices (**Fig. 5C**; data on adult slices calculated from Brandenburger *et al.;* ref. [49]). Consistent with work by Mills, we observed that fatty-acid based maturation media neither inhibited nor enhanced peak twitch force[34]. However, MM pre-treated WTC MPS were sensitized to lower concentrations of extracellular calcium than SM pre-treated controls, with a statistically significant EC_{50} of 0.11±0.06 mM for MM pre-treated MPS versus 0.95±0.46mM for SM-pre-treated controls ($p < 0.05$, 2-way *t*-test). Furthermore, MM pre-treated MPS showed a statistically significant steeper fold-increase in force in response to extracellular calcium over the linear region of the calcium-force response curve, with an initial slope of 12±1.5

mN/mm^2/mM Ca^{2+} versus 3.9±0.26 for SM-pre-treated controls ($p < 0.01$, 2-way *t*-test). Consistent with the trend that MM-treatment enhanced Ca^{2+} handling ($\Delta F/F_0$) more significantly in WTC than in SCVI20 MPS, SCVI20 MPS also showed a trend toward increased force with MM, but even at low extracellular Ca^{2+} levels, the trend towards higher twitch forces with MM was not statistically significant **(Fig. 5D)**.

Analysis of tissue inotropic responses to isoproterenol in MM pre-treated WTC MPS showed a trend toward desensitization, and MM-treated SCVI20 MPS showed a trend toward sensitization to this drug, though neither trend was statistically significant (**Fig. 5E,F**). Similarly to inotropic effects of isoproterenol assessed at constant (paced at 1Hz) beat-rate, MM pre-treatment appeared to slightly desensitize MPS to the chronotropic effects of isoproterenol in both genotypes, although, as with inotropic effects, the changes were not statistically significant (**Fig. 5G,H**). The EC_{50} values for isoproterenol chronotropy fell within the range recently reported for engineered heart tissue subjected to exercise-induced maturation via external pacing[23], and within the range of adult human heart slices[49].

Collectively, these data suggested that MM does not damage sarcomeres or interfere with excitation-contraction coupling or adrenergic responsiveness and enhances calcium contraction coupling when the amount of extracellular calcium is limiting. Furthermore, unlike the divergent trend observed with respect to MM-induced change in APD in SCVI20 vs. WTC, inotropic responsiveness showed a relatively similar trend in both genotypes, suggesting multimodal analysis of tissue function for accurate characterization.

2.3.6 Gene Expression Changes caused by Maturation Media in MPS-Cultured hiPSC-CM

Consistent with previous studies, we observed genotype-based variability in transcription of monolayer hiPSC-CM in standard media[11]. However, there was no significant difference in a panel of ion channel and sarcomere related genes caused by MM treatment of monolayers of either genotype **(Fig. 6A,B)**. Consistent with observations regarding the immaturity of hiPSC-CM, several ion channel transcripts were either deficient or overexpressed in these cells, when compared to commercially available RNA obtained from adult human hearts (**Fig. 6A,B**). Further, the absolute level of SCN5A (related to sodium current, I_{Na}) and several other ion channel transcripts, including KCNJ2 (related to I_{K1}), was highly variable between different batches of purified, 2D monolayer hiPSC-CM. This may point to mis-regulation of expression in these channels in non-physiologic culture formats, or to differences in the relative levels of different cardiomyocyte sub-types obtained from our small molecule-based differentiation protocol[55, 56].

We next assessed gene expression in MPS treated for ten days with either SM or MM. Interestingly, and in contrast to results by Mills *et al.[34]*, we did not observe significant variation in expression of the glycolysis associated gene, GAPDH, relative to other potential “housekeeping” genes (data not shown). A lack of change in GAPDH expression

on the protein level was further verified by immunostaining, which revealed no significant effects of MM on GAPDH expression in either WTC or SCVI20 (**Fig. S7**).

Analysis of a panel of genes involved in electrophysiology, cell identity, contractility and calcium handling did not reveal a global shift in expression as would be expected for gross changes in cell differentiation or population composition in either genotype (**Fig. 6C,D**). Further, we did not observe substantial differences in the transcript expression for most potassium channels, including hERG/KCNH2 (related to I_{Kr}). However, MM-treated WTC MPS showed upregulation of SLN, HCN2 and CACNB2, and downregulation of KCND2 and ALDH1A1 (**Fig. 6E**). In SCVI20, MM treatment caused a trend toward decreased KCNJ2; this gene is related to I_{K1}, and diminishing this current could be one explanation for increasing APD. We also observed KCND2 (I_{to}) upregulation, which increases robustness by counteracting KCNJ2 decrease. When treated with MM, SCVI20 MPS also showed upregulation of CACNB1 and SLN, although these changes were not statistically significant **(Fig. 6F)**.

Sarcolipin (SLN) is known to bind the SERCA pump in the sarcoplasmic reticulum of cardiac and skeletal muscle and act as a regulatory protein to increase heat production[57]. It does so by partially uncoupling SERCA's calcium re-sequestration function from ATP hydrolysis and therefore burn extra ATP without influencing calcium transients[58-60]. It is possible that since MM brings a higher caloric intake to the tissue through fatty acids, MM-treated MPS tissues might upregulate SLN to burn excess ATP. This would be consistent with more mature and efficient metabolism in MM through a metabolic switch from glycolysis to oxidative phosphorylation, which is supported by direct analysis of mitochondrial morphology and transmembrane gradients in MM-treated MPS (**Fig. 4**). SLN is preferentially expressed in atria and in previous work has been used to identify atrial-like iPSC-cardiomyocytes[61]. However, the possibility that MM shifted cardiomyocytes in MPS toward atrial subtypes is contracted by the overall pattern of gene expression – specifically, transcript levels for HEY2, a ventricular cardiomyocyte-specific transcription factor[62], were not affected by MM in WTC (**Fig. 6C**). Similarly, atrial cardiomyocyte specific transcription factor NR2F2[62] and sarcomere gene MYL7 were both downregulated by MM. Altogether, these data suggest that upregulation of SLN is more likely to be directly related to cardiomyocyte metabolism than tied to cardiomyocyte subtype.

The β-subunits of the voltage activated calcium channel expression encoded by CACNB1 and CACNB2 are required for expression of the *L*-type calcium current through regulating trafficking and activation of α-subunits[46, 63]. Changes in the levels of these subunits could potentially alter I_{CaL}. Despite our observation that force production and inotropic responsiveness of MPS were not perturbed by MM pre-treatment, we observed significant downregulation of several genes associated with calcium handling and sarcomere function in WTC, including MYL7, MYL2/MLC2V, and MYH7 (**Fig. 6E,F**). We observed a similar reduction of MYL2 and a trend towards decreased MYH7 in SCVI20. However, our data from immunostaining suggests that levels of the proteins encoded by the genes are

not changed significantly, and trend toward upregulation with MM, in both genotypes (**Fig. S5**), with no changes in cellular localization. This finding suggests that gene expression data does not necessarily correlate perfectly with protein level and localization. However, despite relatively similar levels of MYL2 and MYH7 proteins in WTC and SCVI20, the contractile forces of WTC are substantially higher (**Fig. 5C,D**).

2.3.7 Mathematical modeling of the ion channel and calcium transient contribution to electrophysiological patterns in MM-treated MPS

Although MM has divergent effects on APD in SCVI20 vs. WTC MPS, in both cases, this fatty acid-based media brings tissues closer to an *in-vivo*-like ventricular APD. To gain insight into how this occurs, we applied newly developed mathematical models[64] to estimate the contribution of individual Na^+, K^+, and Ca^{2+} currents, along with calcium handling machinery, to the experimentally measured action potential and calcium transients (**Fig. 7A-C**).

In contrast to gene expression data, but consistent with observed changed in APD, simulations predicted enhanced conductance (g_x•C_m•A/V) for the late rectifier potassium current I_{Kr} (hERG) in WTC (**Fig. 7D**). There was also a trend, albeit not statistically significant, toward increased I_{Kr} in SCVI20 MPS with MM treatment (**Fig. 7D**). No trends were observed in predicted I_{K1} **(Fig. 7E)**. In WTC MPS, simulations also predicted significant reduction of Na^+ current, enhancement of intracellular Ca^{2+} buffering, and repression of sodium-calcium exchange current (I_{NaCaX}) with MM (**Fig. 7F,H-I**); they also predicted trends toward reduced *L*-type Ca^{2+} current and improvements in intracellular calcium transport and RYR function with MM (**Fig. 7G,J,K**). In SCVI20 MPS, MM-treatment did not result in significant changes in any of the simulated currents or calcium handling parameters described by the model. However, the trend toward increased I_{Na}, I_{CaL}, I_{NaCx} and diminished intracellular calcium transport with MM treatment would be expected to delay the onset of repolarizing currents.

Simulations predicted diminished SERCA pump activity in MM-treated MPS of both genotypes; this trend was significant in WTC **(Fig. 7L)**. These results are consistent with gene expression data predicting marked MM-induced upregulation of SLN in WTC MPS, and a trend toward upregulation of this gene in SCVI20 MPS. SLN interacts with and suppresses the SERCA pump.

Consistent with the $\Delta F/F_0$ response (**Fig. 3G**) and the force developed in response to low extracellular calcium levels (**Fig. 5C**), the model shows a significant shift towards higher intracellular calcium in MM-WTC compared to SM-WTC. The overall calcium balance and SR stocks at steady state is shifted towards influx. Lower NCX activity and increase in Ca diffusion in MM-WTC (**Fig. 7H,K**) will rapidly bring calcium away from I_{CaL} and NCX towards sarcomere, acting as a buffer (**Fig. 7I**). Overall, the calcium accumulation in the cell will limit the inward currents and participate in APD shortening. In the case of MM-SCVI20, although the trend showed an increase of $\Delta F/F_0$ (**Fig. 3I**), it was not significant

compared to SM-SCVI20. This is consistent with the model showing a trend towards an increase in I_{CaL} and an increase in NCX (**Fig. 7G,H**) which could help explain the increase in APD and the constant calcium transient.

Consistent with the markedly different action potential waveforms in SCVI20 versus WTC MPS in standard media, simulations predicted significant differences in almost every ion current and calcium handling parameter described by the model (except for potassium currents and calcium buffering; **Fig. 7D-E,J**) for SCVI vs. WTC MPS. Interestingly, and consistent with our observation that fatty acid media brought APD to a very similar range for both genotypes, MM-treatment led to nearly identical predicted currents and calcium handling: no parameters predicted by the model differ between MM-treated SCVI20 and WTC MPS, except for I_{Kr} and calcium buffering, which were predicted to be higher in MM-treated WTC MPS **(Fig. 7D,I)**. The observation that no single simulated current was significantly different in MM vs. SM treated SCVI20 MPS suggests the potential that SCVI20 hiPSC-CM emerge from cardiac differentiation in a more matured state than do WTC hiPSC-CM. However, the potential that SCVI20 hiPSC-CM are more mature is contradicted by the significantly higher force produced by WTC MPS in either SM or MM (**Fig. 5C,D**). It is more likely the case that the significant changes in APD_{80} between SM and MM treated SCVI20 MPS (**Fig. 3D,E,H**) are caused by concurrent but subtle changes in several of the channel fluxes that contribute to the action potential.

To test the possibility that MM treatment causes more calcium to be stored in the sarcoplasmic reticulum of hiPSC-CM, we pharmacologically perturbed SR calcium handling in SM and MM pre-treated WTC MPS. Normally, in mature cardiomyocytes, Ca^{2+} released from the SR via RyR potently inactivates I_{CaL} and curtails sarcolemmal Ca^{2+} influx[65]. However, inhibition of the SERCA pump reduces the SR store, which in turn reduces systolic SR Ca^{2+} release and calcium-dependent inactivation of the membrane-bound L-type calcium channels. This mechanism is supported by observations of MPS treated with a saturating (10mM) dose of Ryanodine, which blocks the cardiac ryanodine receptor. This treatment dramatically increased both Ca^{2+} rise-time and decay time (τ_{75}) in MM-pre-treated, but not SM pre-treated WTC MPS. Moreover, although Ryanodine diminished $\Delta F/F_0$ for both SM and MM pre-treated MPS, MM pre-treated MPS showed a more substantial change in $\Delta F/F_0$ in response to this drug (**Fig. S8**). Neither MM nor SM pre-treated MPS displayed a change in beat rate upon treatment with Ryanodine (**Fig. S8A**). Not only are these findings consistent with predictions from simulations of trend toward greater predicted steady state SR-storage of Ca^{2+} with MM (**Fig. 7**), they are also consistent with a trend toward greater RyR flux in MM treated WTC MPS (**Fig. 7J**).

A second drug, Thapsigargin, which blocks SR Ca^{2+} reuptake via SERCA, also markedly slowed Ca^{2+} reuptake, increasing τ_{75}, in MM but not SM-pretreated MPS. In contrast to Ryanodine, Thapsigargin did not affect $\Delta F/F_0$ or calcium rise-time (**Fig. S9**). This response is consistent with our simulation data, which suggest that although SR calcium storage is enhanced by fatty acid media, there is some predicted suppression of SERCA

activity (**Fig. 7L**). Altogether, these experimental results are consistent with the prediction of the simulations that pre-treatment with MM increases the SR Ca^{2+} store, and its contribution to the cytosolic Ca^{2+} transient that fuels contraction. These results are internally consistent with the results of our simulations, and with previous work where matured hiPSC-CM exhibited a more marked calcium decay time in response to thapsigargin[36]. In previous studies, maturation media containing dexamethasone and triiodothyronine[66], and maturation induced by continuous field pacing[23] have been linked to improvements in hiPSC-CM Ca^{2+} handling through formation of T-tubules. However, in the present study, we observed minimal evidence of T-tubules, although qualitative analysis of Wheat-Germ Agglutinin stained MPS showed some instances of membrane invaginations that were more prominent in MM (**Fig. S10A-C**) than in SM (**Fig. S10D,E**) treated MPS.

2.3.8 Pre-Treatment of hiPSC-Derived-Cardiomyocyte Based MPS with Maturation Media Enhances Prediction of Drug Induced Pro-Arrhythmia

We next assessed whether maturation media treatment could lead to more predictive pharmacology of compounds with known pro-arrhythmic effects, and further whether the simulations predicted pharmacology changes induced by MM-pre-treatment. Pro-arrhythmia effects of these drugs have been quantified in clinical studies by measuring the QT interval of the Electrocardiogram (ECG)[67]. One important drug from these studies is Verapamil, which blocks both I_{CaL} and I_{Kr}, is routinely used in the clinic to shorten the QT interval in patients prone to suffer arrhythmias based on prolonged APD (for example, patients with long-QT syndrome[67]) based on I_{CaL} block. Verapamil is a prototypical example of a “false positive” drug that would appear to prolong APD and QT interval if one only assessed block of the current encoded by hERG/KCNH2, I_{Kr}[67, 68].

When we analyzed Verapamil dose-escalation effects in field-paced MPS and used beating prevalence as the metric for characterizing IC_{50}, we observed that MM-pre-treated WTC MPS exhibited enhanced Verapamil resistance compared to SM-treated MPS (971 nM for MM-pre-treated MPS, versus 90nM for SM-treated MPS; **Fig. 8A**). In contrast, SCVI20 MPS showed a decreased Verapamil resistance with the same media (**Fig. 9A**). Direct analysis of APD revealed a dose-dependent decrease in APD_{80}, consistent with the clinical application of this drug to shorten QT duration (**Fig. 8B, 9B**). However, unlike beating prevalence, the dose-response for APD_{80} did not change appreciably in MM pre-treated, compared to SM-pre-treated MPS, for either genotype. There were, however, weak trends toward Verapamil desensitization in MM-treated WTC and Verapamil sensitization in MM-treated SCVI20 MPS when APD_{80} was used as an *in vitro* metric of drug response (**Fig 8C, 9C**).

These genotype-based shifts in Verapamil responsiveness may be explained by the relative I_{CaL} and I_{NaCax} levels predicted by mathematical models **(Fig. 7G,H)**: in WTC, the trend with MM is toward slightly higher I_{CaL} (increases intracellular Ca^{2+}) and markedly

lower I_{NaCax} (decreases intracellular Ca^{2+}). The net effect of this increases influx and diminished efflux would be higher steady state levels of Ca^{2+} stored in the sarcoplasmic reticulum (SR). Higher SR-calcium levels would tend to increase contractility in response to Ca^{2+} uptake through *L*-type calcium channels, thereby desensitizing cells to I_{CaL} block. Increased steady state Ca^{2+} levels would also be consistent with the observed increase in calcium amplitude ($\Delta F/F_0$; **Fig. 3G**) and contractility in MM-WTC relative to SM-WTC MPS, in the setting of limiting extracellular calcium (**Fig. 5C**). In contrast, within SCVI20 MPS, the trend toward a stronger increase in I_{NaCax} than in I_{CaL} would result in lower SR levels of stored Ca^{2+}. This would likely make cells more sensitive to I_{CaL} block.

We next assessed the ability to predict pharmacology of Flecainide, a class Ic (Na^+ channel blocker) antiarrhythmic drug typically used to treat tachy-arrythmia, has been noted to have a narrow therapeutic index and is counter-indicated in patients with pre-existing structural disease[69]. This drug also blocks the hERG current[70]. Consistent with this narrow therapeutic index, we correctly observed very little difference between the Estimated Therapeutic Plasma Concentration (ETPC) of 1.5μM, and *in vitro* EC_{50} (APD_{80}) and IC_{50} (beating prevalence) (**Fig. 8D-F, Fig. 9D,F**). Unlike Verapamil, Flecainide did not exhibit a differential EC_{50} within MM versus standard media pre-treated MPS for the WTC genotype; however, there was a weak trend toward desensitization of MM-pre-treated WTC MPS to the APD prolonging effects of this drug, which is consistent with improved hERG current in MM-treated WTC MPS. In the SCVI20 genotype, we observed a marked desensitization of MM-treated MPS to both contractile and APD changes induced by Flecainide. Although MM increases APD in SCVI20 MPS, the fatty acid media still causes a trend (albeit, not statistically significant) toward increased hERG current (**Fig. 7D**). Improved hERG current would desensitize MM-treated SCVI20 MPS toward I_{Kr} blocking effects of Flecainide.

Given how sensitive the SM-treated SCVI20 MPS are to the AP altering effects of Flecainide (EC_{50} of 5.5nM), the depressed contractility at 1 Hz pacing may be due to impaired calcium uptake. To test this hypothesis, we compared Ca^{2+} amplitude using OGB-1-AM imaging. This analysis revealed that, concurrent with lengthening the calcium transient timing, Ca^{2+} amplitude increased almost 3-fold over baseline in MM-SCVI20 MPS treated with 1μM Flecainide. In contrast, the amplitude of Ca^{2+} did not exceed baseline in Flecainide treated SM-SCVI20-MPS (**Fig. S11A-C**). The sodium-calcium exchanger can operate in reverse during action potential prolongation[65]. Thus, the observed ability of MM-SCVI20 MPS to withstand the contractility-depressing effects of Flecainide at doses that significantly disrupt contractility in SM-SCVI20-MPS may potentially be explained by the trend in simulations **(Fig. 7H)** toward enhanced NaCx exchange current in MM vs. SM pre-treated SCVI20 MPS. The observation that although Ca^{2+} uptake increases near 1μM Flecainide, but that contractility (beating prevalence) did not increase at this dose in MM-SCVI20 MPS, may potentially be explained by Flecainide-induced RYR block. Consistent with the exaggerated effects of flecainide on APD in SM-treated SCVI20 MPS,

MPS of this genotype were more prone to Early After Depolarizations (EADs) that MM-treated MPS at 100nM dose of this drug (**Fig. S11D,E**).

Finally, we assessed MPS pharmacology of Alfuzosin, an α_1-adrenergic blocking agent that has been shown to increase patients' QT interval by hERG-independent mechanisms[11, 71]. This makes Alfuzosin a "false negative" drug in screens for potential QT prolongation that rely on overexpression of the hERG/KCN2 gene in heterologous cell types. Here, we observed that in WTC, both MM and SM pretreated MPS exhibited IC_{50} near 1μM when measuring beating prevalence (**Fig. 8G**). However, when we tested the effects of this drug on extending APD_{80}, we observed a specific sensitization with MM-pre-treated MPS, relative to MPS pre-treated with SM (**Fig. 8I**). We can explain the drastic change in APD with an unchanged prevalence through the efficient calcium transport of the MM-WTC, enabling the cells to contract despite the short resting time between long-duration actional potentials. In SCVI20, there was a trend toward sensitization of SM-treated MPS to Alfuzosin, although differences in the EC_{50} observed via APD_{80} analyses were not statistically significant **(Fig. 9I)**.

We summarized these observations of drug responsiveness by plotting the safety margin observed for each drug, using either beating prevalence (**Fig. 8J, 9J**) to obtain IC_{50} or APD_{80} prolongation (**Fig. 8K, 9K**) as the metric used to obtain EC_{50}. The safety margin is defined as *in vitro* IC_{50}/ETPC for prevalence (or *in vitro* EC_{50}/ETPC for APD_{80}), and describes the relative risk for beating abnormalities. Typically during pharmaceutical development, a safety margin of 18-20 (green line on **Fig. 8J,K** and **9J,K**) is used as a go/no-go decision for a chemical compound. None of these drugs exhibited differential pharmacology between SM and MM-pre-treated 2D monolayers in either genotype (data not shown). Safety margin analysis revealed that for WTC, culture within MPS and the subsequent maturation of MPS with fatty-acid enriched media had improved the safety margin for Verapamil (using the metric of prevalence) and Alfuzosin (using the metric of APD_{80}), but no statistically significant effect on the safety margin of Flecainide (**Fig. 8J**). There was also a trend, albeit not statistically significant, toward improved safety margin of beating prevalence to Alfuzosin in MM pre-treated MPS, compared to 2D monolayers. In SCVI20, MM-treated MPS showed improved prevalence safety margins (closer to target green line) in the three drugs when compared to 2D platforms (**Fig. 9J**). APD_{80} based safety margin gave improved results for both SM and MM-treated MPS for Alfuzosin and Verapamil (although not significant for the latter one) (**Fig. 9K**). SCVI20 MM and SM treated MPS tissues were hypersensitive to Flecainide when looking at the APD_{80} safety margin, to the point that *in vitro* EC_{50} was less than the clinically reported ETPC **(Fig. 9K).** Besides being self-consistent with predictions of relative levels of specific currents (e.g. I_{Kr}, I_{CaL}) in MM vs. SM treated MPS of each genotype, these pharmacology data suggest that MPS improves the prognostic capability of hiPSC-CM, and that MM pre-treatment further augments the prognostic power of MPS. For example, although Verapamil is routinely used in the clinic, particularly for QT-interval management, it exhibits false positive

toxicity in hERG-assays, and the beating prevalence of 2D monolayer cultures of hiPSC-CM are sensitized to this drug, as shown here (**Fig. 8J and 9J**) and in other studies[11, 13, 22]. Our data suggests that culture within MPS alone dramatically enhances the IC_{50} of this drug, eliminating the false positive toxicity seen in 2D monolayer hiPSC-CM, regardless of genotype. These observations are consistent with our previous studies[13, 22]. The combination of MPS with MM gives a more accurate profile of the safe nature (thereby reducing false positive toxicity) of this drug. In contrast, the fact that Alfuzosin is sometimes observed to cause arrhythmias in the clinic[71], suggests that the higher *in vitro* EC_{50} values observed in monolayer culture and SM-cultured MPS under-predict potential toxicity (false negative). Our findings with MM-cultured MPS, which indicate sensitization to the APD prolongation effects of Alfuzosin, suggest that MM pre-treatment enhances the ability of MPS to accurately predict the clinically observed effects of this drug. Collectively, these data indicate that combining MPS culture with MM can reduce both false positive (Verapamil) and false negative (Alfuzosin) drug response estimates. Enhanced drug resistance is not universally observed in MPS culture, suggesting against the trivial explanation that drug availability is limiting in these 3D systems, likely due to the small and physiologically-relevant scale of our 3D microtissues ~ 150μm in width, consistent with cardiac muscle bounded by collagen fibrils[72]. Our work suggests instead that changes in drug susceptibility are due to changes in density and function of specific ion channels that these drugs target.

2.4 Conclusions

Despite the promise of hiPSC-derived tissue cells as genetically defined human *in vitro* models for drug development and fundamental biology, maturation of hiPSC derivatives including hiPSC-CM into adult-like cells remains an important challenge. In the present study, we demonstrated that the combination of aligned, 3D culture in MPS with fatty-acid based media synergized to promote maturation of hiPSC-CM action potential. Combining *in silico* modeling with experimental measurements provided insights into a putative mechanism linking alterations in individual ion channels and calcium handling machinery to whole-cell changes in action potential. This is the first study to induce maturation of hiPSC-CM in a tissue-chip, and, importantly, we demonstrated that maturation not only affected the baseline physiology of hiPSC-CM, but also yielded cells with pharmacology more reminiscent of adult human cardiomyocytes. Strikingly, this media had opposing effects on the action potential duration of genetically unique hiPSC-derived tissue chips, with the net result of forcing both genotypes towards an actional potential duration range that is typical for adult human ventricular cardiomyocytes. These results suggest that, as in monolayer culture of hiPSC-CM[36], maturation with fatty-acid based media may be a prerequisite to using hiPSC-CM based tissue chips to predict how drugs will affect the adult human heart.

2.5 Materials and Methods

2.5.1 Cell sourcing

Two parent hiPSC were used in the majority of these studies: Wild Type C (WTC) human hiPSC harboring a single-copy of CAG-driven GCaMP6f knocked into the first Exon of the AAVS1 “safe harbor” locus[37] . The parent cell line (WTC) was reprogrammed from fibroblasts derived from a healthy 30-year-old Japanese male with a normal electrocardiogram and no known family history of heart disease and is available from the Coriell Repository (# GM25256 hiPSC from Fibroblast). The second line, Stanford University Cardiovascular Biobank Line 20 (SCVI20), was generated from a healthy, disease genotype 77-year-old Caucasian male[38]. The third cell line, SCVI273, was generated from a 43-year-old Asian female, and was used for comparison of action potential duration and calcium F/F_0 in response to maturation media treatment. SCVI20 and SCVI273 are available from the Stanford University Cardiovascular BioBank.

2.5.2 Cardiomyocyte Differentiation

HiPSC-CM were derived from pluripotent hiPSC and purified using published protocols relying on small molecular manipulation of Wnt signaling[73], with some modifications. Briefly, frozen stocks of pluripotent cells were thawed and plated on hESC-Qualified Matrix (Corning; Corning, NY) in Essential 8 Medium (E8; Thermo Fisher, Tewksbury, MA) containing 10μM Y27632 (Peprotech; Rocky Hill, NJ). Fresh E8 without drug was added the following day. To prepare cells for differentiation, hiPSC were grown to 70-80% confluency, and then passaged three times at a constant density of 20,000 cells/cm^2 (Burridge *et al.* 2014). During passaging, cells were singularized with Accutase (Thermo; Waltham, MA) and plated in E8 with 10μM Y27632. After pre-passaging, hiPSC were plated at a density of 25,000 cells/cm^2, in 10μM Y27632. This was counted as “day – 3” of differentiation. At day 0, hiPSC were >90% confluent and were treated with Roswell Park Memorial Institute Medium 1640 (RPMI) containing B-27 supplement without insulin (RPMI-I), along with 8μM CHIR99021 (Peprotech) and 150μg/mL *L*-ascorbic acid (LAA). Exactly 24 hr after drug was added, medium was exchanged for RPMI-I (day 1). On day 2, medium was replaced with RPMI-I containing 5μM IWP-2 (Peprotech). On day 4, medium was exchanged for RPMI-I. RPMI containing standard B-27 supplement (RPMI-C) was added on days 6,7,9, and 11. Robust spontaneous contractile activity was typically observed on day 8 of differentiation.

On day 15 of differentiation, hiPSC-CM were singularized and cryopreserved. Briefly, cells were washed twice, for 15 minutes, with dPBS, to deplete calcium from extracellular space and sarcomeres. Next, cells were exposed to 0.25% Trypsin (Thermo Fisher) for 10-20 minutes. Cells were triturated gently at every five minutes, then pelleted (300g, 5 minutes). Cell pellets were resuspended into RPMI-C with 10μM Y27632 for counting.

Cells were then pelleted a second time, and resuspended into cryopreservation medium containing 10μM Y27632, then frozen and kept in liquid nitrogen.
Two weeks before MPS experiments, hiPSC-CM were thawed and plated at a density of 100,000 cells/cm^2 onto Matrigel, in RPMI-C with 10μM Y27632. The following day, medium was exchanged for RPMI-C. Three days after plating, monolayers were spontaneously contracting. Cells were then washed with dPBS and exposed to a cardiomyocyte selective medium depleted of glucose and pyruvate (Media-L; RPMI 1640 without glucose or sodium pyruvate, supplemented with 23mM sodium bicarbonate and 5mM Sodium *L*-lacate[74]) for a total of five days. Cells were washed with dPBS and fresh Media-L was added every other day. On the fifth day of purification, significant death of non-beating cells was observed. Cells were washed with dPBS and allowed to recover in RPMI-C for three days. Cardiomyocyte purity both before and after this procedure was characterized by flow cytometry for Cardiac Troponin T (TNNT2; **Table S1; Fig. S1**).

2.5.3 Isogenic Stromal Cell Differentiation

Isogenic iPS-stromal cells (hiPSC-SC) were derived via small molecular activation of Wnt signaling in pluripotent hiPSC, followed by VEGF exposure, as described previously[75]. Briefly, hiPSC were seeded at a density of 25,000 cells/cm^2 onto hESC-Qualified Matrigel. This was termed “day -3” of the culture. On day 0, wells were 80-100% confluent, and the medium was switched to LaSR media (Advanced F12/DMEM, 2.5mM Glutamax; 60ug/ml ascorbic acid), and 7.5uM CHIR99021 for 2 days without medium change. At day 2, the media was changed to LSR media with 50 ng/ml VEGF (Peprotech) for 2 days without medium change. On day 4, medium was replaced to LaSR media only. On day 6, cells were ready for CD31 magnetic sorting. For magnetic sorting on day 6 of differentiation, cells were rinsed with dPBS and trypsinized for 8min. Trypsin was quenched by adding EB20 media (20% FBS, 2.5mM Glutamax, KO DMEM), and cells were centrifuged (300g for 3 minutes) and re-suspended in FACS buffer (PBS, 2% FBS). CD31+ magnetic Dynabeads were added to the cell suspension at a concentration of 8 beads per CD31+ cell and left 20min on ice. The CD31 negative fraction was then expanded (maximum of ten passages) on uncoated tissue culture plastic substrates supplemented with EGM-2 media (Lonza) and characterized (**Fig. S2**). Full details on antibodies used to characterize these cells are provided in **Table S1**.

2.5.4 Plating of hiPSC for 2D Monolayer Studies

In 2D monolayers, hiPS-SC overgrow hiPSC-CM (data not shown). Thus, for 2D pharmacology and gene expression studies, biochemically purified hiPSC-CM were grown in monolayers. Purified cardiomyocytes were singularized with 0.25% trypsin after extensive dPBS washes. The cells were then resuspended into RPMI-C supplemented with 10μM Y27632 and plated at a density of 200,000 cells/cm^2 onto GFR Matrigel. The following day, medium was exchanged for RPMI-C. Three days after plating, monolayers were

spontaneously contracting. Cells were then exposed to either SM or MM for ten days prior to the onset of gene expression and pharmacology studies.

2.5.5 Fabrication of Cardiac MPS

Microfluidic cardiac MPS systems were formed using small modifications of the protocol described in our previous work[22] (see **Fig. 1, Fig. S6**). Briefly, two-step photolithography was used to form a chip comprised of: 1) a cell-loading port leading to a cell culture chamber with two large "anchoring posts" and several smaller micro-posts; and, 2) a media-loading port leading to media channels running alongside the cell culture chamber. The media channels and cell culture chamber (50μm high) are connected by a series of fenestrations (2μm x 2μm high/width) that provide a barrier to convective flow at defined volumetric flowrates, such that all media factors delivered to cells in the culture chamber arrive via diffusion[22]. The cardiac MPS is formed by replica molding Polydimethylsiloxane (PDMS; Sylgard 184 kit, Dow Chemical, Midland, MI) at a 10:1 ratio of Sylgard base to crosslinker from a photolithographically defined wafer. These PDMS chambers were then bonded to glass slides using oxygen plasma.

2.5.6 Self-Assembly of Cardiac Microtissues within Cardiac MPS

hiPSC-CM and hiPSC-SC (passage 5 - 8) were singularized with 0.25% trypsin after extensive PBS washes. We then prepared a cocktail of 80% hiPSC-CM and 20% hiPSC-SC, at a density of $6.6x10^6$ cells/mL, in EB20 media supplemented with 10μM Y27632 and 150μg/mL *L*-ascorbic acid. 3μL of this cocktail, corresponding to $2x10^4$ cells, was injected into the cell loading inlet of each MPS. MPS were then loaded by centrifugation (300g, 3 minutes), and plugged with an SP20 steel rod to prevent cellular regurgitation from the cell chamber during media loading. Next, the same media used to resuspend cells was added to the channels of each MPS. MPS were then individually inspected, and any cell chambers that were not completely filled were filled by applying gentle pressure to the SP20 plug. This time-point was counted as MPS day 0. At MPS day 1, media was changed to RPMI with B27 supplement. At day 3 MPS were continuously fed either maturation media or standard media, using negative pressure for media exchange as described in our previous study[22]. Pump-free, gravity-driven flow was used to feed the tissues. Every 2 days, fresh media was replenished into the inlet reservoir so that hydrostatic pressure would drive a continuous flow through the media channels to the outlet reservoir. This technique is commonly used with microfluidic devices due to its simplicity and low cost (Komeya et al, 2017; ref. [76]). Potential batch-to-batch variability in hiPSC-CM phenotype was mitigated by performing all physiology and gene expression studies with MPS and monolayers derived from a minimum of three independent differentiations.

2.5.7 Robust Design Experiments to Identify the Composition of the Optimal Maturation Media

We hypothesized that switching the carbon source of cardiac MPS from glucose to fatty acids could induce more mature electrophysiology of hiPSC-CM. We employed Robust Design screening to optimize four different media composition variables. Given the likelihood of these variables acting in a synergistic fashion to enhance maturation, the parametric space would require 3^4, or 81 independent experiments (excluding the several replicates required for significant studies). To study this large space in a cost and time-effective manner within MPS, we employed Robust Design[41] screening. With orthogonal arrays, the variable-space spanned by these 81 independent experimental conditions was explored with only 9 independent experiments. These 9 experiments were designed such that the four media input variables (levels of glucose, oleic acid, palmitic acid and BSA) were varied in an orthonormal fashion from one experiment to the next (**Table 1**). BSA (Sigma # A2153) was used directly, without being first stripped of exogenous fatty acids.

In the case where glucose was completely omitted from cardiac media, we added 10mM galactose, as previous studies have shown healthy hiPSC-CM are capable of using galactose as an ATP source[35, 43]. Based on the hydrophobic nature of the primary fatty acids used as ATP sources in the heart (oleic acid and palmitic acid, respectively), we added additional BSA, above the 0.25% already contained in the B27 supplement. In all cases where fatty acids were added to media, they were first incubated at 37°C with concentrated BSA and B27 supplement to allow fatty acids to bind the extra albumin, or the 0.25% albumin already contained in B27. Beating physiology and calcium flux were assessed with high-speed microscopy as described below. Media were screened based on their ability to reduce spontaneous beat-rate, as well as the interval between peak contraction and peak relaxation during 1Hz field pacing, while maintaining a high prevalence of beating (defined as the percent of the tissue with time-averaged motion exceeding a pre-determined threshold) during pacing at 1Hz. MPS were treated with various candidate maturation media for 10 days before beating physiology was assessed.

2.5.8 Image Acquisition for Beating Physiology Studies

During imaging, MPS or 2D monolayers in multi-well plates were maintained at 37°C on a stage equipped with a heating unit (Tokai Hit, Gendoji-cho, Japan). First, baseline readings of spontaneous calcium flux (GCaMP6f), and beating physiology (bright-field video) were taken. After acquiring spontaneous electrical activity, electromechanical activity under field pacing was assessed. MPS were paced via sterile, blunted stainless steel needles that were inserted into the pipette tips leading to both the media inlets and outlets. Care was taken to fill pipettes and prevent bubble formation to maintain electrical conductivity. Before recording videos, cells were paced for 10 seconds (20V, 20msec bipolar

pulses at 1Hz, ION OPTIX Myopacer Field Simulator). Pacing was then maintained at the same intensity and frequency for acquiring images of MPS contracting at 1Hz.
Imaging was performed with a NIKON TE300HEM microscope equipped with a HAMAMATSU digital CMOS camera C11440 / ORCA-Flash 4.0. All videos were recorded at a framerate of 100 frames/second for a duration of 8 seconds. For GCaMP imaging, fluorescent excitation was provided by a Lumencor SpectraX Light Engine (GCaMP: Cyan LED, 470nm) and filtered with a QUAD filter (Semrock). Videos were acquired using Zeiss Zen Pro 2012 software.

2.5.9 Image Analysis

Brightfield videos were analyzed for beating physiology using an updated version of our open source motion tracking software[37] (software available at https://huebschlab.wustl.edu/resources/). The current version of the software uses tools from the open source Bioformats Toolbox[77] to obtain image and metadata from microscopy files.
Briefly, microscopy files (Zeiss Zen, .czi) were directly read into the Matlab-based GUI, and the contractile motion of tissues was analyzed via an exhaustive-search block-matching optical flow algorithm that compared the position of 8x8 pixel macroblocks at frame *i* to their position at frame *i*+5 (corresponding to the motion in 50msec). Motion vectors were used to calculate beat-rate, beating interval (defined as the time delay between maximum contraction velocity and maximum relaxation velocity, which is directly proportional to action potential duration), and beating prevalence. Beating prevalence was defined as the percentage of macroblocks within a region-of-interest (ROI) with a time-averaged contraction speed that exceeds a defined threshold (2μm/sec was defined empirically as a universal threshold for all MPS analyzed). ROI were selected to include the entire cell culture chamber of the MPS.
GCaMP data were quantified using in-house Matlab code that was developed based on previous work by Laughner and colleagues[54, 78]. GCaMP videos were analyzed for τ_{75} decay time (time for calcium amplitude to go from maximum to 25% of maximum), Full Width Half Maximum (FWHM, time for calcium amplitude to go from 50% of maximum during upstroke, to 50% of maximum during decay) as well as peak intensity, a metric of total calcium influx. For spontaneously beating cells, data on beating interval and calcium transient decay times were rate corrected using Fridericia's method[79].

2.5.10 Optical Measurement of Action Potential

BeRST-1 dye was synthesized, and purity verified, as previously described[80]. For action potential recording, MPS were first labeled overnight with 2.5μM BeRST-1. The following day, MPS were equilibrated to media without dye before imaging (RPMI-C without phenol red) as described above, using a Red LED (640nm). For monolayer experiments, cells were labeled with 500nM BeRST-1 for 1h at 37°C, and then equilibrated to RPMI-C

without phenol red. After acquiring videos of spontaneous and 1Hz paced activity at 100 Hz for 8 seconds, BeRST-1 videos were analyzed using similar Matlab code as was used for GCaMP analysis[78]. BeRST-1 videos were analyzed for 80% Action Potential Duration (APD_{80}). Reported values of APD_{80} (**Fig. 3**) are for MPS or monolayers paced at 1Hz.

2.5.11 MPS Tissue Isolation and Immunofluorescence Imaging

Tissues were treated with SM or MM for 10 days. On day 10, MPS were flushed for 10 minutes with PBS at 25°C. Following this wash, 4% PFA was added to the media channel for 15min to fix the tissues. MPS were washed with PBS twice for 5min after that and were then carefully cut with a clean scalpel, to open the device and expose the tissue. At this point, the PDMS component had the tissue structure attached to it. The tissues were then stained by submerging PDMS blocks in different staining solutions: First, tissues were blocked with blocking buffer (1% BSA 10% FBS 0.5% Triton 0.05% sodium azide) overnight at 4˚C. The next day, they were submerged the primary antibodies (Mouse anti α-actinin, Life technologies 41811; Rabbit anti-GAPDH, abcam 9485; Mouse anti-mitochondria, abcam 92824; Mouse anti β-myosin heavy chain, abcam 97715; Rabbit anti myosin Light Chain 2V (MLC2V), Proteintech 10906-1-AP) 1:100 concentration in blocking buffer) for 48h at 4˚C. Tissues were then washed twice at 25˚C in blocking buffer for 2-3 hours and washed a third time at 4˚C overnight. The secondary antibodies (Goat anti-mouse IgG Alexa 568 H+L, Life Technology a11004; Goat anti-rabbit IgG Alexa 488 H+L, Life Technology a11008) along with 1:600 DRAQ5 (Abcam, ab108410) was incubated in blocking buffer for 24h. Tissues were then washed twice at 25˚C in blocking buffer for 2-3 hours and a third time at 4˚C overnight before tissues were imaged.

Both WTC and SCVI20 tissues were imaged with Opera Phenix™ High Content Screening System. All images were taken through proprietary Synchrony™ Optics 63x water immersion lens. Images were acquired using Harmony software. We imaged both DRAQ5 and α-actinin for sarcomere alignment using 640nm and 546nm lasers respectively. We performed z-stacks over 60μm with a step-size of 0.5μm for α-actinin or GAPDH stains. Mitotracker and anti-mitochondrial antibody were imaged with a step size of 0.3μm. Post imaging processing was performed on ImageJ to enhance contrast and decrease background fluorescence. The same post-processing was performed for SM and MM tissues to allow direct comparison between them.

To analyze the regularity of sarcomeres from staining of sarcomeric α-Actinin, we applied Fast Fourier-Transform (FFT) based methods[54] to cellular regions of the MPS that had a constant size (100 x 100 pixels). Next, the real component of the FFT was smoothed with a 3x3 Gaussian filter, and the mean intensity was calculated as a function of radial distance from the center of the centered real-component of the FFT. Structures with regularly repeating features (e.g. sarcomeres) produce distinct bands when analyzed in this manner, resulting in local increases in intensity at specific radial distance. These local intensity increases were quantified[43, 54]. Code is available from the authors upon

request. Representative fields of interest for intensity quantification and analysis of sarcomere regularity (**Fig. S5**) were selected and analyzed by a user blinded to the experimental condition.

2.5.12 Analysis of Mitochondrial Morphology and Potential

Mitochondrial potential was analyzed in 2D monolayers and MPS using MitoTracker Red (M7512 Thermo Scientific). Live MPS and monolayer were incubated with Mitotracker for 30min at 37C in RPMI 1640 supplement with insulin. Samples were then washed with PBS for 10min before being fixed in 4% PFA for 15min and washed again with PBS. Monolayers were directly imaged after that and tissues were isolated from the MPS as described above and placed into wells of 24-well plates with PBS until they were imaged.

2.5.13 Measurement of Contraction Force

Micro-molded PDMS pillars were added to the cell chambers, so that the tissue would deflect them upon each contraction (**Fig. 1B, S6A,B**). By considering each pillar as a cantilever beam fixed at one end and uniformly loaded with horizontal forces along its height, one can apply the Euler-Bernouilli formula for uniformly distributed load and deduce the contraction force from the pillar's elastic modulus, deflection and dimensions. For WTC-MPS, pillar deflection was calculated with ImageJ by measuring the distance between the pillar's centroid coordinates before and after contraction. Same scale (0.5 pixel/micron) was used for all measurements.

To facilitate higher-throughput measurements, a new python-based software was developed to automatically identify pillars in the tissue. The software combined information derived from circle Hough transform[81] and custom template matching[82] algorithms (**Fig. S6C**) to detect the initial coordinates of the pillars at frame 0 of each recording. These initial positions were then fed to an enhanced version of our original tracking algorithm[37] to retrieve the absolute motion of the pillars during contractions (**Fig. S6D**). The motion was then converted to contraction force by using Euler's beam theory as described previously. This higher throughput software was used for SCVI20 MPS force analysis.

2.5.14 Pharmacology in MPS and 2D Monolayers

To avoid any possible confounding effects that different albumin or lipid content might have on drug bioavailability, for all pharmacology, MPS were first equilibrated to phenol red free RPMI with B-27 (SM) containing vehicle control (DMSO, methanol, or water, to a final concentration of 0.1% v/v). On the day upon which studies were performed, freshly measured drug was dissolved into DMSO, except for Flecainide, which came as a methanol stock solution, and Verapamil or Isoproterenol, which were dissolved directly into media. For testing inotropic responsiveness to extracellular calcium concentration, Tyrode's saline (0.1g/L anhydrous $MgCl_2$, 0.2g/L KCl, 8g/L NaCl, 50mg/L anhydrous monobasic

sodium phosphase, 1g/L D-glucose) was used in lieu of RPMI-C, as in previous studies of inotropic responsiveness of macroscale and miniaturized EHM[13, 17]. After recording activity in zero-dose vehicle condition, media were exchanged for the lowest drug dose, and MPS were incubated for 30 minutes at 37°C. Spontaneous activity, and activity with 1 Hz pacing, were recorded as described above. This was repeated for each dose escalation of drug. Drug dose was escalated until all spontaneous and paced activity ceased, or a dose of 10μM was reached.

Media on monolayers of hiPSC-CM was replaced with phenol red free RPMI-C containing 1μM BeRST-1, and monolayers were incubated for 30 minutes at 37°C (5% CO_2). Medium was next replaced with RPMI-C supplemented with the vehicle used to dissolve drug (water, methanol or DMSO, to a final concentration of no more than 0.1% v/v). Similar to dose-escalation studies in MPS, new drug was added and allowed to equilibrate to each increasing drug dose over 30 minutes intervals at 37°C, 5% CO_2. After equilibrating monolayers to vehicle and to each dose of drug, spontaneous beating physiology, calcium flux and action potentials were collected in bright-field, GCaMP and BeRST-1 channels, respectively. Next, cells were paced at 1Hz to collect these same three parameters.Gene Expression in Monolayer Culture

2.5.15 Gene Expression in Monolayer Culture

To characterize gene expression during hiPSC-SC differentiation, cells at various stages of differentiation of hiPSC to endothelial cells were trypsinized, pelleted and lysed (Qiagen RLT lysis buffer supplemented with 1% β-Mercaptoethanol. RNA was recovered using spin columns (Qiagen MicroRNAeasy® kit), with on-column DNAse I digest performed according to the manufacturer's protocol. Purified hiPSC-CM were plated to a density of 200,000 cells/cm^2 on Matrigel coated plates in RPMI-C containing 10μM Y27632. One day after plating medium was exchanged for RPMI-C. Two days following this, monolayers had recovered spontaneous beating, and cells were treated for ten days with either Standard Media (SM) or Maturation Media (MM). Media was exchanged every 3 days. On day 10, cells were washed with PBS and RNA was recovered in the same manner as for monolayer hiPSC-SC. Following RNA recovery from 2D cultures, 500ng of recovered RNA was used to produce cDNA using the SuperScript III kit with Oligo-dT primers (Life Technologies). The obtained cDNA was used to perform SYBR Green and Taqman real-time PCR analysis with the probes described in **Supplemental Tables S1 and S2**. Commercial polyA-RNA obtained from 15 pooled male/female Caucasians adult human left ventricle (Clonetech, Mountain View, CA) was used as a positive control for expression of cardiomyocyte ion channels, as described previously by Liang[11].

2.5.16 Gene Expression in MPS

Purified hiPSC-CM were combined with expanded hiPSC-SC as described above for initial optimization studies and cultured for ten days in either standard SM or MM. We first

optimized protocols for isolating high-quality (R.I.N. > 8.5) RNA from MPS (data not shown). RNA was extracted from tissue using methods similar to those previously applied for macroscale engineered heart muscle preparations[18]. Briefly, on day 10, MPS were flushed for 10 minutes with PBS at 25°C. Following this wash, MPS were carefully cut with a sterile scalpel, to separate the cell culture chamber from the cell loading chamber of the MPS, and to open the device. The PDMS component, with microtissue attached, was transferred to a microcentrifuge tube, and pooled with up to six other microtissues in lysis buffer from the RNAqueous kit (Thermo). Immediately after adding the tissues to lysis buffer, the microcentrifuge tube containing them was flash frozen in liquid nitrogen. Next, RNA was retrieved from samples by following manufacturer instructions on the RNAqueous kit, followed by DNAse I digestion (Ambion). The yield and quality of RNA were assessed with Qbit and Bioanalyzer, and with optimized methods, we routinely achieved RNA Integrity Numbers above 9. RNA isolated from MPS was amplified using a SMARTeR stranded Pico Input Total RNA library prep kit (Clonetech). The cDNA library products were then diluted by a factor of 10 into sterile water for direct quantitative PCR analysis of relative gene expression. RNA from positive controls was reverse-transcribed and amplified using the same kit. For qPCR analysis, cDNA libraries were diluted by a factor of ten into RNA grade water so that gene expression would fall within the linear assay range.

2.5.17 Mathematical Modeling

Time-series of AP and Ca^{2+} flux from MPS paced at 1Hz were inverted to a mathematical model of ion channel activity and calcium dynamics to obtain simulated estimates of channel conductance and calcium handling as described in our recent publication[64]. Briefly, a modified version of a model of an immature stem cell[7] was used to calculate the predicted voltage and calcium dynamics. Parameters of this model, specifically maximal channel conductances, intracellular calcium diffusion terms, and surface to area ratios, were then iteratively perturbed until the error between the measured waveforms and simulated waveforms was minimized. Resulting parameters and produced action potential models were then plotted by group to provide an explanation for mechanistic reasons for changes in action potential. It is known that parameterization of such models based on MPS data is challenging and may yield non-unique results; different channel conductances may results in similar voltage output of the model. This issue is discussed by Jæger in a previous study (Jæger *et al. Chaos* 2019; ref. [83]) where a method for identifying undetectable parameters was derived. In the present work we have used an inversion with regularization[84] to handle non-unique solutions.

2.5.18 Statistical analysis

Direct comparisons were made by unpaired student's *t*-test, with Holm-Bonferonni correction for multiple comparisons. All curve fitting was done using GraphPad Prism. IC_{50}

and EC_{50} curves were fit to four-parameter models. When these models yielded ambiguous fits (**Fig. 5C,D,F,G**), a three-parameter model was used. To analyze the currents and calcium flux parameters generated from model fits of action potential and calcium flux waveforms (Fig. 6), we performed a global 1-way ANOVA analysis followed by post-hoc Tukey tests. Gene expression data were statistically analyzed with ClustVis (web tool for clustering multivariate data) and GraphPad Prism. Overall PCR data were plotted on ClustVis to obtain heatmaps of the gene expression for maturation media treated MPS relative to standard media values. The genes within 90% percentile of differential expression were then selected and plotted on GraphPad Prism where an unpaired non-parametric t-test was performed to compare standard media and maturation media values using the Holm-Sidak method. Significance was determined with p-value < 0.05.

2.6 Acknowledgements

This work was funded in part by the California Institute for Regenerative Medicine DISC2-10090 (K.E.H.), NIH-NHLBI HL130417 (K.E.H.), NIH-NIGMS R35GM1195855 (E.W.M.), NIH-NIGMS T32GM066698 (S.B.), the Research Council of Norway INTPART Project 249885, the SUURPh program funded by the Norwegian Ministry of Education and Research, and the Peder Sather Center for Advanced Study (UC Berkeley). We thank Mary West (UC Berkeley) for assistance with image analysis and flow cytometry and Silvio Weber (Technische Universität Dresden) and Stacey Renschler (Washington University in St. Louis) for helpful advice on RNA isolation, cDNA amplification and data analysis. We thank Yoram Rudy, Jon Silva and Jianmin Cui (Washington University in St. Louis) for critical discussion on action potential acquisition, mathematical modeling and data analysis. We thank Bruce Conklin (Gladstone Institutes, San Francisco, USA) for technical advice on the WTC iPSC line, and Joseph Wu (Stanford University) and the Stanford University Cardiovascular BioBank for providing the SCVI20 iPSC line and providing technical advice regarding this line.

2.7 Figures Legends

2.7.1 Figure 1. Optimized hiPSC-CM Microphysiological Systems (MPS).

A) Representative image of two cardiac chips parallel to one another. The fluidic inlet and outlet, coupled via tubing, flank the cell loading ports. **B)** Representative brightfield image of a cardiac chip, showing cell loading chamber surrounded by media channels, with accompanying SEM images of flexible pillars for *in situ* contraction force measurements (inset top), and fenestrations insuring diffusive transport of nutrients (inset bottom). **C)** Representative confocal micrograph depicting several layers of cell thickness (side view of DRAQ5 stained nuclei). **D)** Representative confocal micrograph of a cardiac MPS indicating robust sarcomere alignment (sarcomeric α-Actinin, green) and **C)** Heatmap of

motion vectors obtained through motion tracking of 8x8 pixel macroblocks overtime. Both length (X) and width (Y) direction of motion vectors are shown, indicating that 95% of the contraction coincides with the orientation of the X axis. These motion vectors were used to analyze the prevalence of beating (center; percent of the tissue that moves with average speed above a defined threshold that was held constant for all tissues).

2.7.2 Figure 2. Design-of-Experiments (DoE) Based Screens Identify Maturation Media for hiPSC-CM Microphysiological Systems.

A) Approach used for initial screen. Computational motion capture is performed on bright-field videos of contracting cardiac MPS, giving the contraction time (defined as the distance between peaks in motion speed for contraction and relaxation, which approximates the interval over which displacement occurs). The knock-in reporter, GCaMP6f, is used to monitor the timing (rate corrected Full-Width-Half-Maximum, FWHM and amplitude of calcium transients in MPS. **B-F)** Results from representative L9 Taguchi Array experiments, depicting **B)** beating interval, **C)** spontaneous beating frequency, and **D)** tissue beating prevalence, all obtained from motion tracking analysis, along with calcium transient **E)** FWHM and **F)** amplitude, obtained from analysis of GCaMP6f fluorescence. **G)** Summary L9 analysis. 1-way ANOVA tests were performed to assess the effects of specific media components. Increases in the parameters measured were denoted as * or ** for *p*-values of 0.05 and 0.01, respectively. **H-I)** Comparison of MPS cultured in standard media (red) to MPS cultured in glucose-free media during L9 studies (black), and MPS cultured in the final Maturation Media (blue). MPS were examined for the effects of glucose depletion and fatty acid addition on **H)** beating prevalence and I) beating interval. Note, beating prevalence and calcium amplitude are ideally maximized, while beating interval, spontaneous beat rate, and calcium transient FWHM, are ideally minimized, in adult left ventricular cardiomyocytes. MPS were cultured for ten days prior to analysis for the L9 experiments. Data: **B-F**: plot of mean ± SEM, $n = 9$; **H-I**: all data points with median, n = 3-12, except for beating interval in media 8, which could only be calculated in one sample (no other samples cultured in this media exhibited either spontaneous or paced beating) ** $p < 0.01$, * $p < 0.05$ (2-way *t*-test with Holm-Bonferonni correction for multiple comparisons).

2.7.3 Figure 3. Action Potential Characterization of Matured Cardiac MPS.

A-D) Representative voltage tracings for **(A,B)** WTC MPS and (**D,E)** SCVI20 MPS, cultured for ten days in either (**A,C**) standard cardiac media, or (**B,D**) Maturation Media (MM). Voltage tracings were obtained by overnight labeling of MPS with BeRST-1. **E,F)** Quantitative analysis of 80% action potential duration (APD_{80}) for **E**) WTC or **F)** SCVI20 MPS (closed shapes) and monolayers (open shapes), cultured in standard cardiac media (SM; red) or maturation media (blue). **G-J)** Background normalized calcium amplitude of **G**) WTC and **I**) SCVI20 cell lines, and maximum Ca2+ upstroke velocity of **H)** WTC and **I**)

SCVI20 lines. All data: plot of all points with median, $n > 5$. (** $p < 0.01$, 2-way *t*-test with Holm-Bonferonni correction for multiple comparisons).

2.7.4 Figure 4. Metabolic Phenotype of MPS Treated with Maturation Media.

A-D) Representative micrographs of (**A,B**) WTC and (**C,D**) SCVI20 MPS treated for 10 days with either (**A,C**) MM or (**B,D**) SM, then stained with MitoTracker Red (red; left) or anti-mitochondrial antibodies (green; right). Nuclei are counterstained with Draq5 (blue). **E,F)** Quantification of MitoTracker Red intensity in cardiac MPS and 2D monolayers for WTC (**E**) or SCVI20 (**F**) (each data point represents one independent MPS or monolayer well; mean MPS intensity values were calculated by averaging five randomly selected fields). (* $p < 0.05$, ** $p < 0.01$, 2-way *t*-test).

2.7.5 Figure 5. Inotropic Responsive of Maturation Media Treated MPS.

A,B) Representative confocal micrographs depicting sarcomere morphology (Sarcomeric α-Actinin Staining, green, with DAPI nuclear counterstain, blue) of MPS treated for ten days with either standard media (SM) or maturation media (MM) for **A)** WTC and **B)** SCVI20. Contractile stress generated by MPS pre-treated with either SM or MM as a function of extracellular calcium (delivered in Tyrode's saline) for **C)** WTC and **D)** SCVI20. The translucent green box denotes the force generated by adult human heart slice cultures (Brandenburger *et al.* 2012). Normalized (**E**) force and (**G**) beat-rate as a function of isoproterenol dose in SM and MM pre-treated WTC MPS. Normalized (**F**) force and (**H**) beat-rate as a function of isoproterenol dose in SM and MM pre-treated SCVI20 MPS. For force calculation (inotropy), MPS were cultured in Tyrodde's saline with 0.9mM Ca^{2+}. For beat rate calculation (chronotropy), MPS were first equilibrated to standard media and then received isoproterenol doses in this media. Data: mean ± *SEM*, $n = 3$-5. Scale bars: **A**: left panels, 20μm and right panels, 10μm.

2.7.6 Figure 6. Gene Expression analysis of Monolayers and MPS Treated with Lipid-Based Maturation Media.

Quantitative RT-PCR analysis of expression of ion channel and sarcomere transcripts in hiPSC-CM 2D monolayers after ten days of culture in either Standard (SM; red) or Maturation Media (MM; blue) for **A)** WTC and **B)** SCVI20. None of the genes tested exhibited statistically significant expression changes as a result of Maturation Media. Data: plot of points with median, $n = 4$. Heat-map of relative gene expression in MM-treated MPS as compared to SM-treated MPS, as assessed by qRT-PCR on cDNA libraries amplified from RNA isolated of MPS treated for ten days with SM or MM for **C)** WTC and **D)** SCVI20. Specific analysis for **E)** WTC and **F)** SCVI20, indicating individual biological replicates (treatments of hiPSC-CM obtained from independent differentiations) of differentially expressed transcripts for ion channels or sarcomere genes in MM and SM treated MPS.

MPS PCR data were plotted on ClustVis to obtain heatmaps of the gene expression. The genes within 70% percentile of differential expression were then selected and plotted (**C,D**). Error bars: SEM, $n = 4$. * p-value < 0.05, 2-way t-test, with Mann-Whitney correction method.

2.7.7 Figure 7. Mathematical Modeling of the Contribution of Individual Currents and Calcium Handling Machinery to the Action Potential of Monolayers and MPS.

A) Schematic of the model. **B)** Examples of experimentally measured individual currents (data obtained with BeRST-1) used as model inputs. **C)** Representative simulated currents based on the corresponding color of experimentally measured current. **D-G)** Simulated current fluxes. **D-E)** Major potassium currents: D, I_{K1} and E, I_{Kr} (hERG). **F)** Sodium current, I_{Na}. **G)** *L*-type Calcium current, I_{CaL}. **H)** Sodium-calcium exchange current, I_{NaCax}. **I-L)** Simulated calcium dynamics. **I)** Calcium buffer; **J)** Ryanodine-receptor flux. **K)** Intracellular Ca^{2+} diffusion. **L)** SERCA pump activity. Media type and genotype had global effects (1-way ANOVA) in all panels except E. * $p < 0.05$, ** $p < 0.01$, $p < 10^{-3}$, post-hoc Tukey tests.

2.7.8 Figure 8. Proarrhythmia Pharmacology of Matured WTC Cardiac MPS.

IC_{50} and EC_{50} analyses were performed in MPS pretreated for ten days with either Maturation Media (blue curves) or Standard Media (Red Curves). For all studies, MPS were equilibrated to Standard Media, and then exposed to escalating doses of **A-C)** Verapamil, **D-F)** Flecainide, and **G-I)** Alfuzosin. IC_{50} curves were obtained by measuring beating prevalence (**A,D,G**) and EC_{50} curves by measuring 80% Action Potential Duration (APD_{80}; **C,F,I**). Representative, intensity normalized action potential traces are depicted for MM-pretreated MPS for each drug (**B,E,H**). Estimated Therapeutic Plasma Concentration (ETPC) values were obtained from the literature. **J-K)** Safety margins (the ratio of *in vitro* IC_{50} from prevalence measurements or EC_{50} from APD_{80} measurements to literature values for ETPC) calculated based on **J**) beating prevalence and **K**) APD_{80}. All MPS were paced at 1 Hz for pharmacology analysis. Data: mean ± *SEM*, $n = 3$-5. (* $p < 0.05$, 2-way *t*-test with Holm-Bonferroni correction for multiple comparisons).

2.7.9 Figure 9. Proarrhythmia Pharmacology of Matured SCVI20 Cardiac MPS.

IC_{50} and EC_{50} analyses were performed in MPS pretreated for ten days with either Maturation Media (blue curves) or Standard Media (Red Curves). For all studies, MPS were equilibrated to Standard Media, and then exposed to escalating doses of **A-C)** Verapamil, **D-F)** Flecainide, and **G-I)** Alfuzosin. IC_{50} curves were obtained by measuring beating prevalence (**A,D,G**) or 80% Action Potential Duration (APD_{80}; **C,F,I**). Representative, intensity normalized action potential traces are depicted for MM-pretreated MPS for each drug

(**B,E,H**). Estimated Therapeutic Plasma Concentration (ETPC) values were obtained from the literature. **J-K)** Safety margins (the ratio of *in vitro* IC_{50} or EC_{50} to literature values for ETPC) calculated based on **J**) beating prevalence and **K**) APD_{80}. All MPS were paced at 1 Hz for pharmacology analysis. Data: mean ± *SEM*, n = 3-5. (* $p < 0.05$, 2-way *t*-test with Holm-Bonferroni correction for multiple comparisons).

2.8 Tables

2.8.1 Table 1. Design of Experiments (L9) for Media Screening

Media Formulation	**Glucose Concentration (mM)**	**Oleic Acid Concentration (µM)**	**Palmitic Acid Concentration (µM)**	**Bovine Serum Albumin Concentration (mg/mL)**
1* (Standard Media, SM)	25	0	0	2.5++
2	25	62.5	100	10
3	25	125	200	25
4	10	62.5	0	25
5	10	125	100	2.5
6	10	0	200	10
7&	0	125	0	10
8&	0	0	100	25
9&	0	62.5	200	2.5
10& (Maturation Media, MM)	2.75	125	100	25
M1&	2.75	125	0	2.5
M2&	2.75	125	0	25
M3&	2.75	125	100	2.5
M4&	2.75	125	100	10

***** The composition of Media 1 is identical to standard RPMI used to feed hiPSC-CM. All media were prepared from the same batch of powdered, glucose free RPMI.

++ The B-27 supplement contains 2.5mg/mL BSA; thus, in media formulations containing only 2.5mg/mL BSA, no extra albumin was added to the system.

& Medias without glucose, and MM, were supplemented with 10mM galactose

In addition to the ingredients described above, all media were supplemented with 2% B-27 supplement and 150µg/mL *L*-ascorbic acid.

2.9 Supplemental Materials and Methods

2.9.1 Formation of Microphysiological Systems Using Defined hiPSC Derived Cardiomyocytes and Stromal Cells

In previous studies, we used cardiomyocytes derived from Wnt-mediated hiPSC cardiac specification[73], along with byproduct stromal cells, with no purification steps. Here, tissue formulation was refined by combining biochemically purified hiPSC-CM with isogenic stromal cells (hiPSC-SC). Methods were first optimized to determine the most reproducible procedure for obtaining a high yield of purified hiPSC-CM. We found that cryopreserving hiPSC-CM at day 15 of differentiation, and then treating cells with glucose depleted, lactate enriched media after thawing was the most reliable method. After lactate purification, hiPSC-CM stayed pure for more than one week (**Fig. S1**).

To obtain a defined hiPSC-SC population, we used the stromal biproducts of endothelial lineage specification of isogenic hiPSC. These hiPSC-derived stromal cells (hiPSC-SC) have a similar lineage to cardiomyocytes, sharing a common MESP1 positive mesodermal progenitor (**Fig. S2A,B**). After expansion, hiPSC-SC exhibited significant transcription of IGF and BMP-2 (**Fig. S2B**), two cytokines known to be important for cardiac development[85, 86].

Immunofluorescence analysis suggested robust expression, with little observable heterogeneity, of the stromal markers α-Smooth Muscle Actin (αSMA), SM22, CD90 and Vimentin. Importantly, hiPSC-SC also express N-Cadherin and the gap junction marker Connexin 43 (Cx43/GJA1; **Fig. S2C**), suggesting these cells would be capable of coupling effectively to cardiomyocytes in micro-tissues. Finally, hiPSC-SC produced ECM transcripts including collagen (I & IV), laminin and fibronectin, although the level of ECM deposition appeared to be substantially higher for collagen IV as compared to collagen I (**Fig. S2C**). These tissue-specific ECM proteins are reminiscent of the composition of ECM in the developing heart[87].

Using these purified, defined cell populations, we fabricated MPS that mimicked the mass composition of the human heart by combining 80% hiPSC-CM and 20% hiPSC-SC. These tissues exhibited a high level of cellular alignment and sarcomere organization (**Fig. S2D**).

2.9.2 Analysis of Force Developed by Cardiac Microphysiological Systems

To facilitate direct measurement of cardiomyocyte contractile forces, micro-molded polydimethylsiloxane (PDMS) pillars were added to the cell chambers, so that the tissue would deflect them upon each contraction (**Fig. S6A**).

The presence and size of pillars was verified by Scanning Electron Microscopy (SEM). Prior to SEM imaging, the PDMS MPS devices were coated with a thin layer of gold-palladium (AuPd) to make the surface conductive. A Cressington 108 SEM Sputter Coater

was used for it. A 0.06 mbar Argon atmosphere was created and the samples were sputtered for 60s at 10mA (1kV) at a distance of 4cm from the target, resulting in 100Å AuPd. Samples were then mounted on a SEM holder using copper tape and adhesive carbon disks. SEM images were taken on a FEI Quanta 3D FEG Dual beam (SEM/FIB) system in standard high vaccum mode with 20kV/120pA electron beam. The imaging parameters for our PDMS MPS were the following: 350x magnification, 45 degrees tilt, working distance 9.5mm.

When micro-tissues were formed within micro-pillar modified MPS, the twitch force of cellular contraction deflected the pillars. By considering each pillar as a cantilever beam fixed at one end and uniformly loaded with horizontal forces along its height, one can apply the Euler-Bernouilli formula for uniformly distributed load and deduce the contraction force from the pillar's elastic modulus, deflection and dimensions (**Fig. S6B**). Pillar deflection was calculated in ImageJ by measuring the distance between the pillar's centroid coordinates at zero and at maximal contraction.

For automated pillar tracking, Python-based algorithms were developed. Pillar deflection is automatically calculated in a two-step process: first, initial pillar position is detected (**Fig. S6C**). The algorithm takes as input the raw bright-field image. By combining the information of the circle Hough transform algorithm to find circular shapes in the input and a template matching algorithm using a scaled and rotated binary template of the chip design and the circle, it is possible to generate a correlation map predicting the initial position of the pillars. Second, pillar deflection is computed automatically (**Fig. S6D**). The tracking software makes it possible to follow the displacement of the pillar in time by taking the mean motion of a population of 200 tracking points placed all over the pillar before contraction and during Supra-max of the contraction with tracking points distributed on the pillar.

2.9.3 Oxygen Consumption Rate analysis

Approximately 30,000 cardiac cells were seeded in each well of an Agilent Seahorse 8-well XF miniplate that was coated overnight with Matrigel (Stem Cells Technologies). Cardiac cells were allowed to incubate with Standard Media or Maturation Media during 7 days in a cell culture incubator at 37°C and 5% CO2. The day of experiment, samples were washed with assay buffer (XF RPMI Medium pH 7.4, 10 mM pyruvate, 10 mM glucose, and 2 mM glutamax) and incubated one hour in a non-CO2 incubator. At this point, mitochondrial respiration via oxygen consumption rate (OCR) was measured in the XF HS Mini Analyzer following the established protocol. Injections of 0.5 µM ATPase inhibitor oligomycin, 1 µM protonophore FCCP, and 0.5 µM ETC Complex I and complex III inhibitor Rotenone/Antimycin-A were made to measure the mitochondrial response (Seahorse XFp Cell Mito Stress Test Kit, Agilent Cat:103010).

2.9.4 Staining of Nascent T-Tubules in Cardiac MPS

MPS were rinsed three times for five minutes with PBS, and then fixed with 4% paraformaldehyde (PFA) for 15 minutes. After 3 more five-minute PBS washes, MPS were carefully cut open with a scalpel and transferred to multiwell plates. After one additional PBS wash, MPS were stained with 20μg/mL Alexa Fluor 488 conjugated Wheat Germ Agglutinin (WGA-488; Thermo Scientific) for 30 minutes. After 3 additional washes in PBS, MPS were mounted on glass slides with ProLong Gold Antifade reagent (Thermo Scientific). Imaging was performed on an Olympus FluoView 1000 confocal microscope (Olympus, Center Valley, PA). The sample was laser-illuminated at 488 nm and fluorescent emission (525 +/- 25 nm) was collected via 60x/1.42 NA oil immersion objective (0.414 um/pixel, 100 nm confocal pinhole). Images were collected in 2D mode at lower laser powers (0.5-3%) and long pixel dwell times (40-100 us) to optimize contrast in these fixed samples.

2.10 Supplemental Figure Legend

2.10.1 Supplemental Figure 1. Characterization of the Purity of iPSC-CM Obtained by Lactate Treatment of Cryopreserved iPSC-Cardiomyocyte Differentiation.

A) Representative plots indicating how gating was performing to identify cells from FSC and SSC plots (left), and contour plots of negative control (center) and lactate-purified cardiomyocytes (right). Because **B)** Representative histogram plots of the relative number of Cardiac Troponin (TNNT2) positive cells present immediately after lactate treatment (left), six days (center) and 180 days (right). Only after extremely long time-periods is there a noticeable reduction in cell purity. All MPS were formed with iPSC-CM within six days of lactate treatment. **C)** Time course of purity of three different batches of iPSC-CM thawed immediately after differentiation and subsequently purified with lactate treatment. **D)** Representative immunofluorescence micrograph of an iPSC-CM after lactate purification. Image on right is magnified to display sarcomeres stained with antibodies against Sarcomeric α-Actinin (green). Error bars: *SD*, $n = 3$.

2.10.2 Supplemental Figure 2. Development and Characterization of iPSC-Stromal Cells.

A) Differentiation tree depicting the lineage of iPSC-cardiomyocytes (hiPS-CM) and the isogenic hiPSC-derived stromal cell population (hiPSC-SC). Specific biomarkers (blue) were verified by qRT-PCR. **B)** Brewer plot identifying gene expression patterns over the course of differentiation of hiPSC into hiPSC-SC, with hiPSC-CM included on the plot for comparison. **C)** Immunofluorescence molecular characterization of hiPSC-SC. These hiPSC-SC were markedly positive for all stromal markers shown, while markers of smooth muscle (Calponin) and endothelial cells (CD31) were not detected. iPS-SC also produce

key ECM proteins: Laminin, Fibronectin and Collagen IV, while substantial Collagen I was not detected. **D)** Representative fluorescence micrograph of cardiac MPS, which shows highly organized, aligned cardiomyocytes stained for sarcomeric α-Actinin (ACTN2, green). Cells were counterstained for nuclei with DAPI (blue) in all fluorescence micrographs. Scale bars: **C**) 500μm **D**) left panel, 20μm and right panel, 10μm.

2.10.3 Supplemental Figure 3. Additional information about the media screen and representative 2D traces of MM-treated monolayers.

A-B) Quantification of action potential time from 20% above baseline to peak ($Upstroke_{80}$) in **A)** WTC MPS and 2D monolayers and **B)** SCVI20 MPS. **C,D** Quantification of C) beat-rate corrected $cAPD_{80}$ and D) background corrected calcium amplitude (F/F_0) in MPS formed from SCVI273 iPSC-CM and stromal cells. **E,F)** Representative voltage tracings for 2D monolayers of **E)** WTC and **F)** SCVI20 cell lines cultured for one week in Maturation Media (MM). Voltage tracings were obtained by overnight labeling of monolayers with BeRST-1. **G-H)** Analysis of changes in **G)** APD80 and **H)** contractile prevalence in MM-pretreated MPS that resulted from modulating the levels of palmitate and albumin in MM. Removing both palmitate and albumin from MM (M1) resulted in MPS with APD80 that were significantly higher than APD80 of MM-treated MPS, and which were no different from APD80 of SM-treated MPS. Removal of Palmitate alone (M2), or of albumin alone (M3) led to a new medium that exhibited APD80 significantly less than MM ($p < 0.05$). Compared to MM, M2 treated MPS exhibited slightly reduced beating prevalence, whereas this metric was enhanced for M3 treated MPS, although these changes were not statistically significant. Slight reduction of the albumin content of MM from 2.5% to 1% (M4) did not have significant effects on APD80 or prevalence of motion in MPS, compared to those treated with MM. All data: plot of all points with median, $n > 5$. (** $p < 0.01$, 2-way t-test with Holm-Bonferonni correction for multiple comparisons).

2.10.4 Supplemental Figure 4. Metabolic analysis of MM and SM-treated 2D iPSC-CM Monolayers.

A) Representative Oxygen Consumption Rate (OCR) tracings of SCVI20 iPSC-CM monolayers after culture in MM (blue) or SM (red) for 10 days. **B,C)** Quantification of reserve OCR (change in OCR from baseline with FCCP treatment) and total ATP capacity indicate a shift toward ß-oxidation with MM in 2D monolayers. **D-G)** Representative images of 2D **D,E)** WTC and **F,G)** SCVI20 iPSC-CM monolayers stained with MitoTrackerRed (left; red) and anti-mitochondrial antibodies (right; green).

2.10.5 Supplemental Figure 5. Expression and localization of sarcomere proteins in MM-treated MPS.

A-B) Fourier domain-based quantification of sarcomeric order in MPS treated with SM versus MM for (**A**) WTC or **(B)** SCVI20 cell line treated with MM (blue) or SM (red) for 10 days. **C,D)** Quantification of protein expression (antibody staining with analysis by a condition-blinded user) for **C)** MYH7 and **D)** MLC-2v in MPS treated for ten days with MM (blue) or SM (red). **E-G)** Representative micrographs of **E)** WTC and **F,G)** SCVI20 MPS after staining for **E,F)** MYH7 and **G)** MLC-2v. Antibody staining in green, with blue Draq5 nuclear counterstain. Scale bars: 20μm.

2.10.6 Supplemental Figure 6. Characterizing Force Developed by Contracting Cardiac Microphysiological Systems.

A) Illustration of the micro-molded PDMS pillars in the heart-on-chip platform. Left to right shows (i) one empty chamber imaged via brightfield microscopy, (ii) SEM image of the magnified pillar array. **B)** Pillar deformation can be described by the formula for uniformly distributed load on a cantilever beam, where δmax [m], the maximal deflection is proportional to the line pressure load q [N/m], the length of the beam L[m] and inversely proportional to the Young's modulus E [N/m^2] (2.63 [Mpa] for 1:10 PDMS network) and the second moment of area I [m^4], for a cylinder of radius R [m]. From this formula, it is possible to isolate final contraction force F [N]. **C-D)** Automated pillar tracking and deflection analysis to measure tissue contractile force. **C) Initial Pillar Position detection**. Left to right (i) The algorithm takes as input the raw bright-field image on which (ii) Hough circle transform (HCT) algorithm is run. This algorithm is able to detect circles in raw images by applying an edge detection filter. Each edge point becomes a center for a new circle. The intersection of all these new circles will give the central position of the initial circular shape in the raw image. (iii) A template matching algorithm is then applied to the raw image with HCT detected circles. The template given is a binary pillar pattern template that will be rotated, zoomed and scaled to find the highest matching probability with HCT circles. The latter will generate a correlation map (iv) predicting the most likely initial position of the pillars (v). **D) Automated pillar tracking**: The tracking software assess pillar displacement by measuring mean motion of a population of 200 tracking points placed all over the pillar before contraction (left) and during maximum of the contraction with tracking points distributed on the pillar (right). Scale bars: A) middle panel, 50μm and right panel, 50μm.

2.10.7 Supplemental Figure 7. Analysis of Glyceraldehyde 3-phosphate dehydrogenase (GAPDH) Expression in MM treated MPS.

A) Quantification of GAPDH protein expression (immunostaining) as (left) raw fluorescence intensity, and (right) pixel-wise ratio of intensity of GAPDH / ACTN2. **B-E)**

Representative micrographs of MPS stained for GAPDH (green) with Draq5 nuclear counterstain (blue) for **B,C)** WTC and **D,E)** SCVI20 MPS. Scale bars: 20μm.

2.10.8 Supplemental Figure 8. Effects of ryanodine on MM and SM pre-treated MPS.

A-D) WTC MPS pre-treated with MM and SM were treated with 10μM ryanodine, and **A)** Normalized beat rate, **B)** Normalized F/F_0, **C)** Normalized beat-rate corrected decay time (τ_{75}) and **D)** upstroke duration were quantified for spontaneous calcium transients (GCaMP6f).

2.10.9 Supplemental Figure 9. Effects of thapsigargin on MM and SM pre-treated MPS.

A-D) WTC MPS pre-treated with MM and SM were treated with 10μM thapsigargin, and **A)** Normalized beat rate, **B)** Normalized F/F_0, **C)** Normalized beat-rate corrected decay time (τ_{75}) and **D)** upstroke duration were quantified for spontaneous calcium transients (GCaMP6f).

2.10.10 Supplemental Figure 10. Qualitative analysis of nascent T-tubules in MM and SM pre-treated MPS.

Cardiac MPS were stained *in situ* with 20μg/mL Alexa Fluor 488 labeld Wheat Germ Agglutinin (WGA-488) with Draq5 nuclear counterstain (blue) to probe for potential T-tubules. **A-C)** Representative staining of MM treated SCVI20 MPS showed some internal membrane invaginations (between the border of the cells and the nucleus, red arrows). **D,E)** Representative staining of SM treated SCVI20 MPS showed less prominent staining of internal membrane invaginations. Scale bar: 5μm.

2.10.11 Supplemental Figure 11. Calcium Flux Amplitude and Kinetics Changes in Flecainide Treated SCVI20 Microphysiological Systems.

A-C) Analysis of calcium transient amplitude and kinetics in SCVI20 MPS pre-treated with either standard media (SM) or maturation media (MM) and then exposed to either 100nM or 1μM flecainide. Calcium transients were analyzed for **A)** upstroke time**, B)** τ_{75}, the time required for calcium amplitude to decay from the maximum value to 30% of the maximum value, and **C)** maximum amplitude of the calcium transient. Values are normalized to the timing (upstroke time and τ_{75}) and amplitude of the calcium transient for the same MPS treated with vehicle. **D-E)** show representative traces of SM-treated **(D)** or MM-treated **(E)** tissues exposed to 100nM flecainide. SM shows clear instances of delayed-after depolarizations (DADs), whereas MM did not show any.

2.11 Supplemental Tables

2.11.1 Table S1. Antibodies

Antibody Target	Species Raised in	Vendor	Cat. No.
Sarcomeric α-actinin	Mouse (clone EA-53)	Sigma Aldrich	A7811
Laminin	Rabbit (polyclonal)	Abcam	ab14055
Cardiac troponin T	Mouse (Clone 13-11)	Thermo Scientific	MS295P
Connexin 43	Rabbit	Sigma Aldrich	C6219
SM22	Rabbit	Abcam	Ab14106
Vimentin	Mouse	Zymed	08-0052
α-Smooth Muscle Actin (αSMA)	Rabbit	Abcam	Ab5694
CD90	Mouse (Clone 5E10)	eBioscience	14-090-80
N-Cadherin	Rabbit (polyclonal)	Abcam	ab23751
Fibronectin (FN)	Rabbit (polyclonal)	Abcam	ab23751
Collagen IV (Col IV)	Mouse (Clone 23IIC3)	Millipore	MAB1910
Collagen I (Col I)	Rabbit (polyclonal)	Abcam	ab21286
Calponin	Rabbit (polyclonal)	Abcam	ab46794
CD31	Mouse (Clone M89D3)	BD Biosciences	558068
Myosin Heavy Chain (MYH7)	Mouse (Clone M14)	Abcam	ab97715
Myosin Light Chain, Ventricular Isoform (MYL2)	Rabbit (polyclonal)	ProteinTech	10906-1-AP

2.11.2 Table S2. Primer Pairs used for SYBR Green Based Gene Expression

Gene	Forward Primer	Reverse Primer
VIM	GACGCCATCAACACCGAGTT	CTTTGTCGTTGGTTAGCTGGT
BMP2	TAATTCGGTGATGGAAACTG	CCCAGAAGGAAGTACATTTG
IGF1	CCCAGAAGGAAGTACATTTG	GTTTAACAGGTAACTCGTGC
COLA1	GCTATGATGAGAAATCAACCG	TCATCTCCATTCTTTCCAGG
COL4A1	AAAGGGAGATCAAGGGATAG	TCACCTTTTTCTCCAGGTAG
GATA2	CTACTAAAGCTGCACAATG	CTTTCTTGCTCTTCTTGGAC

All other SYBR green primer pairs were provided as part of a custom gene array (Super Array Biosciences)

2.11.3 Table S3. Taqman Probes used for Gene Expression

Gene	Taqman Probe ID (Thermo Scientific)
SCN5A	Hs00165693_m1
KCNJ2	Hs00265315_m1
KCNJ3	Hs00158421_m1
CACNA1C	Hs00167681_m1
HCN2	Hs00606903_m1
HCN4	Hs00175760_m1
KCNIP2	Hs01552688_g1
KCND3	Hs00986860_m1
KCNQ1	Hs00923522_m1
KCNA5	Hs00969279_s1
TNNT2	Hs00943911_m1
MYH7	Hs01110632_m1
RYR2	Hs00181461_m1
MYH6	Hs01101425_m1
SLN	Hs00161903_m1
CACNB2	Hs01100744_m1
LDHA	Hs01378790_g1
ADHFE1	Hs00329084_m1
ENO1	Hs00361415_m1
HEY2	Hs01012057_m1
PECAM1	Hs01065279_m1
SERCA (ATP2A2)	Hs00544877_m1
CACNB1	Hs00609503_g1
NPPB	Hs00173590_m1
NR2F2	Hs00819630_m1
KCNH2	Hs04234270_g1
COX41	Hs00971639_m1
MYL7	Hs01085598_g1
MYL2	Hs00166405_m1
KCND2	Hs01054873_m1
ALDH1A1	Hs00946916_m1
GAPDH	Hs02758991_g1

2.12 References

1. Scannell, J.W., et al., *Diagnosing the decline in pharmaceutical R&D efficiency.* Nature Reviews Drug Discovery, 2012. **11**(3): p. 191-200.
2. Laflamme, M.A. and C.E. Murry, *Heart regeneration.* Nature, 2011. **473**(7347): p. 326-35.
3. Ogle, B.M., et al., *Distilling complexity to advance cardiac tissue engineering.* Science Translational Medicine, 2016. **8**(342).
4. Vunjak Novakovic, G., T. Eschenhagen, and C. Mummery, *Myocardial tissue engineering: in vitro models.* Cold Spring Harb Perspect Med, 2014. **4**(3).
5. Robertson, C., D.D. Tran, and S.C. George, *Concise review: maturation phases of human pluripotent stem cell-derived cardiomyocytes.* Stem Cells, 2013. **31**(5): p. 829-37.
6. Iseoka, H., et al., *Pivotal Role of Non-cardiomyocytes in Electromechanical and Therapeutic Potential of Induced Pluripotent Stem Cell-Derived Engineered Cardiac Tissue.* Tissue Eng Part A, 2018. **24**(3-4): p. 287-300.
7. Paci, M., et al., *Human induced pluripotent stem cell-derived versus adult cardiomyocytes: An in silico electrophysiological study on effects of ionic current block.* British Journal of Pharmacology, 2015. **172**(21): p. 5147-5160.
8. Lemoine, M.D., et al., *Human iPSC-derived cardiomyocytes cultured in 3D engineered heart tissue show physiological upstroke velocity and sodium current density.* Scientific Reports, 2017. **7**(1): p. 1-11.
9. Ma, J., et al., *High purity human-induced pluripotent stem cell-derived cardiomyocytes: electrophysiological properties of action potentials and ionic currents.* AJP: Heart and Circulatory Physiology, 2011. **301**(5): p. H2006-H2017.
10. Spencer, C.I., et al., *Calcium transients closely reflect prolonged action potentials in iPSC models of inherited cardiac arrhythmia.* Stem Cell Reports, 2014. **3**(2): p. 269-281.
11. Liang, P., et al., *Drug screening using a library of human induced pluripotent stem cell-derived cardiomyocytes reveals disease-specific patterns of cardiotoxicity.* Circulation, 2013. **127**(16): p. 1677-1691.
12. Shadrin, I.Y., et al., *Cardiopatch platform enables maturation and scale-up of human pluripotent stem cell-derived engineered heart tissues.* Nature Communications, 2017. **8**(1).
13. Huebsch, N., et al., *Miniaturized iPS-Cell-Derived Cardiac Muscles for Physiologically Relevant Drug Response Analyses.* Scientific Reports, 2016. **6**(November 2015): p. 1-12.
14. Mannhardt, I., et al., *Human Engineered Heart Tissue: Analysis of Contractile Force.* Stem Cell Reports, 2016. **7**(1): p. 29-42.
15. Godier-Furnémont, A.F.G., et al., *Physiologic force-frequency response in engineered heart muscle by electromechanical stimulation.* Biomaterials, 2015. **60**: p. 82-91.
16. Hinson, J.T., et al., *Titin mutations in iPS cells define sarcomere insufficiency as a cause of dilated cardiomyopathy.* Science, 2015. **349**(6251): p. 982-986.

17. Zhang, D., et al., *Tissue-engineered cardiac patch for advanced functional maturation of human ESC-derived cardiomyocytes.* Biomaterials, 2013. **34**(23): p. 5813-5820.
18. Nunes, S.S., et al., *Biowire: A platform for maturation of human pluripotent stem cell-derived cardiomyocytes.* Nature Methods, 2013. **10**(8): p. 781-787.
19. Tulloch, N.L., et al., *Growth of engineered human myocardium with mechanical loading and vascular coculture.* Circulation Research, 2011. **109**(1): p. 47-59.
20. Tiburcy, M., et al., *Terminal differentiation, advanced organotypic maturation, and modeling of hypertrophic growth in engineered heart tissue.* Circulation Research, 2011. **109**(10): p. 1105-1114.
21. Zimmermann, W.H., et al., *Tissue Engineering of a Differentiated Cardiac Muscle Construct.* Circulation Research, 2002. **90**(2): p. 223-230.
22. Mathur, A., et al., *Human iPSC-based cardiac microphysiological system for drug screening applications.* Scientific Reports, 2015. **5**.
23. Ronaldson-Bouchard, K., et al., *Advanced maturation of human cardiac tissue grown from pluripotent stem cells.* Nature, 2018. **556**(7700): p. 239-243.
24. Ruan, J.-L., et al., *Mechanical Stress Promotes Maturation of Human Myocardium From Pluripotent Stem Cell-Derived Progenitors.* STEM CELLS, 2015. **33**(7): p. 2148-2157.
25. Kadota, S., et al., *In Vivo Maturation of Human Induced Pluripotent Stem Cell-Derived Cardiomyocytes in Neonatal and Adult Rat Hearts.* Stem Cell Reports, 2017. **8**(2): p. 278-289.
26. Rupert, C.E. and K.L.K. Coulombe, *IGF1 and NRG1 Enhance Proliferation, Metabolic Maturity, and the Force-Frequency Response in hESC-Derived Engineered Cardiac Tissues.* Stem Cells International, 2017. **2017**.
27. Tiburcy, M., et al., *Defined Engineered Human Myocardium With Advanced Maturation for Applications in Heart Failure Modeling and RepairClinical Perspective.* Circulation, 2017. **135**(19): p. 1832-1847.
28. Kuppusamy, K.T., et al., *Let-7 family of microRNA is required for maturation and adult-like metabolism in stem cell-derived cardiomyocytes.* Proceedings of the National Academy of Sciences, 2015. **112**(21): p. E2785-E2794.
29. Fong, A.H., et al., *Three-Dimensional Adult Cardiac Extracellular Matrix Promotes Maturation of Human Induced Pluripotent Stem Cell-Derived Cardiomyocytes.* Tissue Engineering Part A, 2016. **22**(15-16): p. 1016-1025.
30. Yang, X., et al., *Tri-iodo-l-thyronine promotes the maturation of human cardiomyocytes-derived from induced pluripotent stem cells.* Journal of Molecular and Cellular Cardiology, 2014. **72**: p. 296-304.
31. Lopaschuk, G.D. and J.S. Jaswal, *Energy Metabolic Phenotype of the Cardiomyocyte During Development, Differentiation, and Postnatal Maturation.* Journal of Cardiovascular Pharmacology, 2010. **56**(2): p. 130-140.
32. Makinde, A.-O., P.F. Kantor, and G.D. Lopaschuk, *Maturation of fatty acid and carbohydrate metabolism in the newborn heart*, in *Molecular and Cellular Effects of Nutrition on Disease Processes*, G.N. Pierce, et al., Editors. 1998, Springer US: Boston, MA. p. 49-56.

33. Correia, C., et al., *Distinct carbon sources affect structural and functional maturation of cardiomyocytes derived from human pluripotent stem cells.* Sci Rep, 2017. **7**(1): p. 8590.
34. Mills, R.J., et al., *Functional screening in human cardiac organoids reveals a metabolic mechanism for cardiomyocyte cell cycle arrest.* Proc Natl Acad Sci U S A, 2017: p. E8373-E8381.
35. Rana, P., et al., *Characterization of human-induced pluripotent stem cell-derived cardiomyocytes: bioenergetics and utilization in safety screening.* Toxicol Sci, 2012. **130**(1): p. 117-31.
36. Feyen, D.A.M., et al., *Metabolic Maturation Media Improve Physiological Function of Human iPSC-Derived Cardiomyocytes.* Cell Rep, 2020. **32**(3): p. 107925.
37. Huebsch, N., et al., *Automated Video-Based Analysis of Contractility and Calcium Flux in Human-Induced Pluripotent Stem Cell-Derived Cardiomyocytes Cultured over Different Spatial Scales.* Tissue Engineering Part C: Methods, 2015. **21**(5): p. 467-479.
38. Sun, N., et al., *Patient-specific induced pluripotent stem cells as a model for familial dilated cardiomyopathy.* Science Translational Medicine, 2012. **4**(130): p. 130ra47-130ra47.
39. Jha, A.K., W.M. Jackson, and K.E. Healy, *Controlling osteogenic stem cell differentiation via soft bioinspired hydrogels.* PloS one, 2014. **9**(6): p. e98640-e98640.
40. Stile, R.A., et al., *Sequential robust design methodology and X-ray photoelectron spectroscopy to analyze the grafting of hyaluronic acid to glass substrates.* Journal of Biomedical Materials Research, 2002. **61**(3): p. 391-398.
41. Taguchi, G. and M.S. Phadke, *Quality Engineering through Design Optimization*, in *Quality Control, Robust Design, and the Taguchi Method*, K. Dehnad, Editor. 1989, Springer US: Boston, MA. p. 77-96.
42. Naito, H., et al., *Optimizing engineered heart tissue for therapeutic applications as surrogate heart muscle.* Circulation, 2006. **114**(SUPPL. 1): p. 72-78.
43. Wang, G., et al., *Modeling the mitochondrial cardiomyopathy of Barth syndrome with induced pluripotent stem cell and heart-on-chip technologies.* Nature Medicine, 2014. **20**(6): p. 616-623.
44. Naim, J.O., et al., *The Effect of Molecular Weight and Gel Preparation on Humoral Adjuvancy of Silicone Oils and Silicone Gels.* Immunological Investigations, 1995. **24**(3): p. 537-547.
45. Park, E.-J., et al., *Multiple pathways are involved in palmitic acid-induced toxicity.* Food and Chemical Toxicology, 2014. **67**: p. 26-34.
46. Bodi, I., et al., *The L-type calcium channel in the heart: the beat goes on.* The Journal of Clinical Investigation, 2005. **115**(12): p. 3306-3317.
47. Liu, R., et al., *Palmitoylation regulates intracellular trafficking of β2 adrenergic receptor/arrestin/phosphodiesterase 4D complexes in cardiomyocytes.* PloS one, 2012. **7**(8): p. e42658-e42658.
48. Medda, L., M. Monduzzi, and A. Salis, *The molecular motion of bovine serum albumin under physiological conditions is ion specific.* Chem Commun (Camb), 2015. **51**(30): p. 6663-6.

49. Brandenburger, M., et al., *Organotypic slice culture from human adult ventricular myocardium.* Cardiovascular Research, 2012. **93**(1): p. 50-59.
50. Chen, T.-W., et al., *Ultrasensitive fluorescent proteins for imaging neuronal activity.* Nature, 2013. **499**: p. 295-295.
51. Paredes, R.M., et al., *Chemical calcium indicators.* Methods, 2008. **46**(3): p. 143-51.
52. Mot, A.I., et al., *Circumventing the Crabtree Effect: A method to induce lactate consumption and increase oxidative phosphorylation in cell culture.* Int J Biochem Cell Biol, 2016. **79**: p. 128-138.
53. Anmann, T., et al., *Formation of highly organized intracellular structure and energy metabolism in cardiac muscle cells during postnatal development of rat heart.* Biochim Biophys Acta, 2014. **1837**(8): p. 1350-61.
54. Ma, Z., et al., *Contractile deficits in engineered cardiac microtissues as a result of MYBPC3 deficiency and mechanical overload.* Nature Biomedical Engineering, 2018.
55. Lee, J.H., et al., *Human Pluripotent Stem Cell-Derived Atrial and Ventricular Cardiomyocytes Develop from Distinct Mesoderm Populations.* Cell Stem Cell, 2017. **21**(2): p. 179-194.e4.
56. Zhang, J.Z., et al., *A Human iPSC Double-Reporter System Enables Purification of Cardiac Lineage Subpopulations with Distinct Function and Drug Response Profiles.* Cell Stem Cell, 2019. **24**(5): p. 802-811 e5.
57. Campbell, K.L. and A.A. Dicke, *Sarcolipin Makes Heat, but Is It Adaptive Thermogenesis?* Frontiers in Physiology, 2018. **9**(714).
58. Smith, W.S., et al., *Sarcolipin uncouples hydrolysis of ATP from accumulation of Ca2+ by the Ca2+-ATPase of skeletal-muscle sarcoplasmic reticulum.* Biochemical Journal, 2002. **361**(2): p. 277-286.
59. Mall, S., et al., *The presence of sarcolipin results in increased heat production by Ca(2+)-ATPase.* J Biol Chem, 2006. **281**(48): p. 36597-602.
60. Gorski, P.A., D.K. Ceholski, and H.S. Young, *Structure-Function Relationship of the SERCA Pump and Its Regulation by Phospholamban and Sarcolipin*, in *Membrane Dynamics and Calcium Signaling*, J. Krebs, Editor. 2017, Springer International Publishing: Cham. p. 77-119.
61. Josowitz, R., et al., *Identification and purification of human induced pluripotent stem cell-derived atrial-like cardiomyocytes based on sarcolipin expression.* PLoS One, 2014. **9**(7): p. e101316.
62. Schwach, V., et al., *A COUP-TFII Human Embryonic Stem Cell Reporter Line to Identify and Select Atrial Cardiomyocytes.* Stem Cell Reports, 2017. **9**(6): p. 1765-1779.
63. Venetucci, L., et al., *Inherited calcium channelopathies in the pathophysiology of arrhythmias.* Nature Reviews Cardiology, 2012. **9**(10): p. 561-575.
64. Tveito, A., et al., *Inversion and computational maturation of drug response using human stem cell derived cardiomyocytes in microphysiological systems.* Scientific Reports, 2018. **8**(1).
65. Bers, D.M., *Excitation-contraction coupling and cardiac contractile force*. 2001, Dordrecht; Boston: Kluwer Academic Publishers.

66. Parikh, S.S., et al., *Thyroid and Glucocorticoid Hormones Promote Functional T-Tubule Development in Human-Induced Pluripotent Stem Cell-Derived Cardiomyocytes.* Circ Res, 2017. **121**(12): p. 1323-1330.
67. Redfern, W.S., et al., *Relationships between preclinical cardiac electrophysiology, clinical QT interval prolongation and torsade de pointes for a broad range of drugs: Evidence for a provisional safety margin in drug development.* Cardiovascular Research, 2003. **58**(1): p. 32-45.
68. Navarrete, E.G., et al., *Screening drug-induced arrhythmia events using human induced pluripotent stem cell-derived cardiomyocytes and low-impedance microelectrode arrays.* Circulation, 2013. **128**(SUPPL.1).
69. Aliot, E., et al., *Twenty-five years in the making: flecainide is safe and effective for the management of atrial fibrillation.* EP Europace, 2010. **13**(2): p. 161-173.
70. Melgari, D., et al., *Molecular basis of hERG potassium channel blockade by the class Ic antiarrhythmic flecainide.* Journal of Molecular and Cellular Cardiology, 2015. **86**: p. 42-53.
71. Lacerda, A.E., et al., *Alfuzosin Delays Cardiac Repolarization by a Novel Mechanism.* Journal of Pharmacology and Experimental Therapeutics, 2007. **324**(2): p. 427-433.
72. Kanzaki, Y., et al., *Three-Dimensional Architecture of Cardiomyocytes and Connective Tissue in Human Heart Revealed by Scanning Electron Microscopy.* Circulation, 2010. **122**(19): p. 1973-1974.
73. Lian, X., et al., *Robust cardiomyocyte differentiation from human pluripotent stem cells via temporal modulation of canonical Wnt signaling.* Proceedings of the National Academy of Sciences, 2012. **109**(27): p. E1848-E1857.
74. Tohyama, S., et al., *Distinct Metabolic Flow Enables Large-Scale Purification of Mouse and Human Pluripotent Stem Cell-Derived Cardiomyocytes.* Cell Stem Cell, 2013. **12**(1): p. 127-137.
75. Lian, X., et al., *Efficient differentiation of human pluripotent stem cells to endothelial progenitors via small-molecule activation of WNT signaling.* Stem Cell Reports, 2014. **3**(5): p. 804-816.
76. Komeya, M., et al., *Pumpless microfluidic system driven by hydrostatic pressure induces and maintains mouse spermatogenesis in vitro.* Sci Rep, 2017. **7**(1): p. 15459.
77. Linkert, M., et al., *Metadata matters: access to image data in the real world.* Journal of Cell Biology, 2010. **189**(5): p. 777-782.
78. Laughner, J.I., et al., *Processing and analysis of cardiac optical mapping data obtained with potentiometric dyes.* AJP: Heart and Circulatory Physiology, 2012. **303**(7): p. H753-H765.
79. Fridericia, L.S., *The Duration of Systole in an Electrocardiogram in Normal Humans and in Patients with Heart Disease*.* Annals of Noninvasive Electrocardiology, 2003. **8**(4): p. 343-351.
80. Huang, Y.L., A.S. Walker, and E.W. Miller, *A Photostable Silicon Rhodamine Platform for Optical Voltage Sensing.* Journal of the American Chemical Society, 2015. **137**(33): p. 10767-10776.
81. Hough, P.V.C., *Method and means for recognizing complex patterns* US patents, Ser. No. 17,715 6 Claims. (Cl. S40-146.3), 1960.

82. Brunelli, R., *Template Matching Techniques in Computer Vision: Theory and Practice*. 2009: Wiley.
83. Jaeger, K.H., S. Wall, and A. Tveito, *Detecting undetectables: Can conductances of action potential models be changed without appreciable change in the transmembrane potential?* Chaos, 2019. **29**(7): p. 073102.
84. Jaeger, K.H., et al., *Improved Computational Identification of Drug Response Using Optical Measurements of Human Stem Cell Derived Cardiomyocytes in Microphysiological Systems.* Front Pharmacol, 2019. **10**: p. 1648.
85. Zhang, H. and A. Bradley, *Mice deficient for BMP2 are nonviable and have defects in amnion/chorion and cardiac development.* Development, 1996. **122**: p. 2977-2986.
86. McDevitt, T.C., M.A. Laflamme, and C.E. Murry, *Proliferation of cardiomyocytes derived from human embryonic stem cells is mediated via the IGF/PI 3-kinase/Akt signaling pathway.* J Mol Cell Cardiol, 2005. **39**(6): p. 865-73.
87. Hanson, K.P., et al., *Spatial and Temporal Analysis of Extracellular Matrix Proteins in the Developing Murine Heart: A Blueprint for Regeneration.* Tissue Engineering Part A, 2012. **19**(9-10): p. 1132-1143.

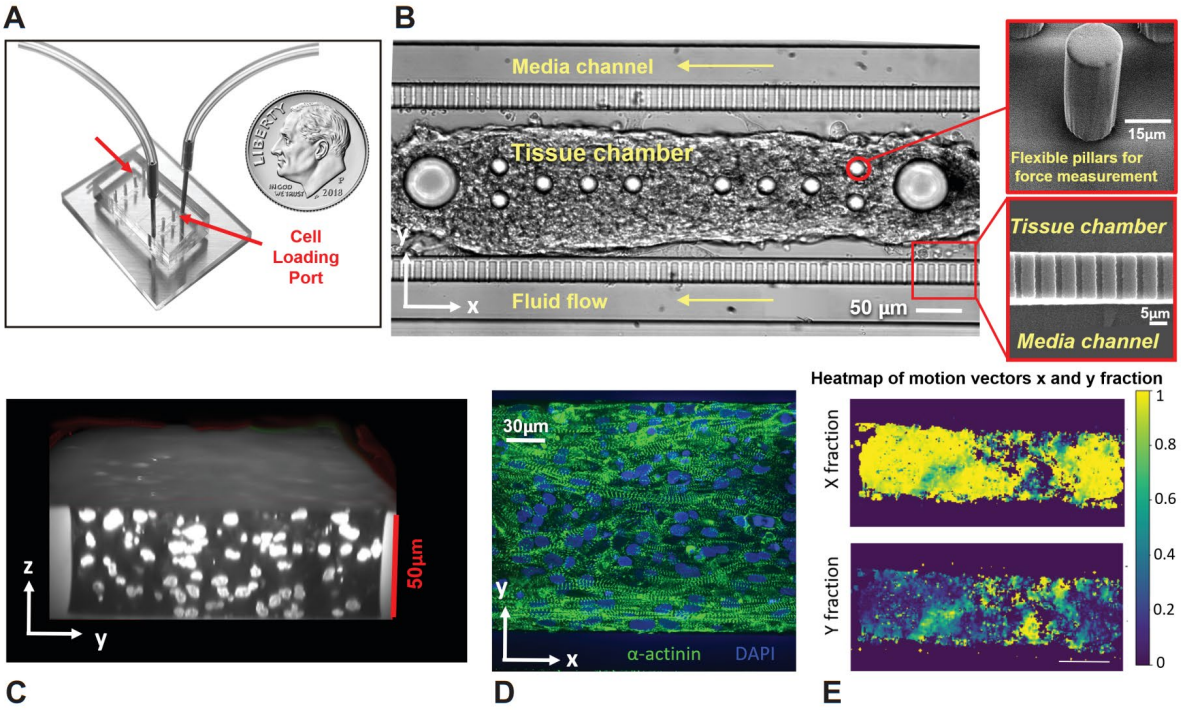
A
Cell
Loading
Port
B
Media channel
Tissue chamber
Fluid flow
50 µm
y
x
15µm
Flexible pillars for
force measurement
Tissue chamber
5µm
Media channel
C
z
y
50µm
D
30µm
y
x
α-actinin
DAPI
E
Heatmap of motion vectors x and y fraction
X fraction
Y fraction
1
0.8
0.6
0.4
0.2
0

Figure 1

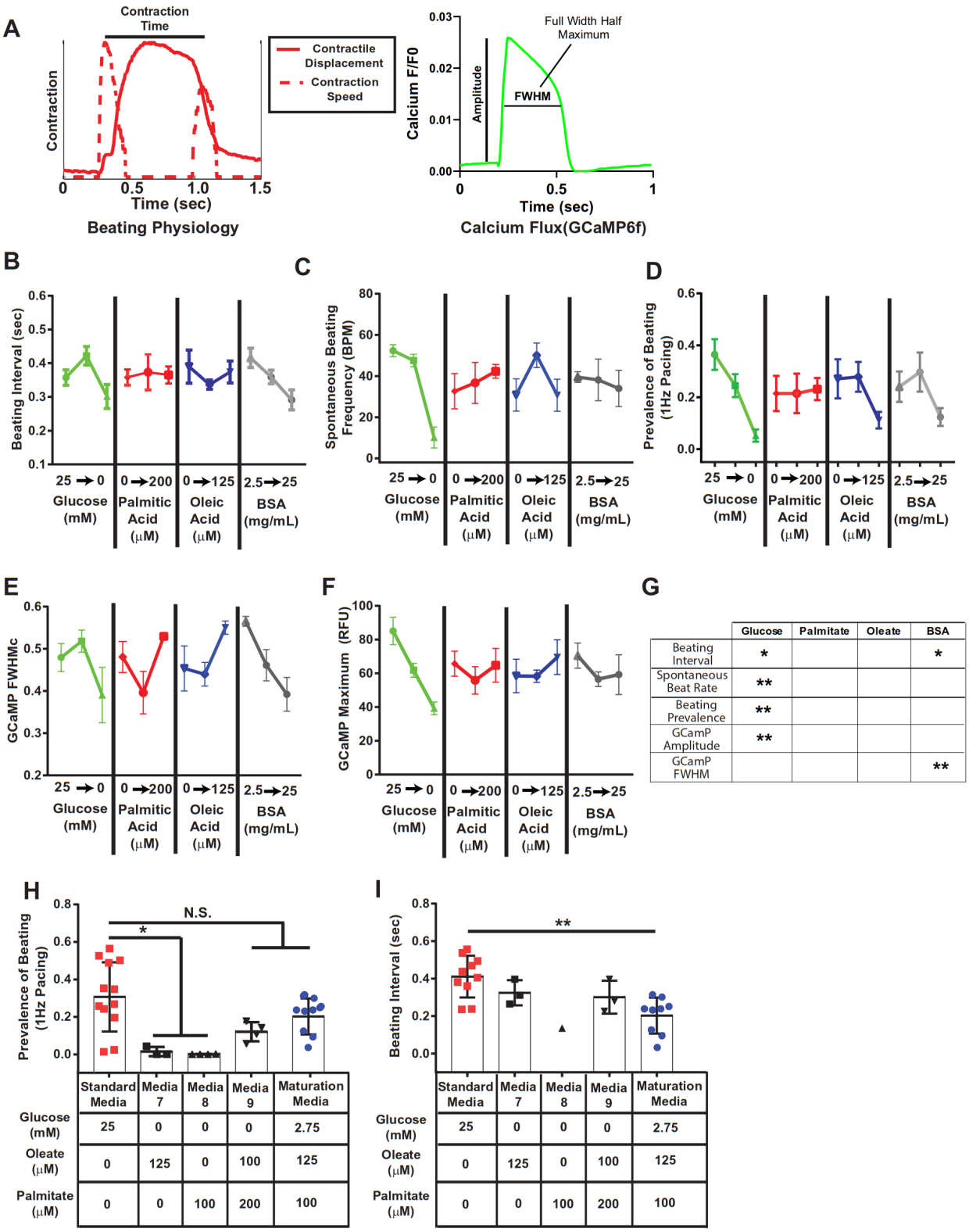

	Glucose	Palmitate	Oleate	BSA
Beating Interval	*			*
Spontaneous Beat Rate	**			
Beating Prevalence	**			
GCamP Amplitude	**			
GCamP FWHM				**

	Standard Media	Media 7	Media 8	Media 9	Maturation Media
Glucose (mM)	25	0	0	0	2.75
Oleate (μM)	0	125	0	100	125
Palmitate (μM)	0	0	100	200	100

Figure 2

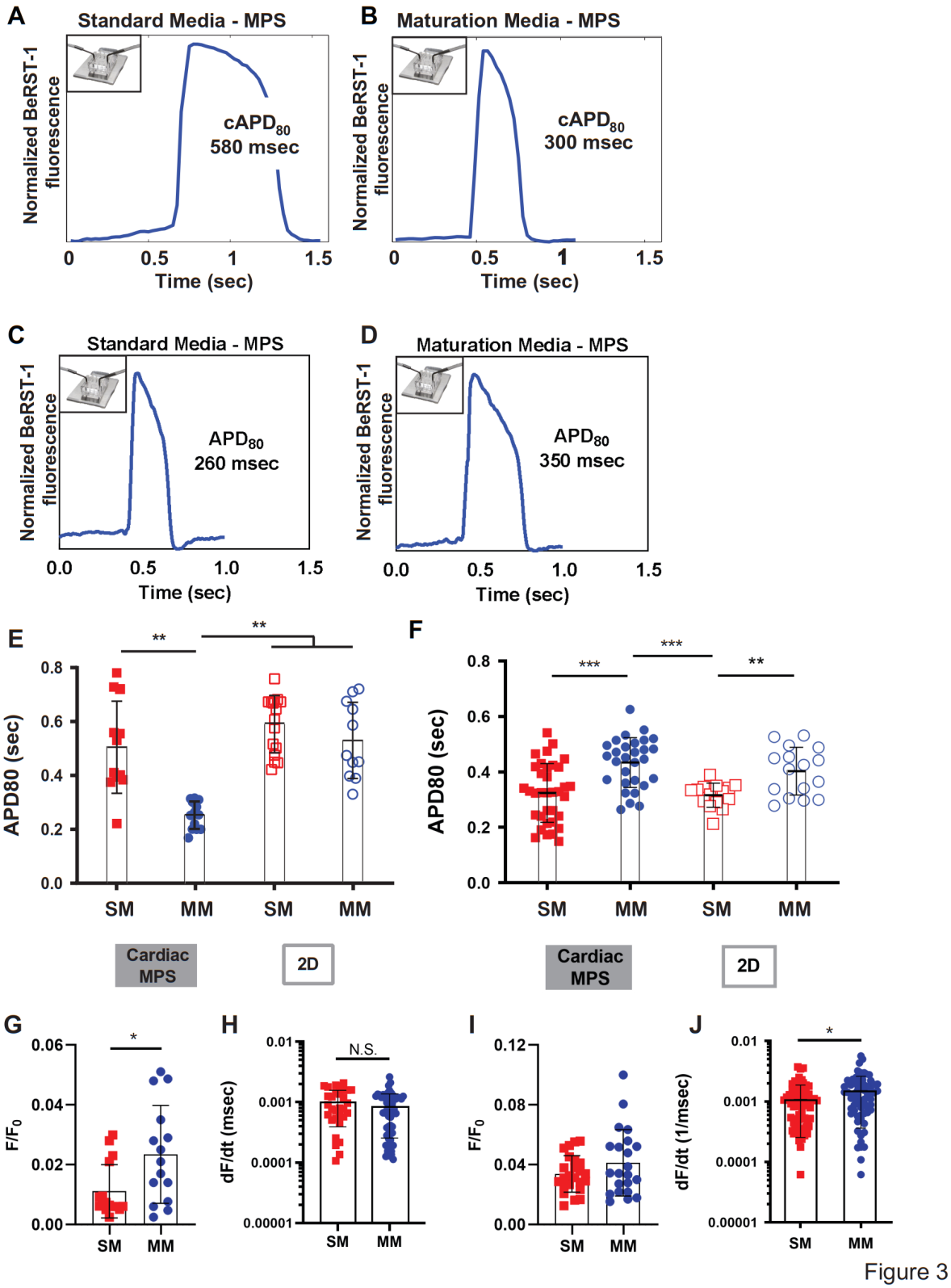
A
Standard Media - MPS
Normalized BeRST-1 fluorescence
cAPD80 580 msec
Time (sec)
B
Maturation Media - MPS
cAPD80 300 msec
C
Standard Media - MPS
APD80 260 msec
D
Maturation Media - MPS
APD80 350 msec
E
APD80 (sec)
SM
MM
Cardiac MPS
2D
F
G
F/F0
H
dF/dt (msec)
N.S.
I
J
dF/dt (1/msec)

Figure 3

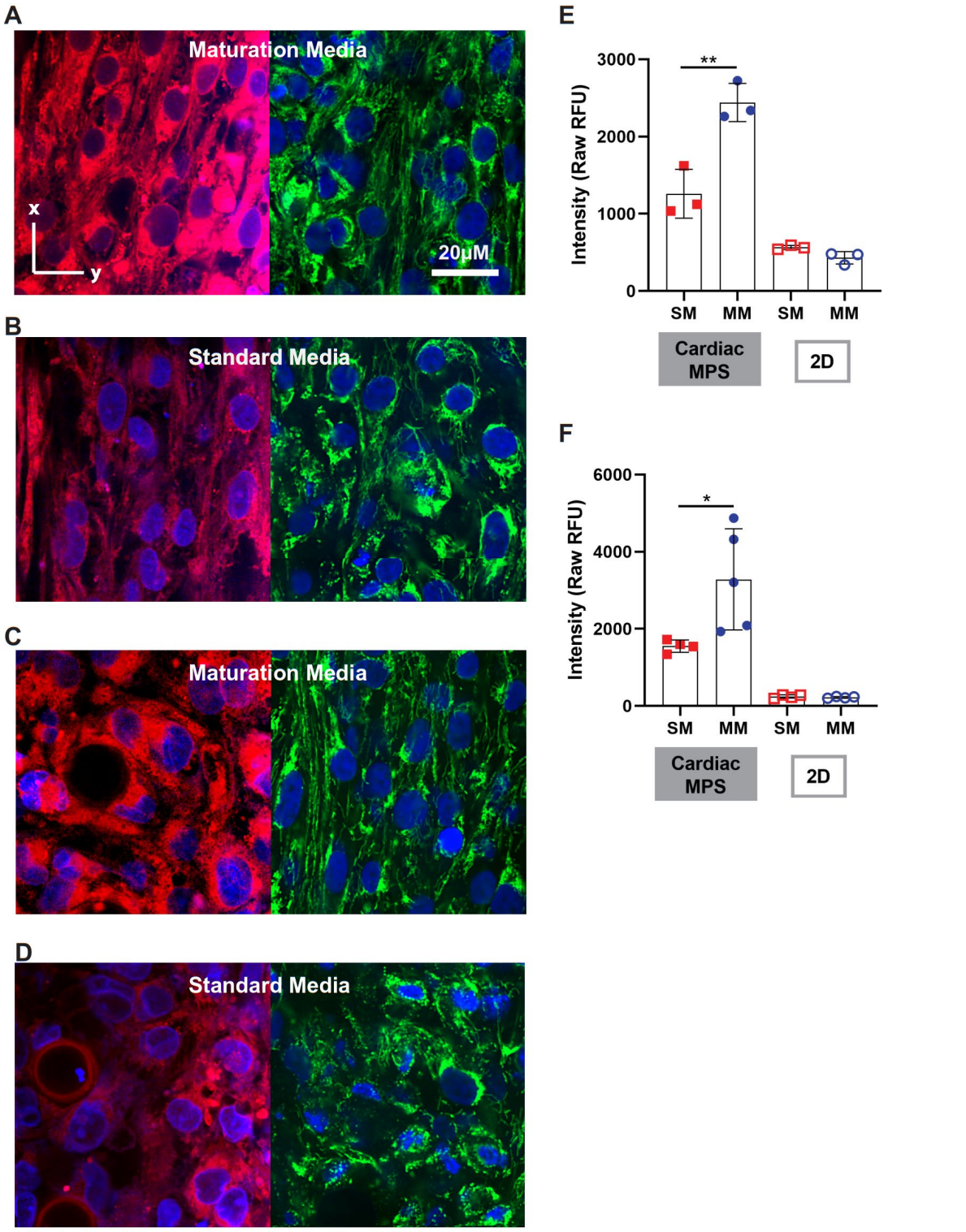

Mitotracker, Mitochondrial antibody, DRAQ5

Figure 4

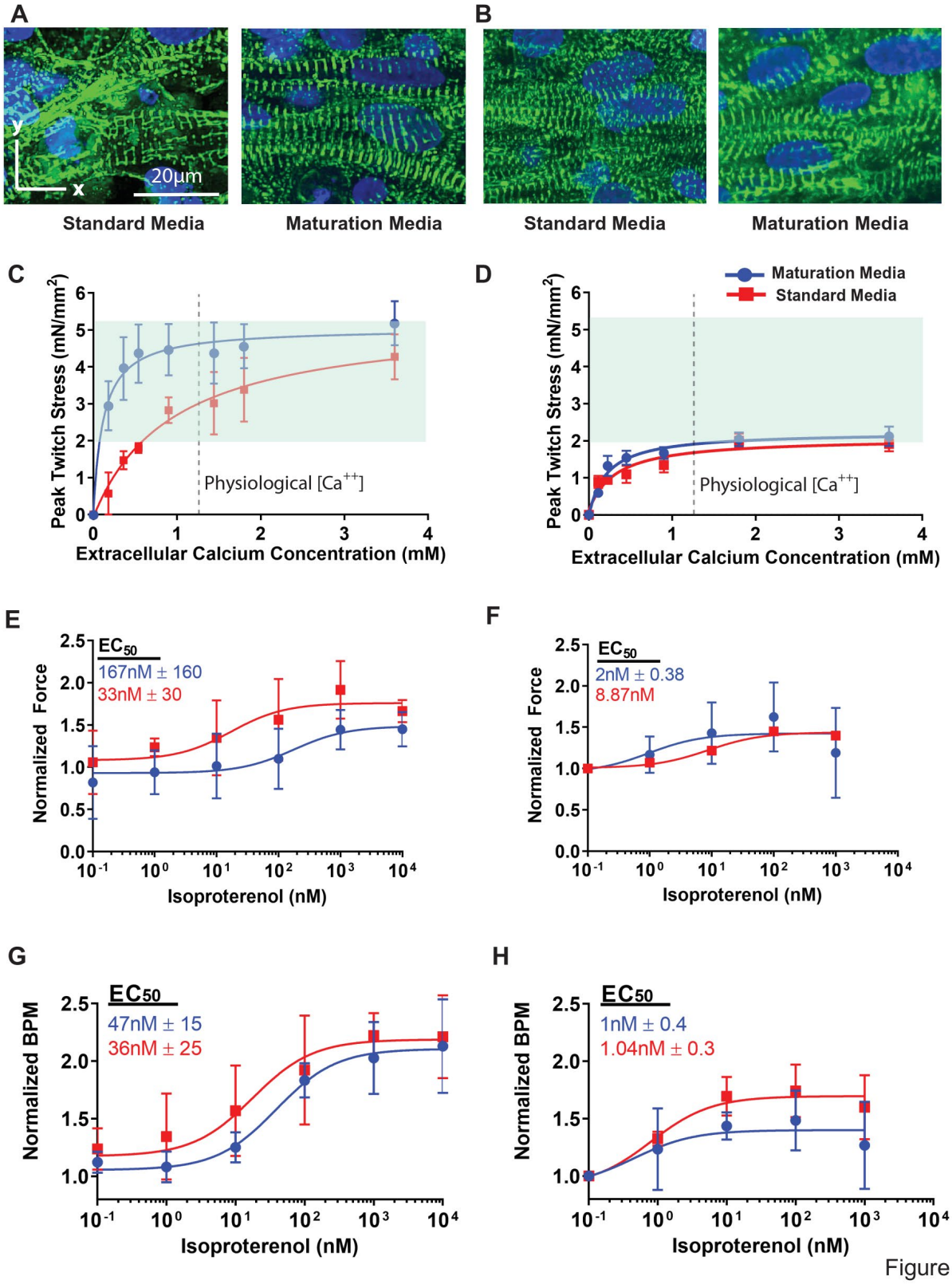
A
B
y
x
20µm
Standard Media
Maturation Media
Standard Media
Maturation Media
C
D
Peak Twitch Stress (mN/mm²)
Physiological [Ca++]
Extracellular Calcium Concentration (mM)
Maturation Media
Standard Media
E
F
Normalized Force
EC50
167nM ± 160
33nM ± 30
2nM ± 0.38
8.87nM
Isoproterenol (nM)
G
H
Normalized BPM
EC50
47nM ± 15
36nM ± 25
1nM ± 0.4
1.04nM ± 0.3
Isoproterenol (nM)

Figure 5

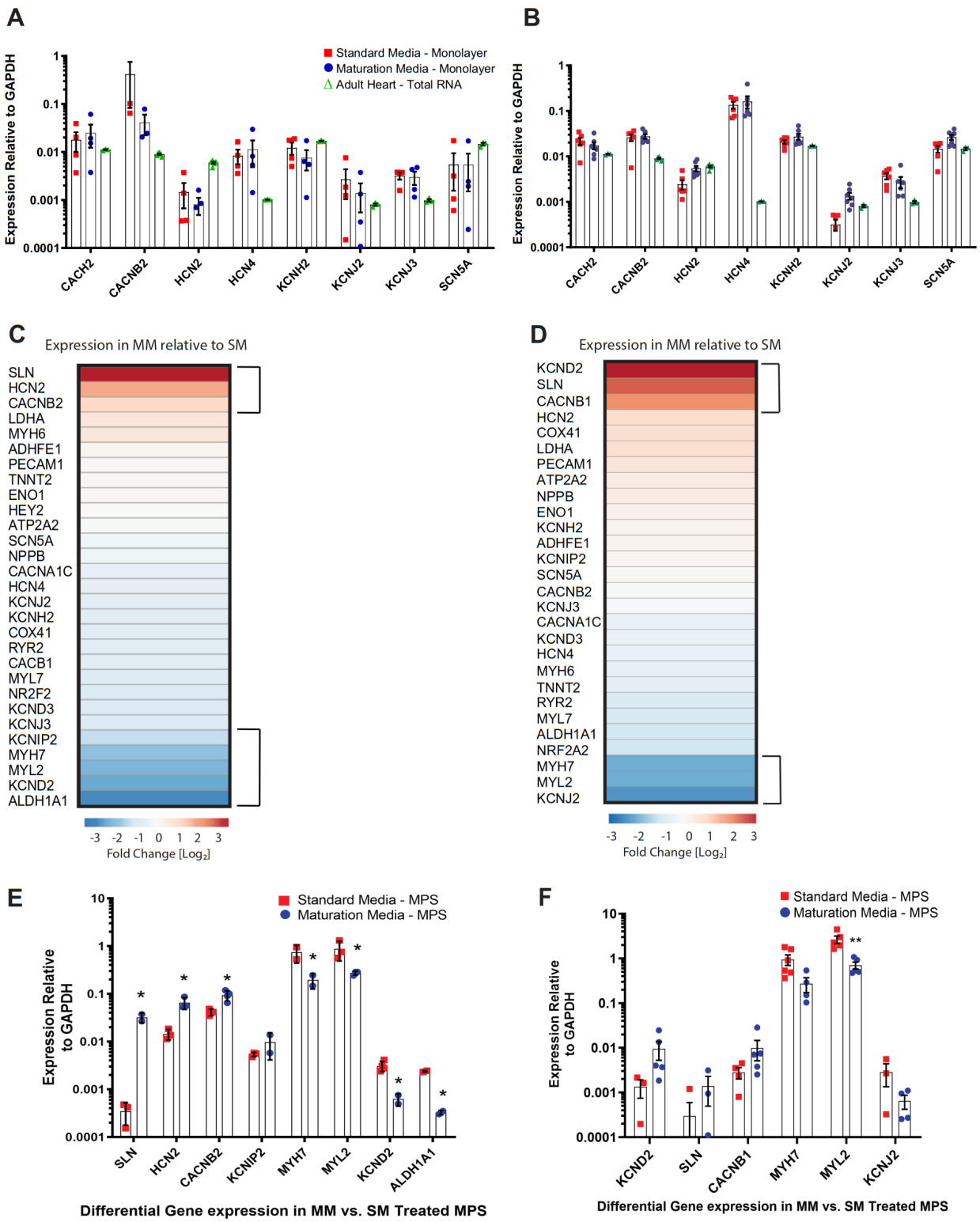
A
Standard Media - Monolayer
Maturation Media - Monolayer
Adult Heart - Total RNA
Expression Relative to GAPDH
CACH2
CACNB2
HCN2
HCN4
KCNH2
KCNJ2
KCNJ3
SCN5A
B
C
Expression in MM relative to SM
SLN
HCN2
CACNB2
LDHA
MYH6
ADHFE1
PECAM1
TNNT2
ENO1
HEY2
ATP2A2
SCN5A
NPPB
CACNA1C
HCN4
KCNJ2
KCNH2
COX41
RYR2
CACB1
MYL7
NR2F2
KCND3
KCNJ3
KCNIP2
MYH7
MYL2
KCND2
ALDH1A1
-3 -2 -1 0 1 2 3
Fold Change [Log2]
D
Expression in MM relative to SM
KCND2
SLN
CACNB1
HCN2
COX41
LDHA
PECAM1
ATP2A2
NPPB
ENO1
KCNH2
ADHFE1
KCNIP2
SCN5A
CACNB2
KCNJ3
CACNA1C
KCND3
HCN4
MYH6
TNNT2
RYR2
MYL7
ALDH1A1
NRF2A2
MYH7
MYL2
KCNJ2
-3 -2 -1 0 1 2 3
Fold Change [Log2]
E
Standard Media - MPS
Maturation Media - MPS
Expression Relative to GAPDH
SLN
HCN2
CACNB2
KCNIP2
MYH7
MYL2
KCND2
ALDH1A1
Differential Gene expression in MM vs. SM Treated MPS
F
Standard Media - MPS
Maturation Media - MPS
Expression Relative to GAPDH
KCND2
SLN
CACNB1
MYH7
MYL2
KCNJ2
Differential Gene expression in MM vs. SM Treated MPS

Figure 6

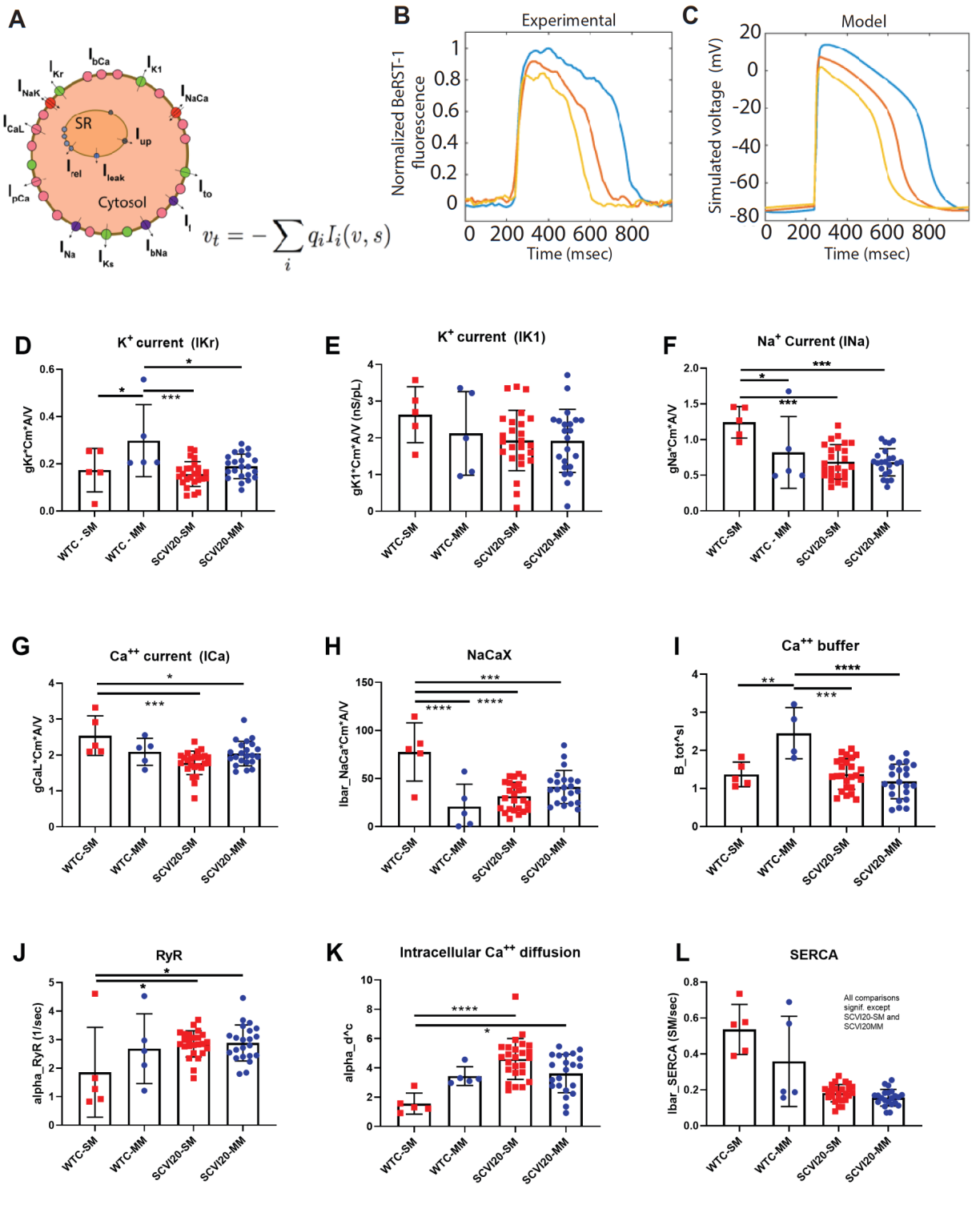
A
B
Experimental
Normalized BeRST-1 fluorescence
Time (msec)
C
Model
Simulated voltage (mV)
Time (msec)
SR
Cytosol
$v_t = -\sum_i q_i I_i(v,s)$
D
K+ current (IKr)
gKr*Cm*A/V
WTC - SM
WTC - MM
SCVI20-SM
SCVI20-MM
E
K+ current (IK1)
gK1*Cm*A/V (nS/pL)
WTC-SM
WTC-MM
SCVI20-SM
SCVI20-MM
F
Na+ Current (INa)
gNa*Cm*A/V
G
Ca++ current (ICa)
gCaL*Cm*A/V
H
NaCaX
Ibar_NaCa*Cm*A/V
I
Ca++ buffer
B_tot^sl
J
RyR
alpha_RyR (1/sec)
K
Intracellular Ca++ diffusion
alpha_d^c
L
SERCA
Ibar_SERCA (SM/sec)
All comparisons signif. except SCVI20-SM and SCVI20MM

Figure 7

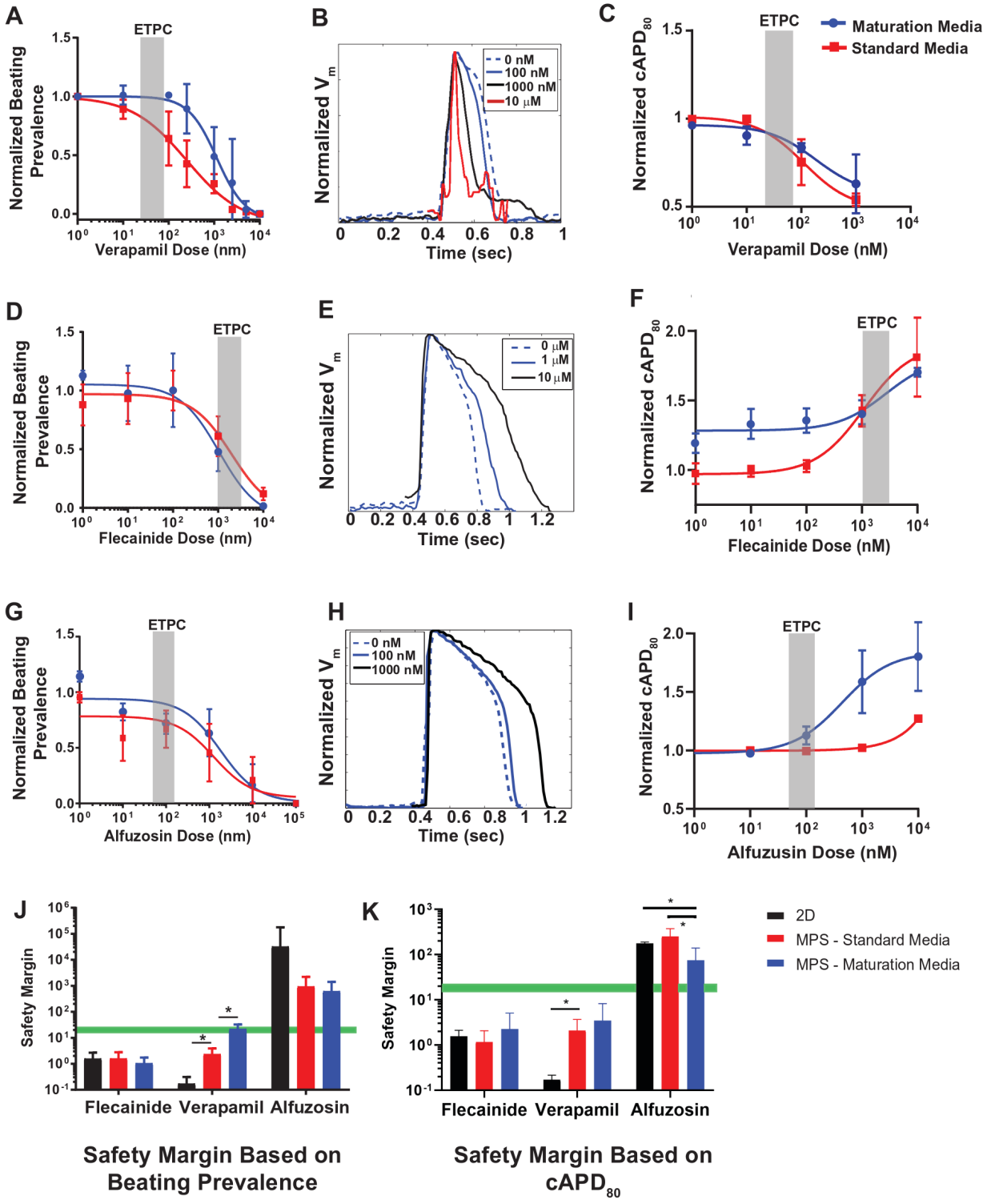
A
ETPC
Normalized Beating Prevalence
Verapamil Dose (nm)
B
Normalized V_m
0 nM
100 nM
1000 nM
10 μM
Time (sec)
C
ETPC
Maturation Media
Standard Media
Normalized $cAPD_{80}$
Verapamil Dose (nM)
D
ETPC
Normalized Beating Prevalence
Flecainide Dose (nm)
E
Normalized V_m
0 μM
1 μM
10 μM
Time (sec)
F
ETPC
Normalized $cAPD_{80}$
Flecainide Dose (nM)
G
ETPC
Normalized Beating Prevalence
Alfuzosin Dose (nm)
H
Normalized V_m
0 nM
100 nM
1000 nM
Time (sec)
I
ETPC
Normalized $cAPD_{80}$
Alfuzusin Dose (nM)
J
Safety Margin
Flecainide Verapamil Alfuzosin
Safety Margin Based on Beating Prevalence
K
Safety Margin
Flecainide Verapamil Alfuzosin
Safety Margin Based on $cAPD_{80}$
2D
MPS - Standard Media
MPS - Maturation Media

Figure 8

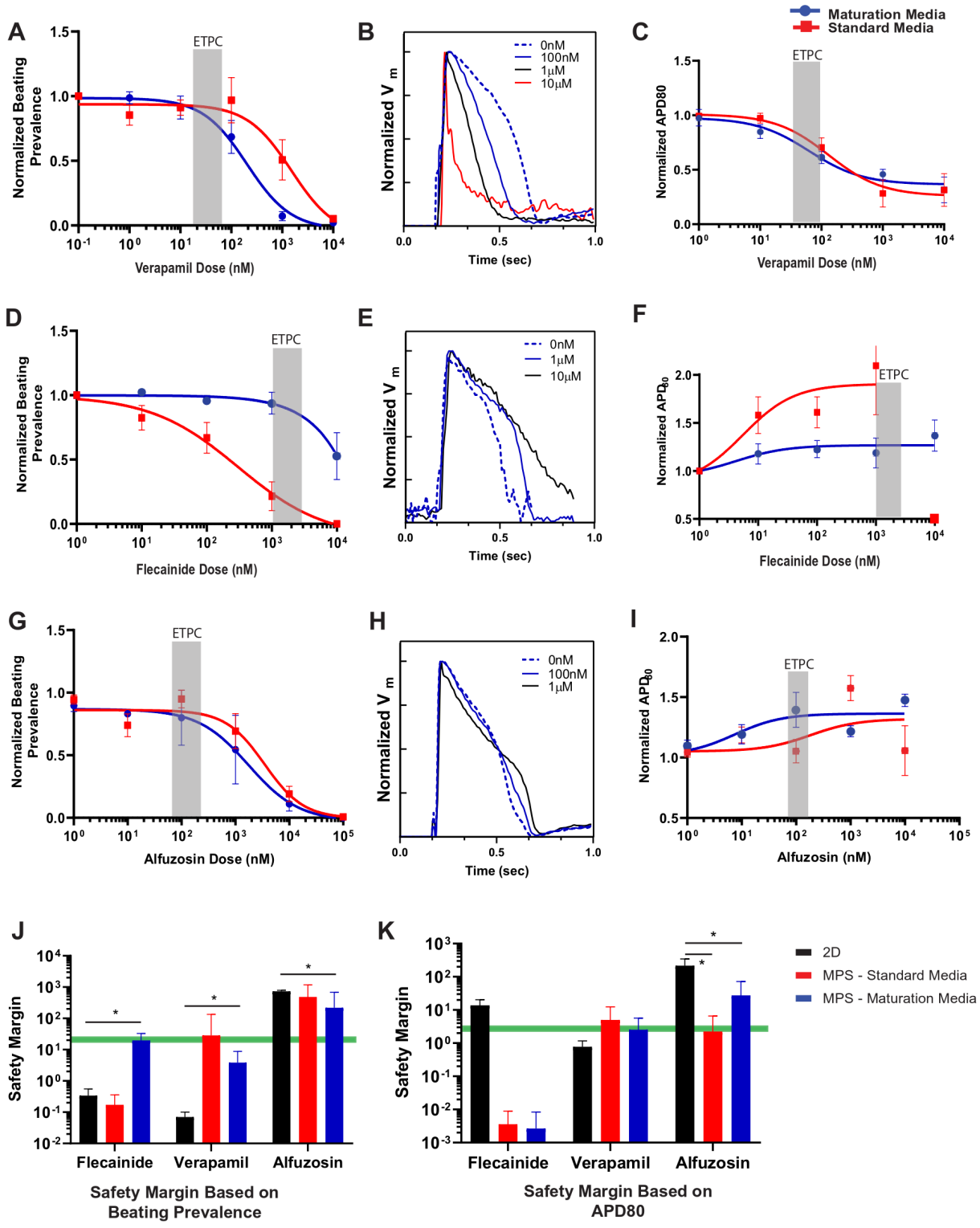
A
Normalized Beating Prevalence
ETPC
Verapamil Dose (nM)
B
Normalized V m
0nM
100nM
1μM
10μM
Time (sec)
C
Maturation Media
Standard Media
Normalized APD80
ETPC
Verapamil Dose (nM)
D
Normalized Beating Prevalence
ETPC
Flecainide Dose (nM)
E
Normalized V m
0nM
1μM
10μM
Time (sec)
F
Normalized APD80
ETPC
Flecainide Dose (nM)
G
Normalized Beating Prevalence
ETPC
Alfuzosin Dose (nM)
H
Normalized V m
0nM
100nM
1μM
Time (sec)
I
Normalized APD80
ETPC
Alfuzosin (nM)
J
Safety Margin
Flecainide
Verapamil
Alfuzosin
Safety Margin Based on Beating Prevalence
K
Safety Margin
Flecainide
Verapamil
Alfuzosin
Safety Margin Based on APD80
2D
MPS - Standard Media
MPS - Maturation Media

Figure 9

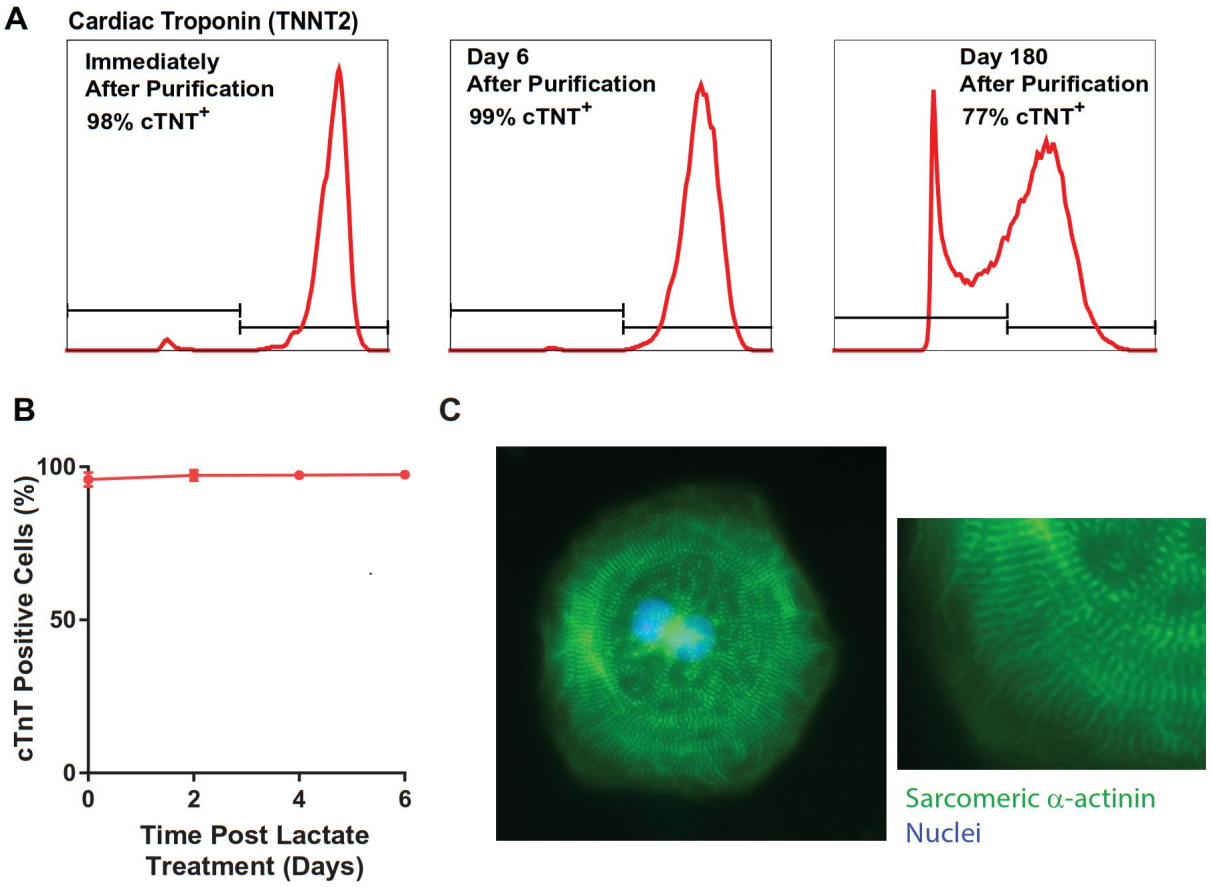

Supp. Figure 1

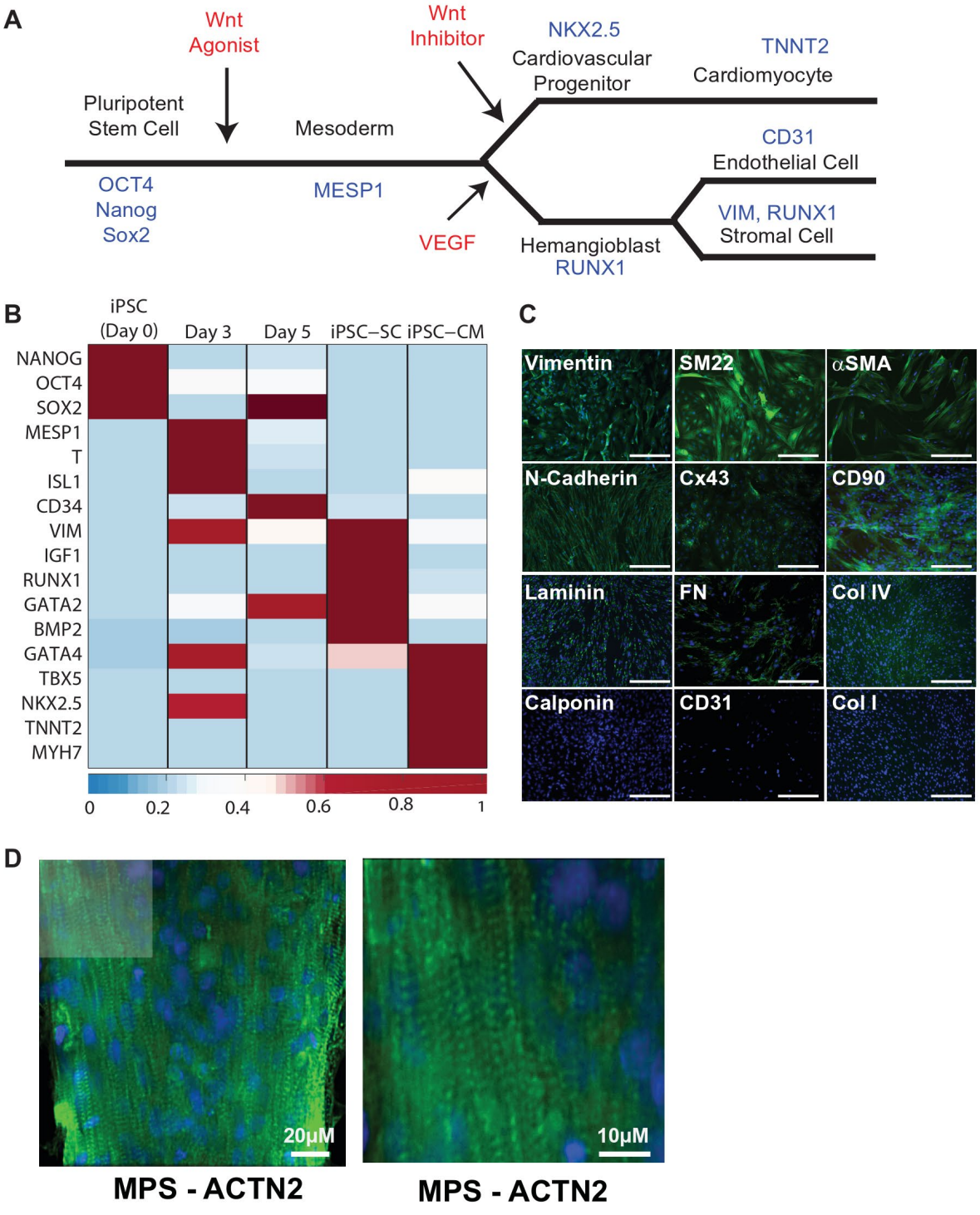

Supp. Figure 2

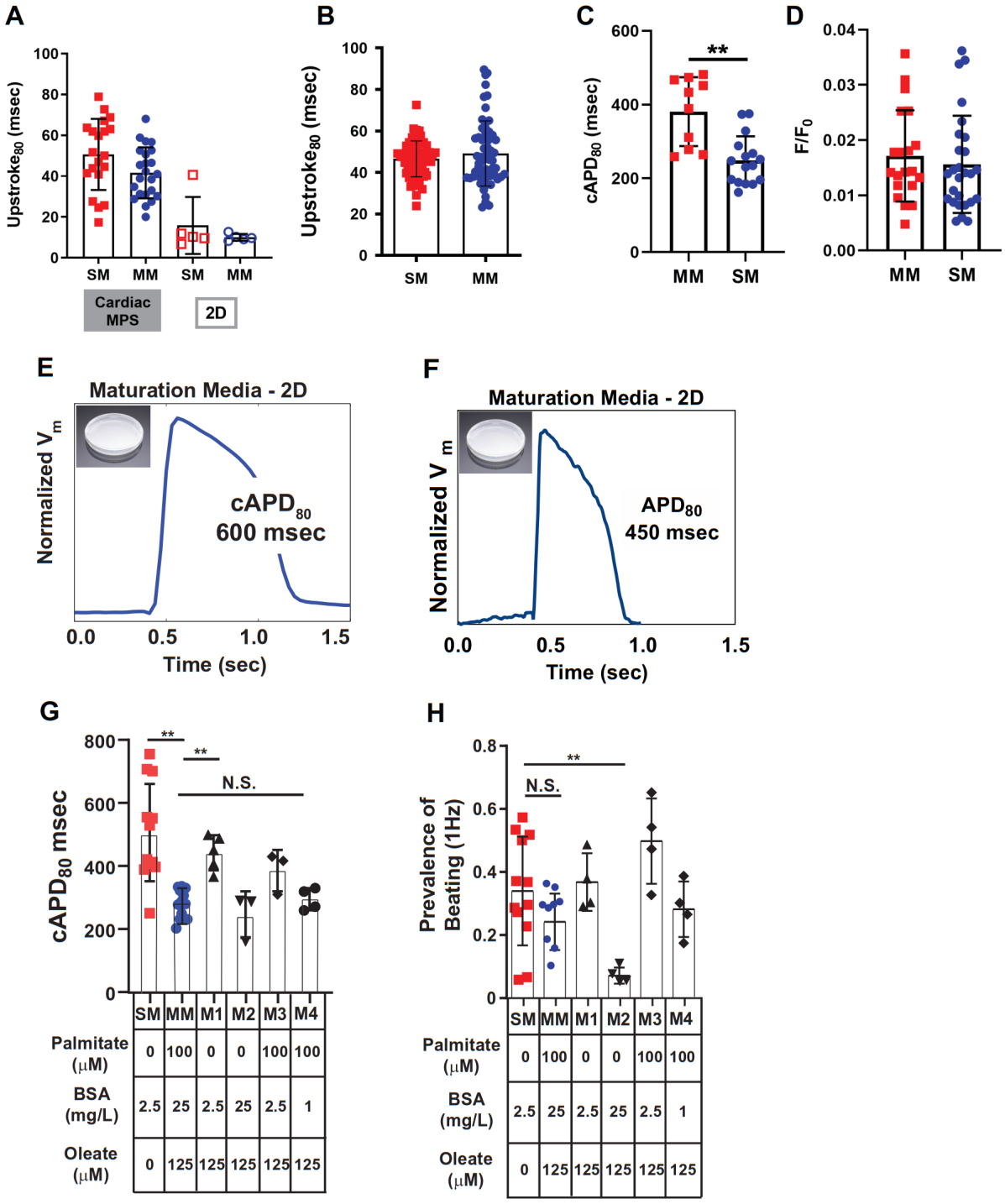

Supp. Figure 3

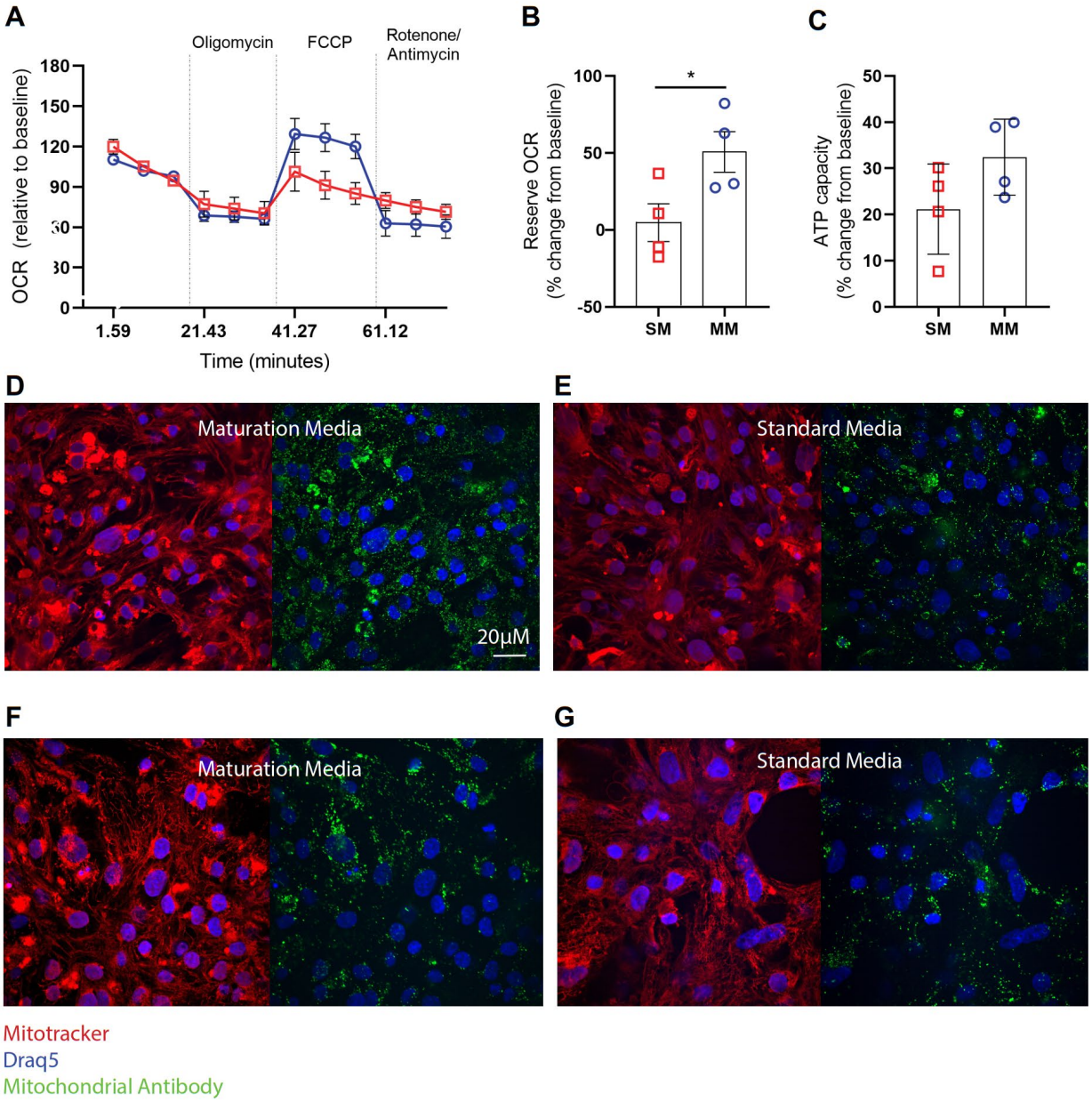

Mitotracker
Draq5
Mitochondrial Antibody

Supp. Figure 4

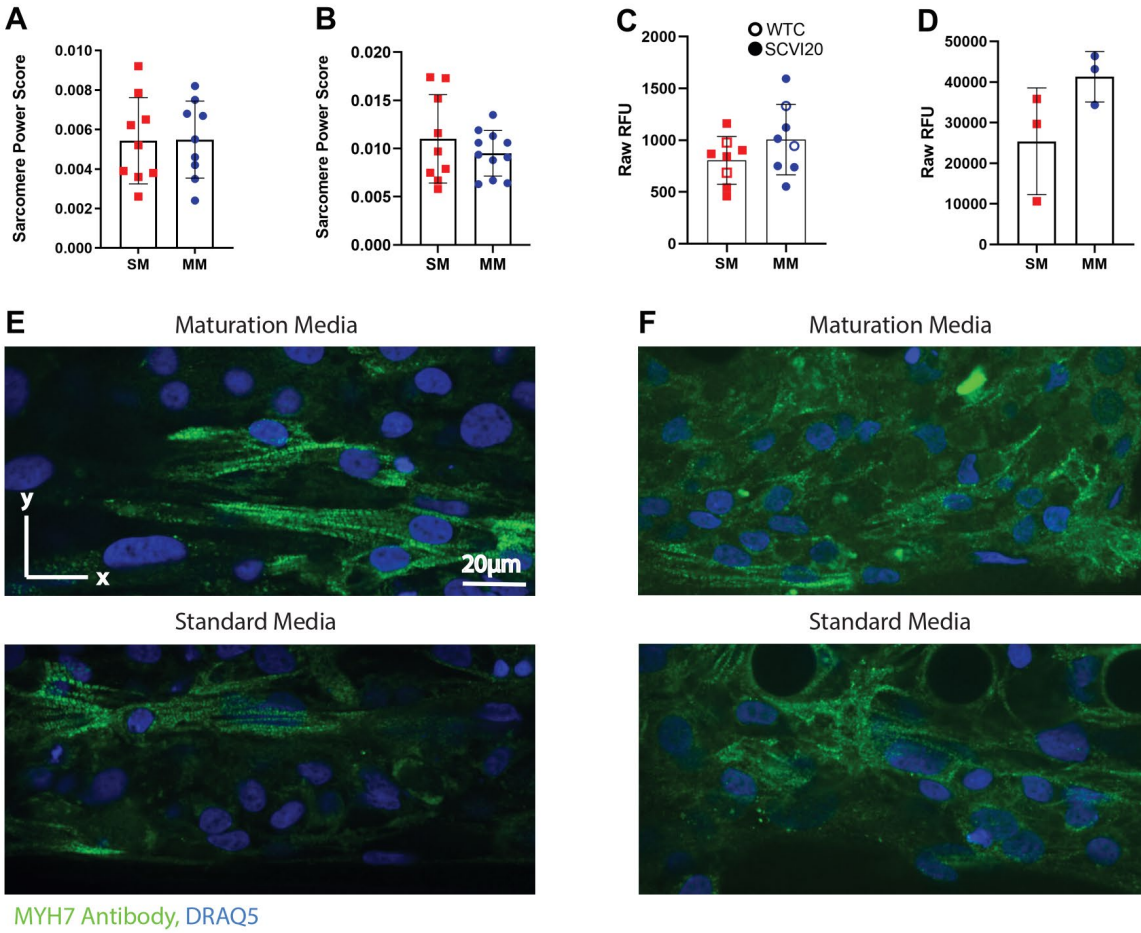

Supp. Figure 5

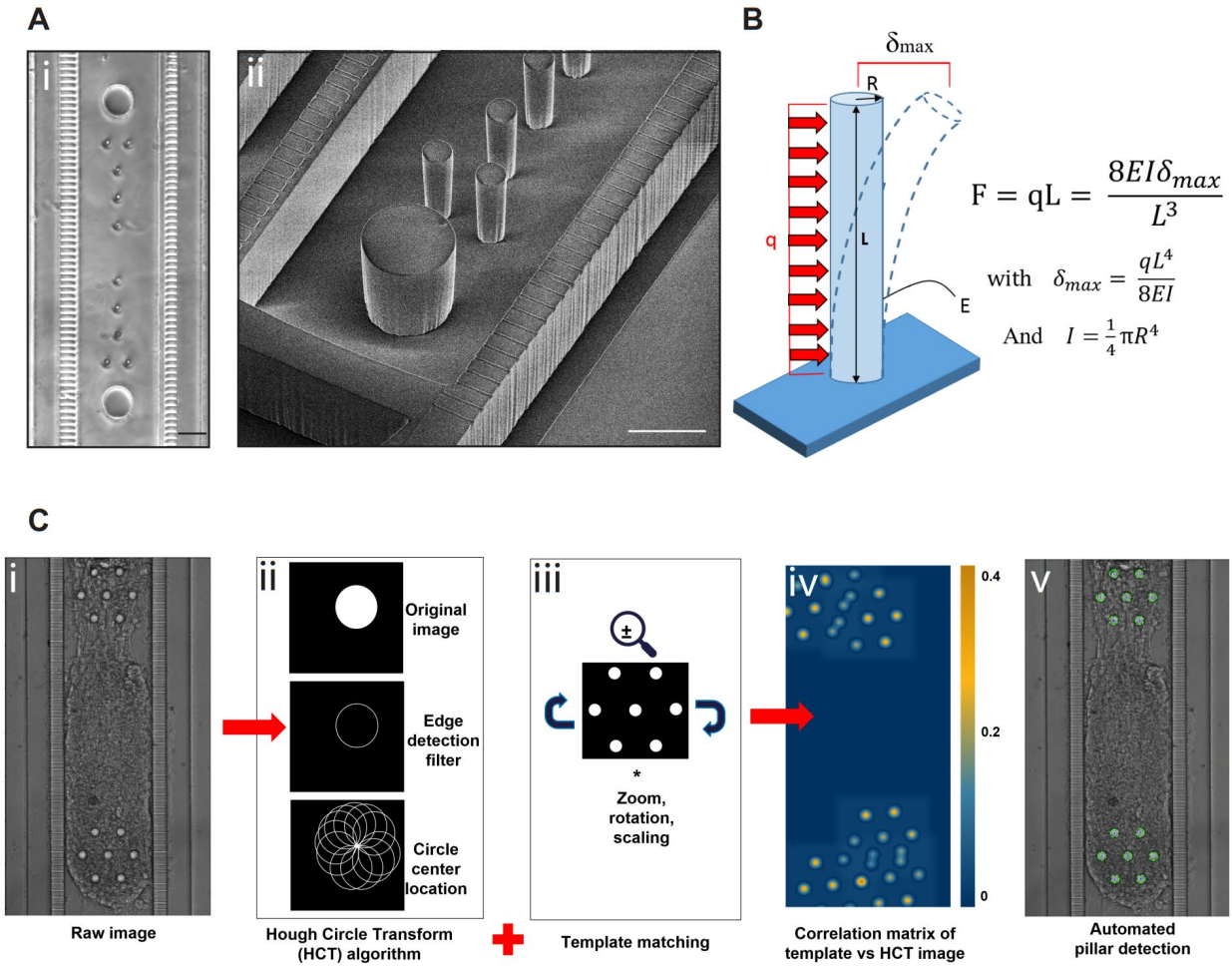

Supp. Figure 6

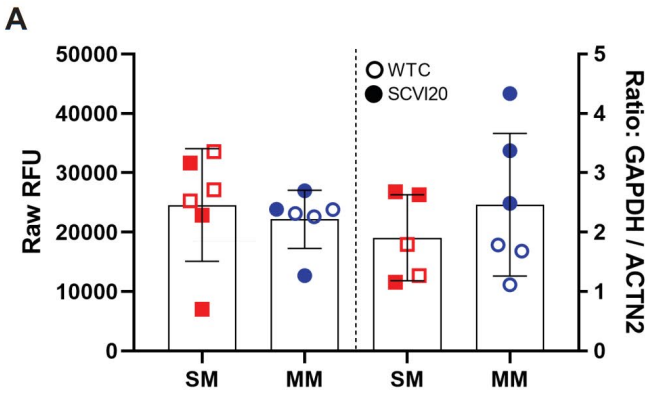

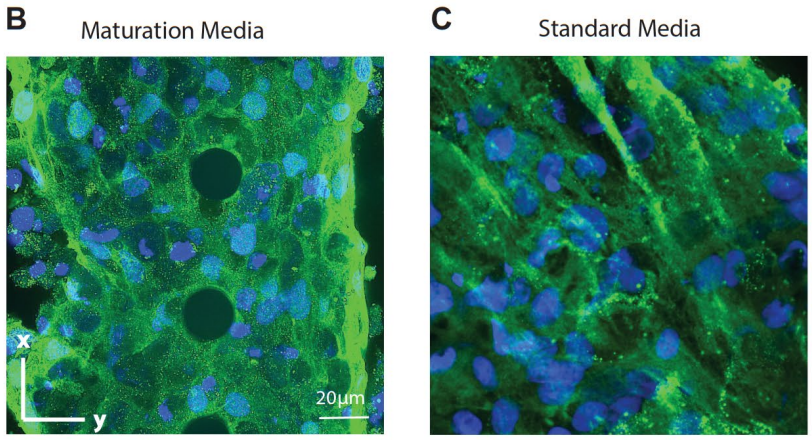

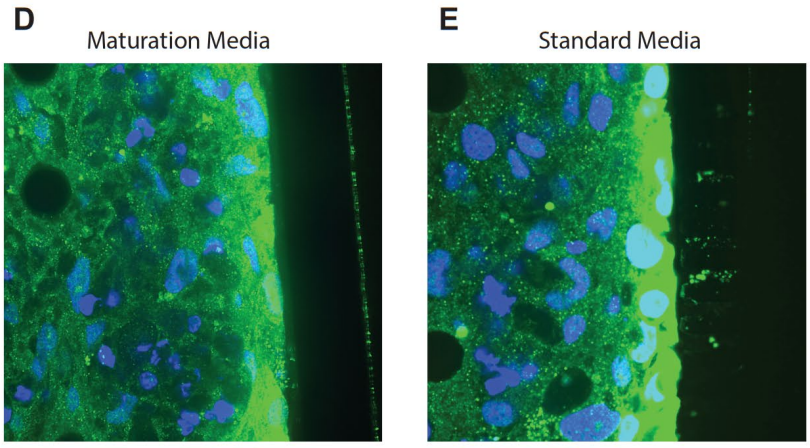

Supp. Figure 7

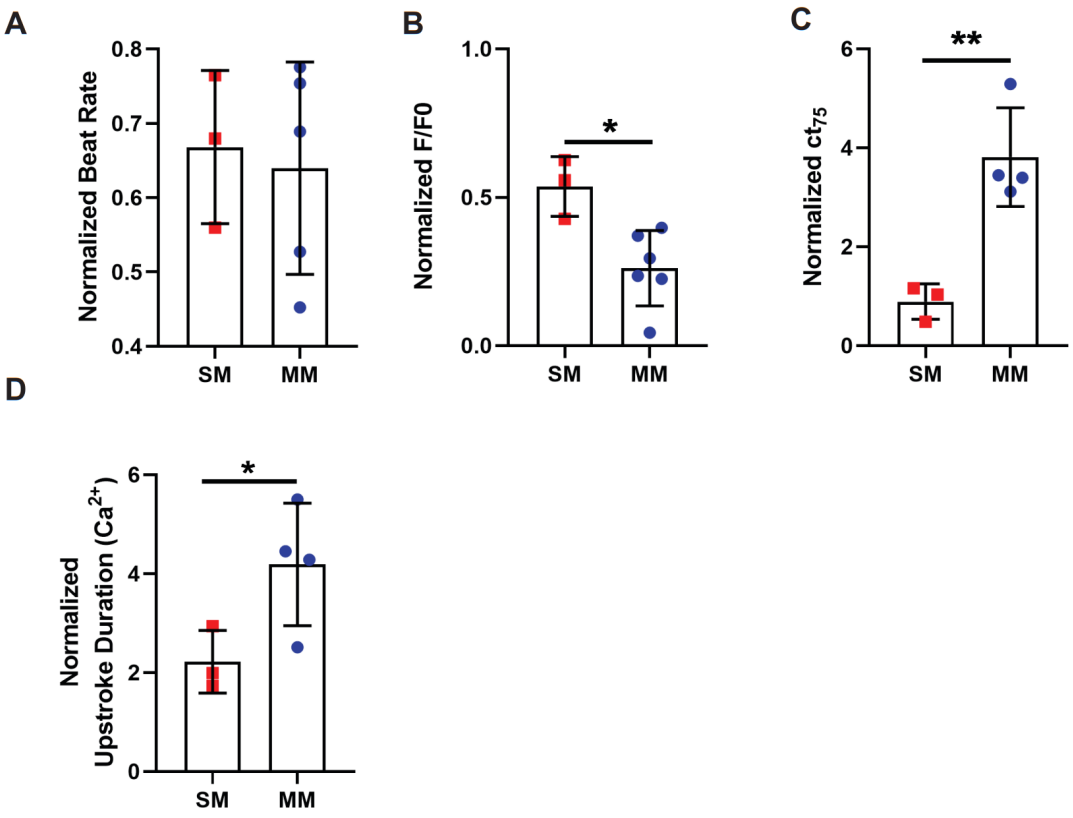

Supp. Figure 8

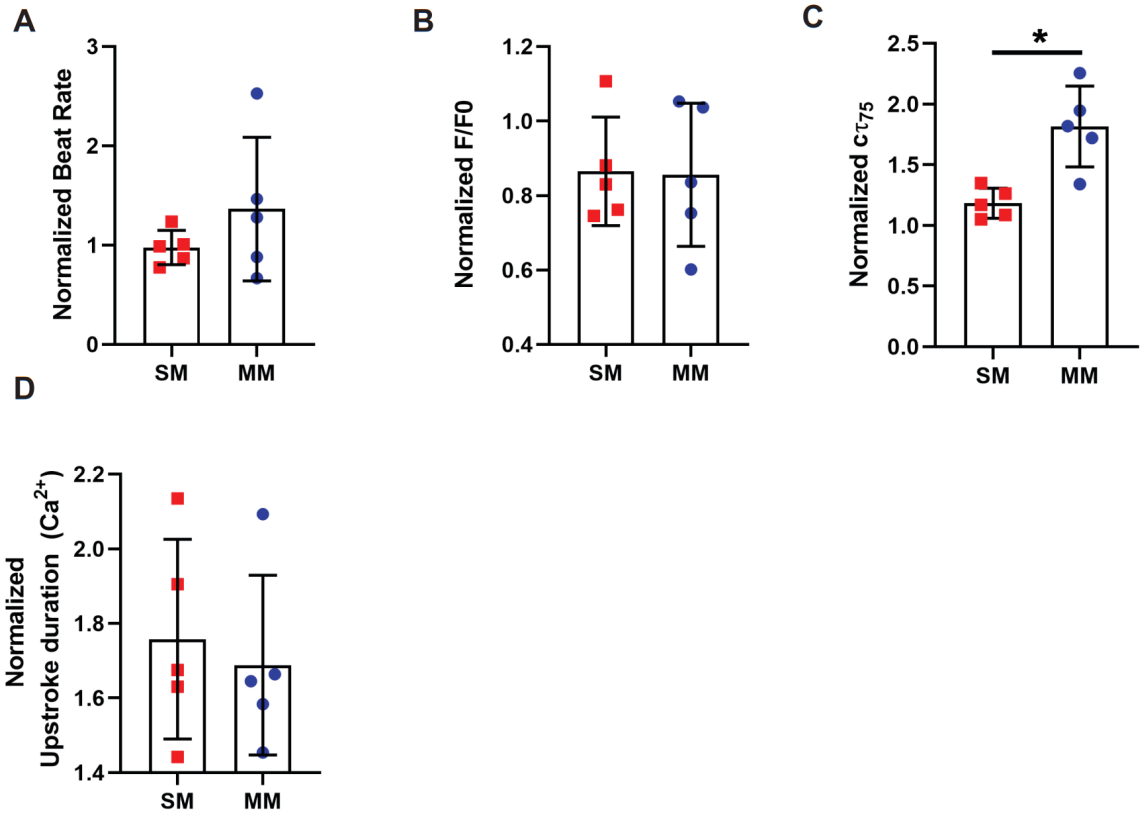

Supp. Figure 9

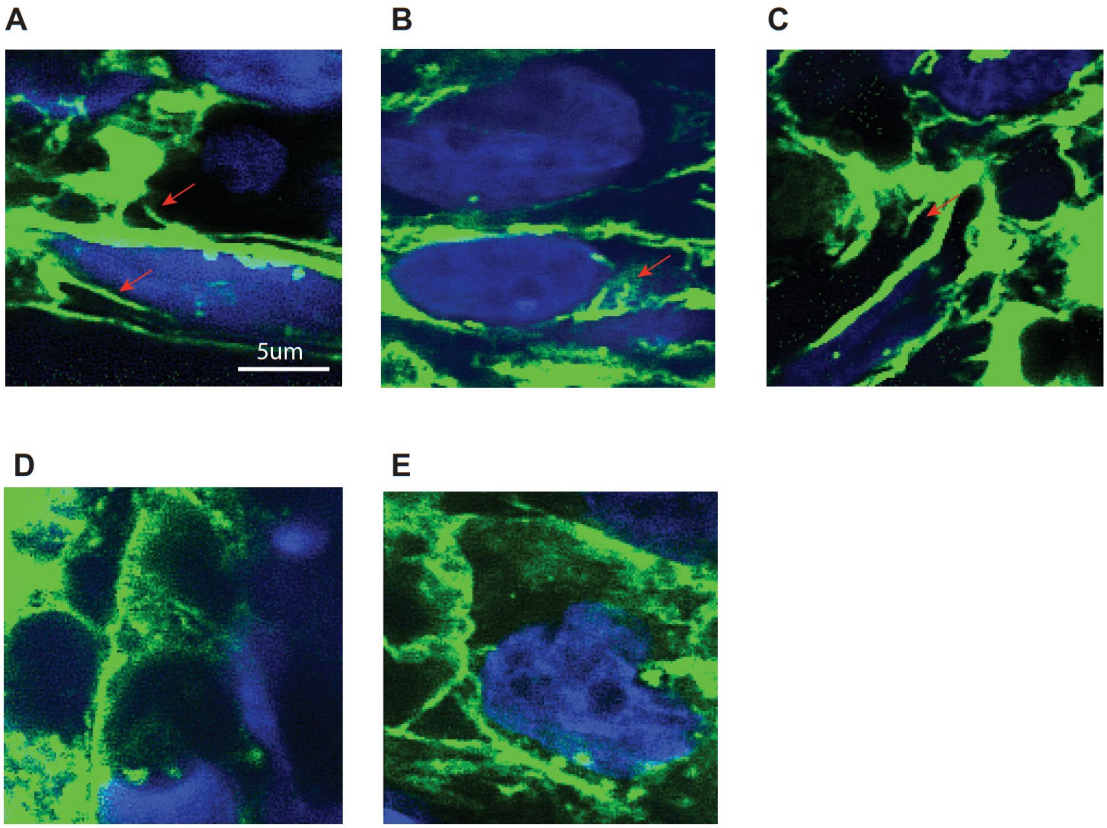

Supp. Figure 10

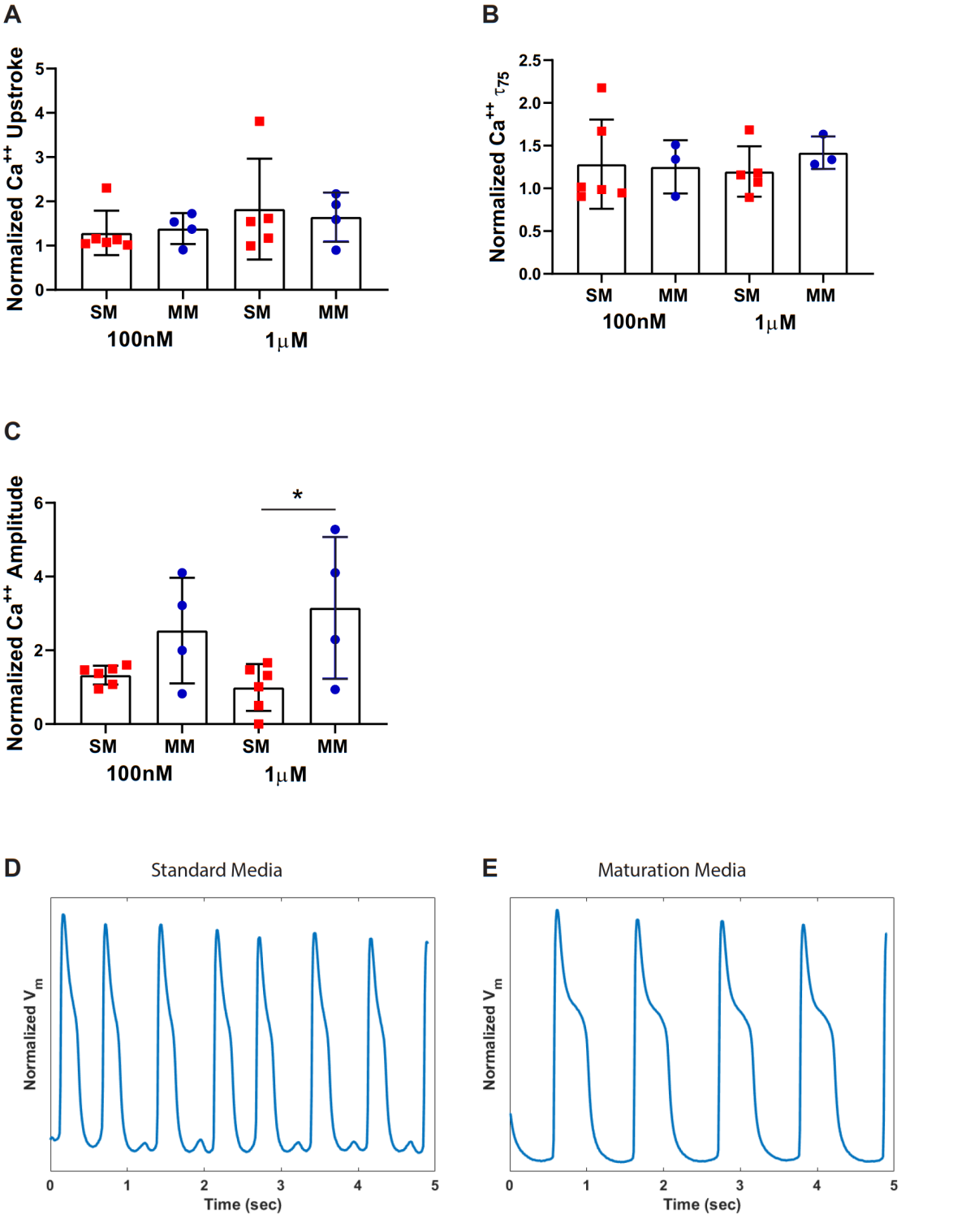

Supp. Figure 11

Chapter 3 Cardiac Muscle Microphysiological System: Optimization of Function and Pharmacology Response

3.1 Abstract

Due to extensive safety and efficacy protocols, and the poor prognostic capability of state-of-the-art pre-clinical drug screening platforms, it can take 15 years and more than $2B to get a drug on the market. This time consuming and expensive approval process limits the access of patients to life-saving therapeutics. As drug-induced effects on the heart are a major safety concern, the development of platforms that robustly predict cardiac liabilities is a necessity to speed a drug to market. The discovery of human induced pluripotent stem cells (hiPSC) and their derived cell types has shown promise as a source for human *in vitro* models for drug development. However, the immaturity of hiPSC-derived cells, particularly cardiomyocytes raises concerns about their predictive capabilities for pharmaceutical safety screening. To improve the maturation of heart muscle in microphysiological systems (MPS), we have screened an array of device designs, selecting for parameters that enhance morphological and contractility outcomes while enabling robust cell loading and tissue formation. Parameters tested included chamber geometry, anchoring pillar array configuration, inlet valve for uni-directional cell flow and diffusion barrier size. We found that inlet valves were the most relevant parameter for improved loading efficiency while chamber geometry and pillar array had a profound impact on mechanical properties. The optimized design demonstrated physiological responses to drugs targeting cardiomyocyte contractility, suggesting our human cardiac muscle is a good prognostic tool for drug screening.

3.2 Introduction

Typical drug development processes are costly and time consuming[1-3], in part due to the extensive preclinical screening required before clinical trials[4]. Unfortunately, state-of-the-art 2D *in vitro* and *in vivo* studies are not representative of human physiology or electrophysiology[5-7]. Therefore, more physiologically relevant platforms have emerged as crucial tools to improve the accuracy (i.e., elimination of false positives and negatives)

and speed of drug safety and efficacy screens. Since drug-induced cardiac liabilities are the most significant reason for drug attrition at every stage of drug safety assessment, preclinical through clinical trials, platforms robustly assessing cardiac safety are sorely needed. The discovery of human induced pluripotent stem cells (**hiPSC**)[8] opened doors to novel *in vitro* drug screening platforms, including disease models[9, 10] exploiting hiPSC-derived cardiomyocytes (**hiPSC-CM**); however, these cells have immature phenotypes, notably in electrophysiology, morphology, calcium handling or contractility[11-15]. To address the limitations of hiPSC-CM for safety pharmacology, numerous strategies have been employed, spanning aligned three dimensional (3D) tissues[16-26], maturation specific media[27, 28], and electronic pacing[29, 30]. We have previously demonstrated that the combination of aligned 3D cardiac muscle in microphysiological systems (**MPS**) with fatty-acid based maturation media synergistically promoted maturation of tissue electrophysiology and metabolism, leading to pharmacology results more reminiscent of adult human cardiomyocytes[27]. However, this approach did not lead to consistent maturation of tissue mechanics, which is essential since heart treatment compounds have inotropic activity that cannot be readily measured in state-of-the art screening platforms (2D *in vitro* or *in vivo*). Tissue contraction in 2D *in vitro* platforms is poorly organized, and platforms require complex and invasive technology for such measurements[31].

Advances in MPS platforms that faithfully predict the inotropic effects of drugs is critical for lead compound optimization through safety pharmacology. In this study, we used Robust Experimental Design[32] combined with conventional parametric studies to optimize the mechanical function of cardiac muscle in a MPS. The cardiac MPS houses a central tissue chamber that is separated from the media channels by micron scale fenestrations that allow for nutrient supply, drug delivery, and waste clearance, while minimizing shear stress on tissue [5] (**Figure 1**). Optimization centered on the addition and arrangement of mechanosensing pillars to the tissue chamber to perform noninvasive and precise measurements of cardiac muscle contraction force [33, 34]. The strategy is based on fixed rigid anchors at the extremities of cardiac tissue that has been shown to develop cardiac muscle with highly aligned sarcomeres, where the local stress is uniaxial[35], a hallmark of cardiac muscle. Our pillar arrangements was designed to model the 3D crossectional position of a fiber matrix that imparts resting pre-load known to improve mechanical maturation and contractility of engineered heart tissues[10]. We also studied the dimensions of the MPS tissue chamber, which promotes 3D confinement and uniaxial and synchronized beating, and correlates to an increase in contraction force and physiologic hypertrophy[17, 18, 36]. To improve the robustness of the system, efficient and reproducible loading of hiPSC-CM into the tissue chamber is necessary, we therefore also varied the design of inlet valves[37]. The final cardiac MPS design enabled rapid and reproducible loading of hiPSC-CM to form uniaxially beating cardiac muscle with physiologically relevant inotropic responses to drugs targeting specific cardiomyocyte contraction pathways.

3.3 Results and Discussion

3.3.1 Tissue Chamber Anchors and Pillars for Structural Support and Contraction Force Measurements Respectively

To further improve the mechanics of the tissue and the subsequent toxicity prognostic abilities of the cardiac muscle platform, further investigation of the MPS design was performed. The initial cardiac MPS[5](**Figure 1A-B, top**) did not have features to support the cardiac muscle in the tissue chamber. The absence of structural support periodically translated into tissues that were disorganized, often in multiple parts and shrunk inwards to form an agglomeration of cells in the center of the chamber (**Figure 1B, top**). When simulating early remodelling process of cardiac tissue formation, such as exposing tissues to resting pre-load, heart constructs would gain in maturity and functionality [10, 35]. We therefore computationally modelled the tissue organization and deformation around two fixed rigid anchors (**Figure 1C**). The dimensions (60 μm diameter, 60 μm height) of the anchors were calculated so that for a reported tissue maximum contraction force [38], the anchors would not deflect. We modeled the total displacement, or deformation, of the tissue towards an elongated longitudinal fiber (**Figure 1C, left**) as well as the Von Mises stress (typically used for modelling soft biological tissues[39]), which showed increased values at the surface of the fixed anchors (**Figure 1C, right**). As predicted by Thavandiran et al.[35], the anchors act as boundaries that create low uniaxial stress and promote remodeling of the tissue. Experimental studies (**Figure 1A-B, bottom**) confirmed the simulated trends: cardiomyocytes self-assembled into an organized tissue, wrapped around the anchors and formed an elongated, uniaxially beating muscle fiber. Not only did the anchors prevent tissue colapsing, but they also acted as resting pre-load for mechanical maturation of the tissues[10].

Contraction force is a critical metric to assess cardiotoxicity in drug screening, since several compounds have inotropic activity that cannot be readily measured in state-of-the art 2D screening platforms or *in vivo* [31]. We modified orginal designs of the mechanosensing pillars within the tissue chamber to perform noninvasive and precise measurements of cardiac muscle contraction force (**Figure 1E**). Upon each contraction, the muscle pulls around the pillar and deflects it (**Figure 1F**). This deflection can be optically measured and the contraction force can be calculated. Although the pillars add Von Mises stress to the muscle (**Figure 1D, right**), they do not alter the the spontaneous fibre formation (**Figure 1D, left & 1F**). Adult cardiac tissue slices contract within a range of 2-8 mN/mm^2[38, 40, 41]. With pillar dimensions of 20 μm in diameter, 60 μm in height, and modulus of 2.63 MPa (for a 1:10 PDMS network[42]) such a force would lead to a deflection in the range of 1.8-9.5 μm. Our optical microscope system has a resolution of 0.61μm, which can accurately measure deflection in this range. Such dimensions of the pillars are within the linear elastic assumptions necessary to apply the Euler beam theory

for uniformly distributed load on a cantilever beam (**Figure 1G**). Pillar deflection was calculated via an in-house motion tracking script for automated monitoring of pillar motion.

3.3.2 Array of pillar arrangement for improved muscle quality, electrophysiology and contractility

The addition of anchors enabled the stabilization of muscle structure and its rearrangement towards an elongated cardiac muscle fiber with uniaxial beating. Since the muscle beats uniaxially, the contraction force will be maximal at the extremity of the muscle (**Supp. Fig 1A**). We fabricated various chip designs with different pillar arrangements to limit the interference of anchors on muscle contraction (**Figure 2A**). Designs 1 & 2 are considered 'control' designs based on prexisting devices. Inspired by design 1&2, we designed arrangements with pillars separated at the extremity of the chamber (designs 3-8). Designs 9-10 had an increased number of pillars in the center of the chamber to assess their role in muscle formation. Design 11 mimics the crossectional fiber arrangement of Ma et al.[10]. Muscle morphology within the chambers and low within-design variance (below 15% as per power analysis) were scored independently by 2 observers (score 1-10, **Supp. Figure 1C**). Designs with muscles of score > 9 or a variance < 15% were selected for further analysis (design 1, 2, 3, 7, 9), while the remaining designs (design 4, 5, 6, 10, 11) were eliminated due to their poor score and high variance (**Figure 2B**). Design 8 showed promising outcomes when compared to control designs. Several metrics were considered to further determine successful designs. This included the action potential duration at 80% of repolarization APD_{80} (**Figure 2C**) in the physiological range of 250-450ms[38]. Design 9 had a significantly lower APD_{80} than control designs, with a mean below physiological range, leading us to exclude it from further analysis. Brightfield videos were processed with an in-house motion tracking software to analyze both the prevalence (**Figure 2D**, percentage of muscle moving above the 2µm/sec threshold) and the uniaxial beating of the muscles (**Figure 2E**, percent of motion vectors aligned in the longitudinal axis). Designs 3 and 7 showed significantly lower prevalence when compared to control designs, excluding them for further analysis. Our analysis led to design 8 as an optimal chamber for muscle quality, APD_{80} in the physiological range, comparable prevalence to control design 2, and higher, although not significant, longitudinal motion than all other designs (**Figure 2E**). Interestingly, design 8 resembles the pattern of the anchor design, to promote structural support while enabling contraction force measurements. The next design iteration will be based of design 8.

3.3.3 Fenestration Height Gradient for Optimal Combination of High Nutrient Diffusion and Muscle Confinement

The cardiac MPS was designed to closely mimic physiological nutrient delivery from blood vessels to the cardiac muscle while being protected from blood flow shear stress[5]. Originally the tissue chamber was separated from the media channels via a fenestration barrier, with 2 μm wide slits to allow for diluted species diffusion while protecting the chamber tissue from flow shear stress[5]. In the orginial design, the fenestration height was of 2 μm, allowing to reach a concentration equilibrium between media channels and tissue chamber in 40 seconds, as simulated in **Figure 3A**. Diffusion is essential for healthier muscle, not only due to fresh nutrient supply, but also because of faster waste clearance[43]. We therefore simulated the the diffusion time of glucose into the tissue chamber with 1.5, 2, 5 and 6 μm high fenestrations (always with a 2 μm width). As expected, 5 and 6 μm fenestrations showed a rapid diffusion of small molecules in the tissue chamber (10 and 2 seconds until saturation respectively), whereas 1.5 μm fenestrations needed more than one minute for full saturation of the empty chamber (**Figure 3A-B**). Singularized cardiomyocytes have an average size of 21 μm, however they can be as small as 11 μm diameter (**Supp. Figure 1B**). Due to their contractile function, cardiomyocytes are naturally flexible cells, that have also been shown to change their shape depending on the substrate patterning[44]. At fenestration heights of 5 and 6 μm, 70 and 90% of the MPS respectively, had cells escaping from the tissue chamber into the media channels, perturbing the media flow and clogging the fenestrations(**Figure 3C-D**). Based on these observations, fenestrations were set at 2 μm since they allow for rapid nutrient diffusion while preventing cells from escaping in the media channels.

3.3.4 Robust Design Experiments Indicate Optimal Loading and Tissue forming Success while Improving Tissue Mechanics

Based on design 8 with 2 μm fenestrations, we further optimized the MPS design to improve muscle morphology and function by varying the width (from 170 μm to 130 μm and 90μm) and the length (from 800 μm to 1300 μm and 1800 μm) of the chamber. The length was defined as the distance between the top and bottom set of pillars and the width was defined as the distance between the fenestration barrier within the chip (**Figure 4A, black arrows**). We also introduced an extension length (150 μm initially to 230 μm and 300 μm) between the inlet and the first set of pillars to improve initial cell loading (**Figure 4A, black arrows**). We also varied the inlet valve design inspired by Klammer et al.[37] to singularize the cardiomyocytes while loading.

Having 4 parameters with three levels each, we employed Robust Experimental Design[32] to screen for the effects of each parameter in an orthonormal fashion, giving us 9 combinations to design and microfabricate versus 3^4, or 81 independent experiments if parametric space was used. In **Figure 4B,** each row represents an individual design that was experimentally tested. **Figure 4C** shows brightfield images cardiac muscle of the different designs.

We first assessed the loading success of the different designs. Based on the mean (**Figure 5A, left**) and the desirability function (**Figure 5A, right**), the optimal combination was length of 1300 μm, width of 170 μm, extension of 150 or 230 μm and valve 2. Five days post loading, tissue formation was assessed (**Figure 5B**), showing an optimal combination of length of 1000 or 1300 μm, width of 170 μm, extension of 150 μm and valve 2 or 3. At that same timepoint, tissues were assessed for their presence of "tail", linking the muscle to the cells that remained in the cell loading port. Optimal designs had a high "no tail" success, represented by any length, width, extension and valve 3 (**Figure 5C**).

Next, we assessed the mechanical function of the cardiac muscles by measuring the fraction of motion vectors aligned in the longitudinal axis (**Figure 6A**), the compressive strain (**Figure 6B**) and the maximal contraction force (**Figure 6C-D**). Longitudinal motion showed the following preferred combination: length of 1000 or 1800 μm, width of 90 μm, any extension or valve. During contraction, the tissue area that was actively contracting, compressed (compressive strain), while the other part of the tissue was stretched (tensile strain). The optimal combination for higher compressive strain was length of 1800 μm, width of 130 μm, extension of 150 μm, and valve 1 or 2. The maximum contraction force identified a preferred length of 1800 μm, width of 130 μm, and extension of 300 μm, and valve 2 (**Figure 6C**). An important metric is also the mechanical maturation of the muscle, defined here by the change in maximum contraction force from day 15 to day 10 (**Figure 6D**). The optimal combination was length of 1800 μm, width of 170 μm, extension of 300 μm, and valve 2.

Robust Experimental Design typically does not identify an optimal design from the original experimental table, so a refined parametric study is required. To determine the next generation designs for further optimization studies, we selected design conditions for each of the 4 parameters. The extension outcomes most relevant for the loading success where extensions 150 μm or 230 μm. We chose to move forward with an extension of 230 μm giving room to maximize a high loading success rate and low tail instances. The valve was expected to have a critical role in the loading, for which valve design 2 and 3 are preferred. We decided to move forward with valve 3 for the next generation designs. We expected the length of the chamber to have an impact on the muscle mechanics (strain and force), for which length of 1800 μm was preferred. However, its role in tissue alignment (longitudinal motion) and muscle formation is also important, in which case length 1000 and 1300 μm were preferred. Since we could not define one preferred length, we added granularity to the length range in the next design iteration: 1000, 1300, 1550, 1800

μm. At last, the width of the tissues was expected to be most relevant for the mechanical output of strain and force, for which 130 μm came out as preferred. To summarize, the next iteration of designs had a fixed width of 130 μm, extension of 230 μm, length range from 1000-1800 μm and valve design3. We further added a design with no valve as a control comparison.

3.3.5 Parametric study of different lengths shows improved loading, mechanics, electrophysiology and response to increased pacing frequencies

Varying chamber length had a significant effect on both the loading and the formation of the tissue (**Figure 7A-B**). 1550 μm significantly improved the loading success, while both 1300 μm and 1800 μm showed better tissue formation 5 days after loading. The same metrics were evaluated for the valves, where no valve was significantly better than valve (**Figure 7C-D**). The Robust Experimental Design study (**Figure 5),** showed little preference for valve 1 design (no valve) for both loading and tissue formation; however, the opposite was observed when compared to valve 3 in the parametric study with near optimized conditions and only length as a variable (**Figure 7)**. We decided to have a no-valve design, since it allows for successful loading despite imperfect cell singularization. Ten days after loading, the maximum muscle strain was calculated from brightfield videos, for which length of 1800 μm was significantly higher (**Figure 7E**). Interestingly, a length of 1550 μm showed a significantly better mechanical maturation than a length of 1000 μm, defined here by the increase in strain from day 7 to day 15 for each muscle (**Figure 7F**). The calcium transient amplitude peak was significantly higher for 1550 μm and trending up for 1800 μm compared to both shorter length (**Figure 7G**). In cardiac biology, the amplitude of the calcium transient, a proxy for intracellular calcium concentration, is directly correlated to the contraction force amplitude[45]. Therefore, an increased strain and calcium transient for 1550 and 1800 μm is a good proxy for mechanical maturation of the muscle. No change was seen in the longitudinal alignment of the tissues (**Figure 7H**), as suggested by **Figure 6A**, where the width had more of an impact than the length.
Adult cardiac tissue shows increased contraction force with increasing pacing frequency[46], a hallmark of immaturity of hiPSC-derived cardiomyocytes. A positive force-frequency relationship requires mature calcium handling and efficient energy conversion (requiring oxidative metabolism) which are typically absent in immature hiPSC-CM. Numerous engineered heart tissues, derived from hiPSC-cardiomyocytes show a neutral or negative force frequency relationship[47-50]. All designs except 1800 μm showed the expected negative strain-frequency relationship when comparing 1Hz to 3Hz. For the 1800 μm design, there was no significant change, but an increasing trend of strain at 1.5Hz compared to 1Hz (**Figure 7I**) was observed. Interestingly, the maximum calcium

amplitude was significantly higher at 1.5Hz for most lengths, but only length of 1550 μm showed no significant decrease at 3Hz and an increasing trend for 1.5 and 2Hz (**Figure 7J**). The decrease in calcium amplitude with higher frequencies demonstrates potential inefficient calcium handling of the muscle. Collectively, the combination of tissue length (1550 and 1800 μm) with maturation media can explain the positive strain-frequency and calcium-frequency relationship at 1.5 and 2Hz. In addition to the neutral strain and calcium-frequency relationship at 3Hz, these designs showed a significant improvement when compared to most engineered heart muscles[47-50].
Based on loading, tissue forming, mechanics, increased frequency relationships and electrophysiology outcomes, we defined an optimal design that has a width of 130 μm, extension of 230 μm, no valve and length of 1550 μm.

3.3.6 Pharmacology analysis shows one optimal length of 1550 μm

We exposed the different length tissues to three different drugs having known changes on contractile function of heart muscle via different pathways. Isoproterenol, a well-known inotrope that increases cardiac contraction via an increase of the calcium transient amplitude[51], did not show a length dependency for the ratio of peak strain to peak calcium (**Figure 8A**), as expected. No length had a significant change compared to 0nM. Omecamtiv mercabil, a small-molecule direct activator of cardiac myosin, works independent of calcium activity. It promotes increased contractility by binding to the myosin catalytic domain and forces myosin filaments to the strongly actin-bound force-generating state[52]. As expected, the ratio of strain to calcium was significantly increased for length 1300 and 1550 μm tissues, with a higher outcome for length 1550 μm at 1 μM and 10 μM (**Figure 8B**). Finally, tissues were exposed to imatinib mesylate, an antitumor drug, blocking selectively the tyrosine kinase activity of c-abl. It has been correlated with toxic cardiomyopathy phenomenon, through mechanisms involving mitochondrial dysfunction[53]. We anticipated a decrease in strain to calcium ratio, which only a muscle length of 1550 μm significantly demonstrated when compared to other lengths (**Figure 8C**). Overall, tissues of 1550 μm long show the best pharmacology response to the three drugs. Furthermore, they showed physiologically relevant EC_{50} or IC_{50} for all drugs when compared to the literature: 2.3 μM for omecamtiv, 70 nM for imatinib, and 300 nM for isoproterenol, which correspond closely to literature values of 2.3 μM omecamtiv[52], 30-600 nM imatinib[54-56], 200nM-1μM isoproterenol [29, 38]. Therefore, the optimal length of 1550μm improved mechanics and loading, and had the most relevant physiological response to three drugs affecting cardiac contractility through different mechanisms. **Figure 8D&F** show 2D design and 3D renderings respectively of the final optimal design with the following properties: width of 130 μm, extension of 230 μm, no valve and length of 1550 μm. **Figure 8E** is a brightfield image of the optimal design loaded with cardiac muscle.

3.4 Conclusion

Robust Experimental Design was combined with conventional parametric studies to optimize the physiological function of cardiac muscle in a microphysiological system. Optimization centered on tissue morphology and mechanics, reproducibility and robustness of device loading, and pharmacology. The final optimal design had a width of 130 μm, extension of 230 μm, no valve and a length of 1550 μm. Importantly, muscle in the final design showed physiologically relevant response to three drugs targeting cardiomyocyte specific mechanical pathways. The combination of fatty-acid based maturation media with an optimized tissue chamber design led to a human cardiac muscle « fit for purpose » as a prognostic tool for inotropic drug screening. This will be the state-of-the-art MPS used in drug screening studies.

3.5 Materials and Methods

3.5.1 Fabrication of cardiac MPS

Microfluidic cardiac MPS systems were formed using an optimized version of the protocol described in our previous work[5, 27]. Two step photolithography was used to fabricate a microdevice silicon wafer mold. The final mold featured different designs of our initial cell culture chamber (55 μm high), linked to the feeding media channels via an array of fenestrations (2 μm x 2 μm high/width), providing nutrients from media to the cells via convective flow while protecting the tissue from media flow shear stress. The media inlet port was leading to the media channels running adjacent to each side of the tissue chamber.

The first layer fabricated onto the virgin silicon wafer was 2 μm high for our fenestration pattern : Virgin silicon wafers were cleaned in piranha bath for 10min (heated sulfuric acid bath at 120C activated with 250ml of H_2O_2) and rinsed thoroughly with deionized water for 5min before being dried. Clean wafers were then heated at 200C for 15min to allow dehydrogenation.

Wafers were successively placed onto the headway. 2ml of SU8 2002 (MicroChem) was poured and spinned (first 500rpm for 10sec with 100rpm/s acceleration ; then 2000rpm for 30sec with 300rpm/sec acceleration ; Headway Research Inc. PWM32). Post spin bake of 1min at 95C was performed prior to 80mJ/cm^2 exposure with vaccum contact mode (Karl Suss MA6 mask aligner with i-line). Post exposure bake was 2min at 95C, followed by a brief development process in SU8 developer (30sec on shaker, 15sec on sonicator and 30sec on shaker). Wafer was rinsed with IPA and water. The first fenestration layer wafer was then hard baked at 180C for 30-45min.

We could then follow similar steps for the 2nd layer with tissue chamber and media channel features. After dehydrogenation, SU8 3050 (MicroChem) was spinned onto the wafers (first 500rpm for 10sec with 100rpm/s acceleration ; then 3000rpm for 30sec with 300rpm/sec acceleration). Post-spin bake was started at 30C and temperature was increased to 65C at a rate of 10C/min. Wafer were kept at 65C for 10min before ramping up the temperature to 95C at a rate of 5C/3min. Wafers were kept at 95C for 45min. After that, heat plate was turned off to let the wafer cool down slowly to room temperature. SU8 was wiped off the alignement marks with acetone, before putting the wafer on the mask aligner. Alignement marks enable the perfect overlay of the 2nd layer mask over the fenestration layer features. The 2nd layer was exposed at 160mJ/cm^2 with vaccum contact. Post exposure bake was the following : start at 30C, temperature was increased to 65C at 10C/min, kept at 65C for 2min before increasing again to 95C at 5C/3min. After 10min at 95C, heat plate was turned off and wafer allowed to cool down to room temperature. The development process was performed in SU8 developer. After the initial 5min in the shaker, wafer was transfered to fresh developer for 15min in sonicator and 15min in shaker. Wafer was rinsed with IPA and water. The final wafer was then hard baked at 180C for 30-45min.
The cardiac MPS is formed by replica molding from the silicon wafer with polydimethylsiloxane (PDMS; Sylgard 184 kit, Dow Chemical, Midland, MI) at a 10:1 ratio of Sylgard base to crosslinker. The PDMS chambers were punched at the defined inlet and outlets with a 0.75 μm surgical hole puncher before being bonded to glass slides using oxygen plasma (PETS inc. RIE system) with the following protocol: RF power 21W, 24sec, 100% oxygen flow. **Supp. Figure 2** shows illustration of the different steps described above.

3.5.2 Robust design experiments to identify the optimal combination of design changes of the tissue chamber

We hypothesized that changing the tissue chamber design could improve cell loading efficiency, tissue formation quality, and mechanical function of the cardiac muscle. We employed Robust Design[32] screening to optimize four different parameters, each with three levels. Given the likelihood of these variables acting in a synergistic fashion, the parametric space would require 3^4, or 81 independent experiments. To study this large space in a cost and time-effective manner within MPS, we could not use standard parametric analysis and therefore employed Robust Design screening. With orthogonal arrays, the variable-space spanned by these 81 independent experimental conditions was explored with only 9 independent experiments. These 9 experiments were designed such that the four parameters (length, width, extension, valve) and their respective three levels (800 μm / 1300 μm / 1800 μm; 170 μm / 130 μm / 90 μm; 150 μm / 230 μm/ 300 μm; valve design 1-3) were varied in an orthonormal fashion from one experiment to the next. Post

processing analysis was performed on JMP software for a Taguchi array L9 design of experiment, 4 parameters, 3 levels. The following parameters were used : larger is better, least square fit, effect screening. Graphs depicted the least square mean (y-axis) of each parameter and level (blue symbol for 1, green for 2 and red for 3) of the orthonormal analysis. Heatmaps showed the desirability value of the different combinations : we found the optimal combination and its associated desirability. From there, we changed the remaining parameters and levels one by one and reported their respective change in desirability. A value of 1 is the most desired combination. As a side note, as we decreased the width of the chamber, the fenestrations were proportionally longer to keep the same media channel fluidic profile.

3.5.3 Cell sourcing

Wild Type C (WTC) hiPSC were used in this study to derive the cardiomyocytes. The parent cell line (WTC) was reprogrammed from fibroblasts derived from a healthy 30-year-old Japanese male with a normal electrocardiogram and no known family history of heart disease (Coriell Repository # GM25256). The cell line harbors a single-copy of CAG-driven GCaMP6f knocked into the first Exon of the AAVS1 “safe harbor” locus[57]. GCaMP6f protein is composed of circularly permuted green fluorescent protein (cpGFP), calcium-binding protein calmodulin (CaM), and CaM-interacting M13 peptide. When calcium is present in the cytosol, it tiggers a conformational changes in CaM/M13 which subsequently increases the brightness of cpGFP[58]. This system enables us to easily measure calcium transient through GFP fluorescence recording. More detailed information can be found in Huebsch et al. [57].

3.5.4 Cardiomyocyte differentiation

hiPSC-CM were derived from pluripotent hiPSC through small molecular manipulation of Wnt signaling pathway. ‘Day-3’ of differentiation, hiPSC in culture were seeded on Matrigel-coated (Corning; Corning, NY) differentiation plates at 30-40,000 cells/cm2 in in mTeSR-1 (StemCell Technologies, Vancouver, Canada) containing 10 µM of the Rho kinase inhibitor (RI) Y27632-dihydrochloride (Peprotech; Rocky Hill, NJ). At day 0, when hiPSC were >90% confluent, differentiation was started following the protocol developed by Palecek et al. [52], which exposes the cells to 8 µM CHIR99021 (Peprotech) in Roswell Park Memorial Institute Medium 1640 (RPMI) containing B-27 supplement without insulin (RPMI-I). At day 1, media was switched to RPMI-I only. On day 2, cells were exposed to 5µM IWP-4 (Peprotech) in RPMI-I with 150 µg/mL L-ascorbic acid (LAA) for two days. On day 4, cells were given only RPMI-I. On day 6 onwards, RPMI containing standard B-27 supplement with insulin (RPMI-C) was added every second day. Spontaneous contractions were typically observed at day 7 or 8 of differentiation. At this point, cells

were washed three times with dPBS -Ca/Mg and left to soak for 10 minutes before being exposed to 0.25% Trypsin (Thermo Fisher) for 10 minutes at 37C. Singularized cells were rinsed once with RPMI-C and directly used for tissue-chip loading. A fraction of the harvested cells were run through flow cytometry with Cardiac Troponin T for cardiomyocyte purity characterization.
The first chamber design iteration had cardiomyocytes issued from an additional lactate purification step: At day 7 of differentiation, singularized cells were plated at a density of 100,000 cells/cm^2 onto Matrigel, in RPMI-C with 10 μM RI ('day 0' after replating). At day 1 after replating, medium was exchanged for RPMI-C. At day 3, cells were washed with dPBS and were exposed to RPMI 1640 (no glucose, no pyruvate, supplemented with 23mM sodium bicarbonate and 5 mM Sodium lacate[53]) for four to five days (exchanged every other day) to select for cardiomyocytes only. At day 8, cells were washed with dPBS and exposed to RPMI-C for two days to allow for recovery. At this point cardiomyocytes were used for loading of the first design iteration chips.

3.5.5 Self-assembly of cardiac microtissues within cardiac MPS

The singularized cardiomyocytes (as described in **Cardiomyocyte differentiation**) were resuspended in EB20 media supplemented with 10 μM Y27632, and 3 μL of the cell suspension, was injected into the cell loading port of each MPS. The densities were dependent on the number of cells required for the different MPS designs (see below). The loaded MPS were centrifugated in two steps at 300g for 3 minutes in both the horizontal and vertical orientation to help cells pellet inside the MPS and be pushed into the chamber. The loading tips were then plugged. Chambers that were not filled at this point were discarded. MPS were incubated at 37C for 1-2 hours before feeding media (EB20 media supplemented with 10 μM Y27632) was added to the media channel inlet of each MPS. The following day and every other day from then on, media was changed to our in-house 'maturation media' (**MM**) as described in [27]. MPS tissues were allowed to mature for 10 days before any subsequent experiments were performed.

3.5.6 Cell loading number calculations

For the second iteration of design changes, we used the hexagonal close pack (HCP) approximation to numerically calculate the number of cells required in the various tissue chamber designs (Run1-Run9). We calculated the volumen of each chamber design (height x width x length). The approximation assumed cells being spheres (as for singularized cells are used for loading), that fill 74% of the total volume, leaving 26% void [59]. To get an idea of the size of singularized cardiomyocytes used for loading, measured the diameter of singularized cells from in BF images on haemocytometer slide. To distinguish cells from debris, cells were stained with nucleoRed to highlight nuclei. The

distribution is shown in **Supp. Figure 1B**, and the average diameter was 21.7+/-14.7 µm. We could then simply calculate how many cells are theoretically needed to fill the tissue chamber volume based on a HCP for Run 1 to Run 9: 1,030; 790; 550; 1,680; 1,285; 890; 2,330; 1,780; 1,230. Three iterations were necessary to adjust to the optimal number of cells required experimentally to fill the chambers just past the two sets of pillars. The final values were the following for Run 1 to 9: 4,500; 5,000; 2,500; 9,000; 4,500; 5,000; 9,000; 9,000 and 5,000. Experimental values are significantly higher than theoretical values, simply because not all cells loaded end up in the cell chamber, some remain in the loading port.
For the third iteration of design changes (**Figure 7-8**), the width of the chamber was 130 µm and the lengths were 1000 µm, 1300 µm, 1550 µm and 1800 µm. The optimized number of cells loaded, was 3,000; 4,000; 6,000 and 8,000 for each length respectively. Fenestrations length was the same as for previous iteration with 130 µm.

3.5.7 Qualitative assessment of loading and tissue quality

Cell loading into the chamber is a critical step in the fabrication of the MPS and different metrics were used to evaluate the cell loading success for each design variation.
Chamber loading success: After MPS went through the two-step centrifugation for cell loading, only chambers that were completely filled with cells past the pillar sets were considered successfully loaded. All other chambers were discarded and counted as failed loading. This included chambers that were not filled completely past the second pillar set as well as chambers that featured any cell-free holes.
"No tail" success: Each chamber must contain just enough cells to fill the chamber past the two pillar sets. Excessive cell numbers or failure to concentrate the cells in the cell chamber can lead to a residual cell clump in the cell loading port and formation of an unwanted tissue strand ("tail") connecting the cells in the main chamber to this inlet clump. Such a "tail" will pull the chamber tissue towards the inlet upon each contraction, and the contraction force of the chamber tissue cannot be accurately measured. Additionally, cells in the inlet are not readily perfused with media and therefore their contraction is not relevant for pharmacology studies. We quantified the number of tissues per design with or without a "tail", and discarded "tail" tissues for subsequent analysis.
Tissue formation: 4 days after loading, a successful tissue was defined as a tissue filling the chamber past the two sets of pillars with no cell-free holes and "no tail" as well as spontaneous synchronized beating of the entire tissue.
Tissue quality scoring: Tissue quality was visually assessed on day 5 after loading by two independent individuals, giving a score from 1-10. 10/9.5 corresponded to a completely full chip (green, **Supp. Figure 1C**); 9 showed intact tissues but not completely filling the chamber (orange, **Supp. Figure 1C**); 8 had tissues not spanning all of the pillar array or showed condensed tissues in the width or the length; 7 and below showed only smaller

cell clumps (red, **Supp. Figure 1C**). Inter-design variance is an important metric to assess the reproducibility of tissue quality. We ran a power analysis (power of 0.9, α=0.05, effect size 1.8-2) based on control chip variance values to define a maximal variance acceptable (15%) for sample size of 5. Based on both the inter-design variance and the tissue quality, designs 4, 5, 6, 10 and 11 were excluded for subsequent analysis.

3.5.8 Preparation of Maturation Media (MM)

A base media was prepared from RPMI 1640 powder (Sigma, R1383-10X1L) and supplemented with 0.5 g/L D-glucose (Fisher, BP350-1), 10 mM D-galactose (Sigma, G5388) and 2 g/L sodium bicarbonate (Fisher, S233-500) . A 9% bovine serum albumin (BSA; Fisher, BP1605-100) solution was prepared in base media and adjusted to pH 7.4. Palmitic acid (PA; Sigma, P0500-10G; 100 mg/ml in DMSO) and oleic acid (OA ; Sigma, O1383-5G) were added to the 9% BSA solution at 10.23 ug/ml for PA and 0.8 mM OA. To dissolve the FA the solution was heated to 60C and sonicated for 3-5min. The final MM was prepared by mixing 1 part FA solution and 3 parts MM base media yielding a final concentration of 2.5575 μg/ml PA and 0.2 mM OA. Finally, the media was supplemented with 2% B27 (Gibco, 17504-044) and 150μg/ml ascorbic acid (Fisher, AC105021000) and sterile filtered.

3.5.9 Optical measurement of electrophysiology and tissue contraction

BeRST-1 voltage sensitive dye was synthesized, and purity verified, as previously described[60]. If action potential recordings were desired, MPS were labeled overnight with 500 nM BeRST-1 and equilibrated to media without dye before imaging. Before analysis MPS were placed onto a heated microscope stage (Tokai Hit, Gendoji-cho, Japan) for 20min to let them stabilize and kept at 37°C during imaging. Voltage fluorescence traces were recorded using a Red LED (640 nm excitation, 4x4 binning, 10 ms). Calcium fluorescence traces (GCaMP reporter) were recorded using a Cyan LED (470 nm excitation, 4x4 binning, 10 ms). The framerate for all fluorescence videos was 100 frames per second. Brightfield videos were acquired at 25 ms exposure (= 40 frames per second) without binning to capture pillar movement with the highest possible resolution. All videos had a length of 5 seconds. Acquisition was performed with a NIKON TE300HEM microscope equipped with a HAMAMATSU digital CMOS camera C11440 / ORCA-Flash 4.0 and Nikon NIS-Elements software. In addition to recording the spontaneous activity, some acquisitions were repeated for tissues paced at a defined beat rate. MPS were subjected to external electrical stimulation at 1 or 1.5 Hz (depending on the capturing frequency of different tissues) via stainless steel needles inserted in both the media inlet and outlet using an ION OPTIX Myopacer Field Simulator (20 V, 20 ms, biphasic). Pacing was initated 10s before starting and maintained during acquisition of another set of videos.

3.5.10 Pharmacology study in MPS

MPS were first equilibrated to maturation media (MM) containing vehicle control (DMSO for omecamtiv mesylate), to a final concentration of 0.1% v/v. On the day of pharmacology studies, freshly weighed drug was dissolved in MM for isoproterenol hydrochloride (TCI, I0260) and imatinib mesylate (Tocris Biotech, 5906) or DMSO for omecamtiv mercabil (Fisher Scientific, HY-14233) at a stock concentration of 10mM. Dose escalation studies were performed at concentrations around each drug's EC50 (2.3 μM omecamtiv[52], 30-600 nM imatinib[54-56], 1 μM isoproterenol [29, 38]). After recording activity in zero-dose vehicle condition, media was exchanged to the lowest drug dose, and MPS were incubated for 30 minutes at 37°C. Spontaneous and paced activity were recorded as described above. This was repeated for each increasing dose of a drug. Doses were escalated in 10-fold increments until all spontaneous and paced activity ceased, or the maximum dose (10x EC50) was reached. The following doses were used : omecamtiv 0, 0.1, 1, 10 μM, imatinib 0, 1, 10, 100, 1000, 10000 nM, isoproterenol 0, 1, 10, 100, 1000 nM.

3.5.11 Pacing frequencies experiment

We assessed whether different length tissues had a different response to increasing pacing frequency. Initial brightfield recordings were acquired of spontaneously beating tissues before tissues were paced at 0.5, 1, 1.5, 2 and 3 Hz. For each new frequency, the tissues were paced for 30sec before acquiring the videos to allow time to reach a new steady-state. Strain values were calculated and plotted for each design length.

3.5.12 Analysis of electrophysiology from fluorescence recordings

Fluorescence videos were analyzed using an in-house developed python library that performs automated background subtraction and normalization, and eliminates baseline drift due to bleaching by fitting a polynomial curve to the baseline via half-quadratic minimization[61]. The resulting traces were used for quantitative analysis of the action potential and calcium transient by calculating duration at 80% repolarization (APD_{80}) or peak amplitude.

3.5.13 Analysis of tissue mechanics from brightfield recordings

Motion Tracking: From the brightfield recordings, we can quantify tissue motion and deduce mechanical properties such as contraction. Using an in-house built block-matching algorithm similar to the one published by Huebsch et al. [57], we tracked 8 x 8 pixel block movement over time. In order to avoid discrete jumps, we applied a Gaussian filter –

giving us a smooth displacement field. We also filtered out all pixel blocks where no movement was detected.

Longitudinal motion: Adult healthy cardiac tissue show aligned sarcomeres and synchronized beating into a uniaxial direction. Here we promote cell alignment by confining the tissue into the MPS chamber in which cells will self-arrange into a uniaxially beating tissue[27]. Therefore, the longitudinal motion of the tissue is an important metric for design optimization. From the displacement, represented by motion vectors, we quantified the fraction of the motion aligned with a unit vector representing the longitudinal direction of the chamber. This was used to quantify the alignment properties of the tissues.

For the following mechanical metrics studied (strain, force, prevalence, longitudinal motion), the video was broken down into time intervals, defined by the pacing trigger (for paced videos) or by the max displacement difference (for spontaneous recordings). Over each interval (corresponding to one beat), we found an average trace for each respective metric. We calculated the peak values of each interval trace, and the average of all peak values was used to quantitatively assess the maximum strain, force of prevalence of each recording.

Tissue strain: In order to differentiate the tissue contraction versus rigid translation, the displacement was used to derive *strain*, quantifying the local deformation of the tissue as it contracts. From the displacement vectors, strain is derived as a tensor quantity: With $\mathrm{u}(\mathrm{x},\mathrm{y}) = \left(\mathrm{u_x}(\mathrm{x},\mathrm{y}), \mathrm{u_y}(\mathrm{x},\mathrm{y})\right)$ as a measured displacement at point (x,y), the *deformation tensor* **F** is given by

$$F = \nabla u + I = \begin{bmatrix} \frac{\partial u_x}{\partial x} + 1 & \frac{\partial u_x}{\partial y} \\ \frac{\partial u_y}{\partial x} & \frac{\partial u_y}{\partial y} + 1 \end{bmatrix}$$

From **F** we compute the Green-Lagrange strain tensor $\mathrm{E} = \frac{1}{2}(\mathrm{F^T F - I})$, defined locally in each point *(x,y)* – and in terms of our discrete algorithm, defined for each pixel, dependent on the values in neighboring pixel blocks. The largest eigenvalue of the strain tensor, in terms of magnitude, determines the principal strain – the strain in the direction of greatest deformation at any given point. The principal strain is a positive quantity (tensile strain) if the tissue is being locally stretched and negative if it is being compressed.

For each experiment we calculated the spatial average of strain for all time points. Then, using the pacing trigger as timepoint reference, we calculated the maximum strain value within each pacing interval (each beat). For each tissue we report the average of these peak values. We also report the difference in peak strain at day 7 versus day 14 for each tissue, as a proxy for mechanical maturation of the tissues.

Contraction force: Micro-molded PDMS pillars were added to the cell chambers not only as anchors that promote stable muscle fiber formation but also to serve as sensors for contraction force. At each beat the tissue would deflect the flexible pillars and the movement of the pillar tip could be non-invasively monitored using brightfield videos.

Considering each pillar as a cantilever beam fixed at one end and uniformly loaded with horizontal forces along its height, one can apply the Euler-Bernouilli formula for uniformly distributed load and deduce the contraction force from the pillar's elastic modulus, deflection and dimension [27]. We observed that the motion tracking software works well for whole tissue tracking, but when looking at single pillars, it sometimes underestimated the motion around the pillars. Therefore, each movie was given a manually adjusted scaling factor for displacement calculations in order to capture the pillar motion as accurately as possible. After that, for each video file, the initial position (frame 0) of the pillars was manually determined via ImageJ and used as input into a motion tracking script. The algorithm selected 200 random points within 20μm diameter circle of the pillar central position and tracked them over the time course of the video. The average values of the 200 points give a displacement trace per pillar over time. That trace was cut into multiple traces based on the beating intervals (as described above), from which the peak values were selected. The average of peak values corresponds to the max displacement for one pillar over the whole recording. From there, we calculated the maximum displacement of all pillars in a tissue and use the Euler Bernouilli formula (with pillar height of 55nm and modulus of $2.63*10^6$ Pa, **Figure 1, Supp. Figure 2**) to deduce the maximum contraction force for every tissue or the difference in force of each tissue at day 10 versus day 15, a proxy for mechanical maturation of the tissues.

Tissue prevalence: Beating prevalence was defined as the percentage of motion vectors within a region-of-interest (ROI) with a time-averaged contraction speed that exceeds a defined threshold (2 μm/sec was defined empirically as a universal threshold for all MPS analyzed). ROIs were selected within the moving tissue only. The max prevalence value per video (aka. per tissue) corresponds to the average of peak values for each time interval.

3.5.14 Mechanical and fluid dynamics modeling

COMSOL Multiphysics V5.4 was used to model both the tissue remodeling around fixed constraints and the fluid dynamics in the MPS system.

Tissue remodeling simulation: In this design we modelled the mechanical properties of the tissue when exposed to fixed constraints as two PDMS anchoring posts at the extremity of the device. The response of the tissue was modelled as linear elastic rubber and isotropic material shrinking around fixed constraints (anchors or pillars) for a lower stress conformation. The properties used for the tissue material were: elastic modulus of 5 kPa; density = 1050 kg/m^3; Poisson ratio = 0.46[62, 63]. The properties used for the PDMS fixed constraints were: E = $2.63 \cdot 10^3$ kPa; density = 970 kg/m^3; Poisson ratio = 0.495, permittivity of 2.75 and thermal conductivity of 0.16 [w/(m$\cdot$K)] for a 1:10 polymer : curing agent mix [42, 64].

Glucose diffusion modelling from the media channel to the tissue chamber: The media flow in the side channels was considered as laminar, newtonian, uniform and incompressible flow. The media physical properties were defined as being water: density of 1000 [kg/m^3], dynamic viscosity of 0.00069 [Pa · s]. No-slip conditions were applied to all walls and the initial conditions were the following: reference pressure of 1 [atm] and outlet pressure of 0 [atm]. The isotropic transport of diluted species such glucose was modelled across 2µm wide fenestrations. We used a diffusion coefficient of 10^{-9} [m^2/s] and an initial concentration of 0 [mol/m^3]. The inflow concentration in the media channel was set at 12 [mol/m^3] and the nutrient and oxygen uptake, also called the reaction rate in the chamber was of -0.00013 [M/s] (the negative sign indicating consumption and not generation).

3.5.15 Scanning electron microscope

PDMS pieces micropatterned with the fluidic structures were sputtered with gold/palladium (AuPd) for 60sec at 10mA to get a 10nm conductive layer at the surface (Cressington sputter coater 108 auto). Soon after, the sample was transfered to a scanning electron microscope (Quantum 3D FEG, Orion Nanofab). The following settings were used: 30µm aperture, 20 kV, 120 pA, 40 degree tilt, 1974 x magnification, 30 µs scan rate.

3.6 Statistics

All statistics were calculated using GraphPad Prism. All parametric analysis with more than 2 designs were analyzed with one way ANOVA and Dunnett's post-hoc correction with multiple comparison to control designs. If some values were missing, mixed-effects model was run. If two designs were compared, t-test with Welch's correction. For pharmacology studies, three parameter non linear fit was used for the curves. Significance between designs at a same drug dose was calculated with one-way ANOVA and Tuckey's multiple comparison. Significance was determined with p-value < 0.05.

3.7 Acknowledgements

All authors participated in the study design, analysis of the data, interpretation of the results and review of the manuscript. BC conducted the main experiments, performed the data analysis and COMSOL diffusion modeling, prepared the figures and caption and wrote the manuscript; AT wrote the mechanical methods and the script for mechanical analysis, performed data analysis and prepared figures. HF wrote the script for mechanical and electrophysiological analysis; VC helped with experiments, design optimization and tissue quality assessment; BS helped with cell culture and MPS loading; NL helped with MPS preparation and loading; SW advised on the mechanical analysis of brightfield

videos; EM provided BeRST-1; KEH wrote the manuscript and funded the work. This work was funded in part by the California Institute for Regenerative Medicine DISC2-10090 (K.E.H.), NIH-NHLBI HL130417 (K.E.H.), NIH-NIGMS R35GM1195855 (E.W.M.), NIH-NIGMS T32GM066698 (S.B.), the Research Council of Norway INTPART Project 249885, the SUURPh program funded by the Norwegian Ministry of Education and Research, the Jan Fandrianto and Selfia Halim Chair Fund (K.E.H.), Lloyd Award in Bioengineering for Excellent Research and Leadership (B.C.). We thank Bruce Conklin (Gladstone Institutes, San Francisco, USA) for technical advice on the WTC iPSC line. We thank Nathaniel Huebsch for his advising on the initial design iterations. We thank Nicholas Jeffreys for his help in initial chip fabrication. We thank the Marvel Nanofabrication laboratory (UC Berkeley) and their staff for assistance and technical advices for microfabrication procedures. We thank Mary West (UC Berkeley) for assistance with image analysis and flow cytometry. Kevin E. Healy, Sam Wall, Brian A. Siemons and Henrik Finsberg have a financial relationship with Organos Inc. and both they and the company may benefit from commercialization of the results of this research.

3.8 Figure legends

3.8.1 Figure 1. Anchoring posts and mechanosensing pillars in the cell chamber.

(**A**) Empty chamber with no anchors (top), corresponding to initial 2015 design[5] and new design with added anchoring post (bottom) for tissue support. (**B**) Cardiomyocyte loaded chip without (top) and with (bottom) anchor. Anchors act as support, preventing tissue condensing (top). (**C-D**) Computational simulation of a linear elastic material shrinking around fixed constraints. (**C, left**) Total displacement of the tissue around fixed rigid anchors towards lower stress (light blue) configuration. (**C, right**) Simulated longitudinal Von Mises Stress upon deformation of the tissue around fixed anchors. (**D, left**) Computational simulation of displacement and Von Mises stress (**D, right**) of a linear elastic material deforming around fixed constraints, with anchoring posts and pillars on one side. (**E**) SEM image of an empty chamber with magnified inset (bottom) on the fenestrations, anchoring posts and pillars. (**F**) Brigthfield images of a tissue at rest (top) and during contraction (bottom) with respective insets of magnified pillars. During contraction, pillars are deflecting as the tissue pulls on it. (**G**) Illustration of a mechanosensing pillar acting as a cantilever beam fixed at one end and deflecting upon contraction of the tissue. The deflection ($\boldsymbol{\delta_{max}}$ [m]) can be optically measured and the contraction force **F** [N]can be deduced using the Euler Bernoulli formula. (line pressure load **q** [N/m], the length of the beam **L** [m], Young's modulus **E** [N/m^2], second moment of area **I** [m^4], radius **R** [m]).

3.8.2 Figure 2. Pillar configuration changes.

(**A**) Illustration of various anchor and pillar configuration (top) and their representative fabricated chambers with tissue (bottom). Design 1 and 2 have anchoring posts whereas 3-11 only have different configuration of mechanosensing pillars (**B**) Double blinded tissue visual quality assessment of each design. Blue designs indicate an average score > 9 and an inter-design variance < 15%. Orange designs correspond to either score > 9 or variance <15% and red designs have both score < 9 and variance > 15%. (**C**) APD_{80} of the preselected designs 3, 7, 8, 9 compared to control design 2. The green band shows physiologically relevant APD_{80} values[38]. (**D**) Prevalence (tissue motion above 2μm/sec threshold) of selected designs. (**E**) Percent of tissue motion vector aligned in the longitudinal axis. *p<0.05, ** p<0.01.

3.8.3 Figure 3. Fenestration height changes.

(A) Time dependent computational modeling of glucose diffusion from media channel (dak red) to the cell chamber with different fenestration heights (top to bottom: 1.5 μm, 2 μm, 5 μm, 6.5 μm). (**B**) Concentration curve of glucose over time at a point in the middle of the cell chamber in different fenestration heights. (**C**) Experimental outcome of cell loading in the varrrying fenestration designs. The higher the fenestrations, the more cells would escape from the chamber to the media channels. (**D**) Brightfield images of cells in the tissue chamber, contained in 1.5 μm fenestration height (SEM image, lower inset) or escaping through 2 μm (middle, representing worst case senario) and 6.5 μm (rightm representing average case).

3.8.4 Figure 4. Chamber dimension and inlet valve changes.

(**A**) Illustration of the four parameters (length, width, extension, valve) that were studied for optimization of tissue mechanics. Each parameter had three levels, distances or valve types. (**B**) Table representing the 9 orthonormal combinations, as defined by Robust Design, equally distributing each level of the four parameters. Those 9 chamber designs (each row) were fabricated, loaded with cardiomyocytes and tissues were subsequently analyzed. (**C**) Brigthfield images of the loaded chambers. Design 4- 9 had longer chambers that did not fit within the 20x field of view, therefore only half the chamber was shown.

3.8.5 Figure 5. Qualitative assessment of design performances.

(**A, B, C, left**) Graphs depicting the mean of each parameter (x-axis) and level (blue symbol for 1, green for 2 and red for 3) of the orthonormal analysis. (**A, B, C, right**) Heatmaps showing the desirability value of the different combinations. A value of 1 is the most desired combination. (**A**) Graph and heatmap for qualitative assessment of loading efficiency in the different designs. Designs that did not have cells in the entire chamber past

the two sets of pillars were discarded from other analysis; however, they were counted as failed loading. (**B**) Qualitative assessment of tissue formation efficiency, typically assessed by two independent users 5 days after loading. (**C**) Graph and heatmap of the efficiency of each design to successfully separate the cell chamber tissue from the remaining cells in the inlet ("no tail"), to have an independently beading tissue in the cell chamber. The following analysis parameters were used: larger is better, least square fit, effect screening.

3.8.6 Figure 6. Quantitative assessment of tissue mechanics within different designs.

(**A, B, left and C, D**) Graphs depicting the mean of each parameter (x-axis) and level (blue symbol for 1, green for 2 and red for 3) of the orthonormal analysis. (**A, B, right**) Heatmaps showing the desirability value of the different combinations. A value of 1 is the most desired combination. (**A**) Quantitative assessment of fraction of motion vector in the longitudinal axis. (**B**) Graphs and heatmap of maximal compressive strain (comparable to deformation) measured in the tissues. (**C**) Maximal contraction force measured through deflection of mechanosensing pillars. (**D**) Values describing the difference between maximum force at day 10 and maximum force at day 15 for the different designs. This is a proxy for mechanical maturation of the tissues. For both (**C**) and (**D**), there were not sufficient replicates to calculate the desirability heatmap. The following analysis parameters were used: larger is better, least square fit, effect screening.

3.8.7 Figure 7. Parametric design changes, qualitative and quantitative analysis.

Graphs showing the loading success across different length (**A**) or valves (**C**). Qualitative tissue assessment for different length (**B**) or valves (**D**). (**E**) Maximum compressive strain across different lengths. (**F**) Difference in average tissue strain from day 15 to day 7, a proxy for mechanical maturation of the tissues across different lengths. (**G**) Peak calcium values (normalized to background) across different lengths. (**H**) Fraction of motion vectors in the longitudinal direction for varying lengths. (**I**) Normalized maximum compressive strain across different lengths for increasing frequencies (1, 1.5, 2, 3Hz). (**J**) Normalized peak calcium amplitude for increasing frequencies in varying lengths. * p<0.05, **P<0.01, ***P<0.001, ****P<0.0001.

3.8.8 Figure 8. Pharmacology study and final optimal design

(**A**) Exposure of tissues to increasing doses of isoproterenol, and subsequent measurement of the peak strain to peak calcium ratio for different lengths. (**B**) Normalized

strain to calcium ratio of tissues exposed to dose escalation of omecamtiv mesylate across lengths. (**C**) Graph showing the change in normalized strain to calcium ratio during acute exposure to imatinib for varying lengths. (**D**) CAD drawing of the optimal design, showing 130 µm width, 230 µm extension, 1550 µm length and no valve. (**E**) 3D rendering of the optimal design at the inlet (top) and outlet (bottom). (**F**) Brightfield image of a tissue loaded in the optimal design. One can observe the pillar arrangement in the tissue chamber and fenestrations around the chamber. *p<0.05 with one-way ANOVA.

3.9 Supplemental figure legends

3.9.1 Supplemental Figure 1.

(**A**) Contraction force measurements on pillars located at the extremity of the tissue versus the center of the chamber, ****p<0.001. (**B**) Frequency distribution histogram for the size of singularized cardiomyocytes from a 2D culture plate before loading them into the cardiac MPS. Mean = 21.7 +/- 15 µm. (**C**) Example images of double blinded tissue quality assessment. Green corresponding to a score of 10 (left) shows a tissue fully filling the cell chamber, as opposed to a score of 8 (middle) where the tissue only fills 60% of the chamber and score of 2 where most of the chamber is empty and the cells do not form one beating tissue. (**D**) Surface plot showing the change in force (z-axis) required for a fixed deflection of 4 µm and Youngs' modulus of 2.2MPa (for 1:10 crosslinker to PDMS polymer ratio) and its dependency on the pillars' radius (y-axis) and length (x-axis).

3.9.2 Supplemental Figure 2. Microfabrication description.

Illustration depicting the main steps performed for microchip fabrication. Left to right: spin coating of photoresist onto silicon wafer, UV exposure of photoresist through a mask with design features, develop non polymerized photoresist and pour soft polydimethylsiloxane (PDMS) onto the master mold, after overnight baking, PDMS with design features can be peeled of the wafer and bonded to glass through oxygen plasma, giving us the final system in which cells will be loaded.

3.10 References

1. Heper, M. *The Cost Of Creating A New Drug Now $5 Billion, Pushing Big Pharma To Change*. 2013; Available from: http://www.forbes.com/sites/matthewherper/2013/08/11/how-the-staggering-cost-of-inventing-new-drugs-is-shaping-the-future-of-medicine/.
2. J. A. Dimasi, R.W.H., and H. G. Grabowski, *The price of innovation : new estimates of drug development costs.* J Health Econ, 2003. **22**: p. 151-185.
3. S. Morgan, P.G., J. Lexchin, C. Cunningham, and D. Greyson, *The cost of drug development : A systematic review*. 2011, Health Policy (New. York). p. 4-17.
4. Paul, S.M., *How to improve R&D productivity: the pharmaceutical industry's grand challenge.* Nat. Rev. Drug Discov., 2010: p. 203-214.
5. Mathur, A., et al., *Human iPSC-based cardiac microphysiological system for drug screening applications.* Sci Rep, 2015. **5**: p. 8883.
6. Administration, F.a.D. *FDA Issues Advice to Make Earliest Stages Of Clinical Drug Development More Efficient*. 2006; Available from: http://www.fda.gov/NewsEvents/Newsroom/PressAnnouncements/2006/ucm108576.htm.
7. Jungho Ahn, J.K., Somin Lee, James Yu, YongTae Kim, Noo Li Jeon, *Microfluidics in nanoparticle drug delivery; From synthesis to pre-clinical screening* Adv Drug Deliv Rev, 2018: p. 29-53.
8. K. Takahashi, S.Y., *Induction of Pluripotent Stem Cells from Mouse Embryonic and Adult Fibroblast Cultures by Defined Factors.* Cell, 2006. **2**: p. 663-676.
9. Ma, Z., et al., *Contractile deficits in engineered cardiac microtissues as a result of MYBPC3 deficiency and mechanical overload.* Nat Biomed Eng, 2018. **2**(12): p. 955-967.
10. Ma, Z., et al., *Three-dimensional filamentous human diseased cardiac tissue model.* Biomaterials, 2014. **35**(5): p. 1367-77.
11. Dunn, K.K. and S.P. Palecek, *Engineering Scalable Manufacturing of High-Quality Stem Cell-Derived Cardiomyocytes for Cardiac Tissue Repair.* Front Med (Lausanne), 2018. **5**: p. 110.
12. Laflamme, M.A. and C.E. Murry, *Heart regeneration.* Nature, 2011. **473**(7347): p. 326-35.
13. Ogle, B.M., et al., *Distilling complexity to advance cardiac tissue engineering.* Science Translational Medicine, 2016. **8**(342).
14. Vunjak Novakovic, G., T. Eschenhagen, and C. Mummery, *Myocardial tissue engineering: in vitro models.* Cold Spring Harb Perspect Med, 2014. **4**(3).
15. Robertson, C., D.D. Tran, and S.C. George, *Concise review: maturation phases of human pluripotent stem cell-derived cardiomyocytes.* Stem Cells, 2013. **31**(5): p. 829-37.
16. Shadrin, I.Y., et al., *Cardiopatch platform enables maturation and scale-up of human pluripotent stem cell-derived engineered heart tissues.* Nature Communications, 2017. **8**(1).
17. Huebsch, N., et al., *Miniaturized iPS-Cell-Derived Cardiac Muscles for Physiologically Relevant Drug Response Analyses.* Scientific Reports, 2016. **6**(November 2015): p. 1-12.

18. Mannhardt, I., et al., *Human Engineered Heart Tissue: Analysis of Contractile Force.* Stem Cell Reports, 2016. **7**(1): p. 29-42.
19. Godier-Furnémont, A.F.G., et al., *Physiologic force-frequency response in engineered heart muscle by electromechanical stimulation.* Biomaterials, 2015. **60**: p. 82-91.
20. Hinson, J.T., et al., *Titin mutations in iPS cells define sarcomere insufficiency as a cause of dilated cardiomyopathy.* Science, 2015. **349**(6251): p. 982-986.
21. Zhang, D., et al., *Tissue-engineered cardiac patch for advanced functional maturation of human ESC-derived cardiomyocytes.* Biomaterials, 2013. **34**(23): p. 5813-5820.
22. Nunes, S.S., et al., *Biowire: A platform for maturation of human pluripotent stem cell-derived cardiomyocytes.* Nature Methods, 2013. **10**(8): p. 781-787.
23. Tulloch, N.L., et al., *Growth of engineered human myocardium with mechanical loading and vascular coculture.* Circulation Research, 2011. **109**(1): p. 47-59.
24. Tiburcy, M., et al., *Terminal differentiation, advanced organotypic maturation, and modeling of hypertrophic growth in engineered heart tissue.* Circulation Research, 2011. **109**(10): p. 1105-1114.
25. Zimmermann, W.H., et al., *Tissue Engineering of a Differentiated Cardiac Muscle Construct.* Circulation Research, 2002. **90**(2): p. 223-230.
26. Mathur, A., et al., *Human iPSC-based cardiac microphysiological system for drug screening applications.* Scientific Reports, 2015. **5**.
27. Huebsch, N., et al., *Metabolically-Driven Maturation of hiPSC-Cell Derived Heart-on-a-Chip*. 2020, Cold Spring Harbor Laboratory.
28. Mills, R.J., et al., *Functional screening in human cardiac organoids reveals a metabolic mechanism for cardiomyocyte cell cycle arrest.* Proc Natl Acad Sci U S A, 2017. **114**(40): p. E8372-E8381.
29. Ronaldson-Bouchard, K., et al., *Advanced maturation of human cardiac tissue grown from pluripotent stem cells.* Nature, 2018. **556**(7700): p. 239-243.
30. Shadrin, I.Y., et al., *Cardiopatch platform enables maturation and scale-up of human pluripotent stem cell-derived engineered heart tissues.* Nat Commun, 2017. **8**(1): p. 1825.
31. Kenichi Arai, D.M., Shoko Takao, Anna Nakamura, Manabu Itoh, Takahiro Kitsuka, Koichi Nakayama *Drug response analysis for scaffold-free cardiac constructs fabricated using bio-3D printer.* Scientific Reports, 2020.
32. Taguchi, G. and M.S. Phadke, *Quality Engineering through Design Optimization*, in *Quality Control, Robust Design, and the Taguchi Method*, K. Dehnad, Editor. 1989, Springer US: Boston, MA. p. 77-96.
33. N. J. Sniadecki, C.S.C., *Microfabricated Silicone Elastomeric Post Arrays for Measuring Traction Forces of Adherent Cells.* Methods Cell Biol., 2007. **83**: p. 313-328.
34. M. L. Rodriguez, B.T.G., L. M. Pabon, S. J. Han, C. E. Murry, and N. J. Sniadecki, *Measuring the contractile forces of human induced pluripotent stem cell-derived cardiomyocytes with arrays of microposts.* J. Biomech. Eng., 2014. **136**.

35. Thavandiran, N., et al., *Design and formulation of functional pluripotent stem cell-derived cardiac microtissues.* Proceedings of the National Academy of Sciences, 2013. **110**(49): p. E4698-E4707.
36. Tiburcy, M., et al., *Defined Engineered Human Myocardium With Advanced Maturation for Applications in Heart Failure Modeling and Repair.* Circulation, 2017. **135**(19): p. 1832-1847.
37. Klammer, I.B., A.; Dura, G.; Mokwa, W.; Schnakenberg, *A novel valve for microfluidic PDMS-based systems.* 2008 IEEE 21st International Conference on Micro Electro Mechanical Systems, 2008.
38. Brandenburger, M., et al., *Organotypic slice culture from human adult ventricular myocardium.* Cardiovasc Res, 2012. **93**(1): p. 50-9.
39. Y.Wanga, S.S., S.M.Swartzc, N.C.Goulbournea, *A mixed Von Mises distribution for modeling soft biological tissues with two distributed fiber properties.* International Journal of Solids and Structures, 2012.
40. Paul M. L. Janssen, S.E.L., Jurgen Prestle and Gerd Hasenfuss, *Preservation of Contractile Characteristics of Human Myocardium in Multi-day Cell Culture.* J Mol Cell Cardiol, 1999.
41. J. van der Velden, L.J.K., M. van der Bijl, J. Witkop, L. Eijsman, C.A. Visser, M.A.J.M. Huybregts, F.C. Visser, W. Stooker, G.J.M. Stienen *Force production in mechanically isolated cardiac myocytes from human ventricular muscle tissue.* Cardiovascular Research 1999.
42. B. L.-M. Angel S. Cruz Félix, A.S.-A., Fernando Iturbide-Jiménez, *Physical-chemical properties of PDMS samples used in tunable lenses.* International Journal of Engineering Science and Innovative Technology, 2014. **3**(2).
43. Xiaojing Su, A.B.T., Craig T. January, David J. Beebe, *Effect of microculture on cell metabolism and biochemistry: Do cells get stressed in microchannels?* Anal Chem, 2013. **85**(3): p. 1562–1570.
44. Po-Ling Kuo, H.L., Mark-Anthony Bray, Nicholas A. Geisse, Yen-Tsung Huang, William J. Adams, Sean P. Sheehy, Kevin K. Parker, *Myocyte Shape Regulates Lateral Registry of Sarcomeres and Contractility.* Am J Pathol, 2012.
45. Judith K. Gwathmey, R.J.H., *Relation Between Steady-State Force and Intracellular [Ca2+] in Intact Human Myocardium.* american heart association, 1990.
46. Rob F Wiegerinck, A.C., Carlo M Zeidenweber, Guoliang Ding, Ming Shen, Ronald W Joyner, Janet D Fernandez, Kirk R Kanter, Paul M Kirshbom, Brian E Kogon, Mary B Wagner *Force Frequency Relationship of the Human Ventricle Increases During Early Postnatal Development.* Pediatric research, 2009.
47. Matsa, E., Burridge, P. W. & Wu, J. C, *Human stem cells for modeling heart disease and for drug discovery.* Sci. Transl. Med, 2014.
48. Feric N. T., R.M., *Maturing human pluripotent stem cell-derived cardiomyocytes in human engineered cardiac tissues.* Adv. Drug Deliv. Rev. , 2016.
49. Nunes, S.S., et al., *Biowire: a platform for maturation of human pluripotent stem cell-derived cardiomyocytes.* Nat Methods, 2013. **10**(8): p. 781-7.
50. Mannhardt, I.e.a., *Human engineered heart tissue: analysis of contractile force.* Stem Cell Reports, 2016.

51. Y Tatsukawa , M.A., T Kiyosue, Y Mikuriya, M Nasu, *A comparative study of effects of isoproterenol and dihydroouabain on calcium transients and contraction in cultured rat ventricular cells.* J Mol Cell Cardiol, 1993.
52. Fady I. Malik, J.J.H., Kathleen A. Elias, Bradley P. Morgan, Hector Rodriguez, Katjuša Brejc, Robert L. Anderson, Sandra H. Sueoka, Kenneth H. Lee, Jeffrey T. Finer, Roman Sakowicz, Ramesh Baliga, David R. Cox, Marc Garard, Guillermo Godinez, Raja Kawas, Erica Kraynack, David Lenzi, Pu Ping Lu, Alexander Muci, Congrong Niu, Xiangping Qian, Daniel W. Pierce, Maria Pokrovskii, Ion Suehiro, Sheila Sylvester, Todd Tochimoto, Corey Valdez, Wenyue Wang, Tatsuo Katori, David A. Kass, You-Tang Shen, Stephen F. Vatner, David J. Morgans, *Cardiac Myosin Activation: A Potential Therapeutic Approach for Systolic Heart Failure.* Science magazine, 2011. **331**.
53. al., K.R.e., *The cancer drug imatinib can cause cardiotoxicity.* Nature Clinical Practice Cardiovascular Medicine 2006.
54. Selleckchem.com. *Imatinib (STI571)*. Available from: https://www.selleckchem.com/products/Imatinib(STI571).html.
55. biotech, T. *Imatinib mesylate*. Available from: https://www.tocris.com/products/imatinib-mesylate_5906.
56. Philippe ROUSSELOT, V.H. *IMATINIB IN COVID-19 DISEASE IN AGED PATIENTS*. 2020; Available from: https://clinicaltrials.gov/ct2/show/NCT04357613.
57. Huebsch, N., et al., *Automated Video-Based Analysis of Contractility and Calcium Flux in Human-Induced Pluripotent Stem Cell-Derived Cardiomyocytes Cultured over Different Spatial Scales.* Tissue Engineering Part C: Methods, 2015. **21**(5): p. 467-479.
58. Tsai-Wen Chen, T.J.W., Yi Sun, Stefan R. Pulver, Sabine L. Renninger, Amy Baohan, Eric R. Schreiter, Rex A. Kerr, Michael B. Orger, Vivek Jayaraman, Loren L. Looger, Karel Svoboda, Douglas S. Kim *Ultrasensitive fluorescent proteins for imaging neuronal activity.* Nature, 2013: p. 295-300.
59. R. Bjørk, V.T., H.L. Frandsena, N. Pryds, *The sintering behavior of close-packed spheres.* Science direct, 2012. **67**: p. 81-84.
60. Huang, Y.L., A.S. Walker, and E.W. Miller, *A Photostable Silicon Rhodamine Platform for Optical Voltage Sensing.* Journal of the American Chemical Society, 2015. **137**(33): p. 10767-10776.
61. Vincent Mazet, C.C., DavidBrie, Jérôme Idier, Bernard Humbert, *Background removal from spectra by designing and minimising a non-quadratic cost function.* Chemometrics and Intelligent Laboratory Systems, 2005. **76**(2): p. 121-133.
62. Cristina Pislaru, M.W.U., Sorin V. Pislaru, Randall R. Kinnick, and James F. Greenleaf, *VISCOELASTIC PROPERTIES OF NORMAL AND INFARCTED MYOCARDIUM MEASURED BY A MULTIFREQUENCY SHEAR WAVE METHOD: COMPARISON WITH PRESSURE-SEGMENT LENGTH METHOD.* Ultrasound med biology, 2014.
63. Duck, F.A., *Physical Properties of Tissues: A Comprehensive Reference Book*. 1990: Academic Press

64. Wang, Z., *Polydimethylsiloxane Mechanical Properties Measured by Macroscopic Compression and Nanoindentation Techniques*. 2011, University of South Florida.

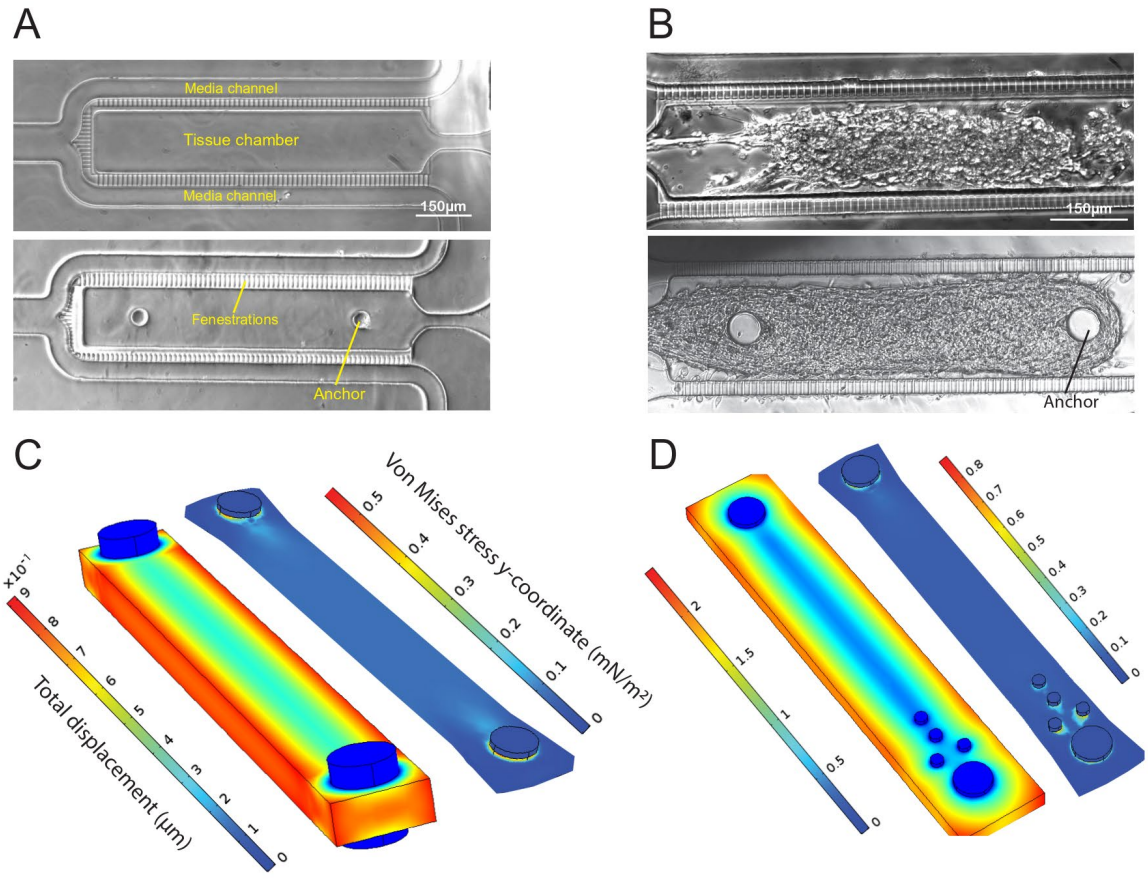
A
Media channel
Tissue chamber
Media channel
150µm
Fenestrations
Anchor
B
150µm
Anchor
C
Von Mises stress y-coordinate (mN/m²)
0.5
0.4
0.3
0.2
0.1
0
x10⁻¹
Total displacement (µm)
9
8
7
6
5
4
3
2
1
0
D
0.8
0.7
0.6
0.5
0.4
0.3
0.2
0.1
0
2
1.5
1
0.5
0
E
Fenestration
Anchor
Pillar
150µm
50µm
F
100µm
Rest
Contraction
G
δmax
q
L
E (Elastic modulus)
R
F = qL = $\frac{8EI\delta_{max}}{L^3}$
with $\delta_{max} = \frac{qL^4}{8EI}$
And $I = \frac{1}{4}\pi R^4$

Figure 1

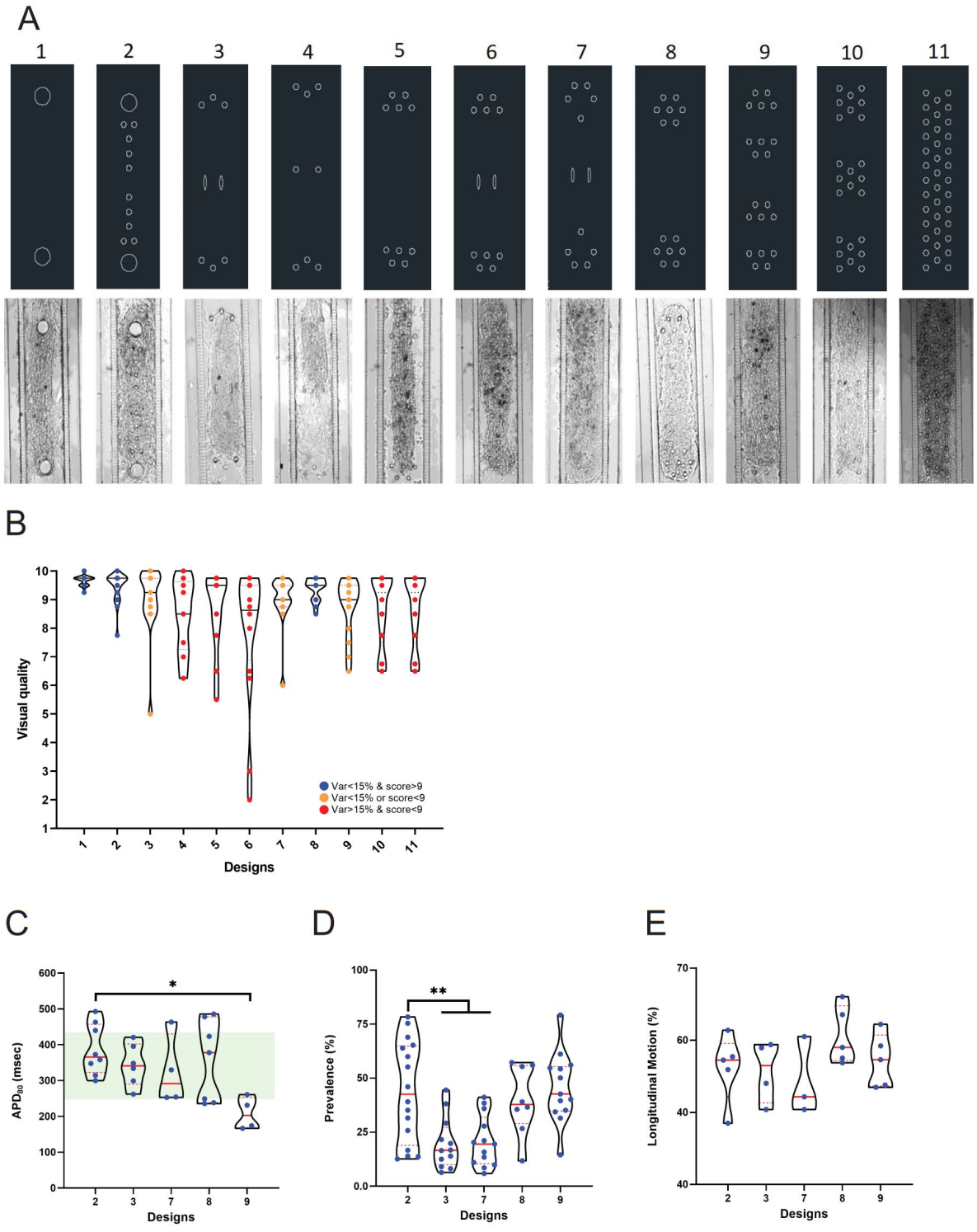
A
1
2
3
4
5
6
7
8
9
10
11
B
Visual quality
Designs
Var<15% & score>9
Var<15% or score<9
Var>15% & score<9
C
APD80 (msec)
Designs
*
D
Prevalence (%)
Designs
**
E
Longitudinal Motion (%)
Designs

Figure 2

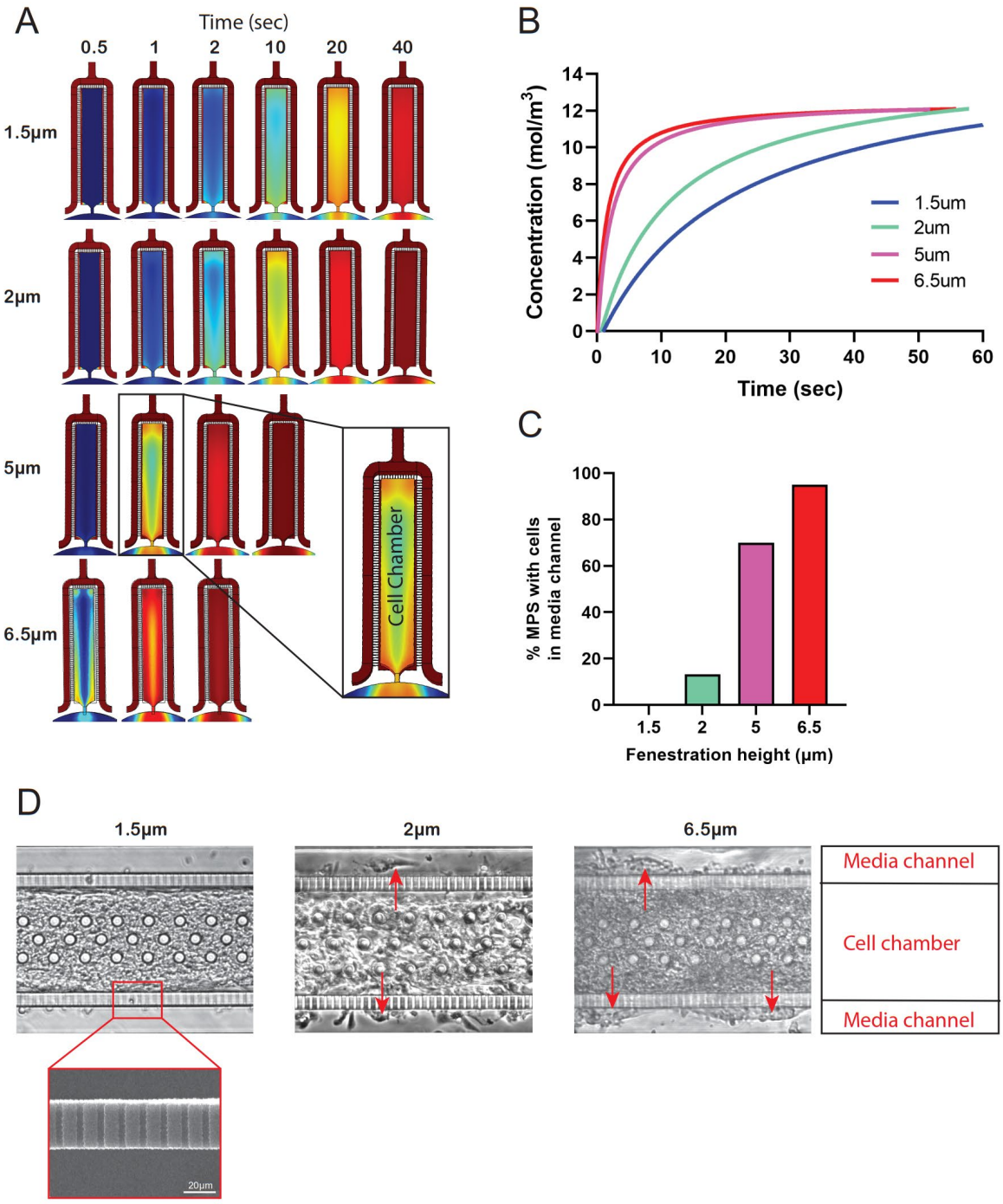
A
Time (sec)
0.5
1
2
10
20
40
1.5µm
2µm
5µm
6.5µm
Cell Chamber
B
Concentration (mol/m3)
Time (sec)
1.5um
2um
5um
6.5um
C
% MPS with cells in media channel
Fenestration height (µm)
D
1.5µm
2µm
6.5µm
20µm
Media channel
Cell chamber
Media channel

Figure 3

A

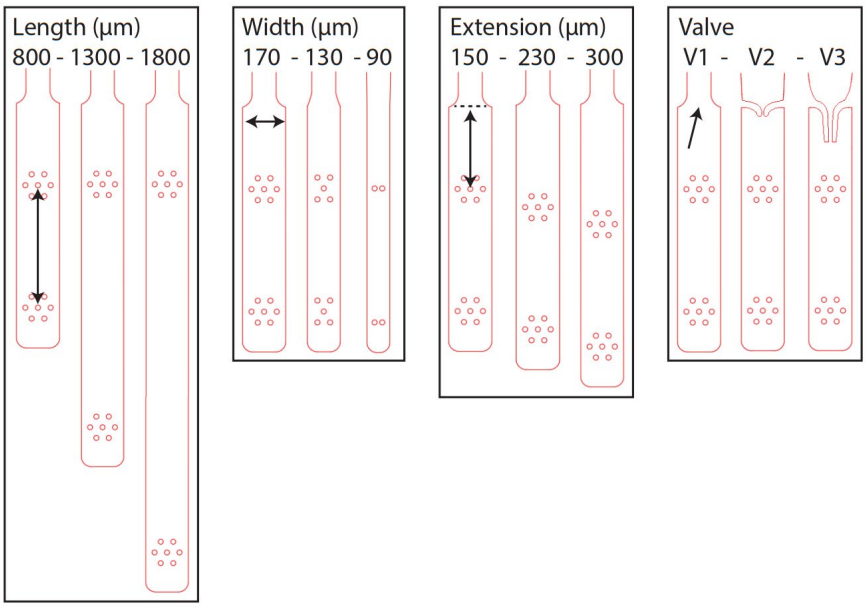

B

Run #	Length (800-1800µm)	Width (170-90µm)	Extension (150-300µm)	Valve (design 1-3)
1	800	170	150	1
2	800	130	230	2
3	800	90	300	3
4	1300	170	230	3
5	1300	130	300	1
6	1300	90	150	2
7	1800	170	300	2
8	1800	130	150	3
9	1800	90	230	1

C

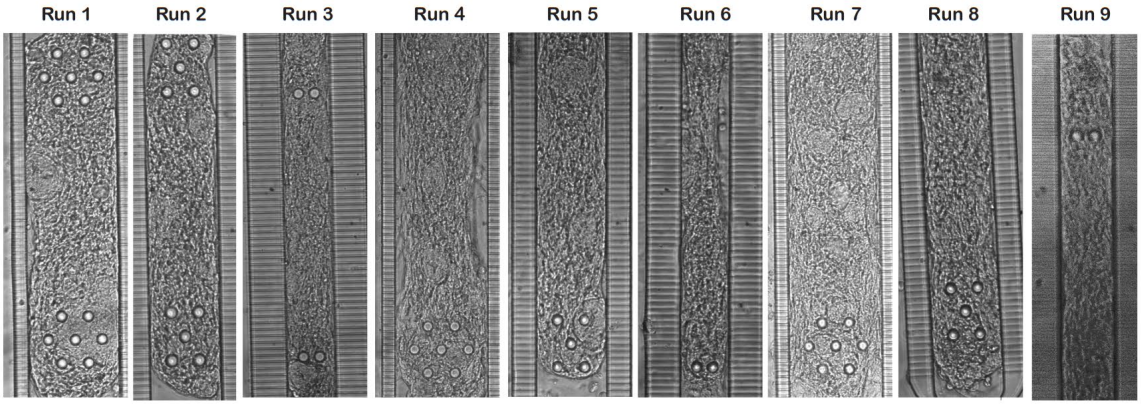

Figure 4

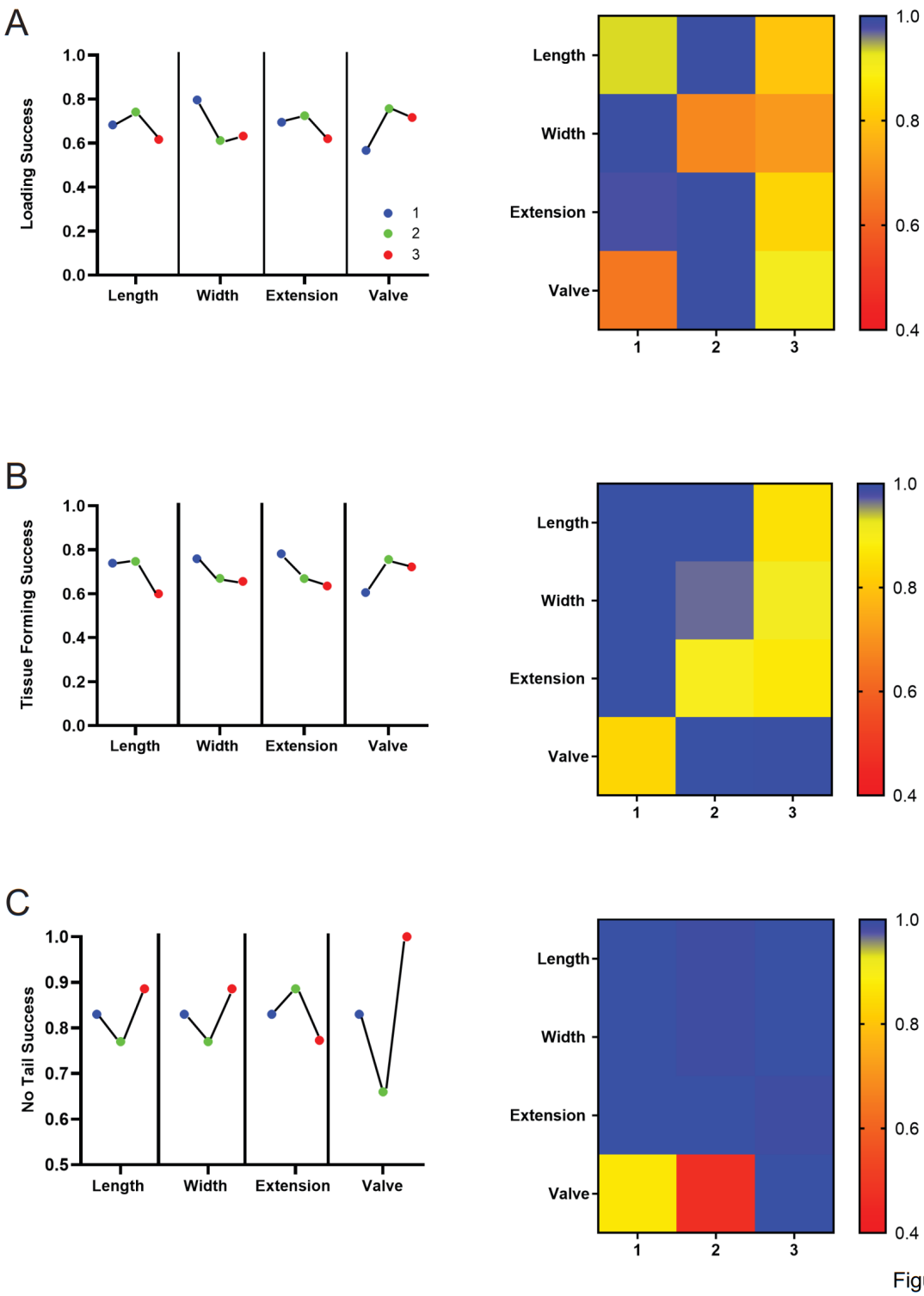
A
Loading Success
1.0
0.8
0.6
0.4
0.2
0.0
Length
Width
Extension
Valve
1
2
3
Length
Width
Extension
Valve
1
2
3
1.0
0.8
0.6
0.4
B
Tissue Forming Success
1.0
0.8
0.6
0.4
0.2
0.0
Length
Width
Extension
Valve
Length
Width
Extension
Valve
1
2
3
1.0
0.8
0.6
0.4
C
No Tail Success
1.0
0.9
0.8
0.7
0.6
0.5
Length
Width
Extension
Valve
Length
Width
Extension
Valve
1
2
3
1.0
0.8
0.6
0.4

Figure 5

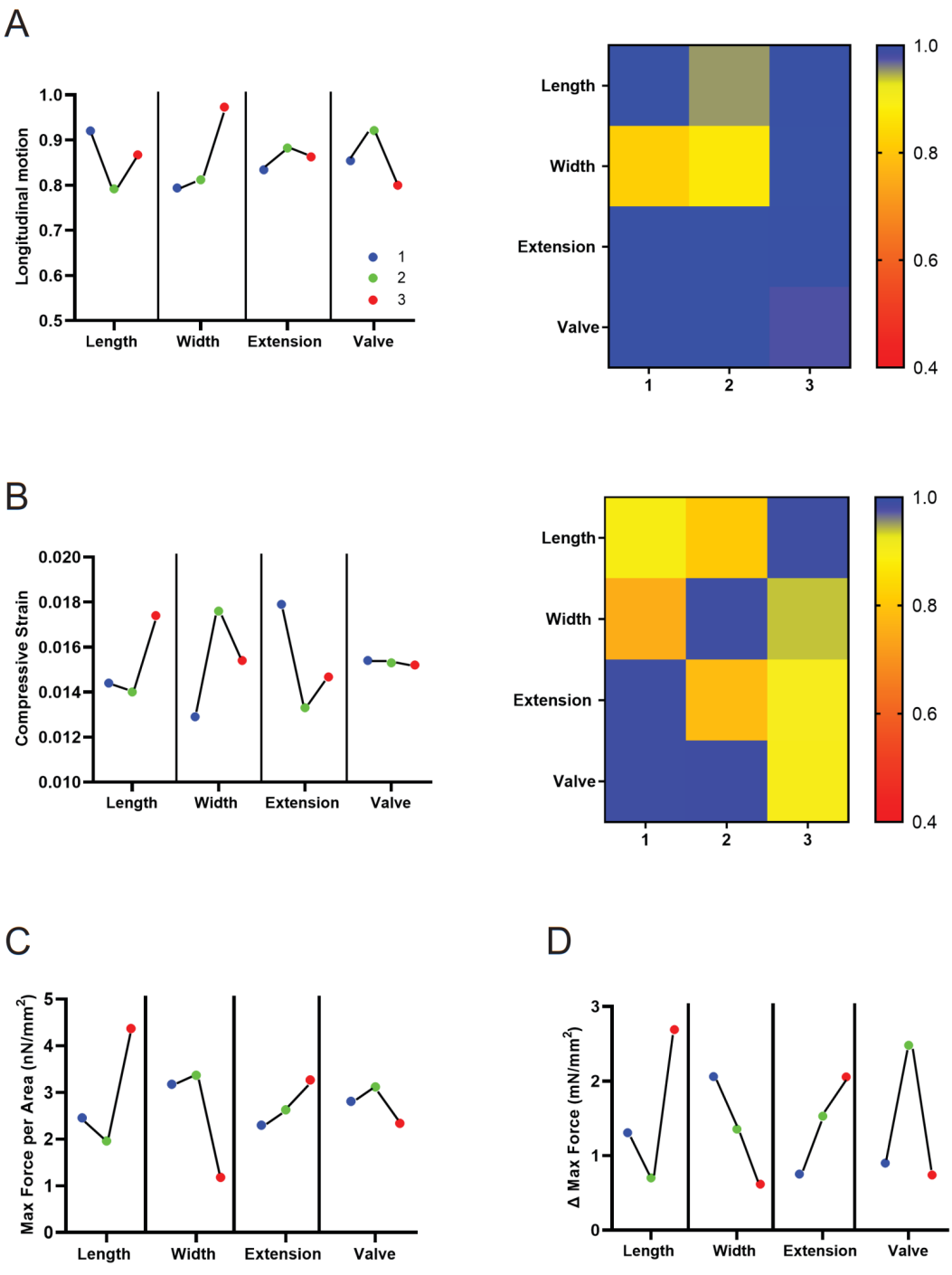
A
Longitudinal motion
1.0
0.9
0.8
0.7
0.6
0.5
Length
Width
Extension
Valve
1
2
3
Length
Width
Extension
Valve
1
2
3
1.0
0.8
0.6
0.4
B
Compressive Strain
0.020
0.018
0.016
0.014
0.012
0.010
Length
Width
Extension
Valve
Length
Width
Extension
Valve
1
2
3
1.0
0.8
0.6
0.4
C
Max Force per Area (nN/mm²)
5
4
3
2
1
0
Length
Width
Extension
Valve
D
Δ Max Force (mN/mm²)
3
2
1
0
Length
Width
Extension
Valve

Figure 6

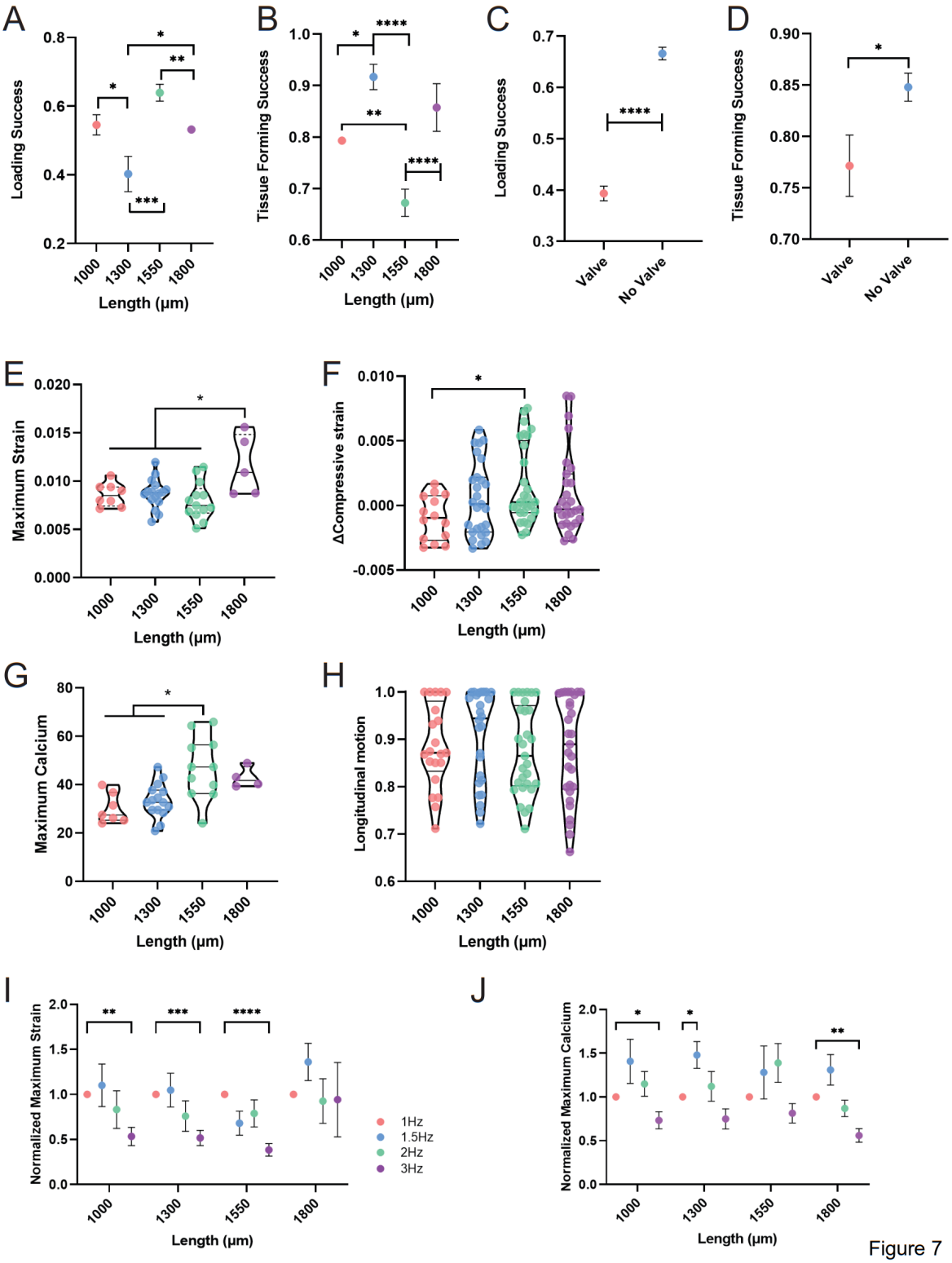
A
Loading Success
0.8
0.6
0.4
0.2
*
**
*
***
1000
1300
1550
1800
Length (µm)
B
Tissue Forming Success
1.0
0.9
0.8
0.7
0.6
*
****
**
****
1000
1300
1550
1800
Length (µm)
C
Loading Success
0.7
0.6
0.5
0.4
0.3
****
Valve
No Valve
D
Tissue Forming Success
0.90
0.85
0.80
0.75
0.70
*
Valve
No Valve
E
Maximum Strain
0.020
0.015
0.010
0.005
0.000
*
1000
1300
1550
1800
Length (µm)
F
ΔCompressive strain
0.010
0.005
0.000
-0.005
*
1000
1300
1550
1800
Length (µm)
G
Maximum Calcium
80
60
40
20
0
*
1000
1300
1550
1800
Length (µm)
H
Longitudinal motion
1.0
0.9
0.8
0.7
0.6
1000
1300
1550
1800
Length (µm)
I
Normalized Maximum Strain
2.0
1.5
1.0
0.5
0.0
**
***
****
1000
1300
1550
1800
Length (µm)
1Hz
1.5Hz
2Hz
3Hz
J
Normalized Maximum Calcium
2.0
1.5
1.0
0.5
0.0
*
*
**
1000
1300
1550
1800
Length (µm)

Figure 7

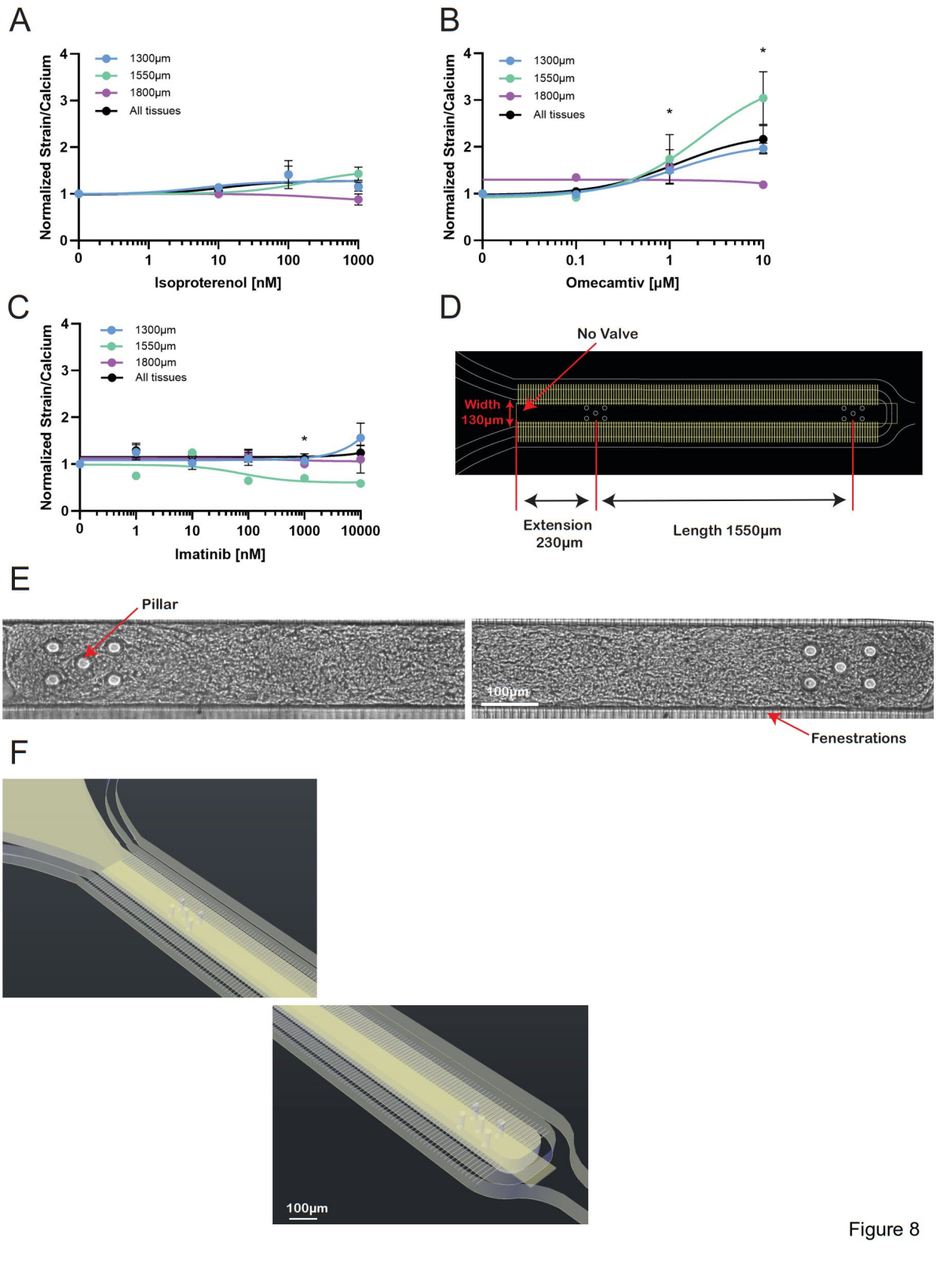
A
Normalized Strain/Calcium
1300µm
1550µm
1800µm
All tissues
Isoproterenol [nM]
B
Omecamtiv [µM]
C
Imatinib [nM]
D
No Valve
Width
130µm
Extension
230µm
Length 1550µm
E
Pillar
100µm
Fenestrations
F
100µm

Figure 8

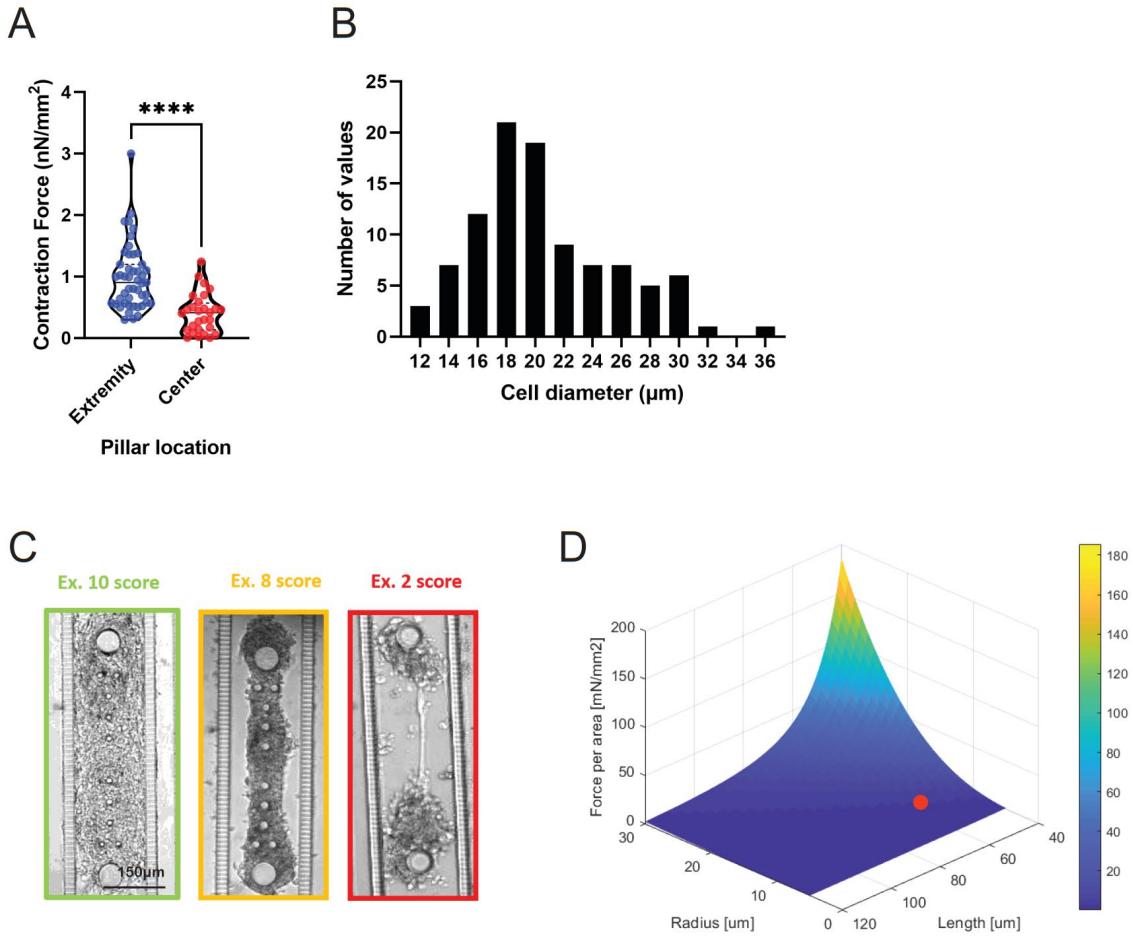

Supp. Figure 1

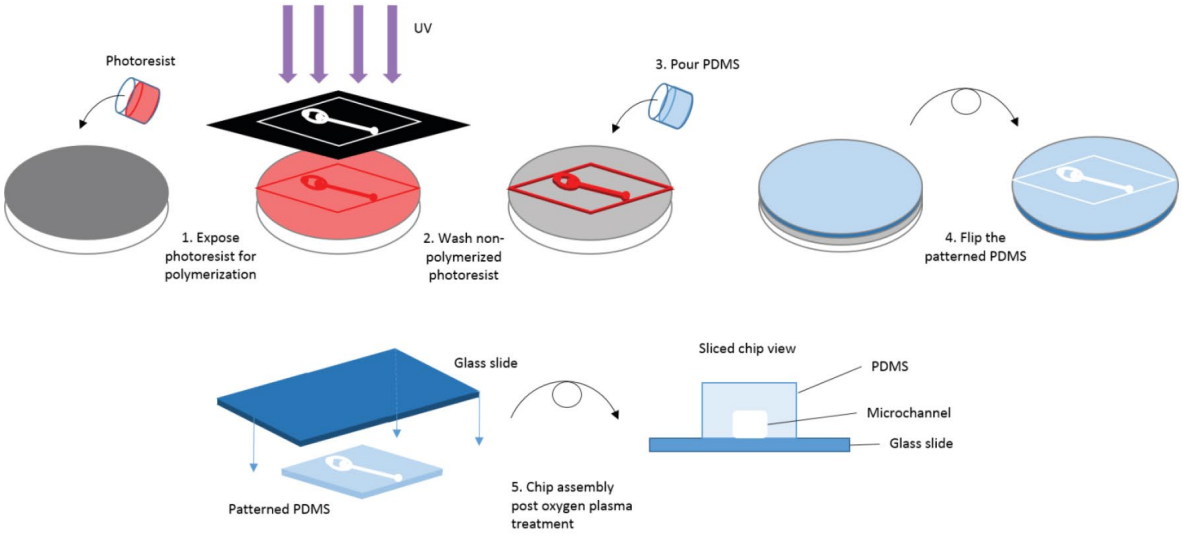

Supp. Figure 2

Chapter 4 In Vitro Safety "Clinical Trial" of the Cardiac Liability oh Hydroxychloroquine and Azithromycin as COVID-19 Polytherapy

4.1 Abstract

Importance
Despite global efforts, there are no effective FDA-approved medicines for the treatment of SARS-CoV-2 infection. Potential therapeutics focus on repurposed drugs, some with cardiac liabilities. Here we report on a preclinical drug screening platform, a cardiac microphysiological system (MPS), to assess cardiotoxicity associated with hydroxychloroquine (HCQ) and azithromycin (AZM) polytherapy.

Objective
Demonstrate the cardiac MPS's potential for identifying clinically-relevant cardiac liabilities associated with HCQ and AZM polytherapy.

Design, Setting, and Participants
Employing the cardiac MPS we designed a mock clinical trial to study the cardiotoxicity of individual and combination (poly)therapy of HCQ and AZM. The MPS contained human heart muscle derived from patient-specific induced pluripotent stem cells. The effect of drug response was measured using outputs that correlate with clinical measurements such as QT interval (action potential duration) and drug-biomarker pairing.

Main Outcomes and Measures
HCQ and AZM individual drug exposure induced cardiac liabilities such as QT prolongation and rhythm instabilities, thus demonstrating good concordance with published clinical trials. Polytherapy caused QT prolongation, but showed compensatory effects with a decrease in arrhythmias and instabilities relative to monotherapy.

Results
Chronic exposure to HCQ, AZM and their combination showed QT prolongation and rhythm instabilities that correlated with arrhythmic events and clinical observations. HCQ alone elicited early afterdepolarizations (EADs) and increased QT interval from day 6 onwards. Chronic exposure to AZM alone elicited an increase in QT interval from day 7 onwards and arrhythmias were observed at days 8 and 10. Upon chronic exposure to HCQ and AZM polytherapy, we observed an increase in QT interval on days 4-8, which closely mimicked clinical trial outcomes where QT interval was increased on days 2-5. Furthermore, biomarkers, most of them measurable in patients' serum, were identified for negative effects of single drug or polytherapy on tissue contractile function, morphology, and antioxidant protection.

Conclusions and Relevance
The cardiac MPS can predict clinical arrhythmias associated with QT prolongation and rhythm instabilities. This high content system can help clinicians design their trials, rapidly project cardiac outcomes, and define new monitoring biomarkers to accelerate access of patients to safe COVID-19 therapeutics.

4.2 Introduction

When the World Health Organization declared a global pandemic on March 11th 2020, little was known about the pathogenesis of the severe acute respiratory syndrome coronavirus 2 (SARS-CoV-2). It was described and treated as a respiratory disease, in which the virus targeted the epithelial cells of the respiratory tract, resulting in alveolar damage, edema and fibrosis. Now, with more than 45 million cases and a million deaths worldwide, there is clinical evidence that the virus also has non-negligible long-term effects on multiple organs, including heart, kidney, vasculature, liver and even brain[1-7]. With the absence of FDA-approved medicines for the treatment or prevention of COVID-19, clinicians have been pressed to treat patients in critical stages without FDA approved protocols. They have therefore relied on several small scale clinical studies to repurpose compounds approved by regulatory bodies as monotherapies in the hope of improving patient outcomes. Early clinical trials identified chloroquine (**CQ**), hydroxychloroquine (**HCQ**) and azithromycin (**AZM**) as promising drugs to help treat or reduce the effects of SARS-CoV-2 [8-12]. A non-randomized clinical trial in France identified HCQ, in combination with AZM, as being capable of significantly reducing respiratory viral loads [8]. This was confirmed by more recent retrospective studies[13, 14], but was also heavily criticized and refuted by other recent studies employing *a priori* designs[15-18]. Several additional small clinical trials have shown mixed outcomes for HCQ treatment of COVID-19 patients[19].
A serious concern with these studies is that patients were treated with drugs that have known cardiac complications, and their effects on the heart in polytherapy were unknown.

HCQ inhibits *hERG* (***I_{Kr}***) potassium channels, it is known to increase in QT interval of cardiomyocytes, and can induce arrhythmias that are responsible for sudden death [20]. AZM is also associated with an increased risk of cardiovascular death, due to Torsade de Pointes (**TdP**) and polymorphic ventricular tachycardia [21]. With respect to polytherapy, clinical trials have demonstrated a synergistic effect of HCQ and AZM to prolong QT interval [22, 23]; however, alterations in arrhythmic event frequency were controversial when compared to HCQ or AZM alone.

In the absence of rapid clinical trials for polytherapy safety, there is an urgent need for screening tools to increase the speed at which potential therapeutics are evaluated for cardiac liabilities. Common *in vitro* systems used for cardiac drug screening include cell 2D monolayers and animal testing, which often fail to replicate human physiology, particularly electrophysiology, and pharmacokinetic properties [24]. Engineered heart tissue, organoids or microfluidic-based microphysiological system are emerging alternatives for state-of-the-art drug screening [25, 26]. With the rapid spread of COVID-19, microphysiological systems (**MPS**) have recently shown to be a promising tool to study virus entry and replication mechanisms, subsequent cytokine production, as well as effects of existing and novel therapeutics or vaccines [27, 28].

In this paper, we demonstrate the utility of a cardiac MPS (**Figure 1**) for determining the cardiac liability associated with HCQ and AZM polytherapy in an *in vitro* design analogous to a Phase I safety clinical trial. Our cardiac MPS contains a three-dimensional (**3D**) cell chamber in which human induced pluripotent stem cell-derived cardiomyocytes (**hiPSC-CMs**) are confined and self-assemble to form uniaxially beating heart muscle [24, 29]. HiPSC-CMs have been successfully used for *in vitro* assessment of drug-induced arrhythmias, especially since they respond consistently to *hERG* channel block (QT prolongation and arrhythmias) and calcium channel block (action potential duration shortening, impaired contractile function) [6, 30]. It makes them excellent candidates to screen for cardiac liability of HCQ and AZM, both of which are known to block hERG channels, and also act upon other cardiac ion channels[31]. By assaying hiPSC-CMs expressing a genetically encoded calcium sensor (GCaMP6f), loaded with a voltage-sensitive fluorescent probe (BeRST), we assessed the electrophysiology and calcium handling of the tissues during serial drug exposures. We showed that HCQ and AZM significantly increase 80% repolarization time (APD_{80}) and rhythm instabilities, starting at clinically relevant exposure days, and were accompanied with EAD and TdP instances. HCQ+AZM combination also showed a significant increase in APD_{80}, however, few instabilities or arrhythmic events were observed. Finally, proteomics analysis of cell culture effluent enabled detection of biomarkers that were directly correlated with cardiotoxicity, apoptosis and contraction mechanics alteration.

4.3 Results and Discussion

4.3.1 Chronic exposure to HCQ for 10 days resulted in QT prolongation and rhythm instabilities that correlated with arrhythmic events and clinical observations

Chronic exposure to an HCQ dose mimicking clinical protocols decreased the beat rate starting at day 4 with a statistically signifcant decrease on days 4, 7 and 8 (**Figure 2A**). APD_{80} increased markedly from day 7 onwards (**Figure 2B**), with the maximum APD_{80} increase reaching 850ms. All but one tissue exhibited an APD_{80} at least 400 ms longer on day 7 and day 9 than prior to HCQ exposure. These arrhythmogenic changes to the AP were tightly correlated with the appearance of instabilities in the HCQ tissues from day 5 onwards (**Figure 3A**). APD_{80} was directly correlated to calcium transient duration (CaD) (**Supp. Figure 1D**), and an increase of CaD_{80} above 600ms was observed at day 2 and increased over the duration of HCQ treatment. Arrhythmic events began appearing at day 4 in 50% of the tissues. At day 7, tissues exhibited both arrhythmogenic AP waveforms and CaD_{80} increase, and by days 9 and 10, 50% of tissues exhibited weak or no dynamic signal change, suggesting loss of resting membrane potential (**Figure 3D**). Representative traces of arrhythmic events are shown in **Figure 3 G-J**, comparing 30 second calcium traces at day 0 and day 9 (**Figure 3G**). Late calcium peaks are a signature of EADs in membrane potential and were clearly observed (red arrows) in day 9 HCQ recordings, as were the marked increases in duration of the calcium transient, itself a marker for APD prolongation. Together these data reflect HCQ's well known block of $I_{Kr,}$ which prolongs the QT interval and its *in vitro* proxy APD [22, 32] which are associated with arrhythmic events[20, 33, 34]. Our AP data, which is consistant with the clinical literature, indicates that the cardiac MPS system is a good predictor of clinical cardiotoxicity of HCQ.

4.3.2 Chronic exposure of AZM for 10 days showed QT prolongation and rhythm instabilities that correlated with arrhythmic events and clinical observations

Chronic AZM exposure did not significantly change beat rate (**Figure 2C**). However, as for HCQ, chronic AZM treatment increased APD_{80} by day 7, and a trend for persisting prolonged APD_{80} continued until day 10, albeit with large variation (**Figure 2D**). Triangulation also trended ($p<0.2$) to increase from day 8 onwards, although this did not reach significance ($p=0.07$ at day 10) (**Supp. Figure 1B**). Instabilities arose at day 6 and worsened over time (**Figure 3B**). Non-parametric analysis of instability showed a significant increase of chaotic polygons in AZM-treated tissues when compared with HCQ ($p<0.05$, not shown). CaD_{80} increased beyond 600ms at day 4, and day 6 onwards in 30-50% of the tissues. Arrhythmic events were observed from day 3 onwards, reaching 60%

of tissues at day 10, with some tissues exhibiting both arrhythmia and CaD_{80} increase. Day 6 and 9 had respectively 16% and 33% of tissues with weak or no signal (**Figure 3E**). **Figure 3** shows a representative trace of arrhythmic events at day 0 versus day 10 (**Figure 3H**) of AZM exposure. Overall, APD_{80} increased on all treatment days compared to day 0, and EADs appeared after day 3, and were most prevalent on day 10. Since clinical AZM application is typically limited to 5 days, the observed incidence of pro-arrhythmic events during longer exposure times cannot be directly compared to clinical outcomes. However, AZM has been associated with increase in cardiovascular death, mostly through QT prolongation and arrhythmia [21, 35], and these outcomes are clearly indicated by our MPS measurements.

4.3.3 Chronic exposure to both HCQ and AZM for 10 days showed QT prolongation and rhythm instabilities that correlated with arrhythic events and clinical observations

Chronic exposure to a combination of HCQ and AZM dose mimicking clinical protocols increased the spontaneous beat rate at day 3 and 6; however, there was no clear overall trend (**Figure 2E**). APD_{80} was significantly increased on days 5 and 8, with a trend towards APD prolongation for all recordings after day 7 ($p<0.2$) (**Figure 2F**). This data set closely mimics clinical trials performed by Chorin et al. [36], where the QT interval increased starting at day 2 to day 5 with high variability in patient population. Triangulation was not significantly altered over the 10 days during our *in vitro* polytherapy trials, although there was a very slight trend towards increasing triangulation at day 4, 5 and 10 ($p<0.2$) (**Supp. Figure 1C**). Interestingly, instabilities were almost absent in this data set, when running non-parametric analysis on Poincare plots from the combination study (**Figure 3C**) versus those for individual HCQ (significant, $p<0.05$) or AZM (non significant trend) (**Figure 3 A,B)**. Although we observed a clear increase in APD_{80}, and an increase of CaD_{80} above 600ms at day 2 and day 4-10 (**Figure 3E**), chronic polytherapy resulted in fewer arrhythmic events and only mild instability compared to monotherapy (**Figure 3I**). At most, 33% of tissues showed arrhythmia at day 3 and 6, with 16% arrhythmias at day 4, 5, 7 and 9 (**Figure 3F**). Non-parametric contigency analysis showed a decrease between EAD instances in polytherapy versus HCQ (significant, $p<0.05$) or AZM (trend, $p<0.1$) monotherapy. No tissues had weak signal or stopped beating. At the pathophysiologic level, this data fit well with prior studies describing the important role of AP triangulation in the transition from benign AP prolongation to unstable repolarization[37].

Together, these observations suggest that polytherapy rescues arrhythmogenesis resulting from the individual drugs. Recent clinical studies demonstrated chronic exposure to combination of HCQ and AZM led to QT increases with few arrhytmia events [17, 35, 38]. The concordance of the cardiac MPS data to arrive at similar conclusions demonstrates its power in predicting cardiac liabilities for combination therapy of

repurposed drugs to treat SARS-CoV-2. Mechanisms explaining how arrhythmic events are absent despite a significant increase of the QT interval, can be complex and additional studies would be required to elucidate HCQ and AZM polytherapy-dependent mechanisms. However, based on the fact that HCQ and AZM have known multichannel blocking effects, and that I_{CaL} and I_{Na} block is known to reduce I_{Kr} dependent arrhythmias[33], we can hypothesize that the combination of both drugs can synergistically increase multichannel block responsible for lower arrhythmic instances when compared to monotherapies.

4.3.4 Proteomics analysis of MPS effluent reveal candidate biomarkers for cardiotoxicity monitoring in patients treated with HCQ and AZM:

For the polytherapy pharmacology study, media were analyzed for over 92 proteins as biomarkers of tissue injury (**Figure 4A**). The proteomics analysis of the MPS effluent included a wide array of biomarkers, most of them measurable in patients' plasma, associated with different cardiac mechanisms, from morphology, cytoskeleton, mechanics to apoptosis and stress response. Cardiac troponin I (TNNI3), is a well known biomarker of cardiac injury and increased risk in mortality, common in COVID19 patients with underlying cardiovascular conditions[39]. Chronic exposure to the combination of AZM and HCQ showed no significant change in TNNI3 expression, suggesting that arrhythmic tissues are not undergoing major tissue damage. However, a clear decrease in erythropoietine (EPO) was observed. HPGDS, an intracellular enzyme that catalyzes the conversion of PGH2 to PGD2, was shown to decrease significantly. Interestingly, similar significant changes were also observed for carbonic anhydrase 14 (CA14) and tyrosine-protein kinase Fes/Fps (FES). These intracellular proteins are typically not secreted[40], and therefore are not strong biomarkers unless cells were damaged. The fact that alterations in levels for these proteins were observed in our study, suggests some degree of cell damage or stress, but not to the extent where troponin-actin complexes break down[41]. It is known that CA14 facilitates lactic acid transport across the cardiac sarcolemma [42], as well as improves myocardial energetics by facilitating mitochondria CO_2 clearance [43]. We hypothesize the drug-related change in CA14 expression is a mechanism for the muscle to adapt antioxidant, contraction or waste management mechanisms to counter-balance cardiotoxic effects. Identification of biomarkers in the context of HCQ and AZM, or other polytherapies, will be a valuable tool in the design of COVID-19 therapeutics trials.

4.4 Summary

The outcomes of this paper suggest that chronic drug exposure in this MPS format elicits arrhythmic outcomes similar to those observed in published clinical trials[17, 22, 23, 35,

36, 38]. Specifically, the known arrhythmia risk of HCQ and AZM alone was recapitulated by our *in vitro* observation of APD_{80} increase in combination with arrhythmic events. Combination therapy also exhibited an increase in QT, but compared to monotherapy, was benign at inducing arrhythmogenic behaviors. This also corresponds with recent clinical findings [38]. Together, these data suggest that this our high content *in vitro* heart muscle model can aid clinicians in clinical trial design, rapidly predict the cardiac outcomes of polytherapy for SARS-CoV-2 treatment, and help to identify relevant biomarkers to monitor during clinical trials for potential COVID-19 therapeutics.

4.5 Limitations:

Clinical QT interval values represent the summation of all the electrical activity in the ventricles. We used APD_{80} as a proxy for clinical QT prolongation, which is a credible and common approach to compare directional effects and provide some mechanistic insight, but is not sufficiently sensitive for precise prediction of instability thresholds [30]. COVID-19 patients with drug-induced QT interval changes of > 60 ms or QT interval values above 500ms are considered high risk, and treatment is suspended[32]. Our cardiac muscle exhibited unphysiologically high APD_{80} values in response to chronic drug exposure. The mechanism for these large responses is unclear, but likely related to a combination of the hiPSC source, well-known modest maturity of hiPSC-CMs relative to the adult human heart, and possibly due to the altered current source-sink relationship in these very small tissues. Additionally, we have used a single patient line to perform this study, albeit with a significant number of replicates. By screening more patient lines one can achieve a clinically relevant dataset; although anticipated patient variability will require further expansion of the data size. In future work, this study can be extended to diseased cell lines to better understand the arrhythmic risk of patients with cardiovascular complications or comorbidities (i.e., diabetes) who are most likely to be seriously affected by SARS-CoV2.

4.6 Conclusion

As the global pandemic of COVID-19 has expanded, clinicians continue to be pressed to treat patients with new drug combinations, in the absence of regulatory approval. Even ten months after the first cases, FDA-approved medicines for the treatment or prevention of COVID-19 are just emerging with mixed results. This study demonstrates that a complex *in vitro* tissue model (i.e., cardiac MPS) can predict arrhythmias and rhythm instabilities under experimental conditions similar to a safety clinical trial. We also identified biomarkers associated with cardiac injury, and that approach can be used to design clinical trial monitoring protocols. Collectively, the features of cardiac MPS should accelerate polytherapy testing and access of patients to potential COVID-19 therapeutics.

4.7 Materials and Methods

4.7.1 Cell Sourcing

The human hiPSC line Wild Type C (WTC) harboring a single-copy of CAG-driven GCaMP6f knocked into the first Exon of the AAVS1 “safe harbor” locus [44] was used for all experiments in this study. It is available from the Coriell Repository (# GM25256 hiPSC from Fibroblast). More detailed information can be found in [44]

4.7.2 Cardiomyocyte Differentiation

HiPSC stocks were thawed and plated on Matrigel hESC-Qualified Matrix (Corning; Corning, NY) coated tissue culture plates in mTeSR-1 (mTeSR-1; StemCell Technologies, Vancouver, Canada) containing 10 μM of the Rho kinase inhibitor (RI) Y27632-dihydrochloride (Peprotech; Rocky Hill, NJ). Media was exchanged the next day to remove the inhibitor, and hiPSC were split three times at a density of 20,000 cells/cm2 to allow for recovery from cryopreservation. After three splits, hiPSC were seeded differentiation plates at 30-40,000 cells/cm2 to allow for full confluency. Initial seeding was considered as ‘day-3’ of differentiation. At day 0, when hiPSC were >90% confluent, differentiation was started following the protocol developed by Palecek et al. [52], which exposes the cells to 8μM CHIR99021 (Peprotech) in Roswell Park Memorial Institute Medium 1640 (RPMI) containing B-27 supplement without insulin (RPMI-I). At day 1, only RPMI-I was added to the cells. On day 2, cells were exposed to 5μM IWP-4 (Peprotech) in RPMI-I supplemented with 150 μg/mL L-ascorbic acid (LAA) for two days. On day 4, only RPMI-I was given to the cells for another two days. From then onwards, RPMI containing standard B-27 supplement with insulin (RPMI-C) was added every second day. Once spontaneous contractions were observed around day 7 or 8 of differentiation, hiPSC-CM were washed several times with dPBS -Ca/Mg and left to soak for 10 minutes to disrupt cadherins. Cells were then exposed to 0.25% Trypsin (Thermo Fisher) for 10 minutes at 37C, and were pipetted gently to break up tissue into single cells and collected. Cells were pelleted at 300g for 5 minutes before being plated at a density of 100,000 cells/cm2 onto Matrigel, in RPMI-C with 10μM RI (‘day 0’ after replating). At day 1 after replating, medium was exchanged for RPMI-C. At day 3, cells were washed with dPBS to remove glucose and were exposed to RPMI 1640 (no glucose, no pyruvate, supplemented with 23mM sodium bicarbonate and 5 mM Sodium L-lacate[53]) for four to five days (exchanged every other day) to select for cardiomyocytes only. At day 8, cells were washed with dPBS and exposed to RPMI-C for two to three days to allow for recovery. Cardiomyocyte purity was characterized by flow cytometry with Cardiac Troponin T both before and after this procedure

4.7.3 Fabrication and cell loading of Cardiac MPS

The microfluidic design for each MPS consisted of 4 identical cell culture chambers (1300 by 130 μm) with media channels running parallel on either side of the cell culture chambers. All 8 media channels were connected to a single media inlet port and a single media outlet port (corresponding to the tubing in **Figure 1A**). Each cell culture chamber had its own cell loading port. Media channels and cell culture chambers were 60μm tall. An array of fenestrations (2 μm x 2 μm height/width and 40 μm length) linked media channels to cell chambers, allowing for media change while protecting the tissue from shear stress [24] (**Figure 1B**).

The microfluidic devices were fabricated from Polydimethylsiloxane (PDMS) using classic replica molding techniques. The basic process is described in our previous work [24, 29] and has been optimized. A master mold featuring the negative structures of the fluidic channels was prepared in a 2-step photolithography process. First the 2 μm thick fenestration layer was patterned on a clean and water-free silicon wafer by spin-coating SU8 2002 (MicroChem) in a 2-step process (500rpm, 10sec, 100rpm/sec acceleration; 2000rpm, 30sec, 300rpm/sec acceleration). A soft bake of 1min at 95C was performed prior to 80mJ/cm^2 exposure. The post exposure bake was 2min at 95C, followed by a development in SU8 developer (30sec on shaker, 15sec on sonicator and 30sec on shaker). For the second layer SU8 3050 (MicroChem) was spun to 60μm thickness (500rpm, 10sec, 100rpm/sec acceleration; 3000rpm, 30sec, 300rpm/sec acceleration). The soft bake was performed for 10min at 65C followed by 45min at 95C with very slow up and down ramping of the temperature. Alignment markers were used to position the 2nd layer mask over the fenestration layer features during the exposure step (160mJ/cm^2). The post exposure bake was 2min at 65C and 10min at 95C again with slow ramping. SU8 developer was applied on a shaker for 20min and sonicator for 15min. A final hard baked was performed at 180C for 30-45min.The cardiac MPS was formed by replica molding from the silicon wafer with Polydimethylsiloxane (PDMS; Sylgard 184 kit, Dow Chemical, Midland, MI) at a 10:1 ratio of Sylgard base to crosslinker. The inlets and outlets were punched into the PDMS with a 0.75 μm biopsy punch before bonding to glass slides using oxygen plasma (PETS inc. RIE system) with the following protocol: RF power 21W, 24sec, 100% oxygen flow (600mTorr).

4.7.4 Self-Assembly of Cardiac Microtissues Within Cardiac MPS

Lactate purified hiPSC-CM were singularized with 0.25% trypsin for 5 min and suspended to a density of 1.33x10^6 cells/mL in EB20 media (Knock Out DMEM (Gibco, 10829-01820%) with 20% FBS (Gibco, 16000-0), 1% MEM non-essential amino acids (Gibco, 11140-050), 1% Glutamax (Gibco, 35050-061) and 400nM beta-mercaptoethanol (Gibco, 21985023)) freshly supplemented with 10μM ROCK-inhibitor Y27632 (Sigma, SCM075). 3μL of the cell suspension, corresponding to 4000 cells, was injected into the cell loading port of each tissue chamber. To move the cells into the cell chamber MPS were

centrifuged twice at 300g for 3 minutes: first in horizontal and then in vertical position. The loading tips were then sealed. Chambers that were not filled at this point were discarded. MPS were incubated at 37C for 1-2h to allow formation of a dense cell cluster and avoid backflow of cells when adding media. EB20 media supplemented with 10 μM Y27632 (200uL per MPS) was added to the media inlet of each MPS and flow was initiated by applying gentle vacuum at the media outlet. The following day and every other day from then on, media was changed to our in-house 'Maturation Media' (MM) as described in [29]. MPS tissues were allowed to mature for at least 10 days before any subsequent experiments were performed. When tissues were fed (every 2 days for maintenance or every day for drug studies), 200 μL of media was added to the inlet tip and media would flow gravimetrically to the outlet until equilibrium was reached.

4.7.5 Preparation of Maturation Media (MM)

A base media was prepared from RPMI 1640 powder (Sigma, R1383-10X1L) and supplemented with 0.5 g/L D-glucose (Fisher, BP350-1), 10mM D-galactose (Sigma, G5388) and 2 g/L sodium bicarbonate (Fisher, S233-500) . A 9% bovine serum albumin (BSA; Fisher, BP1605-100) solution was prepared in base media and adjusted to pH 7.4. Aliquots of fatty acid (FA) stocks were prepared from oleic acid (OA ; Sigma, O1383-5G) and palmitic acid (PA; Sigma, P0500-10G ; 100 mg/ml in DMSO) and stored at -20C. OA was prediluted 1:10 in DMSO. PA and OA were added to the 9% BSA solution at 10.23ug/ml for PA and 0.8mM OA. To dissolve the FA the solution was heated to 60C and sonicated for 5min. The final MM was prepared by mixing 1 part FA solution and 3 parts MM base media yielding a final concentration of 2.5575 ug/ml PA and 0.2 mM OA. Finally, the media was supplemented with 2% B27 (Gibco, 17504-044) and 150μg/ml ascorbic acid (Fisher, AC105021000) and sterile filtered.

4.7.6 Drug Preparation For Pharmacology Studies

We performed all the pharmacology experiments in MM with 5 nM BeRST-1 dye to guarantee a high-quality signal. On the day of pharmacology study, drugs were weighed and dissolved in an adequate solvent to create a stock solution (**Supp. Figure 1E**). From that stock, the highest test dose was prepared and serial dilutions were made for lower doses. Vehicle concentration was kept the same in all doses including dose 0 and controls.

In more detail, hydroxychloroquine sulfate (PHR1782-1G, Sigma) was dissolved in PBS (without calcium or magnesium) at 4.34 mg/ml and sterile filtered to create a 10mM stock solution. The stock was always prepared fresh on the day of the experiment. Azithromycine (75199-25MG-F, Sigma) was dissolved in 100% ethanol to create a 10 mg/ml (=13.35mM) stock. The stock was stored at -20°C for up to 3 days. The chronic drug exposure doses were chosen to mimick clinical trials (HCQ[12], AZM [45]) based on patients' serum concentration. While there is some variability in clinical protocols, we

based our study on the following commonly used protocols: Clinical drug administration for HCQ is 400 mg twice per day followed by 200 mg twice per day for 4 days. For 200 mg, the clinical peak plasma concentration (C_{max}) for oral HCQ sulfate is 50.3 ng/mL (0.12 μM) at t_{max} of 3.74 h after administration[46]. Therefore, to mimick clinical trials, the MPS tissues were exposed to 0.24 μM HCQ at day 1 and 0.12 μM HCQ from day 2 to day 10. Clinical administration of AZM is 500 mg on day 1 followed by 250mg per day for the following 4 days. Following 500mg administration, the area under curve for 24h is 2.67 (+/-0.92) μg*h/ml and C_{max} 0.405 (+/-0.161) μg/ml [47]. Therefore, to mimick clinical trials, the MPS tissues were exposed to 2.67μg*h/ml / 24h = 0.111 μg/ml = 0.15 μM AZM at day 1 and 0.056 μg/ml (0.075 μM) AZM at day 2 and following. We continued AZM application for all 10 days of the study.

4.8 Experimental Setup

24h prior to any experiment, MPS tissues were stained with the action potential dye BeRST-1 (500nM), synthesized and QC as described my Miller et al. (2018). During imaging, MPS were kept at 37°C on a heated microscope stage (Tokai Hit, Gendoji-cho, Japan). MPS were placed onto the heat plate for 20 mins to let them stabilize before imaging. Initial recordings were performed on day 0 prior to any drug exposure. After recordings, supernatants from the inlet and outlet were collected and frozen at -80C for proteomics analysis. Drug doses were always prepared fresh directly before use. Drug containing media (200uL per MPS) was applied daily via the media inlet port and incubated for 24h in a cell culture incubator at 37C where gravimetric perfusion occurred as the liquid levels in inlet and outlet tip equilibrated. The same steps were repeated for 10 days. The same MPS tissues were repeatedly recorded daily for 10 days. Drug doses are outlined in section “Drug preparation for pharmacology studies”. Control tissues were handled equivalent to tissues with drug exposure : every day fresh media containing a solvent concentration identical to the drug vials was applied. Control MPS were subjected to the same imaging protocol, and their effluents were also collected.

4.8.1 Image Acquisition for Pharmacology Studies

Videos of calcium (GCaMP) and voltage (BeRST-1) epifluorescence, were recorded daily (every 24h) in spontaneously beating tissues, and directly before administration of a fresh drug dose. NIKON TE300HEM microscope with a HAMAMATSU digital CMOS camera C11440 / ORCA-Flash 4.0 was used and enabled 100 frames per second acquisition rate. For fluorescence imaging, a Lumencor SpectraX Light Engine and filtered with a QUAD filter (Semrock) was used. GCaMP videos (6s and 30s long) used the Cyan LED, 470 nm (4x4 binning, 10 ms), while BeRST-1 videos (6s long) used the Far-red LED, 640 ms (4x4 binning, 10 ms). Videos were acquired using Nikons Nikon NIS-Elements software. Post-experiment processing was performed with an in-house python library. This library

performs automated background subtraction and normalization, and eliminates baseline drift due to bleaching by fitting a polynomial to the baseline via half-quadratic minimization[48]. The resulting traces were used for quantitative analysis of the action potential by calculating metrics such as 80% and 30% action potential duration (APD_{80} and APD_{30}), triangulation ((APD_{80}-APD_{30})/ APD_{80}) and beat rate. These analyses were also automated by the same python library.

4.8.2 Thorough Action Potential Analysis As A Proxy For Clinical QT Interval Study And Arrhythmia Prediction

Clinically, the QT interval describes the period between Purkinje activation (Q) and ventricular repolarization (T), and drug-induced QT prolongation is a strong predictor of subsequent arrhythmic cardiotoxicity in patients (**Figure 1D**, top). Torsades de pointes (TdP) is a particularly dangerous form of polymorphic ventricular tachycardia and the most common arrhythmic manifestation of drugs that induce dangerous QT prolongation. TdP is a ventricular tachycardia triggered by EADs, where the amplitude and configuration of ECG measurements vary continously. At the cellular level, AP prolongation and increased AP triangulation indicate slowed repolarization and are strong markers of whole heart QT prolongation and arrhythmia [37]. Early afterdepolarizations (EADs) represent a transition from slowed cellular repolarization to unstable (chaotic) repolarisation[49-52] at the cellular level, and are a harbinger of whole-heart TdP[49]. These characteristics formed the basis of our analysis of the MPS voltage (BeRST-1) and calcium (GCaMP) recordings, which were assessed for drug-induced changes to both stable beats (e.g. APD_{30}, APD_{80} etc.) and unstable cellular behaviors (e.g. EADs etc.).

4.8.3 Correlation Between APD_{80} and CAD_{80}

Analysis of the correlation between calcium transient duration (CaD80) and action potential duration (APD80) shows a strong linear correlation (Y = 0.8163*X + 109.1) with R2=0.86 in the relevant range of APD80=250 to 800 ms and slightly higher variation above 800ms (**Supp.Figure 1D**). This good correlation confirms that CaD80 values can be used in place of APD80 values to predict drug induced changes of the beat length.

4.8.4 Stable Beating Analysis

Since patients with QT interval > 500ms are considered at risk for TdP [32], all tissues with baseline APD_{80} > 500ms were *a priori* excluded from the study. Similarly, because APD is inversely proportional to beating frequency [33] (**Figure 1D**, bottom), APD measures were first corrected for differences in beating frequency via the Fridericia method[53]. As per Hondeghem et al., [37] if APD prolongation is accompanied by instability or triangulation then EADs and arrhythmia are very likely to follow. For these

reasons we used the drug-induced changes to APD_{80}, and AP triangulation as primary measures of drug arrhythmogenicity in recordings that exhbited stable AP waveforms.

4.8.5 Unstable Beating Analysis

Large beat-to-beat variation in AP duration is a specific indicator of repolarization instability. EADs represent a form of dynamical chaos in repolarization, and APD alternans is a period-2 dynamic repolarization instability. Both behaviors can be readily visualized by Poincare plots (**Figures 3A-C**). These were again generated by an in-house python script plotting CaD_{80} of each (n^{th}) beat in the 30 second calcium recording, against CaD_{80} of the preceding beat $(n-1)^{th}$, normalized to the CaD_{80} mean. Identical CaD_{80} values in sequence appear as a single point, consistent CaD increase or decrease (anti-arrhythmic) will cluster around the center of the graph and if large deviations between successive CaD_{80s} appear (pro-arrhythmic), points will deviate from the center and meander, giving rise to disorganized polygons[37]. We also performed a qualitative and non-parametric evaluation of drug arrhythmogenesis by categorizing arrhythmic behaviors present in the calcium time-series (spontaneous 30 second recordings, **Figure 3D-F**). The arrhythmic categories included EADs, DADs, irregular beating (successive beats with different APD or resting time), TdP (continous changes in amplitude), overt changes to automaticity (as suggested by Blinova et al. [33]), and weak or quiescent tissues (suggesting loss of resting membrane polarization).

4.8.6 Plasma Protein Profiling Using Olink Multiplex Panel

Effluents were stored at -80C and all samples were sent together on dry ice to Olink Proteomics for quantification of proteins associated with toxicity and tissue damage. Olink Proteomics uses multiplex proximity extension assay (PEA) panels [54]. The basis of PEA is a dual-recognition immunoassay, where two matched antibodies labelled with unique DNA oligonucleotides simultaneously bind to a target protein in solution. This brings the two antibodies into proximity, allowing their DNA oligonucleotides to hybridize, serving as template for a DNA polymerase-dependent extension step. This creates a double-stranded DNA “barcode” which is unique for the specific antigen and quantitatively proportional to the initial concentration of target protein. The hybridization and extension are immediately followed by PCR amplification and the amplicon is then finally quantified by microfluidic qPCR using Fluidigm BioMark HD system (Fluidigm Corporation. South San Francisco, California). In this study, we have used the Organ Damage panel which consist of 92 unique markers of toxicity and cellular damage (https://www.olink.com/products/organ-damage-panel/). In the data post processing, we only included biomarkers with > 65% of samples above limit of detection. The limit of detection is set at 3 standard deviations above negative control values, making it quite conservative.

4.8.7 Statistics

All statistics were calculated using GraphPad Prism. All electrophysiology data were analyzed with one way ANOVA repeated measures and Dunnett's post-hoc correction with multiple comparison to day 0 and to one another was run. If some values were missing, mixed-effects model was run. Non parametric Chi-squared approximation was run for qualitative arrhythmic events assessment in a pairwise manner. Significance was determined with p-value < 0.05.

4.9 Acknowledgements

All authors participated in the study design, analysis of the data, interpretation of the results and review of the manuscript; BC and VC conducted the main experiments and qualitative EAD characterization; BS helped with cell culture and MPS preparation; AGE helped with interpretation of electrophysiological recordings. HF developed the code to analyze action potential waveforms and Poincare plots; EM provided BeRST-1; BC, VC, AGE and KEH wrote the manuscript; BC prepared the figures and caption; KEH funded the work.This work was funded in part by the California Institute for Regenerative Medicine DISC2-10090 (K.E.H.), NIH-NHLBI HL130417 (K.E.H.), NIH-NIGMS R35GM1195855 (E.W.M.) and the Jan Fandrianto and Selfia Halim Chair Fund (K.E.H.), Lloyd Award in Bioenginering for Excellent Research and Leadership (B.C.). We thank Bruce Conklin (Gladstone Institutes, San Francisco, USA) for technical advice on the WTC iPSC line. We thank the Marvel Nanofabrication laboratory (UC Berkeley) and their staff for assistance and technical advices for microfabrication procedures.

4.10 Figure Legends

4.10.1 Figure 1. The cardiac microphysiological system.

(**A**) Photograph of a cardiac MPS in fluorescent light with feeding tubing. **(B)** Brightfield image of a cardiac MPS loaded with 4,000 human induced pluripotent stem cell-derived cardiomyocytes. The cell chamber is separated from adjacent feeding channels via a fenestration barrier of 2μm wide grooves allowing for nutrient diffusion while protecting the tissue in the cell chamber from media flow-induced shear stress. The anchoring pillars on either side of the cell chamber help keep the heart muscle elongated and provide resistance for contraction. (**C**) Representative images of the same tissue under GFP fluorescence for calcium transient recordings (top) or FarRed voltage dye staining (bottom). (**D**) The top graph shows a typical ECG recording from which the clinical QT interval can be determined. We use APD_{80} as a proxy for QT duration, corresponding to the duration of the action potential at 80% of its repolarization (bottom). The APD (red) and Ca (green) waveforms are timestamped identifying temporal kinetics.

4.10.2 Figure 2. Electrophysiology analysis of chronic exposure to hydroxychloroquine (HCQ), azithromycin (AZM) or their polytherapy.

Doses were chosen to closely mimic clinical trial drug prescription used for COVID-19 treatment: 0.24 μM HCQ and 0.15 μM AZM on day1 followed by 0.12 μM and 0.075 μM AZM on day 2 to day 10. Polytherapy was the combination of both monotherapy doses (**Supp. Table 1**). Violin plots demonstrate spontaneous beating during the therapy for HCQ (**A**), AZM (**C**) or polytherapy (**E**). Violin plots depicting the change in APD_{80} during the therapy for HCQ (**B**), AZM (**D**) or polytherapy (**F**). APD_{80} values were calculated from spontaneous recording, corrected for beat rate using the Fredericia correction[53]. In all graphs, the values were normalized to baseline at day 0 for each tissue. Each point corresponds to one heart muscle. The violin plots show the arithmetic median (solid line) and upper and lower quartile (dashed lines) as well as minimum and maximum values (truncation of violin shape). All tissues analyzed were within inclusion criteria of APD_{80} <500ms at baseline. Statistics run were one-way ANOVA repeated measures with multiple comparison to baseline day 0 and Dunnett's post-hoc correction. * $p<0.05$; ** $p<0.01$; *** $p<0.001$.

4.10.3 Figure 3. Instability and arrhythmic study of chronic exposure to hydroxychloroquine (HCQ), azithromycin (AZM) and their polytherapy.

Poincare plots[55] were used to visualize rhythm instabilities in different tissues. Where small cluters of daily traces represent minimal arrhythmic risk, and large complex polygons are indicative of rhythm instability and high arrhythmic risk. **(A)** Representative Poincare graph of a tissue exposed to HCQ only. Disorganized polygons can be observed at day 5 and 10 indicative of drug-indueced arrhythmia. (**B**) Poincare graph of AZM-treated heart muscle where instabilities were observed starting on day 6. (**C**) Representative graph of polytherapy instabilities, which show fewer and smaller polygons when compared to monotherapy, indicative of reduced arrhythmic risk. (**D-F**) Histograms showing weak or no signal (black), CaD_{80} above 600ms with (striated) or without (grey) EAD and arrhythmic event (pink) as percentage of total heart muscles (i.e., MPS). The analysis was performed for HCQ alone (**D**), AZM alone (**E**), and for polytherapy (**F**). Representative calcium transient trace at baseline and after exposure to 9 days of HCQ (**G**) or 10 days of AZM **(H)** where EAD instances can be observed (red arrows). (**I**) Representative calcium transient trace at 10 day exposure polytherapy showing no EAD.

4.10.4 Figure 4. Proteomics analysis of microphysiological systems effluent during chronic exposure to HCQ and AZM polytherapy.

Scatter plot of biomarkers showing significant changes with increasing doses of polytherapy in chronic study. The effluent media was analyzed on day 2, 4, 6, 8 and 10. In the data post-processing, we only included experiments with > 65% of samples above

limit of detection. The limit of detection is set at 3 standard deviation above negative control values. Statistics run were one-way ANOVA with multiple comparison to one another and Dunnett's post-hoc correction. * $p<0.05$; ** $p<0.01$. TNNI3 (cardiac troponin I), EPO (Erythropoietine), HPGDS (Hematopoietic prostaglandin D synthase), CA14 (Carbonic anhydrase 14), FES (FES proto-oncogene, Tyrosine Kinase)

4.11 Supplemental Figure Legends

4.11.1 Supplementary Figure 1. Triangulation analysis of chronic either hydroxychloroquine (HCQ), azithromycin (AZM), or their polytherapy.

Spontaneous triangulation values from action potential traces in tissues treated with HCQ (**A**), AZM (**B**) and polytherapy (**C**). For each tissue, triangulation is defined as the difference between APD_{80} to APD_{30}, normalized to APD_{80}. (**D**) The solid lines shows the linear correlation of CaD80 and APD80 values ($Y = 0.82*X + 109$; $R^2=0.86$) and the the dashed lines indicate the 90%-confidence intervals.

4.11.2 Supplementary Figure 2. Electrophysiology and arrhythmic analysis of control tissues.

(**A**) Graph showing spontaneous beating frequency over the days of measurements. (**B**) Violin plot depicting the change in APD_{80} over increasing days. (**C**) Spontaneous triangulation values from action potential traces. In all graphs, the values were normalized to baseline day 0 of each respective tissue. Every dot corresponds to one tissue. All tissues analyzed were within inclusion criteria of APD_{80} <500 ms at baseline. Statistics run were one-way ANOVA with multiple comparison to baseline day 0 and Dunnett's post-hoc correction. * $p<0.05$. **(D)** *R*epresentative Poincare plot of a control tissue, where no change over the 10 days were observed. (**E**) Histogram showing qualitative EAD and arrhythmic event assessment as percentage of total MPS (microphysiological systems). The graph being empty, corresponds to a complete absence of any arrhythmic effects. (**F**) Representative calcium transient trace at baseline (left) and at ten days measurements (right). No EAD or any arrhythmic even can be observed.

4.12 Supplemental Tables

4.12.1 Supplementary Table 1

Table describing drug references, primary purpose, clinical C_{max} and doses used in this study.

Drug (Reference)	**Primary Purpose**	**Clinical C_{max}**	**Chronic drug dose** (based on clinical trials area under curve over 24h exposure)
Hydroxychloroquine - HCQ *(PHR1782-1G, Sigma)*	Anti-malarial	1 µM	**Day1** = 0.24µM **Day2-10** = 0.12µM
Azithromycin - AZM *(75199-25MG-F, Sigma)*	Macrolide Antibiotic	0.67µM	**Day1** = 0.15 µM **Day2-10** = 0.075 µM
HCQ+AZM combination	SARS-CoV2		same as each respective concentration but combined

4.13 References

1. Varga, Z., et al., *Endothelial cell infection and endotheliitis in COVID-19.* The Lancet, 2020. **395**(10234): p. 1417-1418.
2. Lu, Y., et al., *Cerebral Micro-Structural Changes in COVID-19 Patients – An MRI-based 3-month Follow-up Study.* EClinicalMedicine, 2020. **25**: p. 100484.
3. Fried, J.A., et al., *The Variety of Cardiovascular Presentations of COVID-19.* Circulation, 2020. **141**(23): p. 1930-1936.
4. Farouk, S.S., et al., *COVID-19 and the kidney: what we think we know so far and what we don't.* Journal of Nephrology, 2020.
5. A Pérez-Bermejo, J., et al., *SARS-CoV-2 infection of human iPSC-derived cardiac cells predicts novel cytopathic features in hearts of COVID-19 patients*. 2020, Cold Spring Harbor Laboratory.
6. Arun Sharma, et al., *Human iPSC-Derived Cardiomyocytes are Susceptible to SARS-CoV-2 Infection*. 2020, Cold Spring Harbor Laboratory.
7. Diana Lindner, et al., *Association of Cardiac Infection With SARS-CoV-2 in Confirmed COVID-19 Autopsy Cases.* JAMA Cardiology, 2020.
8. Gautret, P., et al., *Hydroxychloroquine and azithromycin as a treatment of COVID-19: results of an open-label non-randomized clinical trial.* Int J Antimicrob Agents, 2020: p. 105949.
9. Yao, X., et al., *In Vitro Antiviral Activity and Projection of Optimized Dosing Design of Hydroxychloroquine for the Treatment of Severe Acute Respiratory Syndrome Coronavirus 2 (SARS-CoV-2).* Clin Infect Dis, 2020.
10. Wang, M., et al., *Remdesivir and chloroquine effectively inhibit the recently emerged novel coronavirus (2019-nCoV) in vitro.* Cell Res, 2020. **30**(3): p. 269-271.
11. Huang, M., et al., *Treating COVID-19 with Chloroquine.* J Mol Cell Biol, 2020.
12. Xueting Yao, et al., *In Vitro Antiviral Activity and Projection of Optimized Dosing Design of Hydroxychloroquine for the Treatment of Severe Acute Respiratory Syndrome Coronavirus 2 (SARS-CoV-2).* Clinical Infectious Diseases, 2020. **71**(15): p. 732-739.
13. Arshad, S., et al., *Treatment with hydroxychloroquine, azithromycin, and combination in patients hospitalized with COVID-19.* International Journal of Infectious Diseases, 2020. **97**: p. 396-403.
14. Lagier, J.-C., et al., *Outcomes of 3,737 COVID-19 patients treated with hydroxychloroquine/azithromycin and other regimens in Marseille, France: A retrospective analysis.* Travel Medicine and Infectious Disease, 2020. **36**: p. 101791.
15. Molina, J.M., et al., *No Evidence of Rapid Antiviral Clearance or Clinical Benefit with the Combination of Hydroxychloroquine and Azithromycin in Patients with Severe COVID-19 Infection.* Médecine et Maladies Infectieuses, 2020.
16. Gérard, A., et al., *"Off-label" use of hydroxychloroquine, azithromycin, lopinavir-ritonavir and chloroquine in COVID-19: A survey of cardiac adverse drug reactions by the French Network of Pharmacovigilance Centers.* Therapies, 2020.

17. Rosenberg, E.S., et al., *Association of Treatment With Hydroxychloroquine or Azithromycin With In-Hospital Mortality in Patients With COVID-19 in New York State.* JAMA, 2020.
18. Furtado, R.H.M., et al., *Azithromycin in addition to standard of care versus standard of care alone in the treatment of patients admitted to the hospital with severe COVID-19 in Brazil (COALITION II): a randomised clinical trial.* The Lancet, 2020. **396**(10256): p. 959-967.
19. Meyerowitz, E.A., et al., *Rethinking the role of hydroxychloroquine in the treatment of COVID-19.* The FASEB Journal, 2020. **34**(5): p. 6027-6037.
20. Jankelson, L., et al., *QT prolongation, torsades de pointes, and sudden death with short courses of chloroquine or hydroxychloroquine as used in COVID-19: A systematic review.* Heart Rhythm, 2020.
21. Ray, W.M., K. ; Hall, K.; Arbogast, P.; Stein, M., *Azithromycin and the Risk of Cardiovascular Death.* The New England Journal of Medicin, 2012.
22. Bessière, F., et al., *Assessment of QT Intervals in a Case Series of Patients With Coronavirus Disease 2019 (COVID-19) Infection Treated With Hydroxychloroquine Alone or in Combination With Azithromycin in an Intensive Care Unit.* JAMA Cardiology, 2020.
23. Chorin, E., et al., *QT Interval Prolongation and Torsade De Pointes in Patients with COVID-19 treated with Hydroxychloroquine/Azithromycin.* Heart Rhythm, 2020.
24. Mathur, A., et al., *Human iPSC-based cardiac microphysiological system for drug screening applications.* Sci Rep, 2015. **5**: p. 8883.
25. Nunes, S.S., et al., *Biowire: a platform for maturation of human pluripotent stem cell-derived cardiomyocytes.* Nat Methods, 2013. **10**(8): p. 781-7.
26. Loskill, P., et al., *muOrgano: A Lego(R)-Like Plug & Play System for Modular Multi-Organ-Chips.* PLoS One, 2015. **10**(10): p. e0139587.
27. Si, L., et al., *Human organs-on-chips as tools for repurposing approved drugs as potential influenza and COVID19 therapeutics in viral pandemics.* 2020.
28. Tang, H., et al., *Human Organs-on-Chips for Virology.* Trends in Microbiology, 2020.
29. Huebsch, N., et al., *Metabolically-Driven Maturation of hiPSC-Cell Derived Heart-on-a-Chip*. 2020, Cold Spring Harbor Laboratory.
30. Blinova, K., et al., *International Multisite Study of Human-Induced Pluripotent Stem Cell-Derived Cardiomyocytes for Drug Proarrhythmic Potential Assessment.* Cell Reports, 2018. **24**(13): p. 3582-3592.
31. Yang, Z., et al., *Azithromycin Causes a Novel Proarrhythmic Syndrome.* Circulation: Arrhythmia and Electrophysiology, 2017. **10**(4): p. e003560.
32. Asensio, E., et al., *Recommendations for the measurement of the QT interval during the use of drugs for COVID-19 infection treatment. Updatable in accordance with the availability of new evidence.* Journal of Interventional Cardiac Electrophysiology, 2020.
33. Blinova, K., et al., *Comprehensive Translational Assessment of Human-Induced Pluripotent Stem Cell Derived Cardiomyocytes for Evaluating Drug-Induced Arrhythmias.* Toxicol Sci, 2017. **155**(1): p. 234-247.

34. Sharma, T.S., et al., *Hydroxychloroquine Use Is Associated With Decreased Incident Cardiovascular Events in Rheumatoid Arthritis Patients.* Journal of the American Heart Association, 2016. **5**(1): p. e002867.
35. Vouri, S.M., T.N. Thai, and A.G. Winterstein, *An evaluation of co-use of chloroquine or hydroxychloroquine plus azithromycin on cardiac outcomes: A pharmacoepidemiological study to inform use during the COVID19 pandemic.* Research in Social and Administrative Pharmacy, 2020.
36. Chorin, E., et al., *The QT Interval in Patients with SARS-CoV-2 Infection Treated with Hydroxychloroquine/Azithromycin.* 2020.
37. M. Hondeghem, L., L. Carlsson, and G. Duker, *Instability and Triangulation of the Action Potential Predict Serious Proarrhythmia, but Action Potential Duration Prolongation Is Antiarrhythmic.* Circulation, 2001. **103**(15): p. 2004-2013.
38. Cipriani, A., et al., *Arrhythmic profile and 24-hour QT interval variability in COVID-19 patients treated with hydroxychloroquine and azithromycin.* International Journal of Cardiology, 2020.
39. Sandoval, Y., J.L. Januzzi, and A.S. Jaffe, *Cardiac Troponin for Assessment of Myocardial Injury in COVID-19.* Journal of the American College of Cardiology, 2020. **76**(10): p. 1244-1258.
40. F Pontén, K.J., M Uhlen, *The Human Protein Atlas--a tool for pathology* The journal of pathology, 2008. **216**(4): p. 387-393.
41. Luciano Babuin, A.S.J., *Troponin: the biomarker of choice for the detection of cardiac injury.* CMAJ, 2005. **173**(10).
42. Hallerdei, J., et al., *T Tubules and Surface Membranes Provide Equally Effective Pathways of Carbonic Anhydrase-Facilitated Lactic Acid Transport in Skeletal Muscle.* PLoS ONE, 2010. **5**(12): p. e15137.
43. Marie A. Schroedera, M.A.A., Alzbeta Hulikovaa, Claudiu T. Supuranb, Kieran Clarkea,Richard D. Vaughan-Jonesa, Damian J. Tylera, and Pawel Swietacha, *Extramitochondrial domain rich in carbonic anhydraseactivity improves myocardial energetics.* PNAS physiology, 2013.
44. Huebsch, N., et al., *Automated Video-Based Analysis of Contractility and Calcium Flux in Human-Induced Pluripotent Stem Cell-Derived Cardiomyocytes Cultured over Different Spatial Scales.* Tissue Engineering Part C: Methods, 2015. **21**(5): p. 467-479.
45. Gautret, P., et al., *Hydroxychloroquine and azithromycin as a treatment of COVID-19: results of an open-label non-randomized clinical trial.* International Journal of Antimicrobial Agents, 2020. **56**(1): p. 105949.
46. Drugbank, *Hydroxychloroquine, https://www.drugbank.ca/drugs/DB01611.*
47. Liu, P., et al., *Comparative pharmacokinetics of azithromycin in serum and white blood cells of healthy subjects receiving a single-dose extended-release regimen versus a 3-day immediate-release regimen.* Antimicrob Agents Chemother, 2007. **51**(1): p. 103-9.
48. Vincent Mazet, C.C., DavidBrie, Jérôme Idier, Bernard Humbert, *Background removal from spectra by designing and minimising a non-quadratic cost function.* Chemometrics and Intelligent Laboratory Systems, 2005. **76**(2): p. 121-133.
49. Zhilin Qu , L.-H.X., Riccardo Olcese, Hrayr S Karagueuzian, Peng-Sheng Chen, Alan Garfinkel, James N Weiss, *Early afterdepolarizations in cardiac myocytes:*

beyond reduced repolarization reserve Cardiovascular Research, 2013. **99**(1): p. 6-15.
50. Diana X Tran , D.S., Arik Yochelis, James N Weiss, Alan Garfinkel, Zhilin Qu, *Bifurcation and chaos in a model of cardiac early afterdepolarizations* Physical Review Letter, 2009. **102**(25).
51. Daisuke Sato, L.-H.X., Ali A. Sovari, Diana X. Tran, Norishige Morita, Fagen Xie, Hrayr Karagueuzian, Alan Garfinkel, James N. Weiss, and Zhilin Qu, *Synchronization of chaotic early afterdepolarizations in the genesis of cardiac arrhythmias.* PNAS, 2009. **106**(9): p. 2893-2988.
52. Yuanfang Xie , G.H., Daisuke Sato, James N Weiss, Alan Garfinkel, Zhilin Qu, *Dispersion of refractoriness and induction of reentry due to chaos synchronization in a model of cardiac tissue* Physical Review Letter, 2007. **99**(11).
53. Vandenberk, B., et al., *Which QT Correction Formulae to Use for QT Monitoring?* Journal of the American Heart Association, 2016. **5**(6): p. e003264.
54. Erika Assarsson , et al., *Homogenous 96-Plex PEA Immunoassay Exhibiting High Sensitivity, Specificity, and Excellent Scalability.* PLOS ONE, 2014.
55. J N Weiss , A.G., H S Karagueuzian, Z Qu, P S Chen, *Chaos and the transition to ventricular fibrillation: a new approach to antiarrhythmic drug evaluation.* Circulation, 1999. **99**(21): p. 2819-2826.

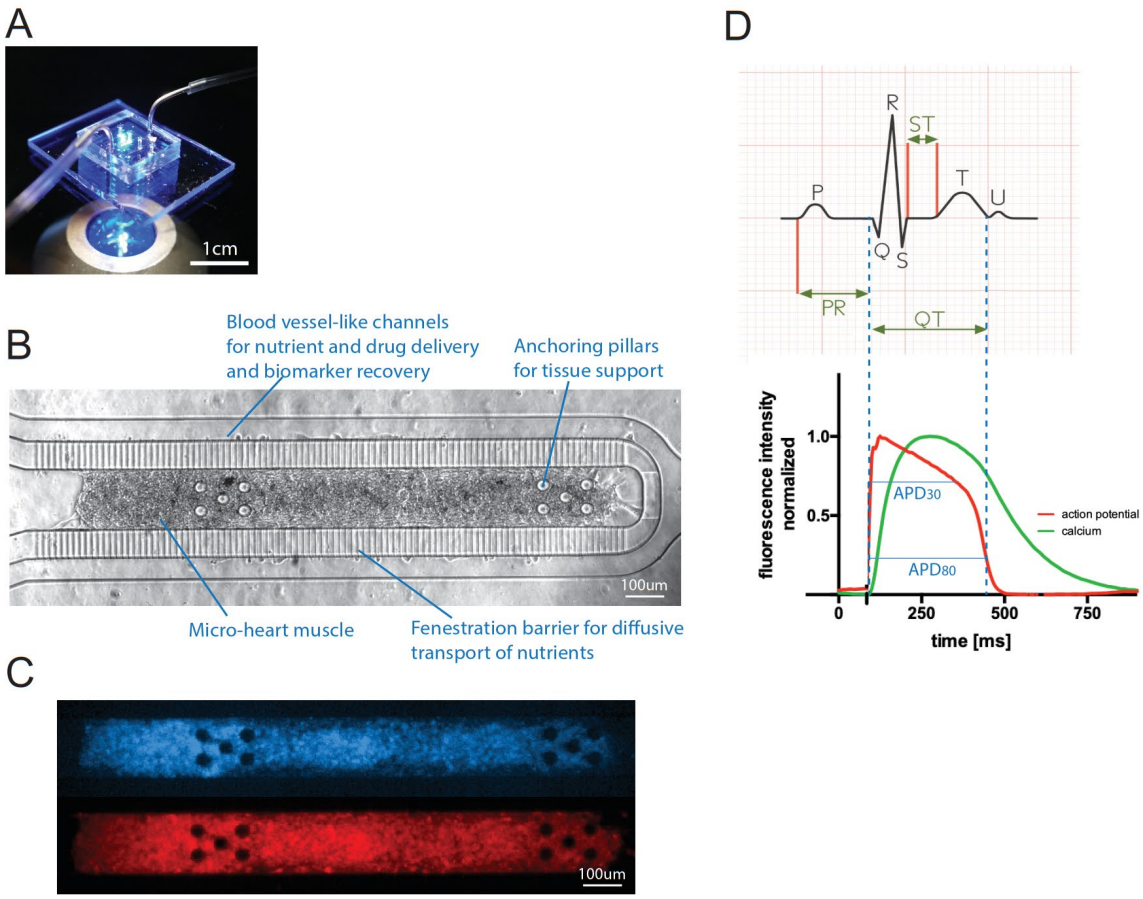
A
1cm
B
Blood vessel-like channels
for nutrient and drug delivery
and biomarker recovery
Anchoring pillars
for tissue support
100um
Micro-heart muscle
Fenestration barrier for diffusive
transport of nutrients
C
100um
D
R
ST
T
P
U
Q
S
PR
QT
fluorescence intensity
normalized
1.0
0.5
APD30
APD80
action potential
calcium
0
250
500
750
time [ms]

Figure 1

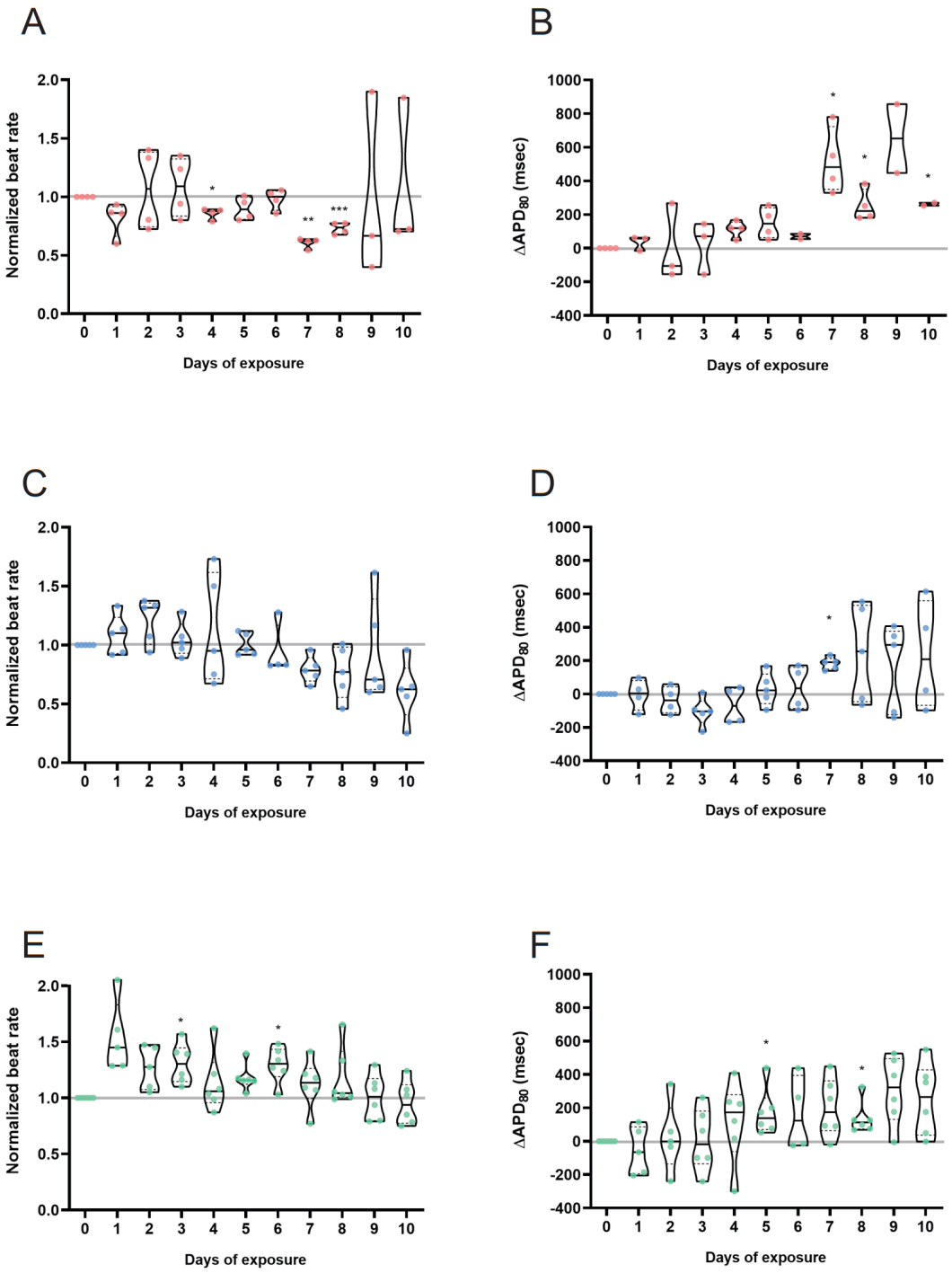
A
Normalized beat rate
2.0
1.5
1.0
0.5
0.0
0 1 2 3 4 5 6 7 8 9 10
Days of exposure
B
ΔAPD80 (msec)
1000
800
600
400
200
0
-200
-400
0 1 2 3 4 5 6 7 8 9 10
Days of exposure
C
Normalized beat rate
2.0
1.5
1.0
0.5
0.0
0 1 2 3 4 5 6 7 8 9 10
Days of exposure
D
ΔAPD80 (msec)
1000
800
600
400
200
0
-200
-400
0 1 2 3 4 5 6 7 8 9 10
Days of exposure
E
Normalized beat rate
2.0
1.5
1.0
0.5
0.0
0 1 2 3 4 5 6 7 8 9 10
Days of exposure
F
ΔAPD80 (msec)
1000
800
600
400
200
0
-200
-400
0 1 2 3 4 5 6 7 8 9 10
Days of exposure

Figure 2

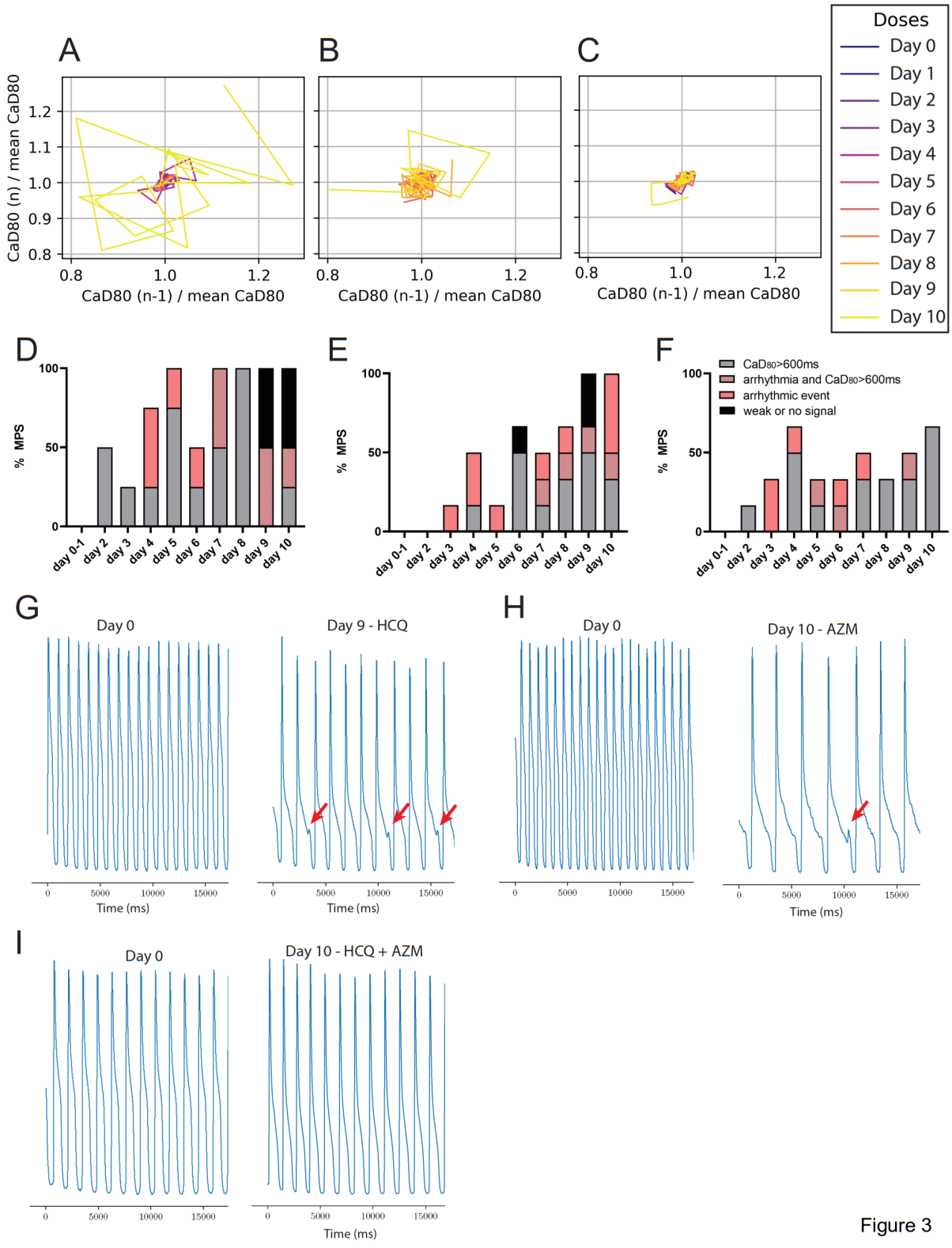
A
B
C
Doses
Day 0
Day 1
Day 2
Day 3
Day 4
Day 5
Day 6
Day 7
Day 8
Day 9
Day 10
CaD80 (n) / mean CaD80
CaD80 (n-1) / mean CaD80
D
E
F
% MPS
CaD80>600ms
arrhythmia and CaD80>600ms
arrhythmic event
weak or no signal
day 0-1
day 2
day 3
day 4
day 5
day 6
day 7
day 8
day 9
day 10
G
H
I
Day 0
Day 9 - HCQ
Day 10 - AZM
Day 10 - HCQ + AZM
Time (ms)

Figure 3

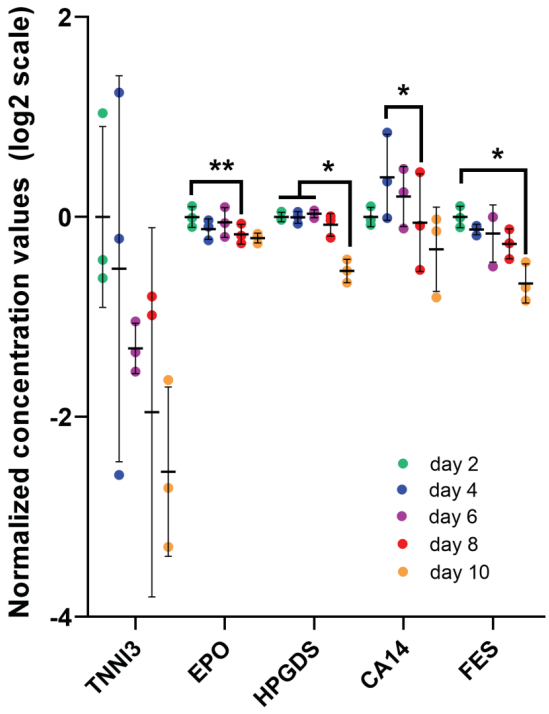
Normalized concentration values (log2 scale)
2
0
-2
-4
**
*
*
*
day 2
day 4
day 6
day 8
day 10
TNNI3
EPO
HPGDS
CA14
FES

Figure 4

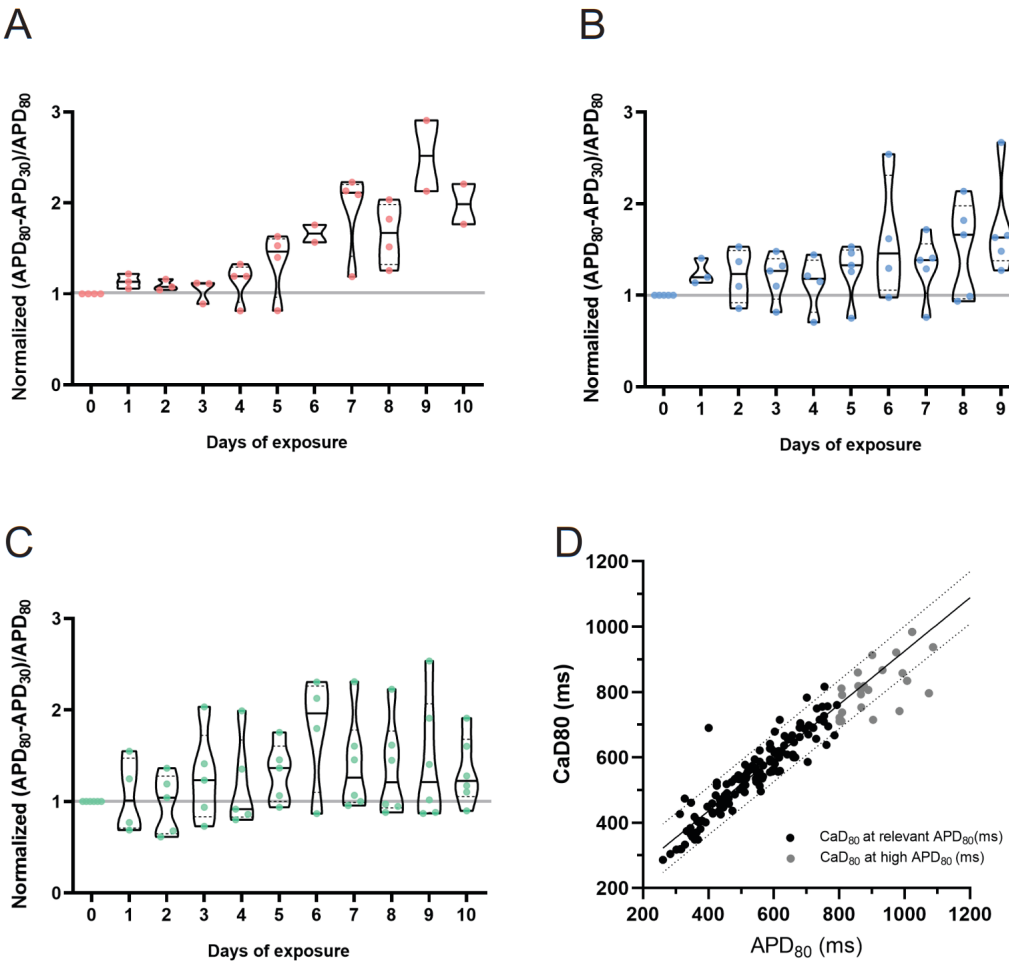

Supp. Figure 1

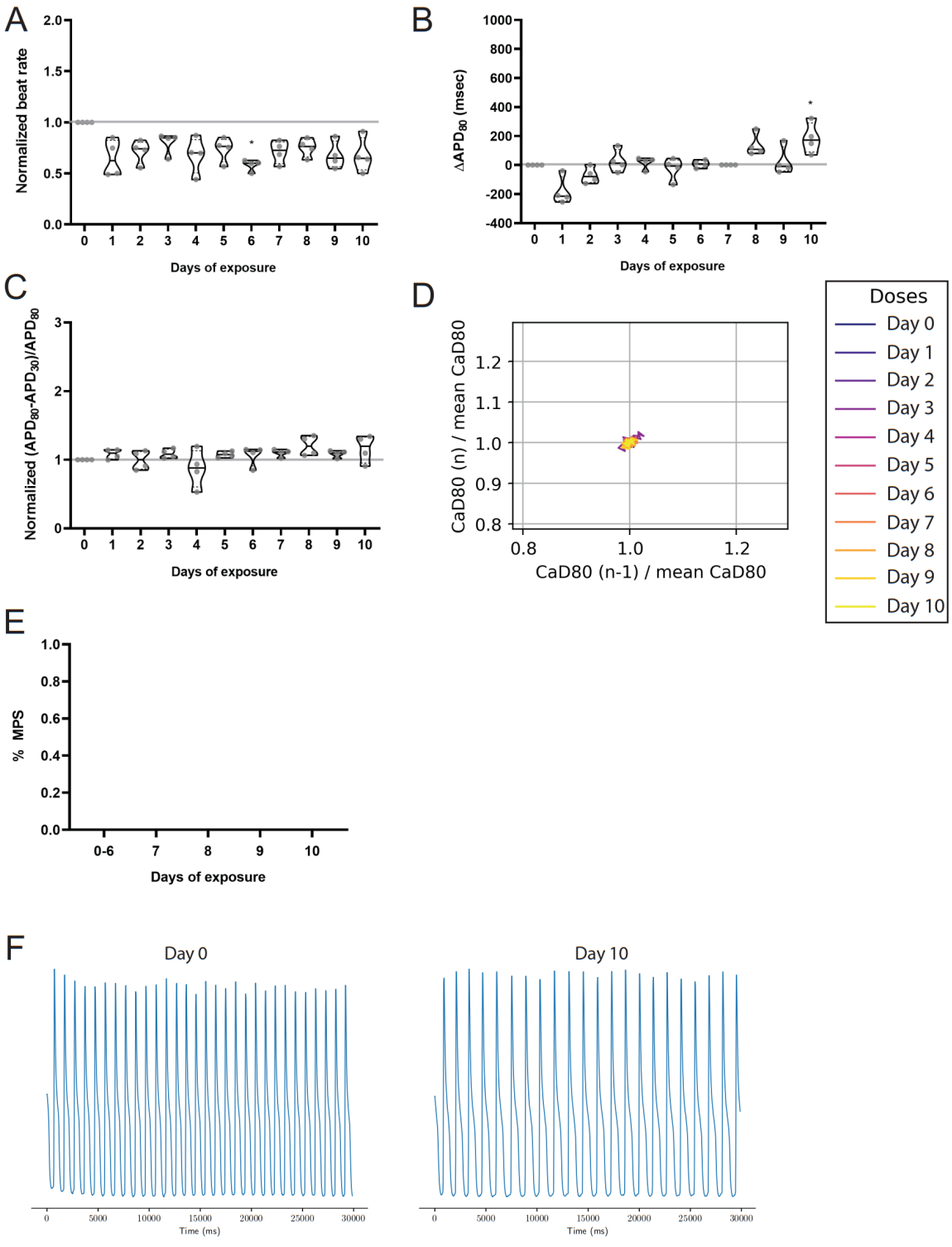

Supp. Figure 2

Chapter 5 Heart Microphysiological System to Assess Cardiac Liability Prediction of COVID19 Therapeutics

5.1 Abstract

Despite global efforts, it took seven months between the official announcement of global pandemic and the first FDA-approved medicines for the treatment of COVID-19 infection. During this timeframe, clinicians focused their efforts on repurposing drugs, such as hydroxychloroquine (HCQ) or azithromycin (AZM) to treat hospitalized COVID-19 patients. While clinical trials were progressing slowly, the exponential increase in infections pressed the FDA to grant an emergency use authorization for HCQ and AZM as treatment for COVID-19 patients, although there was scarce evidence of their combined efficacy and safety. The authorization was revoked four months later, giving rise to controversial political and scientific debates illustrating important problems such as the authorization of potentially ineffective or unsafe therapeutics, while diverting resources from screening of effective drugs. Here we report on a preclinical drug screening platform, a cardiac microphysiological system (MPS), to rapidly identify clinically-relevant cardiac liabilities associated with polytherapy to treat COVID-19, such as HCQ and AZM. The cardiac MPS is a microfabricated fluidic system in which cardiac cells, derived from human induced pluripotent stem cells, self-arrange into a uniaxially beating tissue. The effect of drug response was measured using outputs that correlate with clinical measurements such QT interval (action potential duration) and drug-biomarker pairing. The cardiac microphysiological system predicted clinical arrhythmias associated with QT prolongation and rhythm instabilities in tissues treated with HCQ. We showed no change in QT interval upon acute exposure to AZM, while still observing a significant increase in arrhythmic events. These results suggest that our MPS system can not only predict arrhythmias, but it can also identify arrhythmias even when QT prolongation is absent. When exposed to HCQ and AZM polytherapy, our MPS system successfully supports clinical data, in that the combination of both drugs synergistically increase QT interval when compared to single drug exposure, while not worsening the overall frequency of arrhythmic events. The high content, user-friendly and inexpensive properties of cardiac MPS could be accessible to

clinicians and help them rapidly evaluate the cardiac safety of potential therapeutics in times of crisis, ultimately accelerating patients' access to treatments and better allocation of clinical resources.

5.2 Introduction

With an exponential increase in COVID-19 cases worldwide, almost 72 million people have been infected, leading to more than 1.6 million deaths. Despite promising vaccine results, the protection level and duration they confer is still unknown [1], and their global deployment is unlikely within the next 12 months. It is therefore critical to continue to treat infections with repurposed therapeutics. Early clinical trials identified hydroxychloroquine (**HCQ**) and azithromycin (**AZM**) as promising therapeutics to help treat or reduce the effects of SARS-CoV-2 [2-6]. By March 28th, the FDA granted an emergency use of authorization for oral administration of HCQ as treatment against COVID-19. In early June, FDA cautioned the use of HCQ for COVID-19 treatment outside of hospital settings due to reported risk of heart complications[7]. The authorization was then revoked on June 22nd 2020, as no published study since March showed effective reduction of viral load after HCQ treatment[8-12]. This process was politically and scientifically controversial and illustrated important problems that can arise with emergency drug authorizations during crises, notably the authorization of potentially ineffective or unsafe therapeutics, while diverting resources from screening of effective drugs[13]. Moreover, 250 clinical trials were started to study the efficacy of HCQ treatment for COVID-19, 80 of them a polytherapy by combining HCQ with the antibiotic AZM. Only 11 polytherapy trials were completed, while several trials were withdrawn due to adverse cardiac side effects associated with the treatments [14, 15]. Although the FDA has recently approved other therapeutics for the treatment of COVID-19, such as the anti-viral remdesivir [16], the World Health Organization (**WHO**) withdrew its approval a month later[17]. Clearly, there is an urgent need for *in vitro* screening tools to increase the speed that potential therapeutics are evaluated and reach the clinic.

To address this issue, in this study, we show the clinically predictive potential of microphysiological systems (**MPS**; also called organ-on-a-chip) for rapid screening of cardiac liabilities associated with repurposed drug polytherapy. We chose the heart as a tissue, since all drugs need to be screened for cardiac liabilities such as arrhythmias, tachycardia, QT prolongation, and Torsade's de pointes (**TdP**), all of which can lead to sudden cardiac arrest. Furthermore, as recent studies have shown that COVID-19 infections can damage the heart's contractile proteins[18], and cardiac comorbidities increase the likelihood of hospitalization and death [19-21], there is an urgency for rapid drug screening tools predictive of clinical cardiology. Our cardiac MPS is a microfabricated fluidic system, that promotes human induced pluripotent stem cells-derived cardiomyocytes (**hiPSC-CMs**) to self-arrange into a three-dimensional and organized beating cardiac muscle [22]. We further enhanced the prognostic capability of our system by exposing the tissues to

an in-house maturation media, leading to pharmacology outcomes more reminiscent of adult drug response [23, 24].

We chose HCQ and AZM as an example of polytherapy, since clinical trial data are available and the cardiac liability associated with treatment is poorly understood with no preclinical *in vitro* or animal supporting data. The latter misled the FDA into approving its emergency use for safe and efficient treatment of COVID-19. Our focus was on drug-induced proarrhythmia detection, and therefore drug dose escalation studies were conducted where we measured corrected action potential duration prolongation (**cAPD**) (i.e., a proxy for clinical QT prolongation), triangulation for arrhythmia induction, and the occurrence of early after depolarizations (**EADs**) and delayed after depolarizations (**DADs**) as a function of dose, to identify the cardiac risk for each drug tested. Employing voltage sensitive dyes and hiPSC-CMs with a genetically encoded calcium reporter, we obtained precise electrophysiology outcomes of the cardiac muscle as they were treated with HCQ and AZM.

We identified a QT increase in HCQ treated tissue, and its correlation to arrhythmic events, consistent with retrospective studies [25-27] or clinical literature [28, 29]. Our MPS shows no change in QT interval upon acute exposure to AZM, while observing a significant increase in arrhythmic events, indicating that our MPS can predict arrhythmias even though QT prolongation is absent [30]. Polytherapy showed a synergetic increase of QT interval when compared to monotherapy treatments supporting literature data that observed a worsening of QT interval increase with the combination therapy [29, 31, 32]. Finally, proteomics analysis of effluent enabled the discovery of biomarkers that were directly correlated with cardiotoxicity and showed cellular damage. The outcomes of this paper correlate with published clinical results, validating our cardiac MPS a good predictor of drug-induced arrhythmias.

5.3 Results

5.3.1 Acute exposure to hydroxychloroquine triggers QT prolongation and rhythm instability, leading to arrhythmic events and tissue death

We performed a dose escalation study for HCQ using the cardiac MPS. It is known that HCQ inhibits *hERG* and I_{Kr} potassium channels [26], triggering an increase in QT interval of cardiomyocytes. QT interval above 500ms is typically correlated with arrhythmias that are responsible for sudden death. We observed an increase of APD_{80} at the clinical C_{max} of 1μM as well as an increase in the APD triangulation after 10μM (**Figure 2A and 2C**). The beat frequency did not show a trend with increasing HCQ dose (**Figure 2B**). However, at doses above 10 μM we observed high variability in triangulation, suggesting a change in calcium transient waveform. The voltage upstroke velocity decreased at 10μM, although not significantly (**Figure 2D),** while the calcium upstroke velocity showed a dramatic decrease with HCQ increasing dose, especially at 10 and 100μM (**Figure 2E**).

Rhythm instabilities were also observed in Poincaré plots for 67% of the tissues at 10μM (**Figure 2F)**. Interestingly, APD and triangulation increases were correlated with EAD (Ca traces) and TdP-like instances (**Figure 5A).** TdP are typically observed on ECG when traces continuously change configuration and amplitude [28]. We observed arrhythmic events in 72% of the tissues at 10μM and 22% at 100μM. 78% of tissues showed weak or no beating signal at 100μM (**Figure 5D**).

5.3.2 Acute exposure to azithromycin triggers rhythm instability, correlated to arrhythmic events and tissue death

We performed a dose escalation study for AZM using the cardiac MPS. AZM is also associated with an increased risk of cardiac arrhythmia [33], although not necessarily related to QT increase [30, 34]. The APD_{80} did not show any change up to 6.7μM. At 67μM, only 12% of AZM-treated tissues were beating, and therefore, a decrease in APD_{80} was most likely due to toxicity (**Figure 3A**). We observed an increase in AP triangulation at 6.7μM (**Figure 3C**). No change was seen in beating frequency (**Figure 3B**) or AP upstroke velocity (**Figure 3D**). Calcium transient upstroke velocity, however, showed a significant decrease starting at 6.7μM (**Figure 3E**). There was a correlation of increased rhythm instability starting at 0.67μM (C_{max}) to 6.7μM, where 60% of the tissues were unstable (**Figure 3F**). A typical arrhythmic observation in AZM arrhythmic MPS were delayed after depolarization (DAD, **Figure 5B**). **Figure 5E** shows that arrhythmic events occur in 75% of the tissues at 6.7μM and by 67μM 12% of tissues showed arrhythmias, while the remaining tissues had weak or no beating signal. Compared to HCQ, AZM trended towards a lower instance of arrhythmic events.

5.3.3 Acute exposure of HCQ and AZM polytherapy triggers triangulation and rhythm instability, which correlated with arrhythmic events

As observed in HCQ alone data (**Figure 2A**), the addition of HCQ at C_{max} increased the APD_{80} significantly (**Figure 4A**). Dosing of AZM further increased the APD_{80} up to the HCQ C_{max} + AZM C_{max} (0.67μM). HCQ + 6.7μM AZM APD_{80} reverted to the baseline value, probably due to toxicity, as electrophysiology signals became weak with arrhythmic events. No change was observed in beat frequency (**Figure 4B**). The AP triangulation did not show a significant increase with 1μM HCQ alone; however, the addition of AZM increased it continuously until a significant change at the highest dose (**Figure 4C**). The combination of both drugs decreased the upstroke velocity for both AP (**Figure 4D**) and calcium (**Figure 4E**). Instabilities were also observed in 70% of the tissues, where first instabilities were observed with the addition of HCQ and the remaining ones with the increasing dose of AZM, up to 0.67μM (**Figure 4F**). Increases of QT interval accompanied

with triangulation, increased rhythm instabilities and triggered arrhythmic events. Interestingly, most arrhythmic outcomes were TdP-like events (**Figure 5C**), where traces changed shape and amplitude; the plateau phase was absent and the signal became weak. We observed the appearance of arrhythmic events in 16% of the tissues starting with HCQ only and increasing to 33% and 50% with HCQ + 0.67μM AZM. At the highest dose, 30% of remaining tissues showed weak or no beating signals (**Figure 5F**).

5.3.4 Proteomics analysis of MPS effluent show cardiotoxic biomarkers to be potentially monitored in patients treated with HCQ and/or AZM

We analyzed the effluent from the cardiac MPS microfluidic channels. We report only the most significant changes, where HCQ acute exposure showed a significant increase of different biomarkers related to cardiotoxicity at the highest dose of 100μM. We observed a significant increase of VASH1 (**Figure 6A**) and GALNT10 (**Figure 6A**) at 100μM HCQ when compared to 0μM. Cardiac troponin I, TNNI3, a well-known biomarker of cardiac injury, showed a significant increase at 100μM when compared to both 0 and 1μM HCQ (**Figure 6A**). Acute AZM exposure showed a significant decrease in EPO (Erythropoietine) (**Figure 6B)** at 67μM when compared to 0μM. Finally, we observed a decrease in TOP2B for acute HCQ+AZM combination from 1μM HCQ to 1μM HCQ with 0.67μM AZM (**Figure 6C**). No change in TNNI3 was observed for both AZM and polytherapy, suggesting that HCQ has more cardiotoxic activity on the cells.

5.4 Discussion

The maturity of hiPSC-CMs in drug screening has been a major issue challenging the 'fit for purpose' approach. By combining our cardiac MPS to create a 3D heart muscle with previously developed maturation media, we have improved the maturity of the hiPSC-CMs so that the cardiac MPS accurately predicts drug-induced effects on the heart [23, 24]. In the context of this work, HCQ has been shown to decrease beat frequency in guinea pigs via the inhibition of I_f current [35], responsible for the "funny current" present in immature cardiomyocytes [36]. In acute exposure to HCQ, we do not observe a HCQ dependent decrease in beat rate (**Figure 2B**), suggesting that our hiPSC-CM are sufficiently mature to limit the impact of I_f current on spontaneous beat rate. Similarly, no change was observed in the beating frequency over polytherapy doses (**Figure 4B**), supporting the hypothesis of matured hiPSC-CM comprising the cardiac muscle.
Maximal AP upstroke velocity is a common measure of I_{Na} [37], and is an important metric to assess safety features of drugs; its dysfunction may cause life-threatening cardiac arrhythmias by reducing cardiac excitability [38]. For HCQ, a decreasing trend in AP upstroke velocity is consistent with known HCQ-dependent I_{Na} block [39] (**Figure 2D**), while AZM can potentiate cardiac I_{Na} [30], consistent with the absence of AP upstroke

velocity change (**Figure 3D**). However, the polytherapy showed a synergistic decrease in the AP upstroke velocity when compared to monotherapy (**Figure 4D**), suggesting that HCQ-dependent block of I_{Na} dominates the effect of AZM on I_{Na}.

Maximal calcium upstroke velocity is directly correlated to the speed of sarcoplasmic reticulum Ca^{2+} release, executed by ryanodine receptors opening (RyR) [40]. HCQ has been shown to facilitate the oxidation and dysfunction of RyR [41], which negatively impacts calcium upstroke velocity. HCQ is also an I_{CaL} blocker [35], which will decrease both calcium transient upstroke velocity and amplitude [42]. We identified a decrease in calcium upstroke velocity with HCQ acute exposure (**Figure 2E**). AZM-dependent I_{Na} potentiation can also promote intracellular sodium loading, and subsequently dysregulates intracellular calcium concentration, that will lead to DAD [43] (**Figure 5B**), and a decrease in calcium transient upstroke velocity (**Figure 3E**). The polytherapy synergistically decreased the calcium transient upstroke velocity (**Figure 4E**), suggesting that and AZM-dependent I_{Na} potentiation is required in addition to 1μM HCQ to significantly decrease calcium upstroke velocity.

Increases in APD and triangulation, accompanied by instabilities (i.e., Poincaré plots), typically leads to arrhythmias [44]. HCQ has a known I_{Kr} block associated with QT prolongation and arrhythmic events [25-27]. Our experimental action potential data, are consistent with the clinical literature [28, 29] and indicate that the cardiac MPS system is a good predictor of the clinical cardiotoxicity of HCQ. Interestingly AZM has been associated with an increase in cardiovascular death, mostly through QT prolongation and arrhythmia [33, 45]. However it has also been shown that AZM lacks strong pharmacodynamic evidence of I_{Kr} inhibition [34], and that it can cause ventricular tachycardia in the absence of QT prolongation, indicating a novel proarrhythmic syndrome [30]. Both of these findings were observed in our cardiac MPS: unchanged APD_{80} up to 6.7μM AZM, with increased instabilities and arrhythmic events. The AZM data clearly show that the cardiac MPS system can not only predict arrhythmias with triangulation and instabilities, but it can also identify phenomenon by which these arrhythmias arise even though APD_{80} prolongation is absent. The latter is for critical arrhythmia prediction and has been a focus of revised International Conference on Harmonization (IHC) E14 recommendations by both the CiPA initiative [46, 47] and the pharmaceutical industry. The E14 guidance, provided by the FDA, is intended to encourage the assessment of drug effects on the QT/QTc interval as a standard part of drug development and Investigational New Drug (IND) applications [48].

The polytherapy study showed a significant increase of APD_{80}, triangulation and instability as AZM dose was escalated with constant HCQ concentration, supporting literature that observed a worsening of QT interval increase with combination therapy [29, 31, 32]. In polytherapy we observed arrhythmia in 30-50% of the tissues at C_{max} HCQ + C_{max} AZM, corresponding to clinical data where 75% of patients who were given a combination of HCQ and AZM had ventricular arrhythmias [9]. Despite the presence of arrhythmic

behavior, we did not see a significant change or trend in arrhythmia instances when comparing C_{max} HCQ to C_{max} HCQ + AZM in polytherapy recordings. The latter suggests no worsening of arrhythmic behavior when AZM is added to C_{max} HCQ. This is in concordance with clinical data, concluding that there were no significant differences in the relative likelihood of abnormal ECG findings for polytherapy compared to monotherapy [10].
The biomarker study showed an increase in numerous cardiotoxicity related proteins when tissues were exposed to HCQ (**Figure 6A**). Those included VASH1, which increase was previously shown to correlate with stiffer cardiac tissues and slower relaxation of failing human cardiomyocytes [49]. GALNT10 has a critical role for correct protein folding, secretion and stability, and its disruption in its normal function can have dramatic cardiotoxic effects [50]. Finally, a significant increase in cardiac troponin I (TNNI3), a well-known biomarker of cardiac injury [51-53], correlates well with cardiotoxicity effects and known HCQ-related troponin I increase [54]. AZM exposure significantly decreased EPO (**Figure 6B**), while the polytherapy decreased TOP2B, both responses are correlated with cardiotoxicity [55, 56] (**Figure 6C**). In cardiomyocytes, GALNT10, TOP2B are typically intracellular proteins, suggesting cellular damage of the tissues at high doses.
As infections are peaking every day, the FDA has just recently approved remdesivir (Veklury®) as the first medicine for the treatment of COVID-19, although approval was revoked by the WHO a month later. In seven months since the official declaration of global pandemic, emergency use of authorization of drugs like HCQ and AZM have been granted and revoked, due to inconclusive efficacy of the drugs to reduce viral load. In 250 clinical trials that were started, with significant costs and resources of the healthcare system, many studies had inconclusive efficacy outcomes or withdrawals due to cardiac liability issues. Collectively, our MPS system would have successfully predicted the clinical cardiology response of a number of these studies [28, 29, 31, 32], in that the combination of both drugs synergistically increase QT interval when compared to single drug exposure, while not worsening the overall frequency of arrhythmic events. Employing systems like our cardiac MPS prior to polytherapy of promising COVID-19 therapeutics would help the healthcare system rapidly evaluate the cardiac safety of potential drugs in crisis times.

5.5 Conclusion

Our cardiac MPS system, containing a 3D human heart muscle, can not only predict arrhythmias with triangulation and instabilities, but it can also identify arrhythmia that arise even though action potential duration prolongation is absent. The methodology of this study can be extended to novel more promising therapeutics, and on diseased muscle, to better understand the arrhythmic risk of patients with cardiovascular complications, who are also most likely to be seriously affected by COVID-19. The high content, controlled and cheap MPS system should help the clinicians rapidly evaluate safety properties of potential therapeutics in crisis times, and accelerate their clinical deployment.

5.6 Materials and Methods

5.6.1 Multiplexing of cardiac MPS system and fluid dynamic modeling

We optimized our previous our previously published cardiac MPS [22] on multiple fronts, including chamber design, cell composition, multiplexing and pressure driven fluidic pump. As tissues were recorded prior or during experiments, both voltage (with BERST-1 voltage sensitive dye) and calcium transient (GCAMP encoded calcium sensor) traces were recorded (**Figure 1A**). We added 5 mechanosensing pillars of 20um diameter (**Figure 1B, right**) at the top and the bottom of the cell chamber to act as a resistance against which the tissue will exercise for enhanced tissue development and contraction force (see, **Chapter 3**). When tissues were paced, one could overlap both traces together based on the exact timing of the paced signal (**Figure 1C**). The cell chamber dimensions were 1300um x 130um (**Figure 1D**). Characterization of fluid flow and wall shear stresses in the cardiac MPS was done via solving the Navier-Stokes equation using the finite element solver, COMSOL Multiphysics® (v 5.4, COMSOL, Inc. Burlington, MA, U.S.A.). The computational domain was constructed by importing the geometry of the fluidic channels of the MPS. Fluid was modeled to be Newtonian and incompressible with a density of 1 g/mL and a dynamic viscosity of 1 mPa·s, and the flow within the fluidic channels were assumed to be laminar. Inlet boundary condition was set to mass-influx (based on the design flowrate of 30 μL/min) and outlet boundary condition was set to a gauge pressure of 0 Pa. For all other boundaries (i.e. walls), no-slip conditions were applied. Discretization of the computational domain was performed using the physics driven extra fine mesh. Steady state solver was used to obtain the velocity (**Figure 1E)** as well as the wall shear stress (**Figure 1F**) profiles within the MPS. Our analyses show that the maximum values of velocity and wall shear stress within the MPS are 16mm/s and 1.6Pa, respectively. Furthermore, the simulations confirmed that the cardiac tissue is protected from the media shear stress by the endothelial-like fenestration barrier [22].

5.6.2 Fabrication of cardiac MPS

Microfluidic cardiac MPS systems were formed using an optimized version of the protocol described in our previous work[22, 23]. Each MPS consisted of four multiplexed cell-loading port leading to their respective cell culture chambers (1300μm x 130μm) and two media ports, one media inlet and outlet per MPS. The media channels run adjacent to each side of the four cell chambers, separated by an array of fenestrations (2μm x 2μm high/width) to deliver nutrients while protecting the tissue from media flow shear stress. Two step photolithography was used to fabricate the microdevice silicon wafer mold, containing the features of multiple MPS. The first photolithography step was 2μm high for the

fenestration pattern: Pirranha cleaned wafer was put onto a headway spinner where SU8 2002 (MicroChem) was poured and spun (first 500rpm for 10sec with 100rpm/sec acceleration; then 2000rpm for 30sec with 300rpm/sec acceleration). Wafer was baked for 1min at 95C, exposed at 80mJ/cm^2 UV exposure (Karl Suss MA6 mask aligner with i-line) and baked again for 2min at 95C. Non-crosslinked photoresist was developed in SU8 developed for 1min 15sec, and wafer was hard baked at 180C for 30-45min. The second layer for cell chamber and media channel (55µm high) could then be fabricated onto of the fenestration with a similar protocol. SU8 3050 (MicroChem) was used and spun (first 500rpm for 10sec with 100rpm/sec acceleration; then 3000rpm for 30sec with 300rpm/sec acceleration). Wafer was baked slowly to allow for improved resolution: starting at 30C, the temperature was increased to 65C at a rate of 10C/min. Once at 65C, temperature was kept for 10min before ramping up to 95C at a rate of 5C/3min. Wafers were kept at 95C for 45min. The wafer was then allowed to cool down slowly to room temperature before being exposed to UV at 160mJ/cm^2. Alignment marks allowed for perfect overlay of both layers. Post exposure bake was the same as previously described, with only 2min at 65C and 10min at 95C. Finally, wafers were developed for 35min in shaker and sonicator before being hard baked at 180C for 30-45min. The cardiac MPS was formed by replica molding from the silicon wafer with polydimethylsiloxane (PDMS; Sylgard 184 kit, Dow Chemical, Midland, MI) at a 10:1 ratio of Sylgard base to crosslinker. PDMS chips were then bonded to glass slides using oxygen plasma for 24sec, RF power 21W, and 100% oxygen flow.

5.6.3 Cell source

Wild type C 11 (WTC11) hiPSC was used for this study. The cell line has a single-copy of CAG-driven GCaMP6f knocked into the first Exon of the AAVS1 “safe harbor” locus [57]. It can be purchased from the Coriell Repository (# GM25256 hiPSC from fibroblast).

5.6.4 Cardiomyocyte differentiation

WTC11 hiPSC were differentiated to cardiomyocytes (CM) through small molecular manipulation of Wnt signaling pathway[58]. Thawed iPSCs were passaged three times at a density of 20,000 cells/cm2 in Essential 8 Medium (E8; Thermo Fisher, Tewksbury, MA) with 10µM Y27632 (Peprotech; Rocky Hill, NJ). The final passaging was considered as ‘day-3’ of differentiation. At day 0, the 90% confluent iPSC wells were exposed to 8µM CHIR99021 (Peprotech) and 150µg/mL L-ascorbic acid (LAA) in Roswell Park Memorial Institute Medium 1640 (RPMI) containing B-27 supplement without insulin (RPMI-I). The next day, cells were fed with RPMI-I only. On day 2, cells were exposed to 5µM IWP-2 (Peprotech) in RPMI-I for two days. On day 4, cells were fed with RPMI-I only. From then onwards, RPMI containing standard B-27 supplement with insulin (RPMI-C) was added

every second day. Typically, CM start beating on day 8 of differentiation. After 15 days, hiPSC-CM were singularized with 0.25% Trypsin (Thermo Fisher) for 10-20 minutes at 37C and subsequently plated at a density of 100,000 cells/cm2 onto Matrigel, in RPMI-C with 10μM Y27632 (‘day 0’ after replating). The next day, medium was exchanged for RPMI-C. At day 3, cells were fed with RPMI 1640 (no glucose, with pyruvate supplemented with 23mM sodium bicarbonate and 5mM Sodium L-lacate[59]) for a total of five days (exchanged every other day) to allow for cardiomyocytes only to survive. At day 8, cells were washed with dPBS and fed with RPMI-C. Two days after that, cardiomyocyte were singularized, a fraction of them was characterized by flow cytometry for Cardiac Troponin T and the remaining cells were loaded in cardiac MPS.

5.6.5 Loading of cardiomyocytes and microtissues assembly within MPS

Singularized- Lactate-purified WTC hiPSC-derived cardiomyocytes were suspended in EB20 media supplemented with 10μM Y27632. Density was calculated so that 3μL of the cell suspension corresponded to 4000 cells, that were injected into the loading port of each MPS. After 3 minutes centrifugation at 300g, MPS were inspected under the microscope. Chambers that were not filled at this point were discarded. MPS were fed with 200μl EB20 media supplemented with 10μM Y27632 into the inlet tip and gravity would allow for a constant flow to the outlet until equilibrium was reached. The following day and every other day from then on, media was changed to our in-house ‘Maturation Media’ (MM) as described in [23]. MPS tissues were allowed to mature for 10 days before any subsequent experiments were performed.

5.6.6 Pharmacology studies

Twenty four hours prior to any experiment, MPS tissues were stained with 500nM of the action potential dye, BeRST-1, synthesized and quality controlled as described by Miller et al. [60]. On the day of pharmacology study, drugs were weighted and dissolved in maturation media (**MM**) with 50nM BeRST-1 voltage dye and adjusted vehicle concentration: all AZM doses had the same solvent conc. 0.5% EtOH. Hydroxychloroquine Sulfate (PHR1782-1G, Sigma) was dissolved in PBS at 4.34mg/mL and sterile filtered to create a 10mM stock solution. The stock was always prepared fresh at the day of the experiment. Azithromycin (75199-25MG-F, Sigma) was dissolved in 100% ethanol to create a 10 mg/mL (=13.35mM) stock. The stock was stored at -20°C for up to 3 days. From the stock concentration, drugs were diluted to the highest dose tested and serial dilutions were made up to the lowest concentration range. Doses were chosen to vary around clinical C_{max} of HCQ at 1μM [6] and AZM at 0.67μM [61] (**Table 1**). We exposed tissues to 0, 0.1, 1, 10, 100, 1000* C_{max} for HCQ; 0, 0.1, 1, 10, 100* C_{max} for AZM; 1*C_{max} HCQ + 0, 0.1, 0.3, 1, 3, 10* C_{max} AZM for the polytherapy. Once the drug solutions were freshly

prepared, MPS were placed onto a heated plate (Tokai Hit, Gendoji-cho, Japan) at 37°C for 20min to let them stabilize. Their action potential was recorded and only tissues with APD<500ms were selected for study. A pressure driven pump system (Fluigent) comprising a 10-way selection valve (M-switch) and flow sensor (size M) was used for controlled and automated perfusion of increasing drug doses through the cardiac MPS. The flow sensor enabled a regular flow of 30µL/min throughout the experiment. See **Supp. Figure 1** for a schematic of the setup. When two microfluidic chips were hooked up in parallel, micrometering needle valves were included downstream of the MPS to adjust for equal flow into both sides. Each chip housed four tissue chambers (**Figure 1**). Once the tissues were selected based on their inclusion criteria (APD<500ms and good visual quality), the fresh drug solutions were added to the Fluigent system. The tubing was primed with the different drug doses and the MPS inlet was connected to the fluigent system outlet. The MPS outlet tubing was connected to an eppendorf for effluent collection. Aligator clips, connected to the ION OPTIX Myopacer Field Simulator, were attached to the stainless steel elbows of the MPS inlet and outlet to pace the tissues. Once the whole system was setup, with constant 30µL/min flowrate through the MPS, the tissues were left for 30min to stabilize. At this point, initial dose 0 recordings of spontaneous and paced activity were performed. The pump M-switch was then changing its output to the lowest drug dose, dose 0 effluent tube was replaced by an empty tube. MPS were incubated for 30 minutes. Spontaneous and paced activity was then recorded for the first dose and the process was iterated for increasing doses until all spontaneous and paced activity ceased or the highest dose was reached.

5.6.7 Image acquisition for pharmacology studies

Initial spontaneous recordings were the following: 6 and 30 seconds videos of fluorescent calcium flux as well as 6 seconds voltage dye videos. After that, the tissues were field paced at 1 or 1.5Hz (depending on the capturing frequency of different tissues) for 10 seconds (3V, 20msec bipolar pulses at 1Hz) via stainless steel elbow fluidic connectors inserted in both the media inlet and outlet. Pacing was maintained while 6 seconds calcium and voltage videos were acquired. Once spontaneous and paced recordings were performed, MPS were exposed to higher drug concentration, incubated for 30min before the next recording sequence was started. A NIKON TE300HEM microscope with a HAMAMATSU digital CMOS camera C11440 / ORCA-Flash 4.0 was used and enabled 100 frames per second videos. For fluorescence imaging, a Lumencor SpectraX Light Engine and filtered with a QUAD filter (Semrock) was used. GCaMP videos used the Cyan LED, 470nm (4x4 binning, 10ms), while BeRST-1 videos used the Far-red LED, 640ms (4x4 binning, 10ms). Videos were acquired using Nikons Nikon NIS-Elements software. Post-experiment processing was performed with an in-house developed python library that could analyze the fluorescence intensity over the time of the recording.

5.6.8 Thorough electrophysiology analysis as a proxy for clinical QT interval study and arrhythmia prediction

Clinically, QT interval increase, is often associated with arrhythmias, such as Torsade de Pointes (**TdP**) [44]. Patients with QT interval > 500ms are considered at risk for TdP [28], therefore all tissues with baseline APD > 500ms were excluded from the study. In this study, we used rate corrected action potential duration at 80-90% of its repolarization (APD_{80}) as a proxy for QT interval measurements [25]. Rate correction is performed with the Fridericia correction [62], or by using data from 1Hz paced tissues. Hondeghem et al. showed that if APD prolongation was accompanied by instability or triangulation then EADs and proarrhythmia were certain to follow [44]. In this study, we defined triangulation as (APD_{80} - APD_{30}) normalized to APD_{80}. We also used Poincaré plots to study the instances of instabilities, where the n^{th} APD_{80} is plotted against the $(n-1)^{th}$ APD_{80}, all of it normalized to the mean APD_{80}. If there are large deviations between successive APD, disorganized polygons will be observed[44]. We characterized arrhythmic instances qualitatively by studying 30 seconds long calcium traces. EAD, DAD or change in shape (loss of plateau phase) were considered arrhythmic events. If the maximal amplitude of a trace was less than 60% the one of control data, or if no beating was observed, the datapoint was qualified as weak or no beating signal.

5.6.9 Plasma protein profiling using olink multiplex panel

All effluent samples were kept at -80C until sent on dry ice and shipped to Olink Proteomics for toxicity and damage protein quantification. Olink Proteomics uses multiplex proximity extension assay (PEA) panels [63], where two matched antibodies labelled with unique DNA oligonucleotides simultaneously bind to a target protein in solution. Their DNA oligonucleotides will hybridize into a double-stranded DNA “barcode” which is unique for the specific antigen and quantitatively proportional to the initial concentration of target protein. The hybridization and extension are followed by PCR amplification and the amplicon is then finally quantified by microfluidic qPCR using Fluidigm BioMark HD system (Fluidigm Corporation. South San Francisco, California). The Organ Damage panel (https://www.olink.com/products/organ-damage-panel/) was used in this study. It consists of 92 unique markers of toxicity and cellular damage. In the data post processing, we only included experiments with > 65% of the samples above the limit of detection. The limit of detection is set at 3 standard deviation above negative control values.

5.6.10 Drug absorption into PDMS

In order to quantify the actual drug concentration available to the microtissues, drug

absorption into the device (PDMS, Polydimethylsiloxane, or tubing) was measured. Drug absorption experiments were performed via liquid chromatography-mass spectrometry (LC-MS/MS) for HCQ (**Supp. Figure 2A**) or AZM (**Supp. Figure 2B**). The drug doses were prepared the same way as for the cell experiments. The experimental setup of acute studies was replicated in the absence of cells and the effluent was collected 3 min after switching to the respective dose. Additional samples from freshly prepared drug doses were collected at control. All samples were immediately frozen at -80°C.

5.6.11 Drug free fraction in media

The binding of test compounds to plasma proteins is an important factor affecting drug efficacy, metabolism and pharmacokinetic properties. In many cases, drug efficacy is determined by the concentration of free drug (unbound), rather than the total concentration in plasma. If the drug is highly bound to plasma proteins, the amount of drug available to reach the target is reduced. We therefore measured the portion of free drug in the media with RED (rapid equilibrium analysis) assays (Thermo Scientific, 90006) to determine the media-bound versus free fraction of drug following manufacturer's instructions (**Supp. Figure 2C**). Experimental media (maturation media, MM) spiked with test compound is added to the left chamber of a commercial plate based RED (rapid equilibrium dialysis) device. Blank, isotonic sodium phosphate buffer is added to the outer chamber of the RED device and the plate is incubated at 37C. Aliquots of the buffer and MM are taken at pre-determined time points and the concentration of free and bound test compound is determined by LC/MS/MS analysis.

5.6.12 SEM

Freshly fabricated PDMS MPS were sputtered with gold/palladium (AuPd) for 60sec at 10mA to get a 10nm conductive layer at the surface (Cressington sputter coater 108 auto). The sample was then imaged in a scanning electron microscope (Quantum 3D FEG, Orion Nanofab) with the following settings : 30μm aperture, 20kV, 120 pA, 40 degree tilt, 1974x magnification, 30μs scan rate.

5.6.13 Statistics

All statistics were calculated using GraphPad Prism. All electrophysiology graphs statistics were analyzed with one-way ANOVA with Dunnett's post-hoc correction and multiple comparison to dose 0 for HCQ and AZM. Multiple comparison to no drug and and HCQ only was run for AZM + HCQ combination acute drug study. One way ANOVA, multiple comparison to dose 0 and to one another with Dunnett's post-hoc correction was also run

on the Olink proteomics graphs. Non parametric Chi-squared approximation was run for qualitative arrhythmic events assessment in a pairwise manner. Significance was determined with p-value < 0.05.

5.7 Acknowledgements

This work was funded in part by the California Institute for Regenerative Medicine DISC2-10090 (K.E.H.), NIH-NHLBI HL130417 (K.E.H.), NIH-NIGMS R35GM1195855 (E.W.M.), and the Peder Sather Center for Advanced Study (UC Berkeley). We thank Bruce Conklin (Gladstone Institutes, San Francisco, USA) for technical advice on the WTC iPSC line. We thank the Marvel Nanofabrication laboratory (UC Berkeley) and their staff for assistance and technical advices for microfabrication procedures. Professor Kevin E. Healy, Brian A. Siemons, Andrew Edwards, and Sam T. Wall have a financial relationship with Organos Inc. and both they and the company may benefit from commercialization of the results of this research.

5.8 Figure Legends

5.8.1 Figure 1. Design of the multiplexed cardiac microphysiological system (MPS).

(**A**) 20x images of a cardiac MPS loaded with 4,000 human induced pluripotent stem cell derived cardiomyocytes. Top image shows brightfield capture of the tissue, middle image shows GFP fluorescence for calcium transient recordings, and bottom shows FarRed fluorescence for the voltage dye staining. (**B**) To the left is a SEM image of the fenestrations (2 µm x 2 µm x 20 µm: h-w-l) required for protecting tissue in the cell chamber from media flow-induced shear stress while enabling diffusion of nutrients. The right SEM image is a close up on mechanosensing pillars. Both images correspond to area from panel (**A**) denoted by 1 and 2 respectively. (**C**) When tissues are paced, we could time stamp the trigger signal to temporally coordinate the action potential (AP, red) and calcium transient (Ca, green) traces. (**D**) Illustration of the 4-plex tissue chamber MPS (left) and a three dimensional schematic (right) of top (1) and bottom (2) portions of one tissue chamber, which dimensions were 1300µm x 130µm with 5 20µm diameter pillars of at the top and the bottom of the chamber. (**E**) Illustration of the fluidics velocity profile obtained with COMSOL Multiphysics on the whole chip, ranging from 30mm/s at the inlet and dropping to 16mm/s equally around each cell chamber. (**F**) Close up showing shear stress profiles in the media channels around the cell chamber (1), at the first (2) and last (3) bifurcation of the multiplex chip. Microfenestrations separating the chamber from the media channel protect the tissue from flow shear stress reaching 1.6Pa at most.

5.8.2 Figure 2. Electrophysiology analysis of acute HCQ exposure.

(**A**) Violin plot depicting the change in APD_{80} in 1Hz paced tissues over increasing doses (100μM was not shown, due to poor signal quality). Values were normalized to baseline 0μM of each tissue chamber. (**B**) Graph showing spontaneous beating frequency in Hz, for up to 10μM doses. The 100μM tissues stopped beating spontaneouly and were therefore excluded from the graph. (**C**) Change in triangulation of corrected action potential traces. Triangulation values were calculated from spontaneous recording, corrected for beat rate using the Fredericia correction. (**D**) Violin plot showing the action potential maximum upstroke velocity, calculated as the maximum of the upstroke slope of 1Hz paced traces. The 100μM data were not shown dut to poor signal quality and suspended beating. (**E**) Graph describing the maximum upstroke velocity of 1Hz paced calcium transient traces. (**F**) Representative Poincare plot of different concentrations to HCQ exposure. All tissues analyzed were within inclusion criteria of APD_{80} <500ms at baseline. Statistics run were one-way ANOVA with multiple comparison to baseline 0μM and Dunnett's post-hoc correction. * $p<0.05$; ** $p<0.01$; **** $p<0.0001$.

5.8.3 Figure 3. Electrophysiology analysis of acute AZM exposure.

(**A**) Violin plot depicting the change in APD_{80} in 1Hz paced tissues over increasing doses. Values were normalized to baseline 0μM of each respective tissue chamber. (**B**) Graph showing spontaneous beating frequency in Hz, for up to 6.7μM doses. 67μM tissues stopped beating spontaneouly and were therefore excluded from the graph. (**C**) Change in triangulation of action potential traces. Triangulation values were calculated from spontaneous recording, corrected for beat rate using the Fredericia correction. The 67μM data was not shown, due to poor signal quality. (**D**) Violin plot showing the action potential maximum upstroke velocity, calculated as the maximum of the upstroke slope of 1Hz paced traces. (**E**) Graph describing the maximum upstroke velocity of 1Hz paced calcium transient traces. (**F**) Representative Poincare plot of different concentrations to AZM exposure. All tissues analyzed were within inclusion criteria of APD_{80} <500ms at baseline. Statistics run were one-way ANOVA with multiple comparison to baseline 0μM and Dunnett's post-hoc correction. * $p<0.05$; ** $p<0.01$; *** $p<0.001$, **** $p<0.0001$.

5.8.4 Figure 4. Electrophysiology analysis of acute combination of HCQ and AZM exposure.

(**A**) Violin plot depicting the change in APD_{80} in 1Hz paced tissues over increasing doses. Values were normalized to baseline 0μM of each respective tissue. (**B**) Graph showing spontaneous beating frequency in Hz. (**C**) Change in triangulation of action potential

traces. Triangulation values were calculated from spontaneous recording, corrected for beat rate using the Fredericia correction. (**D**) Violin plot showing the action potential maximum upstroke velocity, calculated as the maximum of the upstroke slope of 1Hz paced traces. (**E**) Graph describing the maximum upstroke velocity of 1Hz paced calcium transient traces. (**F**) Representative Poincare plot of different concentrations to HCQ exposure. All tissues analyzed were within inclusion criteria of APD_{80} <500ms at baseline. Statistics run were one-way ANOVA with multiple comparison to baseline 0μM and 1μM HCQ and Dunnett's post-hoc correction. Unpaired t-test with Welch's correction were performed in (A, significant) and (C, trending with $p<0.1$) for 0μM and 1μM HCQ. * $p<0.05$; ** $p<0.01$; *** $p<0.001$, **** $p<0.0001$.

5.8.5 Figure 5. Drug induced arrhythmia for acute HCQ, AZM, and polytherapy.

(A) Representative calcium transient trace at baseline (top) and 10μM (bottom) HCQ, where early after-depolarization (EAD) can be observed (red arrow). (**B**) Representative calcium transient trace at baseline (left) and 6.7μM (right) AZM, where delayed after-depolarization (DAD) can be observed (red arrow in bottom close up). (**C**) Representative calcium transient trace at baseline (top) and 1μM HCQ combined with 2μM AZM (bottom), where calcium trace amplitude and configuration changes. (**D**) Histogram showing qualitative EAD and arrhythmic event (red) and weak signal or beating cecassion assessment (black) as percentage of total MPS (microphysiological systems) for HCQ only, AZM only (**E**) and combination therapy (**F**). Traces used were spontaneous 30 seconds recording of calcium traces.

5.8.6 Figure 6. Proteomics Analysis of MPS mono and polytherapy.

Scatter dot plot with biomarkers showing significant changes with increasing doses of HCQ alone (**A**), AZM alone (**B**) or polytherapy dose escalation (**C**). In the data post-processing, we included experiments with > 65% of samples above limit of detection. The limit of detection was set at 3 standard deviation above negative control values. Biomarkers with significant changes include VASH1, GALNT10, TNNI3, EPO, and TOP2B. Statistics run were one-way ANOVA with multiple comparison and Dunnett's post-hoc correction. * $p<0.05$; ** $p<0.01$.

5.9 Tables

5.9.1 Table 1. Drug and doses used for both acute and chronic exposure

Drug	**Primary Purpose**	**Clinical C_{max}**	**Acute drug dose (*C_{max})**
Hydroxychloroquine - HCQ *(PHR1782-1G, Sigma)*	Anti-malarial	1μM	0, 0.1, 1, 10, 100
Azithromycin - AZM *(75199-25MG-F, Sigma)*	Macrolide Antibiotic	0.67μM	0, 0.1, 1, 10, 100
HCQ+AZM combination	SARS-CoV2		**HCQ**: 0, 1, 1, 1, 1, 1, 1 **AZM**: 0, 0, 0.1, 0.3, 1, 3, 10

5.10 Supplemental Figure Legends

5.10.1 Supplemental Figure 1. Illustration of the experimental setup for automated dose escalation studies.

A pressure driven pump system comprising a 10-way selection valve (M-switch) and flow sensor (size M) was used for controlled and automated perfusion of increasing drug doses (vials with pink to blue gradient) through the cardiac MPS. The flow sensor enabled a regular flow of 30μL/min throughout the experiment. The MPS were imaged on a 37°C heated microscope stage and directly connected to a myopacer with aligator clips. Automated pacing signal was sent to the tissue typically below 3V and between 1-1.5Hz depending on the frequency at which the tissues paced. At the outlet, an eppendorf tube was connected for effluent collection and subsequent proteomics analysis.

5.10.2 Supplemental Figure 2. Drug absorption in the device components and free drug in media.

Absorption studies for dose escalation exposure to HCQ alone (**A**), or AZM alone (**B**). In dose escalation cases, the effluent was collected 3 minutes after switching to the respective dose. Graphs show normalized values to control of 0μM HCQ or 0μM AZM respectively. (**C**) Graph showing the percentage of drug (HCQ or AZM) free fraction in either experimental media (maturation media) or buffer (blank, isotonic sodium phosphate). No significant differences were observed between the media and buffer.

5.11 References

1. Callaway, E., *What Pfizer's landmark COVID vaccine results mean for the pandemic.* nature, 2020.
2. Gautret, P., et al., *Hydroxychloroquine and azithromycin as a treatment of COVID-19: results of an open-label non-randomized clinical trial.* Int J Antimicrob Agents, 2020: p. 105949.
3. Yao, X., et al., *In Vitro Antiviral Activity and Projection of Optimized Dosing Design of Hydroxychloroquine for the Treatment of Severe Acute Respiratory Syndrome Coronavirus 2 (SARS-CoV-2).* Clin Infect Dis, 2020.
4. Wang, M., et al., *Remdesivir and chloroquine effectively inhibit the recently emerged novel coronavirus (2019-nCoV) in vitro.* Cell Res, 2020. **30**(3): p. 269-271.
5. Huang, M., et al., *Treating COVID-19 with Chloroquine.* J Mol Cell Biol, 2020.
6. Xueting Yao, et al., *In Vitro Antiviral Activity and Projection of Optimized Dosing Design of Hydroxychloroquine for the Treatment of Severe Acute Respiratory Syndrome Coronavirus 2 (SARS-CoV-2).* Clinical Infectious Diseases, 2020. **71**(15): p. 732-739.
7. FDA. *FDA cautions against use of hydroxychloroquine or chloroquine for COVID-19 outside of the hospital setting or a clinical trial due to risk of heart rhythm problems*. 2020; Available from: https://www.fda.gov/drugs/drug-safety-and-availability/fda-cautions-against-use-hydroxychloroquine-or-chloroquine-covid-19-outside-hospital-setting-or.
8. Molina, J.M., et al., *No Evidence of Rapid Antiviral Clearance or Clinical Benefit with the Combination of Hydroxychloroquine and Azithromycin in Patients with Severe COVID-19 Infection.* Médecine et Maladies Infectieuses, 2020.
9. Gérard, A., et al., *"Off-label" use of hydroxychloroquine, azithromycin, lopinavir-ritonavir and chloroquine in COVID-19: A survey of cardiac adverse drug reactions by the French Network of Pharmacovigilance Centers.* Therapies, 2020.
10. Rosenberg, E.S., et al., *Association of Treatment With Hydroxychloroquine or Azithromycin With In-Hospital Mortality in Patients With COVID-19 in New York State.* JAMA, 2020.
11. Furtado, R.H.M., et al., *Azithromycin in addition to standard of care versus standard of care alone in the treatment of patients admitted to the hospital with severe COVID-19 in Brazil (COALITION II): a randomised clinical trial.* The Lancet, 2020. **396**(10256): p. 959-967.
12. Wesley H. Self, M.W.S., Lindsay M. Leither, *Effect of Hydroxychloroquine on Clinical Status at 14 Days in Hospitalized Patients With COVID-19.* JAMA, 2020: p. 2165-2176.
13. Kyle Thomson, H.N., *Emergency Use Authorizations During the COVID-19 Pandemic.* JAMA network, 2020: p. 1282-1283.
14. Andrea Natale, M. *Prophylactic Benefit of Hydroxychloroquine in COVID-19 Cases With Mild to Moderate Symptoms and in Healthcare Workers With High Exposure Risk*. 2020; Available from:

https://www.clinicaltrials.gov/ct2/show/study/NCT04371926?term=hydroxychloroquine&recrs=i&cond=Covid19&draw=2&rank=7.
15. Rupesh Agrawal, M. *Safety And Efficacy Of Hydroxychloroquine For At Risk Population (SHARP) Against COVID-19*. 2020; Available from: https://www.clinicaltrials.gov/ct2/show/study/NCT04342156?term=hydroxychloroquine&recrs=i&cond=Covid19&draw=2&rank=18.
16. FDA. *FDA Approves First Treatment for COVID-19*. 2020; Available from: https://www.fda.gov/news-events/press-announcements/fda-approves-first-treatment-covid-19.
17. Organization, W.H. *WHO recommends against the use of remdesivir in COVID-19 patients*. 2020; Available from: https://www.who.int/news-room/feature-stories/detail/who-recommends-against-the-use-of-remdesivir-in-covid-19-patients.
18. Juan A. Pérez-Bermejo, S.K., Sarah J. Rockwood, Camille R. Simoneau, David A. Joy, Gokul N. Ramadoss, Ana C. Silva, Will R. Flanigan, Huihui Li, Ken Nakamura, Jeffrey D. Whitman, Melanie Ott, Bruce R. Conklin, Todd C. McDevitt, *SARS-CoV-2 infection of human iPSC-derived cardiac cells predicts novel cytopathic features in hearts of COVID-19 patients.* BioRXIV, 2020.
19. Masataka Nishiga, D.W.W., Yaling Han, David B. Lewis, Joseph C. Wu, *COVID-19 and cardiovascular disease: from basic mechanisms to clinical perspectives.* Nature Reviews Cardiology, 2020: p. 543–558.
20. Adekunle Sanyaolu, C.O., Aleksandra Marinkovic, Risha Patidar, Kokab Younis, Priyank Desai, Zaheeda Hosein, Inderbir Padda, Jasmine Mangat, Mohsin Altaf, *Comorbidity and its Impact on Patients with COVID-19.* SN Compr Clin Med., 2020.
21. Paddy Ssentongo , A.E.S., Emily S. Heilbrunn, Djibril M. Ba, Vernon M. Chinchilli, *Association of cardiovascular disease and 10 other pre-existing comorbidities with COVID-19 mortality: A systematic review and meta-analysis.* Plos one, 2020.
22. Mathur, A., et al., *Human iPSC-based cardiac microphysiological system for drug screening applications.* Sci Rep, 2015. **5**: p. 8883.
23. Huebsch, N., et al., *Metabolically-Driven Maturation of hiPSC-Cell Derived Heart-on-a-Chip*. 2020, Cold Spring Harbor Laboratory.
24. Tveito, A., et al., *Inversion and computational maturation of drug response using human stem cell derived cardiomyocytes in microphysiological systems.* 2018.
25. Blinova, K., et al., *Comprehensive Translational Assessment of Human-Induced Pluripotent Stem Cell Derived Cardiomyocytes for Evaluating Drug-Induced Arrhythmias.* Toxicol Sci, 2017. **155**(1): p. 234-247.
26. Jankelson, L., et al., *QT prolongation, torsades de pointes, and sudden death with short courses of chloroquine or hydroxychloroquine as used in COVID-19: A systematic review.* Heart Rhythm, 2020.
27. Sharma, T.S., et al., *Hydroxychloroquine Use Is Associated With Decreased Incident Cardiovascular Events in Rheumatoid Arthritis Patients.* Journal of the American Heart Association, 2016. **5**(1): p. e002867.
28. Asensio, E., et al., *Recommendations for the measurement of the QT interval during the use of drugs for COVID-19 infection treatment. Updatable in*

accordance with the availability of new evidence. Journal of Interventional Cardiac Electrophysiology, 2020.
29. Bessière, F., et al., *Assessment of QT Intervals in a Case Series of Patients With Coronavirus Disease 2019 (COVID-19) Infection Treated With Hydroxychloroquine Alone or in Combination With Azithromycin in an Intensive Care Unit.* JAMA Cardiology, 2020.
30. Yang, Z., et al., *Azithromycin Causes a Novel Proarrhythmic Syndrome.* Circulation: Arrhythmia and Electrophysiology, 2017. **10**(4): p. e003560.
31. Mercuro, N.J., et al., *Risk of QT Interval Prolongation Associated With Use of Hydroxychloroquine With or Without Concomitant Azithromycin Among Hospitalized Patients Testing Positive for Coronavirus Disease 2019 (COVID-19).* JAMA Cardiology, 2020.
32. Chorin, E., et al., *The QT Interval in Patients with SARS-CoV-2 Infection Treated with Hydroxychloroquine/Azithromycin.* 2020.
33. Ray, W.M., K. ; Hall, K.; Arbogast, P.; Stein, M., *Azithromycin and the Risk of Cardiovascular Death.* The New England Journal of Medicin, 2012.
34. Timothy F. Simpson, R.J.K., Eric C. Stecker, *Ventricular Arrhythmia Risk Due to Hydroxychloroquine-Azithromycin Treatment For COVID-19.* American college of cardiology, 2020.
35. Capel, R.A., et al., *Hydroxychloroquine reduces heart rate by modulating the hyperpolarization-activated current If: Novel electrophysiological insights and therapeutic potential.* Heart Rhythm, 2015. **12**(10): p. 2186-2194.
36. Zhao, Z., et al., *Ion Channel Expression and Characterization in Human Induced Pluripotent Stem Cell-Derived Cardiomyocytes.* Stem Cells International, 2018. **2018**: p. 1-14.
37. Casini, S., et al., *Intracellular calcium modulation of voltage-gated sodium channels in ventricular myocytes.* Cardiovascular Research, 2009. **81**(1): p. 72-81.
38. H L Tan , M.T.B.-B., C R Bezzina, P C Viswanathan, G C Beaufort-Krol, P J van Tintelen, M P van den Berg, A A Wilde, J R Balser, *A sodium-channel mutation causes isolated cardiac conduction disease* Nature, 2001: p. 1043-1047.
39. Chatre, C., et al., *Cardiac Complications Attributed to Chloroquine and Hydroxychloroquine: A Systematic Review of the Literature.* Drug Safety, 2018. **41**(10): p. 919-931.
40. Jaimes, R., et al., *A technical review of optical mapping of intracellular calcium within myocardial tissue.* American Journal of Physiology-Heart and Circulatory Physiology, 2016. **310**(11): p. H1388-H1401.
41. Zhang, X.-L., et al., *Pharmacological and cardiovascular perspectives on the treatment of COVID-19 with chloroquine derivatives.* Acta Pharmacologica Sinica, 2020.
42. C.J. Grantham, M.B.C., *Ca2+ Influx During the Cardiac Action Potential in Guinea Pig Ventricular Myocytes.* Circularion Research, 1996.
43. Antzelevitch, C. and A. Burashnikov, *Overview of Basic Mechanisms of Cardiac Arrhythmia.* Cardiac Electrophysiology Clinics, 2011. **3**(1): p. 23-45.

44. M. Hondeghem, L., L. Carlsson, and G. Duker, *Instability and Triangulation of the Action Potential Predict Serious Proarrhythmia, but Action Potential Duration Prolongation Is Antiarrhythmic.* Circulation, 2001. **103**(15): p. 2004-2013.
45. Vouri, S.M., T.N. Thai, and A.G. Winterstein, *An evaluation of co-use of chloroquine or hydroxychloroquine plus azithromycin on cardiac outcomes: A pharmacoepidemiological study to inform use during the COVID19 pandemic.* Research in Social and Administrative Pharmacy, 2020.
46. Dutta, S., Chang, K.C., Beattie, K.A., Sheng, J., Tran, P.N., Wu, W.W., Wu, M., Strauss, D.G., Colatsky, T. & Li, Z., *Optimization of an In silico Cardiac Cell Model for Proarrhythmia Risk Assessment.* Front Physiol, 2017.
47. Dutta, S., Chang, K.C., Beattie, K.A., Sheng, J., Tran, P.N., Wu, W.W., Wu, M., Strauss, D.G., Colatsky, T. & Li, Z., *Corrigendum: Optimization of an In silico Cardiac Cell Model for Proarrhythmia Risk Assessment. .* Front Physiol 2017.
48. Food and Drug Administration, H., *International Conference on Harmonisation; guidance on E14 Clinical Evaluation of QT/QTc Interval Prolongation and Proarrhythmic Potential for Non-Antiarrhythmic Drugs; availability. Notice* Fed Regist, 2005: p. 61134-61135.
49. Christina Yingxian Chen, A.K.S., Matthew A. Caporizzo, Sam Curry, Neil A. Kelly, Kenneth Bedi, Alexey I. Bogush, Elisabeth Krämer, Saskia Schlossarek, Philip Janiak, Marie-Jo Moutin, Lucie Carrier, Kenneth B. Margulies, Benjamin L. Prosser, *Depletion of Vasohibin 1 Speeds Contraction and Relaxation in Failing Human Cardiomyocytes.* Circulation Research, 2020. **127**(2).
50. Muhammad Ramzan Manwar Hussain, D.C.H., and Min Fang, *N-acetylgalactosaminyltransferases in cancer.* Oncotarget, 2016: p. 54067–54081.
51. Sandoval, Y., J.L. Januzzi, and A.S. Jaffe, *Cardiac Troponin for Assessment of Myocardial Injury in COVID-19.* Journal of the American College of Cardiology, 2020. **76**(10): p. 1244-1258.
52. Arun Sharma, et al., *Human iPSC-Derived Cardiomyocytes are Susceptible to SARS-CoV-2 Infection*. 2020, Cold Spring Harbor Laboratory.
53. Diana Lindner, et al., *Association of Cardiac Infection With SARS-CoV-2 in Confirmed COVID-19 Autopsy Cases.* JAMA Cardiology, 2020.
54. Joyce, E., A. Fabre, and N. Mahon, *Hydroxychloroquine cardiotoxicity presenting as a rapidly evolving biventricular cardiomyopathy: key diagnostic features and literature review.* European Heart Journal: Acute Cardiovascular Care, 2013. **2**(1): p. 77-83.
55. Santhanam, A.V.R., L.V. D'Uscio, and Z.S. Katusic, *Cardiovascular Effects of Erythropoietin*, in *Cardiovascular Pharmacology - Endothelial Control*. 2010, Elsevier. p. 257-285.
56. Tolulope A. Agunbiade, R.Y.Z., Ana Barac, MD, PhD, *Heart Failure in Relation to Anthracyclines and Other Chemotherapies.* Methodist Debakey Cardiovasc J., 2019.
57. Huebsch, N., et al., *Automated Video-Based Analysis of Contractility and Calcium Flux in Human-Induced Pluripotent Stem Cell-Derived Cardiomyocytes Cultured over Different Spatial Scales.* Tissue Engineering Part C: Methods, 2015. **21**(5): p. 467-479.

58. Dunn, K.K. and S.P. Palecek, *Engineering Scalable Manufacturing of High-Quality Stem Cell-Derived Cardiomyocytes for Cardiac Tissue Repair.* Front Med (Lausanne), 2018. **5**: p. 110.
59. Tohyama, S., et al., *Distinct Metabolic Flow Enables Large-Scale Purification of Mouse and Human Pluripotent Stem Cell-Derived Cardiomyocytes.* Cell Stem Cell, 2013. **12**(1): p. 127-137.
60. Huang Y.L, W.A., E. Miller, *A Photostable Silicon Rhodamine Platform for Optical Voltage Sensing.* 2015.
61. Gautret, P., et al., *Hydroxychloroquine and azithromycin as a treatment of COVID-19: results of an open-label non-randomized clinical trial.* International Journal of Antimicrobial Agents, 2020. **56**(1): p. 105949.
62. Vandenberk, B., et al., *Which QT Correction Formulae to Use for QT Monitoring?* Journal of the American Heart Association, 2016. **5**(6): p. e003264.
63. Erika Assarsson , et al., *Homogenous 96-Plex PEA Immunoassay Exhibiting High Sensitivity, Specificity, and Excellent Scalability.* PLOS ONE, 2014.

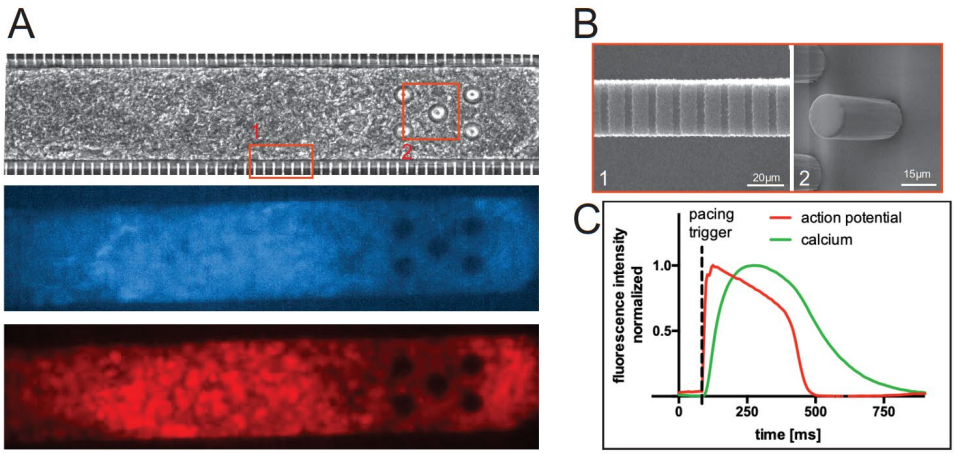
A
1
2
B
1
20µm
2
15µm
C
pacing
trigger
action potential
calcium
fluorescence intensity
normalized
1.0
0.5
0
250
500
750
time [ms]
D
1
2
1mm
1
2
E
Velocity
[m/s]
×10⁻³
30
25
20
15
10
5
0
2
1
3
F
Shear Stress
[Pa]
2
1.8
1.6
1.4
1.2
1
0.8
0.6
0.4
0.2
0
2
1
3

Figure 1

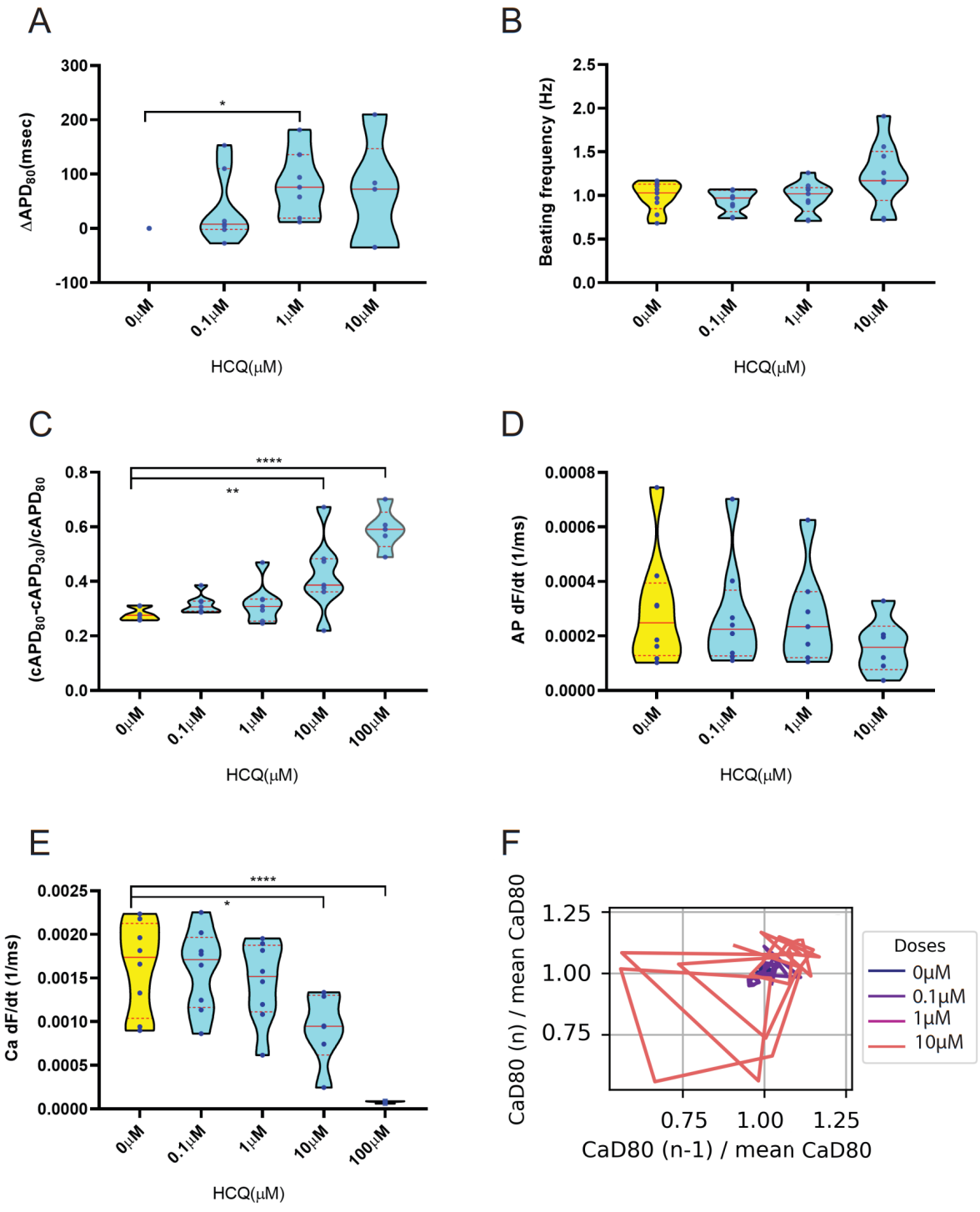
A
ΔAPD80(msec)
300
200
100
0
-100
*
0μM
0.1μM
1μM
10μM
HCQ(μM)
B
Beating frequency (Hz)
2.5
2.0
1.5
1.0
0.5
0.0
0μM
0.1μM
1μM
10μM
HCQ(μM)
C
(cAPD80-cAPD30)/cAPD80
0.8
0.6
0.4
0.2
0.0
****
**
0μM
0.1μM
1μM
10μM
100μM
HCQ(μM)
D
AP dF/dt (1/ms)
0.0008
0.0006
0.0004
0.0002
0.0000
0μM
0.1μM
1μM
10μM
HCQ(μM)
E
Ca dF/dt (1/ms)
0.0025
0.0020
0.0015
0.0010
0.0005
0.0000
****
*
0μM
0.1μM
1μM
10μM
100μM
HCQ(μM)
F
CaD80 (n) / mean CaD80
1.25
1.00
0.75
0.75
1.00
1.25
CaD80 (n-1) / mean CaD80
Doses
0μM
0.1μM
1μM
10μM

Figure 2

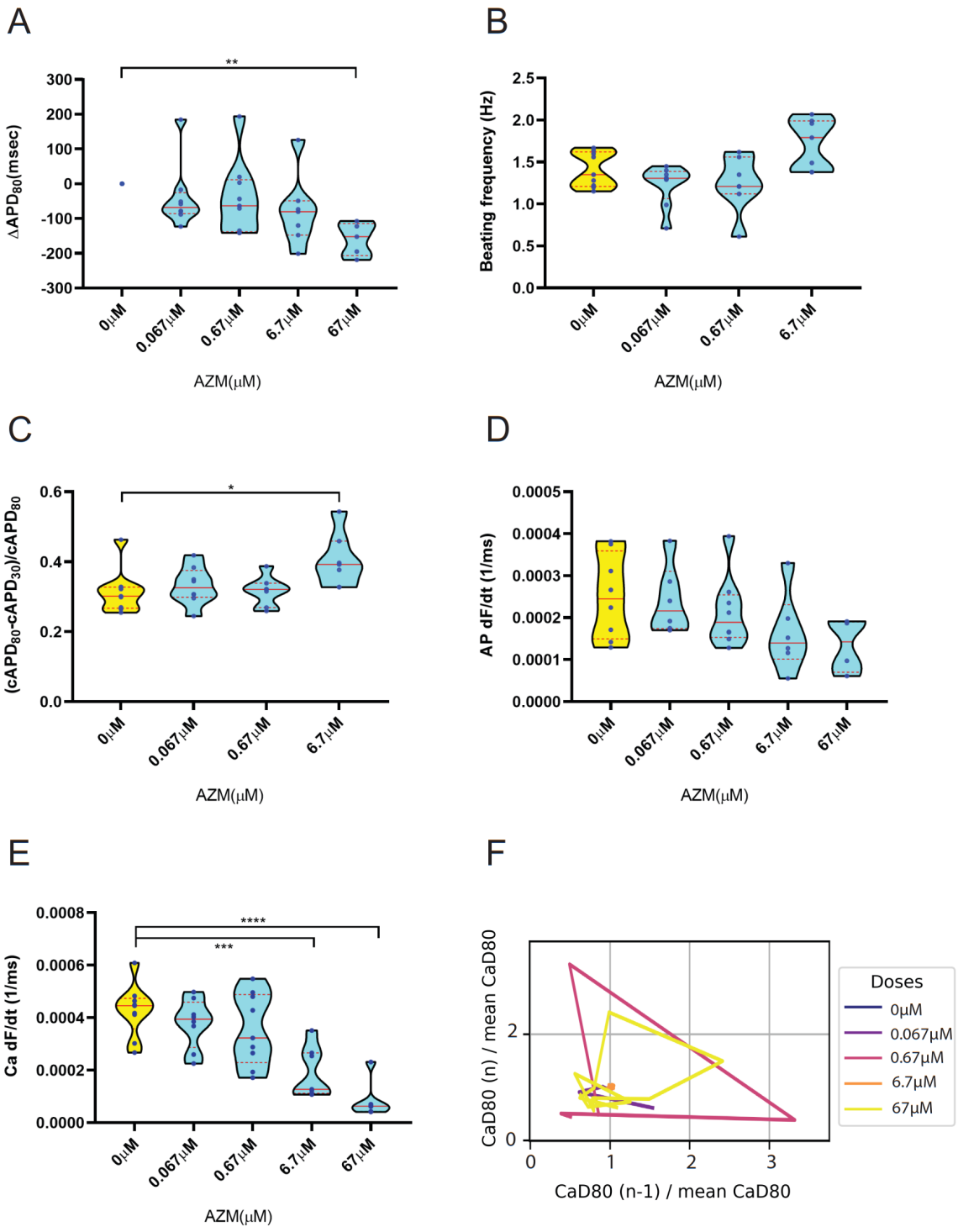
A
B
C
D
E
F
ΔAPD80(msec)
Beating frequency (Hz)
(cAPD80-cAPD30)/cAPD80
AP dF/dt (1/ms)
Ca dF/dt (1/ms)
AZM(μM)
0μM
0.067μM
0.67μM
6.7μM
67μM
**
*
***
****
CaD80 (n) / mean CaD80
CaD80 (n-1) / mean CaD80
Doses

Figure 3

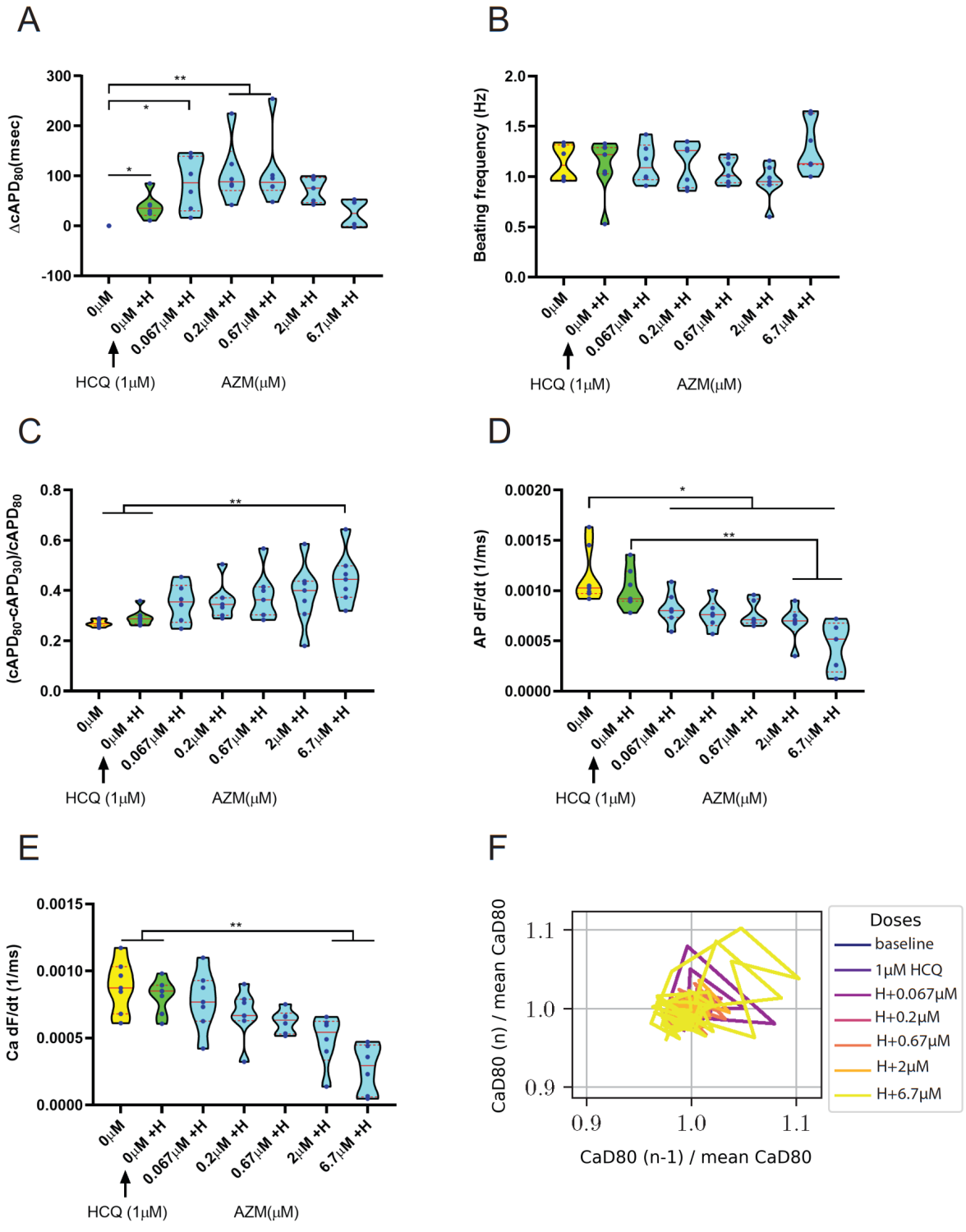
A
B
C
D
E
F
ΔcAPD80(msec)
Beating frequency (Hz)
(cAPD80-cAPD30)/cAPD80
AP dF/dt (1/ms)
Ca dF/dt (1/ms)
0μM
0μM +H
0.067μM +H
0.2μM +H
0.67μM +H
2μM +H
6.7μM +H
HCQ (1μM)
AZM(μM)
CaD80 (n) / mean CaD80
CaD80 (n-1) / mean CaD80
Doses
baseline
1μM HCQ
H+0.067μM
H+0.2μM
H+0.67μM
H+2μM
H+6.7μM

Figure 4

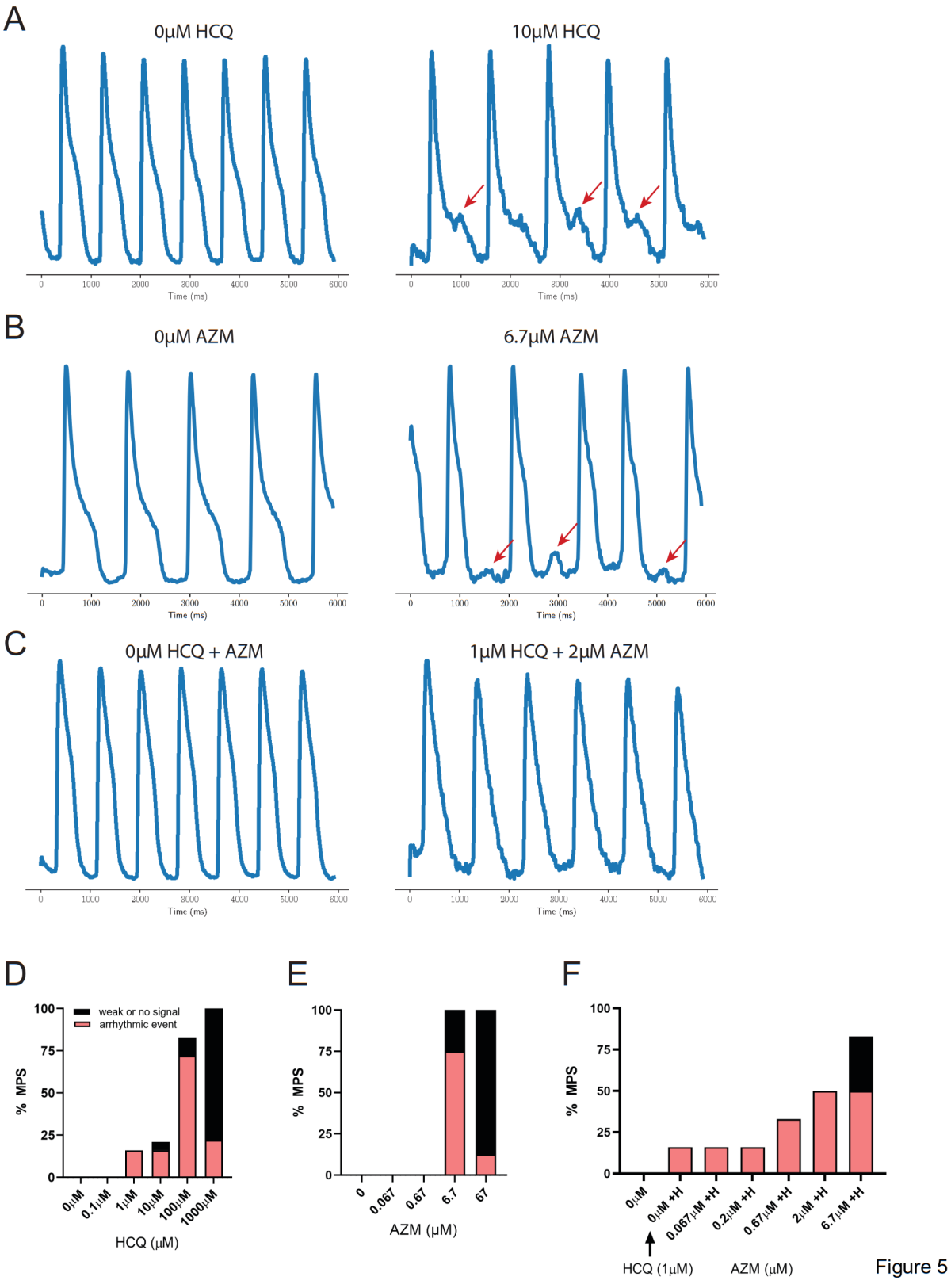
A
0μM HCQ
10μM HCQ
B
0μM AZM
6.7μM AZM
C
0μM HCQ + AZM
1μM HCQ + 2μM AZM
Time (ms)
D
E
F
weak or no signal
arrhythmic event
% MPS
HCQ (μM)
AZM (μM)
HCQ (1μM)

Figure 5

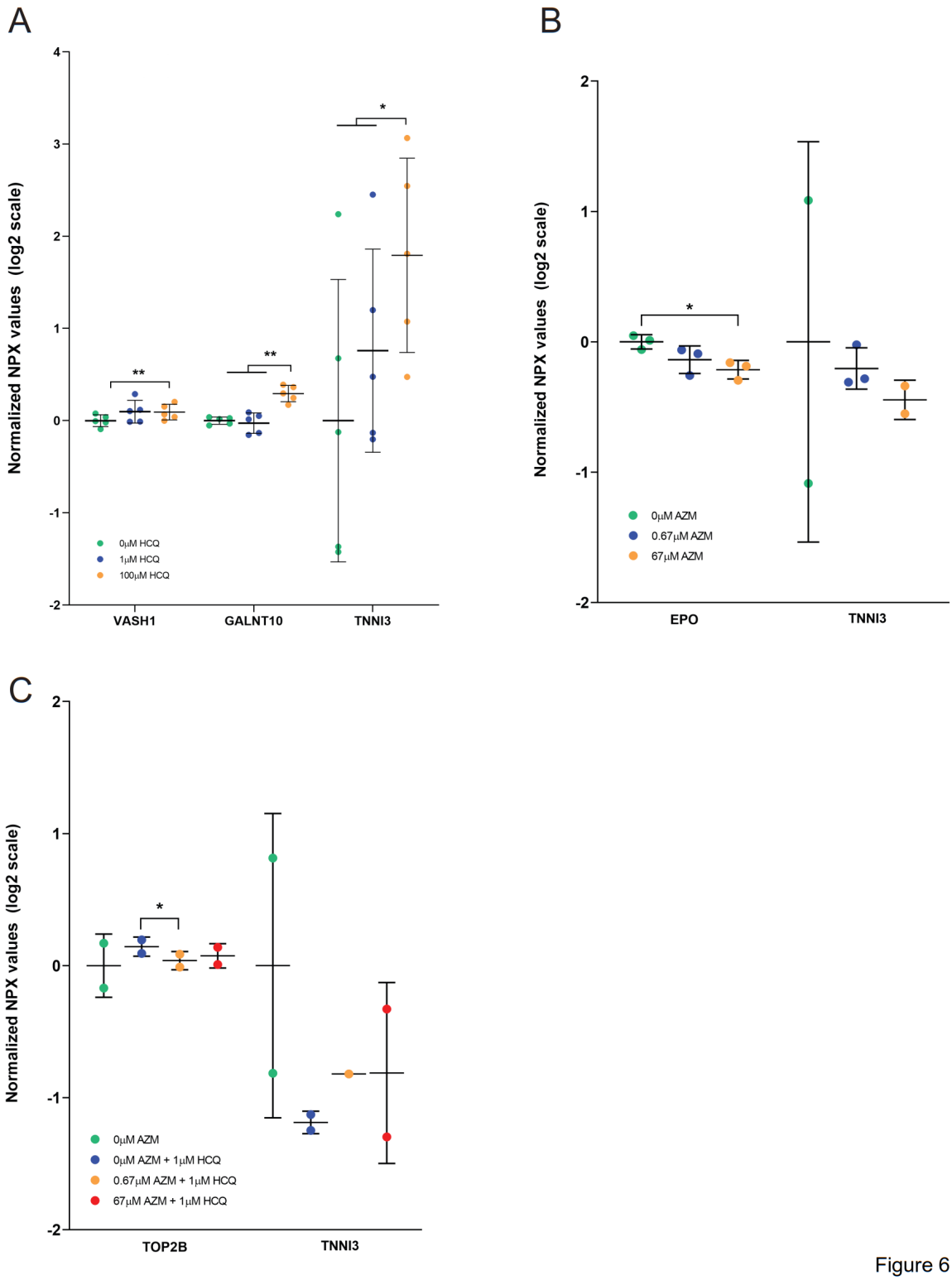
A
Normalized NPX values (log2 scale)
4
3
2
1
0
-1
-2
**
**
*
0μM HCQ
1μM HCQ
100μM HCQ
VASH1
GALNT10
TNNI3
B
Normalized NPX values (log2 scale)
2
1
0
-1
-2
*
0μM AZM
0.67μM AZM
67μM AZM
EPO
TNNI3
C
Normalized NPX values (log2 scale)
2
1
0
-1
-2
*
0μM AZM
0μM AZM + 1μM HCQ
0.67μM AZM + 1μM HCQ
67μM AZM + 1μM HCQ
TOP2B
TNNI3

Figure 6

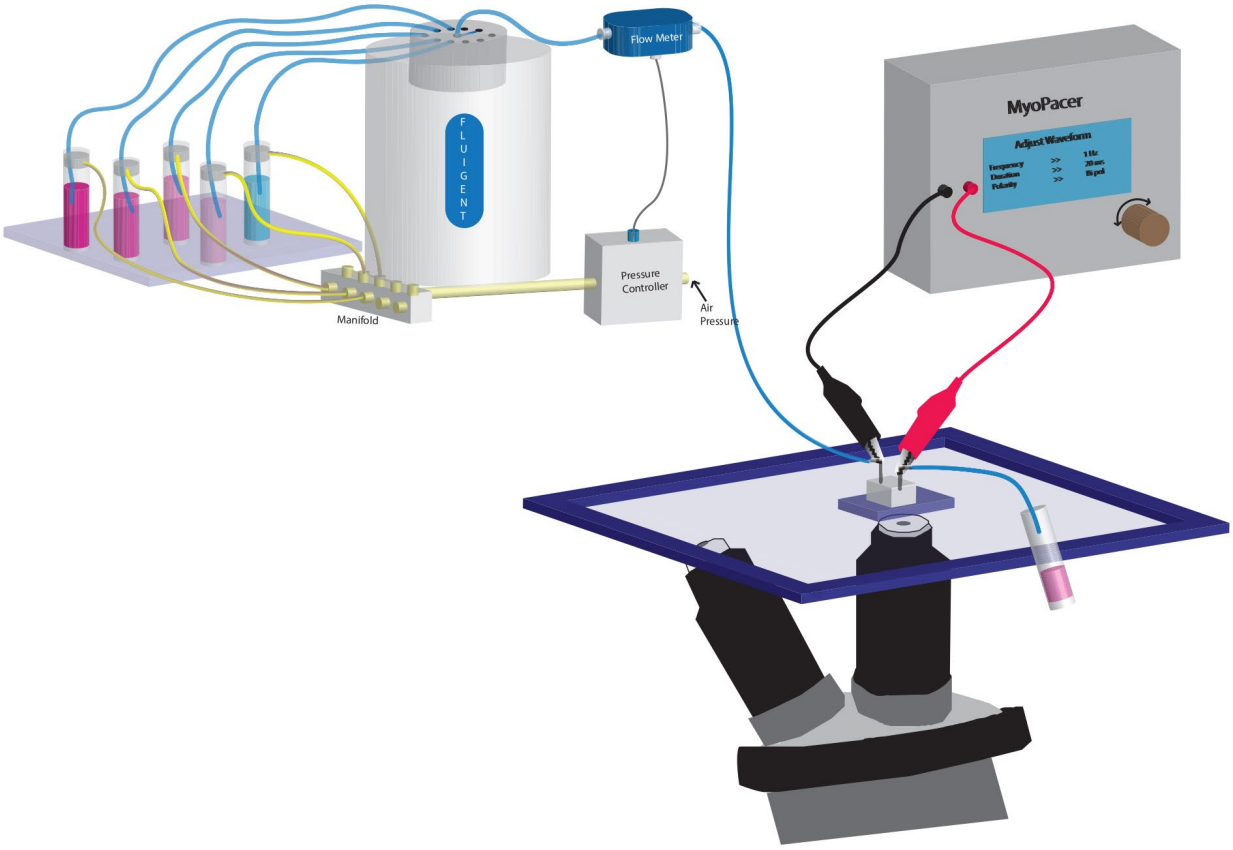

Supp. Figure 1

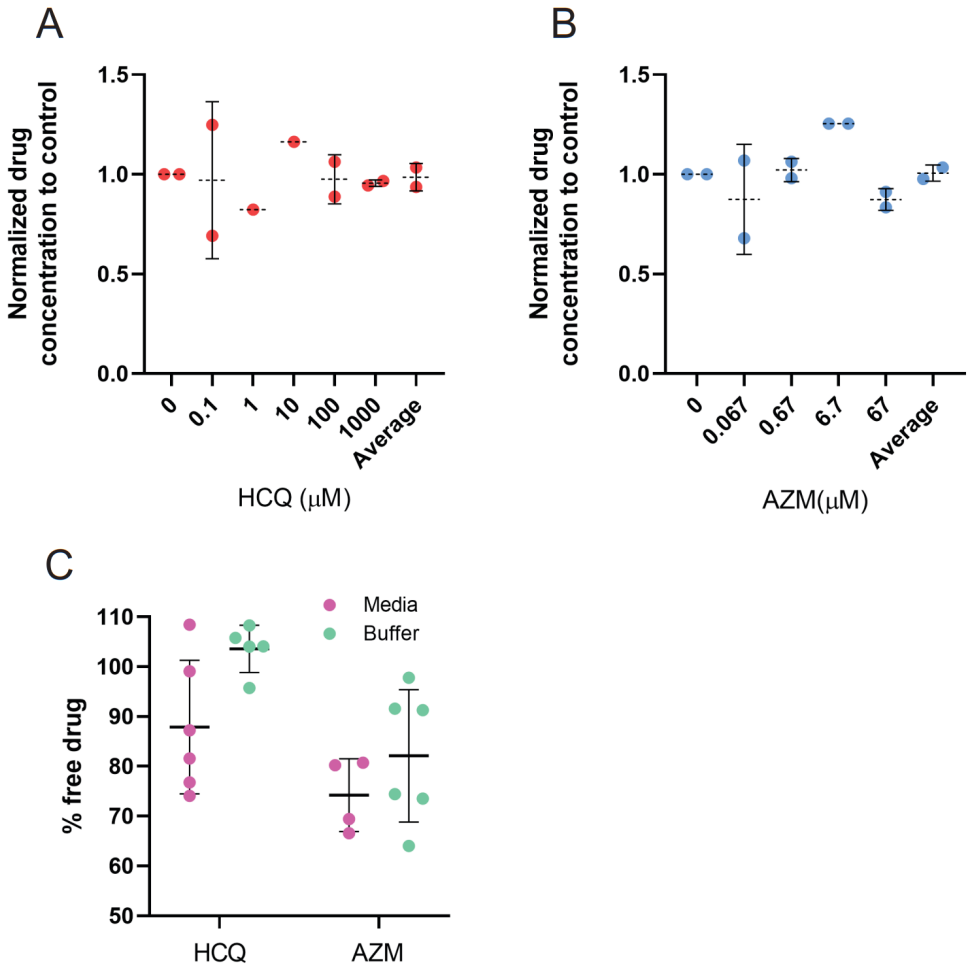

Supp. Figure 2

Chapter 6 Conclusion

In this work, we demonstrated that the combination of aligned, 3D culture in MPS with fatty-acid based media synergized to promote maturation of hiPSC-CM metabolism and electrophysiology. Combining *in silico* modeling with experimental measurements provided insights into a putative mechanism linking alterations in individual ion channels and calcium handling machinery to whole-cell changes in action potential. This is the first study to induce maturation of hiPSC-CM in a MPS, and, importantly, we demonstrated that maturation not only affected the baseline physiology of hiPSC-CM, but also yielded cells with pharmacology more reminiscent of adult human cardiomyocytes. These results suggest that maturation with fatty-acid based media may be a prerequisite to using hiPSC-CM based tissue chips to predict how drugs will affect the adult human heart.

However, this fatty acid-based media approach did not lead to consistent maturation of tissue mechanics or morphology. We therefore further improved the maturation of the tissues by screening through different confinement chamber designs and selecting for parameters that enhance mechanical, morphological and contractility outcomes of tissues while enabling for robust cell loading and tissue formation in the systems. Importantly, tissues in the final preferred design successfully showed physiological responses to drugs targeting specific mechanical pathways, making our platform relevant to accelerate drug safety and efficacy screening.

As the global pandemic of COVID-19 expanded, clinicians were pressed to treat patients with new drug combinations, in the absence of regulatory approval. Even ten months after the first cases, FDA-approved medicines for the treatment or prevention of COVID-19 are just emerging with mixed results. We extended the use of our matured platform as an analogous to a Phase I safety clinical trial, for better understanding and predicting cardiac liability associated with HCQ and AZM polytherapy and hopefully accelerate the access of patients to safe treatments. My thesis work demonstrates that a complex in vitro tissue model (i.e., cardiac MPS) can predict arrhythmias and rhythm instabilities under experimental conditions similar to a safety clinical trial. We hope our model can aid clinicians in designing clinical trials, and identify relevant biomarkers to monitor for potential COVID-19 therapeutics.

We additionally performed a dose escalation study of acute HCQ, AZM and polytherapy exposure, which, in few hours gave clinically relevant outcomes : the MPS system could not only predict arrhythmias for HCQ and polytherapy, but it could also pickup

phenomenon by which these arrhythmias arise even though QT prolongation is absent when exposed to AZM dose escalation. This final experiment shows that the cardiac MPS can rapidly evaluate safety properties of potential therapeutics in crisis times to better allocate resources for safe and meaningful clinical trials.

Collectively, I have developed a metabolically and mechanically mature heart-on-a-chip technology that provides unprecedented opportunities for high content assessment of COVID-19 therapeutics-associated cardiac liability.

Such results open doors to a variety of potential uses for our matured cardiac drug screening platform. Since the FDA has mandated that all drugs must be screened for the potential to alter ventricular repolarization prior to first in man studies, our MPS could eventually replace Phase I clinical trials not only for cardiac drugs but for all compounds. Because hiPSC-CM can be derived from different patients, we have the ability to fabricate MPS from diverse genetic population, giving the opportunity to model and predict clinical trial outcomes at a population level.

Another important application of the heart-on-chip system can be related to disease modeling and the study of dilated or hypertrophic cardiomyopathies, which represent more than 60% of the cardiomyopathies. In both cases, the long-term therapy is transplantation and very little is understood concerning the physiological properties of both myopathies, making the patients' clinical outcomes difficult to predict. Often cardiomyopathies arise from genetic defect, such as MYBPC3[1] or BAG3[2] mutation, which can be replicated on our chip through differentiation of hiPSC issued from diseased patients. There is therefore a need for human models to better understand and eventually treat those diseases.

One can also imagine using the platform to study for the cardiac impact of environmental toxins, like chemicals or plastic nanoparticles. The MPS can serve a unique role in studying toxicity and understanding complex translocation, accumulation or inflammation processes related to cardiac tissue exposure to environmental chemicals[3, 4]. This would be the first time that biological impact of environmental toxins will be performed on hiPSC-derived MPS systems.

The MPS system can also be used to study the diffusion kinetics of nanoparticles in representative human tissues. This application will be important for the study and optimization of the Cas9-sgRNA complex (RNP) delivery. As the research community is developing new RNP delivery vehicles, the editing efficiency is typically screened on 2D cell culture models which do not accurately reflect the *in vivo* environment and consequently select for delivery vehicles with poor tissue diffusion properties[5]. Using the MPS to screen through RNP delivery vectors and editing efficiency in dense cardiac tissue will significantly improve the speed at which patients will have access to gene editing technology.

Finally, the next-level application of such heart-on-chip system is the multi-organ-on-a-chip to mimic physiological aspects and biology of a whole human body, where multiple organs interact together through blood circulation in humans or microchannels in chips[6,

7]. It is indeed possible to transfer the media flow, corresponding to biological blood, from one organ-on-a-chip to another[8]. Such a complex integrated system would enable to evaluate drug ADME (absorption, distribution, metabolism, and excretion) processes in humans and study systemic toxicity: an absorbed drug will not have the same toxicity in all organs, but usually demonstrates major toxicity in the targeted organ. This is mainly due to the way it is metabolized by the body: in the liver, induction of the hepatic drug metabolizing enzyme (DME) is responsible for converting the absorbed drug into its reactive metabolites. The activity of drug deactivating enzyme (DDE) involved in deactivating chemically reactive metabolites is also critical in drug toxicity effect. Both DME and DEE's balance, their respective induction or inactivation determines the toxicological outcome of a drug and complicates the development of new drugs leading to altered efficacy. *In vitro* models are currently prone to multiple false positive results as a drug directly administered to the cardiomyocytes might not show toxic effects, unless it is metabolized by the liver or other digestive organs (stomach, intestine, kidney, etc.) previously. On the other hand, animal models result in different induction responses to chemical compounds as DME induction does not always correspond to the human model [9].

Another important cause of drug adverse side effects are drug-drug interactions (DDI), where the effect of one drug on an organ can affect the toxicity of another drug on a different organ. This complex interaction is poorly mimicked by animal models, for which multi-organ-chip systems can become a powerful predictive tool. Our laboratory has showed that the combination of our liver-MPS and cardiac-MPS provided the opportunity to investigate patient-specific drug responses and correctly predicting drug-drug interaction [10].

Body-on-chip systems have also shown to be successful in predicting process of inflammation response [11], evaluating nanoparticle interactions with human tissues [12], ADME profiling and repeated dose systemic toxicity testing [13], modeling physiological pharmacokinetics of drugs [14], or studying cancer metastasis and progression [15].

It is important to push organ-on-a-chip research towards human-on-a-chip to better represent spatial and functional complexity of human organs, predict novel therapeutic candidates during preclinical stages and eventually replace animal models thereby reducing costs and time to market and subsequently accelerate patients' access to therapeutics.

6.1 References

1. Ma, Z., et al., *Contractile deficits in engineered cardiac microtissues as a result of MYBPC3 deficiency and mechanical overload.* Nat Biomed Eng, 2018. **2**(12): p. 955-967.
2. Xi Fang, J.B., Tongbin Wu, Wei Zhang, Canzhao Liu, Jennifer Veevers, Matthew J, et al., *Loss-of-function mutations in co-chaperone BAG3 destabilize small HSPs and cause cardiomyopathy.* J. Clin. Invest., 2017: p. 3189–3200.
3. Mattsson, K., et al., *Brain damage and behavioural disorders in fish induced by plastic nanoparticles delivered through the food chain.* Sci Rep, 2017. **7**(1): p. 11452.
4. Wright, S.L. and F.J. Kelly, *Plastic and Human Health: A Micro Issue?* Environ Sci Technol, 2017. **51**(12): p. 6634-6647.
5. Rubul Mout, M.R., Gulen Yesilbag Tonga, Yi-Wei Lee, Tristan Tay, Kanae Sasaki, Vincent M Rotello, *Direct Cytosolic Delivery of CRISPR/Cas9-Ribonucleoprotein for Efficient Gene Editing* ACS Nano, 2017.
6. C. Oleaga, C.B., A. S. T. Smith, B. Srinivasan, M. Jackson, W. McLamb, V. Platt, R. Bridges, Y. Cai, N. Santhanam, B. Berry, S. Najjar, N. Akanda, X. Guo, C. Martin, G. Ekman, M. B. Esch, J. Langer, G. Ouedraogo, J. Cotovio, L. Breton, M. L. Shuler, and J. J. Hickman, *Multi-Organ toxicity demonstration in a functional human in vitro system composed of four organs.* Sci. Rep., 2016.
7. S. K. Maschmeyer I, L.A., *A four-organ-chip for interconnected long-term co-culture of human intestine, liver, skin and kidney equivalents.* Lab Chip, 2015: p. 2688–2699.
8. A. R. Perestrelo, A.C.P.Á., A. Rainer, and G. Forte, *Microfluidic organ/body-on-a-chip devices at the convergence of biology and microengineering.* Sensors (Switzerland), 2015: p. 31142–31170.
9. M. A. Mohutsky, A.R., V. Meador, W. M. Lee, J. Fowler, and S. Francke-Carroll, *Hepatic Drug-Metabolizing Enzyme Induction and Implications for Preclinical and Clinical Risk Assessment.* Toxicol. Pathol., 2010: p. 799–809.
10. Felipe T. Lee-Montiel, A.L., Laure Dumont, Caleb S. Lee, Nathaniel Huebsch, Verena Charwat, Hideaki Okochi, Matthew J. Hancock, Brian Siemons,Steven C. Boggess, Ishan Goswami, Evan W. Miller, Holger Willenbring, Kevin Healy, *Integrated hiPSC-based liver and heart microphysiological systems predict unsafe drug-drug interaction.* Biorxiv, 2020.
11. Huang NT, C.W., Oh BR, Cornell TT, Shanley TP, Fu J, Kurabayashi K, *An integrated microfluidic platform for in situ cellular cytokine secretion immunophenotyping.* Lab Chip, 2012.
12. Esch MB, M.G., Stokol T, Shuler ML, *Body-on-a-chip simulation with gastrointestinal tract and liver tissues suggests that ingested nanoparticles have the potential to cause liver injury.* Lab Chip, 2014.
13. Maschmeyer I, H.T., Jaenicke A, Lindner M, Lorenz AK, Zech J, Garbe LA, Sonntag F, Hayden P, Ayehunie S, Lauster R, Marx U, Materne EM, *Chip-based human liver-intestine and liver-skin co-cultures--A first step toward systemic repeated dose substance testing in vitro.* Eur J Pharm Biopharm, 2015.

14. Sung J.H., S.B., Esch M.B., McLamb W.T., Bernabini C., Shuler M.L., Hickman J.J. , *Using physiologically-based pharmacokinetic-guided "body-on-a-chip" systems to predict mammalian response to drug and chemical exposure.* Exp. Biol. Med., 2014.
15. Zhang Z., S.H., Lin J., Chen G., Reddy R.M., Azizi E., Fouladdel S., Chang A.C., Lin L., Jiang H., *Expansion of CTCs from early stage lung cancer patients using a microfluidic co-culture model.* Oncotarget, 2014.

Appendix I – Python Script for Automated Analysis of Electrophysiological Measurements

```
"""
Berenice Charrez / UC Berkeley / 2020
"""

import os
from collections import defaultdict, OrderedDict
import sys
import pandas as pd
import numpy as np
import matplotlib.pyplot as plt
import numbers
import csv
from pprint import pprint as pp
from scipy.stats import ttest_ind

from data_layer_ePhys import read_prev_layer
from command_line_ePhys import get_input_files, get_manual_csv

def get_pacing_freq(argument_list):
    file = str(argument_list)
    index = file.index("Hz")
    freq = str(file[index-3] + "." + file[index-2]+ file[index-1])
    return float(freq)

def get_dose_max(input_files:list):

    dose_max = 0
    for files in input_files:
            index = files.index("dose")
            dose_val = int(files[index+4])
            if dose_val>dose_max:
                dose_max = dose_val
```

```
    return dose_max

def get_dose_val(file):
    index = file.index("dose")
    dose_val = int(file[index+4])
    return dose_val

def get_chipName(file):
    path, tail = os.path.split(file)
    filename = tail.split("_")
    for i in filename:
        if i.find("Point") != -1:
            return i

def get_info_pacing(file):
    index = file.index("dose")
    pacing = str(f"{file[index+6]}{file[index+7]}{file[index+8]}")
    if pacing == "spo":
        return "False"
    if pacing == "pac":
        return "True"

    else:
        print("pacing info not found")

def process_data (metric_info:dict):
    apd30, apd80, apd90, freq, bpm = 0.0, 0.0, 0.0, 0.0, 0.0

    if not np.isnan(metric_info["beating_frequency"]):
        freq = metric_info["beating_frequency"]
        bpm = freq*60
        metric_info["bpm"] = bpm
        if metric_info["pacing"] == "True":
            if not np.isnan(metric_info["apd30"]):
                if not np.isnan(metric_info["apd80"]):
                    metric_info["apd80/apd30"] = metric_info["apd80"]/metric_info["apd30"]
                    metric_info["apd80-apd30"] = metric_info["apd80"]-metric_info["apd30"]
                    metric_info["(apd80-30)/80"] = (metric_info["apd80"]-metric_info["apd30"])/met-
ric_info["apd80"]
        elif metric_info["pacing"] == "False":
            if not np.isnan(metric_info["apd30"]):
                metric_info["c_apd30"] = metric_info["apd30"]/(freq**(-1/3))
                if not np.isnan(metric_info["apd80"]):
                    metric_info["apd80/apd30"] = metric_info["apd80"]/metric_info["apd30"]
                    metric_info["apd80-apd30"] = metric_info["apd80"]-metric_info["apd30"]
                    metric_info["c_apd80"] = metric_info["apd80"]/(freq**(-1/3))
                    metric_info["c_apd80-apd30"] = \
                        (metric_info["apd80"]/(freq**(-1/3)))-(metric_info["apd30"]/(freq**(-1/3)))
                    metric_info["(c_apd80-30)/80"] = metric_info["c_apd80-apd30"] / metric_info["c_apd80"]
```

```
                if not np.isnan(metric_info["apd90"]):
                    metric_info["c_apd90"] = metric_info["apd90"]/(freq**(-1/3))
            else:
                if not np.isnan(metric_info["apd90"]):
                    metric_info["c_apd90"] = metric_info["apd90"]/(freq**(-1/3))
        else:
            if not np.isnan(metric_info["apd80"]):
                metric_info["c_apd80"] = metric_info["apd80"]/(freq**(-1/3))
                if not np.isnan(metric_info["apd90"]):
                    metric_info["c_apd90"] = metric_info["apd90"]/(freq**(-1/3))
            else:
                if not np.isnan(metric_info["apd90"]):
                    metric_info["c_apd90"] = metric_info["apd90"]/(freq**(-1/3))

    else:
        if metric_info["pacing"] == "True":
            for key in metric_info.keys():
                if not key == "pacing":
                    metric_info[key] = np.nan  #set all at nan if beating freq bad or not paced --> ignore the chip
        else:
            if not np.isnan(metric_info["apd30"]) and not np.isnan(metric_info["apd80"]):
                    metric_info["apd80/apd30"] = metric_info["apd80"]/metric_info["apd30"]
                    metric_info["apd80-apd30"] = metric_info["apd80"]-metric_info["apd30"]

    return metric_info

def test_metric (pacing_freq: float, name:str, dose_val:int, list_name:str, \
                            metric_info:dict, manual_metrics: dict):

    for key in manual_metrics.keys():
        for val in manual_metrics[key]:
            if key == "Dose":
                assert isinstance(val, int), f"Error: type_dose expected to be "\
                    "an integer (0,1,2 etc.) but argument {val} was given."
            elif key == "Pacing":
                exp_pacing_info = [True, False]
                assert val in exp_pacing_info, f"Error: type_dose expected "\
                    "to be {exp_pacing_info} but argument {val} was given."
            elif key == "List":
                exp_list_info = ["red", "cyan", "long_cyan"]
                assert val in exp_list_info, f"Error: type_dose expected "\
                    "to be {exp_list_info} but argument {val} was given."

    key_to_change = ["apd30", "apd80", "apd90", "dFdt_max", "beating_frequency"]

    metric_info["beating_frequency"] = str(metric_info["beating_frequency"][0] +\
            metric_info["beating_frequency"][1] + metric_info["beating_frequency"][2]\
            + metric_info["beating_frequency"][3])
```

```
    for (index, nameM) in enumerate(manual_metrics["Name"]):
        if name == nameM and metric_info["pacing"] == str(manual_metrics["Pacing"][index]) \
            and dose_val == int(manual_metrics["Dose"][index]) and list_name == str(manual_met-
rics["List"][index]):
            for key in key_to_change: #overwrites value with manual input only if input is not "nan"
                if manual_metrics[key][index] == "ign" or manual_metrics[key][index] == "ign ":
                    continue
                elif manual_metrics[key][index] == "nan" or manual_metrics[key][index] == "nan ":
                    metric_info[key] = np.nan
                else:
                    metric_info[key] = float(manual_metrics[key][index])

    if metric_info["beating_frequency"] =="inf" or metric_info["beating_frequency"] =="nan":
        metric_info["beating_frequency"] = np.nan
    elif float(metric_info["beating_frequency"]) > 4:
        metric_info["beating_frequency"] = np.nan
    else:
        metric_info["beating_frequency"] = float(metric_info["beating_frequency"])
        if metric_info["pacing"] == "True" and metric_info["beating_frequency"] < (pacing_freq-0.1*pac-
ing_freq)\
                and metric_info["beating_frequency"] > (pacing_freq+0.1*pacing_freq):
                 #test if freq is within 10% of supposed frequency
            metric_info["beating_frequency"] = np.nan

    if not np.isnan(metric_info["beating_frequency"]):
        max_ePhys = (1/metric_info["beating_frequency"])*1000
        if metric_info["apd30"] < 20 and metric_info["apd30"] > max_ePhys:      #apd30 not in range 20->max
            metric_info["apd30"] = np.nan
            if metric_info["apd80"] < 100 or metric_info["apd80"] > max_ePhys:  #apd80 not in range 100-
>max
                metric_info["apd80"] = np.nan
                if metric_info["apd90"] < 100 or metric_info["apd90"] > max_ePhys:  #apd90 not in range 100-
>max
                    metric_info["apd90"] = np.nan
            else:                                                   #apd80 in range 100->max
                if metric_info["apd90"] < 100 or metric_info["apd90"] < metric_info["apd80"] \
                        or metric_info["apd90"] > max_ePhys:    #apd90 not in range 100->max or <apd80
                    metric_info["apd90"] = np.nan
        else:                                                       #apd30 in range
            if metric_info["apd80"] < 100 or metric_info["apd80"] < metric_info["apd30"] \
                    or metric_info["apd80"] > max_ePhys:   #apd80 not in range 100->max or <apd30
                metric_info["apd80"] = np.nan
                if metric_info["apd90"] < 100 or metric_info["apd90"] < metric_info["apd30"] \
                        or metric_info["apd90"] > max_ePhys:   #apd90 not in range 100->max or <apd30
                    metric_info["apd90"] = np.nan
            else:                                           #apd80 in range 100->max and >apd30
                if metric_info["apd90"] < 100 or metric_info["apd90"] < metric_info["apd80"] \
                        or metric_info["apd90"] < metric_info["apd80"] or \
                            metric_info["apd90"] > max_ePhys:  #apd90 not in range 100->max or <apd80
```

```
                metric_info["apd90"] = np.nan

    else:
        metric_info["upstroke80"] = np.nan
        metric_info["tau75"] = np.nan
        for key in key_to_change:
            metric_info[key] = np.nan

    return metric_info

def read_metric_data (f_in: str, metrics: list):
    """

    Gets metric information from results from the mechanical analysis.

    Args:
        f_in - filename/path to BF file
        metrics - list of which metrics we're interested in

    Returns:
        dictionary with metrics as keys, corresponing calculated metric
            for the given input file as values

    metrics = ["apd30","apd80", "apd90", "dFdt_max", "beating_frequency"]

    """

    metric_information = {}
    analyze_mps_results = read_prev_layer(f_in)

    dFF0_max = analyze_mps_results["unchopped_data"]["trace"].max()
    ePhys_metrics = analyze_mps_results["features"]
    bpm_metrics = analyze_mps_results["attributes"]
    pacing_metrics = str(analyze_mps_results["chopping_parameters"])

    for key in ePhys_metrics:
        for key2 in bpm_metrics:
            for metric in metrics:
                if metric == key:
                    metric_information[metric] = ePhys_metrics[key]
                elif metric == key2:
                    metric_information[metric] = bpm_metrics[key2]

    if "True" in pacing_metrics:
        metric_information["pacing"] = "True"
    elif "False" in pacing_metrics:
        metric_information["pacing"] = "False"

    return metric_information, dFF0_max
```

```
def get_metrics_across_experiments(input_files: list,
                                   list_name: str,
                                   metrics: list,
                                   processed_metrics_spont: list,
                                   processed_metrics_paced: list,
                                   dose_max:int,
                                   argument_list,
                                   pacing_freq:float):
    """

    Extract the information we need; make it into statisitcs.

    Args:
        input_files - list of nd2 files to do analysis for
        average_across - dictionary where
            keys = which kind of thing we consider (e.g. "doses")
            values = list of corresponding possible values (e.g. "dose0", "dose1")
        metrics - list of metrics we want to consider

    Returns:
        list of 4 dictionaries (mean, std, num_samples, sem) where each is a
            nested dictionary with information from average_across on first level,
            metric on second level and a single value on the third level

    """

    # first dimension: str of combination of across values; second dimension: metric
    metric_data = defaultdict(lambda: defaultdict(list))
    norm_metric_data = defaultdict(lambda: defaultdict(list))
    all_data={}
    deltaF_all = {}
    data_type=["spont", "paced"]
    for pace in data_type:
        for i in range (dose_max +1):
            all_data[f"dose{i}_{pace}"]={}
            metric_data[f"dose{i}_{pace}"]={}
            deltaF_all[f"dose{i}_{pace}"]={}

    for key in metric_data.keys():
        temp_pace = key.split("_")[1]
        if temp_pace == "spont":
            for metric in processed_metrics_spont:
                metric_data[key][metric]=[]
        elif temp_pace == "paced":
            for metric in processed_metrics_paced:
                metric_data[key][metric]=[]

    metric_information = {}
```

```
manual_metrics = get_manual_csv (argument_list)

for f_in in input_files:
    name=get_chipName(f_in)         #return chip name = Point2b
    dose_val = get_dose_val(f_in)   #return what dose it is at

    metric_information, dFF0 = read_metric_data(f_in, metrics)
    metric_information = test_metric (pacing_freq, name, dose_val, \
                    list_name, metric_information, manual_metrics)
    metric_info_processed = process_data(metric_information)    # with triangulation and cAPD:

    for key in all_data.keys():
        temp_dose = key.split("_")[0]
        temp_val = int(temp_dose[4])
        temp_pace = key.split("_")[1]

        if temp_pace == "spont":
            temp_val2 = "False"
        elif temp_pace == "paced":
            temp_val2 = "True"

        if dose_val == temp_val and metric_info_processed["pacing"] == temp_val2 :
            if temp_val2 == "False":
                all_data[f"dose{dose_val}_spont"][name] = metric_info_processed
                deltaF_all[f"dose{dose_val}_spont"][name] = dFF0
                for key2 in metric_info_processed.keys():
                    for metric in metric_data[f"dose{dose_val}_spont"]:
                        if key2 == metric and str(metric_info_processed[key2]) != "nan":
                            metric_data[f"dose{dose_val}_spont"][metric].append(metric_info_processed[key2])
            elif temp_val2 == "True":
                all_data[f"dose{dose_val}_paced"][name] = metric_info_processed
                deltaF_all[f"dose{dose_val}_paced"][name] = dFF0
                for key2 in metric_info_processed.keys():
                    for metric in metric_data[f"dose{dose_val}_paced"]:
                        if key2 == metric and str(metric_info_processed[key2]) != "nan":
                            metric_data[f"dose{dose_val}_paced"][metric].append(metric_info_processed[key2])

norm_all_data = normalize (all_data, dose_max)

# Instantiate
norm_metric_data = {}
for key in norm_all_data.keys():
    norm_metric_data[key] = {}
    for name in norm_all_data[key]:
        for metric in norm_all_data[key][name]:
            norm_metric_data[key][metric] = []
# Append
```

```
    for key in norm_all_data.keys():
        for name in norm_all_data[key].keys():
            for metric in norm_all_data[key][name]:
                norm_metric_data[key][metric].append(norm_all_data[key][name][metric])

    stats = calc_stats(metric_data)
    norm_stats = calc_stats(norm_metric_data)

    return stats, norm_stats, all_data, norm_all_data, deltaF_all

def normalize(all_data:dict, dose_max:int):

    name_spont = []
    name_paced = []
    norm_all_data = defaultdict(lambda: defaultdict(list))

    for key in all_data.keys():
        norm_all_data[key] = {}
        for chip in all_data["dose0_spont"]:
            name_spont.append(chip)
        for chip in all_data["dose0_paced"]:
            name_paced.append(chip)
        for name in all_data[key]:
            norm_all_data[key][name] = {}
    for name in name_spont:
        for i in range (dose_max+1):
            if name in all_data[f"dose{i}_spont"]:
                for data_metric in all_data[f"dose{i}_spont"][name]:
                    if data_metric in all_data["dose0_spont"][name] and data_metric != "pacing" \
                            and str(all_data["dose0_spont"][name][data_metric]) != "nan" \
                            and str(all_data[f"dose{i}_spont"][name][data_metric]) != "nan":
                        norm_all_data[f"dose{i}_spont"][name][data_metric] = \
                        (all_data[f"dose{i}_spont"][name][data_metric])/(all_data["dose0_spont"][name][data_met-
ric])
                        if data_metric == "c_apd80":
                            norm_all_data[f"dose{i}_spont"][name][f"delta_{data_metric}"] = \
                                (all_data[f"dose{i}_spont"][name][data_metric])-
(all_data["dose0_spont"][name][data_metric])
    for name in name_paced:
        for i in range (dose_max+1):
            if name in all_data[f"dose{i}_paced"]:
                for data_metric in all_data[f"dose{i}_paced"][name]:
                    if data_metric in all_data["dose0_paced"][name] and data_metric != "pacing" \
                            and str(all_data["dose0_paced"][name][data_metric]) != "nan" \
                            and str(all_data[f"dose{i}_paced"][name][data_metric]) != "nan":
                        norm_all_data[f"dose{i}_paced"][name][data_metric] = \
                            all_data[f"dose{i}_paced"][name][data_met-
ric]/all_data["dose0_paced"][name][data_metric]
                        if data_metric == "apd80":
```

```
                    norm_all_data[f"dose{i}_paced"][name][f"delta_{data_metric}"] \
                    = (all_data[f"dose{i}_paced"][name][data_metric]) -
(all_data["dose0_paced"][name][data_metric])
    return norm_all_data

def calc_stats(metric_data):
    """
    From a dictionary of lists to 4 dictionaries of statistical quantities.

    Args:
        metric_data - nested dictionary with [combination to take average across] as
            keys on the first level, metric on the second level, and list/array
            of floats on third level

    Returns:
        mean - nested dictionary
        std - nested dictionary
        num_samples - nested dictionary
        sem - nested dictionary; where all of these have the same structure as
            metric_data, except from having a single float at last level

    """
    mean = defaultdict(lambda: defaultdict(float))
    std = defaultdict(lambda: defaultdict(float))
    num_samples = defaultdict(lambda: defaultdict(float))
    sem = defaultdict(lambda: defaultdict(float))
    for key in metric_data.keys():
        for metric in metric_data[key]:
            if len(metric_data[key][metric]) >1:

                metric_data[key][metric] = outliers(metric_data[key][metric])
                mean[key][metric] = np.mean(metric_data[key][metric])
                std[key][metric] = np.std(metric_data[key][metric])
                num_samples[key][metric] = len(metric_data[key][metric])
                sem[key][metric] = std[key][metric]/np.sqrt(num_samples[key][metric])

    return mean, std, num_samples, sem

def outliers(array):
    #print("array:", array)
    if len(array) > 5:
        Q1 = np.quantile(array, .25)
        Q3 = np.quantile(array, .75)
        IQR = Q3-Q1
        lowbound = Q1 - (IQR*1.5)
        upbound = Q1 + (IQR*1.5)

        new_array = []
```

```
        for data in array:
            if data >= lowbound and data <= upbound:
                new_array.append(data)
        return np.array(new_array)

    else:
        return array
    #print("newarray:", new_array)

def save_dict_to_csv(metric_data: dict, list_in:list, norm:int):
    """
    dictionary -> csv file

    Arguments:
        metric_data - list of a dictionary with name: max force, symmerty diff, str_info
        output_folder - save plot here
    """
    #print(metric_data)
    if norm == 1:
        output_file = os.path.join(output_folder, f"metric_dict_{list_in}.csv")
        for key in metric_data.keys():
            dict_copy = {}
            for key2 in metric_data[key].keys():
                dict_copy[f"[1]_{key2}"] = metric_data[key][key2]
            dataframe = pd.DataFrame(dict_copy)
            dataframe.to_csv(output_file, mode="a")

        print(f"Data saved to {output_file}.")

    elif norm == 2:
        output_file = os.path.join(output_folder, f"metric_dict_{list_in}_normalized.csv")
        for key in metric_data.keys():
            dict_copy = {}
            for key2 in metric_data[key].keys():
                dict_copy[f"[1]_{key2}"] = metric_data[key][key2]
            dataframe = pd.DataFrame(dict_copy)
            dataframe.to_csv(output_file, mode="a")

        print(f"Data saved to {output_file}.")

    elif norm ==3:
        output_file = os.path.join(output_folder, f"metric_dict_{list_in}_dFF0.csv")
        dataframe = pd.DataFrame(metric_data)
        dataframe.to_csv(output_file, mode="a")

def save_data_to_csv(stats: list, input_files: list, list_in:list, norm:bool):
    """

    dictionary -> csv file
```

```
    TODO: Work with this to get the output format you want.

    Arguments:
        stats - list of 4 dictionaries
        output_folder - save plot here

    """

    mean, std, num_samples, sem = stats
    if norm:
        output_file = os.path.join(output_folder, f"metrics_stats{list_in}_normalized.csv")
    else:
        output_file = os.path.join(output_folder, f"metrics_stats{list_in}.csv")

    # assume here all stats dictionaries have the same keys
    metrics_data = defaultdict(lambda: defaultdict(float))


    for str_info in mean.keys():
            for metric in mean[str_info].keys():
                #print(str_info)
                #print(metric)
                metrics_data[str_info][f"{metric}_mean"] = mean[str_info][metric]
                metrics_data[str_info][f"{metric}_SEM"] = sem[str_info][metric]
                metrics_data[str_info][f"{metric}_n"] = num_samples[str_info][metric]


    metrics_data["input_files"]["all files"] = input_files
    metrics_data["values"]["all values"] = mean

    dataframe = pd.DataFrame(metrics_data)
    dataframe.to_csv(output_file)
    print(f"Data saved to {output_file}.")


def plot_all_metrics(stats: list, metrics: list, units: list, output_folder: str):
    """

    This isn't as pretty as Prism plot but give a quick overview.

    Args:
        stats - list of dictionaries, expected to be [mean, std, num_samples, sem]
        metrics - metrics we want to consider
        units - corresponding units
        output_folder - save plot here

    """
```

```
    mean, _, _, sem = stats

    all_info_str = list(mean.keys())

    _, axes = plt.subplots(len(metrics), sharex=True)

    for (metric, unit, axis) in zip(metrics, units, axes):
        for (index, info_str) in enumerate(all_info_str):
            axis.errorbar([index], mean[info_str][metric], yerr=sem[info_str][metric], fmt='o')

        ylabel = f"{metric} ({unit})"
        ylabel = ylabel.replace("_", " ")
        ylabel = ylabel.capitalize()

        axis.set_ylabel(ylabel)

    num_labels = len(all_info_str)
    axes[-1].set_xlim(-0.5, num_labels-0.5)    # just making it pretty
    axes[-1].set_xticks(range(num_labels))
    axes[-1].set_xticklabels(all_info_str, rotation=45)

    plt.tight_layout()
    plt.savefig(os.path.join(output_folder, "metrics.png"))
    plt.show()      # comment this one out if it's annoying

if __name__ == "__main__":

    output_folder = sys.argv[1]
    red_input_files = get_input_files(sys.argv[1:], "Red")        # all files in all folders given on the command
line
    cyan_input_files = get_input_files(sys.argv[1:], "Cyan")
    long_cyan_input_files = get_input_files(sys.argv[1:], "Cyan_shorterROI")

    dose_max = get_dose_max(red_input_files)
    pacing_freq = get_pacing_freq(sys.argv[1:])
    data = {}
    file_list = {}
    file_list["red"] = red_input_files
    file_list["cyan"] = cyan_input_files
    file_list["long_cyan"] = long_cyan_input_files
    metrics = ["apd30","apd80", "apd90", "dFdt_max", "beating_frequency", "upstroke80", "tau75"]
    processed_metrics_spont = ["apd30", "beating_frequency", "apd80", "apd90", "dFdt_max", \
        "bpm", "apd80/apd30", "apd80-apd30", "c_apd30", "c_apd90", "c_apd80", \
        "c_apd80-apd30", "upstroke80", "tau75"]
    processed_metrics_paced = ["apd30", "apd80", "apd90", "dFdt_max", \
        "apd80/apd30", "apd80-apd30", "upstroke80", "tau75"]
    stats = [{}, {}, {}, {}]
    norm_list = ["normalized", "", "dFF0"]
    for list_in in file_list.keys():
```

```
stats, norm_stats, all_data, norm_all_data, deltaF_all = \
get_metrics_across_experiments(file_list[list_in], list_in, \
metrics, processed_metrics_spont, processed_metrics_paced, dose_max, sys.argv[1:], pacing_freq)

output_folder = "output"
os.makedirs(output_folder, exist_ok=True)

save_dict_to_csv(all_data, list_in, 1)
save_dict_to_csv(norm_all_data, list_in, 2)
save_dict_to_csv(deltaF_all, list_in, 3)
save_data_to_csv(stats, file_list[list_in], list_in, False)
save_data_to_csv(norm_stats, file_list[list_in], list_in, True)
```

Appendix II – Python Script for Automated Analysis of Mechanical Measurements

```
"""
Berenice Charrez / UC Berkeley / 2020
"""

import os
from collections import defaultdict, OrderedDict
import sys
import pandas as pd
import numpy as np
import matplotlib.pyplot as plt

from mpsmechanics.utils.data_layer import read_prev_layer
from mpsmechanics.utils.command_line import get_input_files
from mpsmechanics.mechanical_analysis.mechanical_analysis import \
        analyze_mechanics


def get_info_length(f_in: str):
    """

    Extracts information about the experiment from the path,

    Args:
        f_in - path to file; information about experiment
            should be specified here

    Taguchi array examples:
L1 = length1 = average of run1 run2 run3
W2 = width2 = average of run2 run5 run8 etc.

Run#    1       2       3       4       5       6       7       8       9
Length  1       1       1       2       2       2       3       3       3
Width   1       2       3       1       2       3       1       2       3
Exten   1       2       3       2       3       1       3       1       2
Valve   1       2       3       3       1       2       2       3       1
"""
```

```
    for run in ["Run1", "Run2", "Run3"]:
        if run in f_in:
            return "Length1"

    for run in ["Run4", "Run5", "Run6"]:
        if run in f_in:
            return "Length2"

    for run in ["Run7", "Run8", "Run9"]:
        if run in f_in:
            return "Length3"

    print("Error: Was not found to have any given length")


def get_info_width(f_in: str):


    for run in ["Run1", "Run4", "Run7"]:
        if run in f_in:
            return "Width1"

    for run in ["Run2", "Run5", "Run8"]:
        if run in f_in:
            return "Width2"

    for run in ["Run3", "Run6", "Run9"]:
        if run in f_in:
            return "Width3"

    print("Error: Was not found to have any given width")

def get_info_extension(f_in: str):


    for run in ["Run1", "Run6", "Run8"]:
        if run in f_in:
            return "Extension1"

    for run in ["Run2", "Run4", "Run9"]:
        if run in f_in:
            return "Extension2"

    for run in ["Run3", "Run5", "Run7"]:
        if run in f_in:
            return "Extension3"

    print("Error: Was not found to have any given ext")
```

```
def get_info_valve(f_in: str):

    for run in ["Run1", "Run5", "Run9"]:
        if run in f_in:
            return "Valve1"

    for run in ["Run2", "Run6", "Run7"]:
        if run in f_in:
            return "Valve2"

    for run in ["Run3", "Run4", "Run8"]:
        if run in f_in:
            return "Valve3"

    print("Error: Was not found to have any given valve")


def read_metric_data(f_in: str, metrics: list, type_metric: str):
    """
    Gets metric information from results from the mechanical analysis.

    Args:
        f_in - filename/path to BF file
        metrics - list of which metrics we're interested in
        type_metric - str giving kind of metrics; expected to be in
            ["metrics_max_avg", "metrics_avg_avg", "metrics_max_std",\
             "metrics_avg_std", "metrics_int_avg", "metrics_int_std""]

    Returns:
        dictionary with metrics as keys, corresponing calculated metric
            for the given input file as values

    """

    exp_type_metrics = ["metrics_max_avg", "metrics_avg_avg", \
    "metrics_max_std", "metrics_avg_std", "metrics_int_avg", "metrics_int_std"]
    assert type_metric in exp_type_metrics, \
            f"Error: type_metric expected to be in {exp_type_metrics}, " + \
                    f"but argument {type_metric} given."

    metric_information = {}
    #print("f_in_read:", f_in)
    analyze_mechanics_results = read_prev_layer(f_in, analyze_mechanics)


    all_metrics = analyze_mechanics_results[type_metric]

    #print(all_metrics)
```

```
    for metric in metrics:
        metric_information[metric] = all_metrics[metric]

    return metric_information



def get_metrics_across_experiments(input_files: list,
                                   average_across: dict,
                                   metrics: list,
                                   type_metric: str,
                                   get_info):
    """
    Args:
        input_files - list of (BF) files to do analysis for
        average_across - dictionary where
            keys = which kind of thing we consider (e.g. "doses")
            values = list of corresponding possible values (e.g. "dose0", "dose1")
        metrics - list of metrics we want to consider
        type_metric - str giving kind of metrics; expected to be in
            ["metrics_max_avg", "metrics_avg_avg", "metrics_max_std", "metrics_max_std"]

    Returns:
        list of 4 dictionaries (mean, std, num_samples, sem) where each is a
            nested dictionary with information from average_across on first level,
            metric on second level and a single value on the third level

    """

    # first dimension: str of combination of across values; second dimension: metric

    metric_data = defaultdict(lambda: defaultdict(list))
    all_data={}

    for f_in in input_files:
        start,end = os.path.split(f_in)
        end2 = os.path.splitext(end)
        name=end2[0]
        all_data[name]={}
        str_information = get_info(f_in)        # e.g. "dose1_1Hz"
        metric_information = read_metric_data(f_in, metrics, type_metric)
         # e.g. {"velocity" : 2}

        for keys in metric_information:
            all_data[name][keys] = metric_information[keys]

        for metric in metrics:
            metric_val = metric_information[metric]
            if not np.isnan(metric_val):
```

```
                metric_data[str_information][metric].append(metric_val)

    stats = calc_stats(metric_data)

    return stats, all_data


def calc_stats(metric_data):
    """
    From a dictionary of lists to 4 dictionaries of statistical quantities.

    Args:
        metric_data - nested dictionary with [combination to take average across] as
            keys on the first level, metric on the second level, and list/array
            of floats on third level

    Returns:
        mean - nested dictionary
        std - nested dictionary
        num_samples - nested dictionary
        sem - nested dictionary; where all of these have the same structure as
            metric_data, except from having a single float at last level

    """
    mean = defaultdict(lambda: defaultdict(float))
    std = defaultdict(lambda: defaultdict(float))
    num_samples = defaultdict(lambda: defaultdict(float))
    sem = defaultdict(lambda: defaultdict(float))

    for str_info in metric_data.keys():
        for metric in metric_data[str_info].keys():

            metric_data[str_info][metric] = outliers(metric_data[str_info][metric])
            mean[str_info][metric] = np.mean(metric_data[str_info][metric])
            std[str_info][metric] = np.std(metric_data[str_info][metric])
            num_samples[str_info][metric] = len(metric_data[str_info][metric])
            sem[str_info][metric] = std[str_info][metric]/np.sqrt(num_samples[str_info][metric])

    return mean, std, num_samples, sem


def outliers(array):
    Q1 = np.quantile(array, .25)
    Q3 = np.quantile(array, .75)
    IQR = Q3-Q1
    lowbound = Q1 - (IQR*1.5)
    upbound = Q1 + (IQR*1.5)

    new_array = []
```

```
    for data in array:
        if data >= lowbound and data <= upbound:
            new_array.append(data

    return np.array(new_array)

def save_dict_to_csv(metric_data: dict):
    """
    dictionary -> csv file

    Arguments:
        metric_data - list of a dictionary with name: max force, symmerty diff, str_info
        output_folder - save plot here
    """
    print(metric_data)

    output_file = os.path.join(output_folder, f"metric_dict.csv")

    dataframe = pd.DataFrame(metric_data)

    dataframe.to_csv(output_file)
    print(f"Data saved to {output_file}.")


def save_data_to_csv(stats: list, input_files: list):
    """
    dictionary -> csv file

    Arguments:
        stats - list of 4 dictionaries
        output_folder - save plot here

    """

    mean, std, num_samples, sem = stats
    output_file = os.path.join(output_folder, f"metrics_stats.csv")

    # assume here all stats dictionaries have the same keys
    metrics_data = defaultdict(lambda: defaultdict(float))


    for str_info in mean.keys():
            for metric in mean[str_info].keys():
                #print(str_info)
                #print(metric)
                metrics_data[str_info][f"{metric}_mean"] = mean[str_info][metric]
                metrics_data[str_info][f"{metric}_SEM"] = sem[str_info][metric]
                metrics_data[str_info][f"{metric}_n"] = num_samples[str_info][metric]
```

```
    metrics_data["input_files"]["all files"] = input_files
    metrics_data["values"]["all values"] = mean

    dataframe = pd.DataFrame(metrics_data)
    dataframe.to_csv(output_file)
    print(f"Data saved to {output_file}.")


def plot_all_metrics(stats: list, metrics: list, units: list, output_folder: str):
    """
    Args:
        stats - list of dictionaries, expected to be [mean, std, num_samples, sem]
        metrics - metrics we want to consider
        units - corresponding units
        output_folder - save plot here
    """

    mean, _, _, sem = stats

    all_info_str = list(mean.keys())

    _, axes = plt.subplots(len(metrics), sharex=True)

    for (metric, unit, axis) in zip(metrics, units, axes):
        for (index, info_str) in enumerate(all_info_str):
            axis.errorbar([index], mean[info_str][metric], yerr=sem[info_str][metric], fmt='o')

        ylabel = f"{metric} ({unit})"
        ylabel = ylabel.replace("_", " ")
        ylabel = ylabel.capitalize()

        axis.set_ylabel(ylabel)

    num_labels = len(all_info_str)
    axes[-1].set_xlim(-0.5, num_labels-0.5)    # just making it pretty
    axes[-1].set_xticks(range(num_labels))
    axes[-1].set_xticklabels(all_info_str, rotation=45)

    plt.tight_layout()
    plt.savefig(os.path.join(output_folder, "metrics.png"))
    plt.show()      # comment this one out if it's annoying

def get_mean(input_files: list, metrics: list, type_metric: str):
    """
    Extract the information we need; give us mean values.

    Args:
```

```
        input_files - list of (BF) files to do analysis for
        metrics - list of metrics we want to consider
        type_metric - "metrics_avg_avg"

    Returns:
        list of 1 dictionaries (mean)
    """

    metric_data = defaultdict(lambda: defaultdict(list))
    mean = defaultdict(lambda: defaultdict(float))

    for f_in in input_files:

        #str_information = get_info(f_in)        # e.g. "dose1_1Hz"
        metric_information = read_metric_data(f_in, metrics, type_metric)
         # e.g. {"velocity" : 2}

        for metric in metrics:
            metric_val = metric_information[metric]
            if not np.isnan(metric_val):
                metric_data[f_in][metric].append(metric_val)

    for str_info in metric_data.keys():
        for metric in metric_data[str_info].keys():

            metric_data[str_info][metric] = outliers(metric_data[str_info][metric])
            mean[str_info][metric] = np.mean(metric_data[str_info][metric])

    return mean

if __name__ == "__main__":

    output_folder = sys.argv[1]
    input_files = get_input_files(sys.argv[1:], "BF")
    # all files/folders given on the command line

    average_across = ["Length", "Width", "Extension", "Valve"]
    metrics = ["xmotion","principal_strain", "tensile_strain", "compressive_strain"]

    get_info_functions = [get_info_length, get_info_width, get_info_extension, get_info_valve]
    stats = [{}, {}, {}, {}]

    for avg_across, get_info in zip(average_across, get_info_functions):
        av_acr = {avg_across : [f"{avg_across}{i+1}" for i in range(3)]}
        print(av_acr)
        new_stats, all_data = get_metrics_across_experiments(input_files, \
        av_acr, metrics, "metrics_int_avg", get_info)
        for i in range(4):
            stats[i] = {**stats[i], **new_stats[i]}
```

```
output_folder = "output"
os.makedirs(output_folder, exist_ok=True)

save_dict_to_csv(all_data)
save_data_to_csv(stats, input_files)

units = ["-","-", "-", "-"]

plot_all_metrics(stats, metrics, units, output_folder)
```

Appendix III – Python Script for Automated Analysis of Contraction Force

```
"""
Berenice Charrez / UC Berkeley / 2020
"""

import os
import glob
from collections import defaultdict, OrderedDict
import sys
import pandas as pd
import numpy as np
import matplotlib.pyplot as plt

from mpsmechanics.utils.data_layer import read_prev_layer
from mpsmechanics.utils.command_line import get_input_files
from mpsmechanics.pillar_tracking.pillar_tracking import \
        track_pillars, calc_int_avg
from mpsmechanics.mechanical_analysis.mechanical_analysis import \
        analyze_mechanics

def get_info_length(f_in: str):
    """

    Extracts information about the experiment from the path,

    Args:
        f_in - path to file; information about experiment
            should be specified here

    Taguchi array examples:
L1 = length1 = average of run1 run2 run3
W2 = width2 = average of run2 run5 run8 etc.

Run#    1       2       3       4       5       6       7       8       9
Length  1       1       1       2       2       2       3       3       3
Width   1       2       3       1       2       3       1       2       3
Exten   1       2       3       2       3       1       3       1       2
```

```
Valve   1       2       3       3       1       2       2       3       1
"""

    for run in ["Run1", "Run2", "Run3"]:
        if run in f_in:
            return "Length1"

    for run in ["Run4", "Run5", "Run6"]:
        if run in f_in:
            return "Length2"

    for run in ["Run7", "Run8", "Run9"]:
        if run in f_in:
            return "Length3"

    print("Error: Was not found to have any given length")


def get_info_width(f_in: str):


    for run in ["Run1", "Run4", "Run7"]:
        if run in f_in:
            return "Width1"

    for run in ["Run2", "Run5", "Run8"]:
        if run in f_in:
            return "Width2"

    for run in ["Run3", "Run6", "Run9"]:
        if run in f_in:
            return "Width3"

    print("Error: Was not found to have any given width")

def get_info_extension(f_in: str):


    for run in ["Run1", "Run6", "Run8"]:
        if run in f_in:
            return "Extension1"

    for run in ["Run2", "Run4", "Run9"]:
        if run in f_in:
            return "Extension2"

    for run in ["Run3", "Run5", "Run7"]:
        if run in f_in:
            return "Extension3"
```

```
    print("Error: Was not found to have any given ext")

def get_info_valve(f_in: str):

    for run in ["Run1", "Run5", "Run9"]:
        if run in f_in:
            return "Valve1"

    for run in ["Run2", "Run6", "Run7"]:
        if run in f_in:
            return "Valve2"

    for run in ["Run3", "Run4", "Run8"]:
        if run in f_in:
            return "Valve3"

    print("Error: Was not found to have any given valve")


def read_metric_data(f_in: str, metrics: list, param_list: dict):
    """
    Gets metric information from results from the pillar tracking.

    Args:
        f_in - filename/path to BF file
        metrics - list of which metrics we're interested in

    Returns:
        dictionary with metrics as keys, corresponing calculated metric
            for the given input file as values

    """

    metric_information = {}
    track_pillars_results = read_prev_layer(f_in, track_pillars, param_list)


    for metric in metrics:
        metric_information[metric] = track_pillars_results[metric]

    return metric_information



def get_metrics_across_experiments(input_files: list,
                                   average_across: dict,
                                   param_dict: dict,
                                   metrics: list,
```

```
                        get_info):
"""

Extract the information we need; make it into statisitcs.

Args:
   input_files - list of (BF) files to do analysis for
   average_across - dictionary where
      keys = which kind of thing we consider (taguchi - length, width, ext, valve)
      values = list of corresponding possible values (1, 2, 3)
   metrics - list of metrics we want to consider (force per area)

Returns:
   list of 4 dictionaries (mean, std, num_samples, sem) where each is a
      nested dictionary with information from average_across on first level,
      metric on second level and a single value on the third level

calc_relevant metric: gives out a dictionary with stats for given metrics
      "all_values": values,
      "folded": folded,
      "over_time_avg": over_time_avg,
      "over_time_std": over_time_std,
      "metrics_max_avg": metrics_max_avg,
      "metrics_avg_avg": metrics_avg_avg,
      "metrics_max_std": metrics_max_std,
      "metrics_avg_std": metrics_avg_std,
      "metrics_int_avg": metrics_int_avg,
      "metrics_int_std": metrics_int_std,

"""

param_list = [{},{},{}]
interval_list = []
data_dict = {}

metric_data = defaultdict(lambda: defaultdict(list))

for f_in in input_files:
   name=os.path.splitext(f_in)
   for keys in param_dict.keys():
      name2=os.path.split(keys)
      name3, end = os.path.split(name2[0])
      if name[0] == name3:
         param_list=[{},{},{'motion_scaling_factor': param_dict[keys]}]

      else:
         continue

   str_information = get_info(f_in)
```

```
        metric_information = read_metric_data(f_in, metrics, param_list)
        # force per area, 195x4x2
        interval_list = get_intervals(f_in)

        for arrays in metric_information:
            metrics_int_avg=calc_int_avg(metric_information[arrays], interval_list)
             #max force per pillar [1x #pillar]

        metric_max = get_max_metric (metrics_int_avg)  # one number = max force
        data_dict[f_in] = {}
        for values in data_dict:
                data_dict[f_in]["metrics_int_avg"] = metrics_int_avg
                data_dict[f_in]["metric_max"] = metric_max
                data_dict[f_in]["str_info"] = str_information

    print("data_dict", data_dict)
    metric_data = match_max(data_dict)
#metric data is a dict with keys as chip_name and values as (max_force and symmetry_diff and str_info)
    stats = calc_stats (metric_data, average_across)
    return stats, metric_data

def match_max(data_dict: dict):

    metric_data = {}
    chip_name = []
    pair_dict = {}
    for (counter,f_in) in enumerate(data_dict.keys()):
        start,end = os.path.split(f_in)
        end2 = os.path.splitext(end)
        run = ["Run1", "Run2", "Run3"]
        if any (x in f_in for x in run):
            end3=end2[0].rsplit('_',3)
            chip_name.append(end3[0])
            max_top = 0
            max_bottom = 0

            for i in range (int(len(data_dict[f_in]["metrics_int_avg"])/2)):
#look at the top and bottom pillars of the same file and compare max force from top with max force from
bottom
                i_2= i + int(len(data_dict[f_in]["metrics_int_avg"])/2)
                if data_dict[f_in]["metrics_int_avg"][i] > max_top:
                    max_top = data_dict[f_in]["metrics_int_avg"][i]
                if data_dict[f_in]["metrics_int_avg"][i_2] > max_bottom:
                    max_bottom = data_dict[f_in]["metrics_int_avg"][i_2]

                match_diff = (max_top-max_bottom)**2
                chip_name_counter = chip_name[counter]
                metric_data[chip_name_counter]={}
                metric_data[chip_name_counter]["max_force"] = data_dict[f_in]["metric_max"]
```

```
            metric_data[chip_name_counter]["symmetry_diff"] = match_diff
            metric_data[chip_name_counter]["str_info"] = data_dict[f_in]["str_info"]

        else:
            end3=end2[0].rsplit('_',4)
            chip_name.append(end3[0])

    pair_dict = find_duplicates(chip_name)

    for names in chip_name:
#look at same file names (top vs bottom), compare each files metric_max
        for keys in pair_dict:
            if names == keys:
                position1 = pair_dict[keys][0]
                position2 = pair_dict[keys][1]
                key_temp1 = list(data_dict)[position1]
                key_temp2 = list(data_dict)[position2]
                match_diff = (data_dict[key_temp1]["metric_max"] - data_dict[key_temp2]["metric_max"])**2

                if data_dict[key_temp1]["metric_max"] > data_dict[key_temp2]["metric_max"]:
                    metric_max = data_dict[key_temp1]["metric_max"]
                else:
                    metric_max = data_dict[key_temp2]["metric_max"]

                chip_name_pos = chip_name[position1]
                metric_data[chip_name_pos]={}
                metric_data[chip_name_pos]["max_force"] = metric_max
                metric_data[chip_name_pos]["symmetry_diff"] = match_diff
                metric_data[chip_name_pos]["str_info"] = data_dict[key_temp1]["str_info"]

    return metric_data

def find_duplicates(chip_name: list):
    new_dict = {}
    tally = defaultdict(list)
    for counter,item in enumerate(chip_name):
        tally[item].append(counter)
    for key,locs in tally.items():
        if len(locs)>1:
            new_dict[key] = locs
    return new_dict

def get_max_metric (metrics_int_avg):

    if isinstance(metrics_int_avg, float):
        metric_max = metrics_int_avg
    else:
        for values in metrics_int_avg:
            metric_max = np.nanmax(metrics_int_avg)
```

```
    return metric_max

def _walk_glob(argument_list):
    input_files = []
    for arg in argument_list:
        input_files.extend(glob.glob(arg))
    return input_files

def find_param_dict(argument_list):

    param_dict = {}
    input_files =_walk_glob([os.path.join(argument_list, "*", "*", "*")])

    for a_file in input_files:
        if a_file.find("track_pillars") != -1:
            #print("found .npy track pillar?", a_file)
            base=os.path.basename(a_file)
            scaling=base.rsplit('_',1)[1]
            scaling_factor=float(f"{scaling[0]}.{scaling[2]}")
            new_dict = {a_file : scaling_factor}
            param_dict.update(new_dict)

        else:
            continue

    return param_dict

def get_intervals(f_in: str):

    interval_list = []
    analyze_mechanics_results = read_prev_layer(f_in, analyze_mechanics)
    interval_list = analyze_mechanics_results["intervals"]

    return interval_list

def calc_stats(metric_data, average_across: dict):
    """

    From a dictionary of lists to 4 dictionaries of statistical quantities.

    detects outliers

    Args:
        metric_data - nested dictionary with [combination to take average across] as
            keys on the first level, metric on the second level, and list/array
            of floats on third level

    Returns:
```

```
        mean - nested dictionary
        std - nested dictionary
        num_samples - nested dictionary
        sem - nested dictionary; where all of these have the same structure as
            metric_data, except from having a single float at last level

    """
    mean = defaultdict(lambda: defaultdict(float))
    std = defaultdict(lambda: defaultdict(float))
    num_samples = defaultdict(lambda: defaultdict(float))
    sem = defaultdict(lambda: defaultdict(float))

    for av_acr in average_across:
        for  param in average_across[av_acr]:
            temp_dict = {}
            temp_dict["max_force"] = []
            temp_dict["symmetry_diff"] = []

            for names in metric_data:
                if metric_data[names]["str_info"] == param:
                    temp_dict["max_force"].append(metric_data[names]["max_force"])
                    temp_dict["symmetry_diff"].append(metric_data[names]["symmetry_diff"])

            for keys in temp_dict:
                if len(temp_dict[keys])!= 0:
                    temp_dict[keys] = outliers(temp_dict[keys])
                    mean[param][keys] = np.mean(temp_dict[keys])
                    std[param][keys] = np.std(temp_dict[keys])
                    num_samples[param][keys] = len(temp_dict[keys])
                    sem[param][keys] = std[param][keys]/np.sqrt(num_samples[param][keys])

                else:
                    continue

    return mean, std, num_samples, sem


def outliers(array):

    Q1 = np.quantile(array, .25)
    Q3 = np.quantile(array, .75)
    IQR = Q3-Q1
    lowbound = Q1 - (IQR*1.5)
    upbound = Q1 + (IQR*1.5)

    new_array = []

    for data in array:
        if data >= lowbound and data <= upbound:
```

```
            new_array.append(data)
    return np.array(new_array)

def save_stats_to_csv(stats: list, input_files: list):
    """

    dictionary -> csv file

    TODO: Work with this to get the output format you want.

    Arguments:
        stats - list of 4 dictionaries
        output_folder - save plot here

    """

    mean, std, num_samples, sem = stats
    output_file = os.path.join(output_folder, f"force_metrics_stats.csv")

    # assume here all stats dictionaries have the same keys
    metrics_data = defaultdict(lambda: defaultdict(float))

    for str_info in mean.keys():
            for metric in mean[str_info].keys():
                metrics_data[str_info][f"{metric}_mean"] = mean[str_info][metric]
                metrics_data[str_info][f"{metric}_SEM"] = sem[str_info][metric]
                metrics_data[str_info][f"{metric}_n"] = num_samples[str_info][metric]

    dataframe = pd.DataFrame(metrics_data)
    dataframe.to_csv(output_file)
    print(f"Data saved to {output_file}.")

def save_dict_to_csv(metric_data: dict):
    """

    dictionary -> csv file

    Arguments:
        metric_data - list of a dictionary with name: max force, symmerty diff, str_info
        output_folder - save plot here
    """
    output_file = os.path.join(output_folder, f"force_metric_dict.csv")

    dataframe = pd.DataFrame(metric_data)

    dataframe.to_csv(output_file)
    print(f"Data saved to {output_file}.")

def plot_all_metrics(stats: list, output_folder: str):
```

```
    """

    This isn't as pretty as Prism plot but give a quick overview.

    Args:
        stats - list of dictionaries, expected to be [mean, std, num_samples, sem]
        metrics - metrics we want to consider
        units - corresponding units
        output_folder - save plot here

    """

    mean, _, _, sem = stats

    all_info_str = list(mean.keys())
    length=[]
    units= ["mN/mm2", "-"]
    for keys in mean:
        for count, key2 in enumerate(mean[keys].keys()):
            length.append(count)

    num_subplot = int(len(length)/len(mean.keys()))

    _, axes = plt.subplots(num_subplot, sharex=True)
    for keys in mean:
        for (axis, key2, unit) in zip(axes, mean[keys], units):
            for (index, info_str) in enumerate(all_info_str):
                axis.errorbar([index], mean[info_str][key2], yerr=sem[info_str][key2], fmt='o')

            ylabel = f"{key2} ({unit})"
            ylabel = ylabel.replace("_", " ")
            ylabel = ylabel.capitalize()
            axis.set_ylabel(ylabel)

    num_labels = len(all_info_str)
    axes[-1].set_xlim(-0.5, num_labels-0.5)    # just making it pretty
    axes[-1].set_xticks(range(num_labels))
    axes[-1].set_xticklabels(all_info_str, rotation=45)

    plt.tight_layout()
    plt.savefig(os.path.join(output_folder, "force_metrics.png"))
    plt.show()      # comment this one out if it's annoying


if __name__ == "__main__":

    output_folder = sys.argv[1]
    input_files = get_input_files(sys.argv[1:], "BF")
    # all files/folders given on the command line
```

```
    param_dict = find_param_dict (sys.argv[1])

    average_across = ["Length", "Width", "Extension", "Valve"]
    metrics = ["force_per_area"]

    get_info_functions = [get_info_length, get_info_width, get_info_extension, get_info_valve]
    stats = [{}, {}, {}, {}]

    for avg_across, get_info in zip(average_across, get_info_functions):
        #print("function", get_info)
        av_acr = {avg_across : [f"{avg_across}{i+1}" for i in range(3)]}
        print(av_acr)
        new_stats, all_data = get_metrics_across_experiments(input_files, av_acr, param_dict, metrics,
get_info)
        for i in range(4):
            stats[i] = {**stats[i], **new_stats[i]}

    output_folder = "output"
    os.makedirs(output_folder, exist_ok=True)

    save_dict_to_csv(all_data)
    save_stats_to_csv(stats, input_files)

    plot_all_metrics(stats, output_folder)
```